PERFLUOROCARBON NANODROPLETS FOR EXTRAVASCULAR IMAGING APPLICATIONS

A Dissertation
Presented to
The Academic Faculty

by

Steven Karl Yarmoska

In Partial Fulfillment
of the Requirements for the Degree
Doctor of Philosophy in the
Wallace H. Coulter Department of Biomedical Engineering

Georgia Institute of Technology & Emory University
May 2020

PERFLUOROCARBON NANODROPLETS FOR EXTRAVASCULAR IMAGING APPLICATIONS

Approved by:

Dr. Stanislav Y. Emelianov, Advisor
School of Electrical and Computer Engineering
Georgia Institute of Technology

Dr. Melissa Gilbert-Ross
Department of Hematology and Medical Oncology
Emory University

Dr. J. Brandon Dixon
George W. Woodruff School of Mechanical Engineering
Georgia Institute of Technology

Dr. Brooks D. Lindsey
Wallace H. Coulter Department of Biomedical Engineering
Georgia Institute of Technology and Emory University

Dr. Paul S. García
Department of Anesthesiology
Columbia University Medical Center

Date Approved: March 13, 2020

To Karl Rudolf Maier, who helped me to reach this point from up above

ACKNOWLEDGEMENTS

First, I would like to thank the M.D.-Ph.D. Program at the University of Texas Medical Branch at Galveston and the (now defunct) joint training program with the University of Texas at Austin. I was spurned by every other dual-degree training program to which I applied, but the program at UTMB and UT Austin believed in me and gave me the opportunity to pursue training as a physician-scientist. Everything I have accomplished since, and everything that I will go on to achieve in my future career, is rooted in this show of faith. To Larry Sowers, Randy Goldblum, and Karen Browning: thank you. Although I ultimately elected to transfer from this program, I will be forever grateful for your belief and generosity. You opened the door to make all of this possible.

I would like to thank my original cohort of M.D.-Ph.D. students at UTMB: Maria Ansar, Ron Besandre, Maggie Hsu, Amanda Randolph, and Shinji Strain. You got me through the darkest depths of my preclinical training in medical school. Leaving all of you was the most difficult part of my decision to come to Georgia. I would also like to thank my unofficial M.D.-Ph.D. "Big," Yekki Song, as well as my friends and colleagues from the M.D. Class of 2017 at UTMB. I've enjoyed seeing your medical careers blossom during my time in graduate school. I look forward to rejoining you in the clinic soon.

Next, I would like to thank my labmates from UT Austin: Carolyn Bayer, Yun-Sheng Chen, Jason Cook, Nich Dana, Geoffrey Luke, Seung Yun Nam, Laura Ricles, Doug Yeager, and Soon Joon Yoon. Thank you for showing me the ropes. I've particularly enjoyed seeing Carolyn and Geoff at conferences as faculty while I've pursued my Ph.D. at Tech. You showed me what a collegial and thriving lab should be. If I am entrusted to

run my own research program, I hope to emulate the environment that you all created during our time together in Austin.

Now, I would like to thank my labmates at Georgia Tech:

I would like to thank Alex Hannah. Like Geoff, you showed me the ropes as a fledgling graduate student. One of my first memories from my time in the lab was going to your Fourth of July party in Austin. Thank you for taking the time to make me feel like I belonged, both in and outside the lab. I appreciate all of the effort you spent in helping to set up our operation at Georgia Tech, and I miss our office conversations and volleyball games.

I would like to thank Andrea Martínez. It was a privilege and a pleasure to mentor you in research. Everyone else who I will mentor in a research setting for the rest of my career will have the difficult task of measuring up to the high standard that you set. I am immensely proud of what you accomplished during our brief time together in the lab, and I am even more proud of what you will continue to accomplish in your studies of medicine at Emory. I look forward to seeing you on the wards.

I would like to thank Andrei Karpiouk. Your expertise in lasers saved my experimental hardware setup on more than one occasion. I enjoyed travelling with you in Scotland last year. Thank you for all of the Russian chocolates over the years. I appreciate everything you've done for the lab managing equipment and laser safety. We are lucky to have you.

I would like to thank Andrew Zhao. Your help and advice really helped get the adjuvant particle work off the ground. I will remember our time exploring Glasgow and Edinburgh fondly, and I enjoy our conversations about academia and Tech. I hope your committee is as transformative for your projects as my committee were for mine, and I wish you all the best in the remainder of your Ph.D. studies.

I would like to thank Brandyn Orr. You were critical in executing a lot of my studies. I am truly thankful for all of the histology sectioned, reagents prepped, and cells fed. My dissertation wouldn't have been completed without you. Your hard work does not go unnoticed, and I am sure that other members are just as grateful for your contributions to the lab. I've enjoyed our office conversations and impromptu lunch trips over the years, especially these last few months.

I would like to thank Daniela Santiesteban. Your positive and exuberant energy lifted up the lab. Although Andrew quickly supplanted you as the messiest lab member after you graduated, no one could ever replace your spirit. Many of my favorite memories from my time in grad school are times that we spent together: the Brunch Festival, bar hopping in Buckhead, Karaoke Melody, Music Midtown, and Oktoberfest in Helen. I am an only child, but our relationship is what I imagine having an older sister feels like.

I would like to thank Diego Dumani. I appreciate all of the time you took to help me with animal work and the patience you had for me in both in and out of the lab. I'll always fondly remember our trips to United and Hawks matches, crazy outings with Daniela, and your wild birthday party that Changhan unfortunately couldn't attend. I look

forward to seeing your lab and career take off in Costa Rica. I hope the science is rewarding and the avocados are plentiful. ¡Pura vida!

I would like to thank Don VanderLaan. I admire the sense of awe and wonder you exude when talking about your research or explaining equipment. I would be fortunate to retain even a fraction of this level of exuberance as I continue through my academic career. Thank you for the design of the well-plate lasing system; it has proven invaluable for my and other *in vitro* studies in the lab. I wish you continued joy and productivity in the lab and hope you find what you're looking for in academic life.

I would like to thank Eleanor (Donnelly) Barber. You were truly the "Fairy Lab Mother." I don't think that I would have finished my Ph.D. without your teaching, wisdom, and guidance. Your last piece of advice to me before leaving the lab really turned my graduate experience around. I loved our lunchtime conversations and our impromptu lunch escapades. It was a joy to visit you and your family in Ireland. I'm glad that you are living your dreams and that we will both be "mudphuds" when this is all over.

I would like to thank Heechul Yoon. My research would have gone nowhere without your help. When you become a professor, your students will be lucky to have you as a mentor. I miss our car rides to and from Emory University Hospital Midtown, our long days and late nights in the dry lab working on the Verasonics, and our conversations about everything from research to how much your son loved Minecraft. Thank you and your mom for hosting Kelsey and I in Seoul; it is a beautiful city and I will have to come back to see more of it.

I would like to thank In-Cheol Sun. I still chuckle every time I think of your “Me no speak English” one-liner to get out of reviewing applicant resumes. I enjoyed exploring downtown D.C. with you at IUS 2016. You always knew where to find the best food and, more importantly, the free food around campus. I wish I got to know you better during our time together in Texas and Georgia. I hope you are enjoying life at KIST.

I would like to thank Jingfei Liu. I have enjoyed our thoughtful conversations over the years, both about science and about life. I learned much from you; I hope my contributions to our discussions were equally as enlightening. I admire your ability to balance obligations in research, teaching, and family life. I would be lucky to have even a fraction of this level of stability as I move on in my own career. I look forward to seeing your successful transition into professorship. Your mentees will be lucky to have you!

I would like to thank Jisha Vadakkancheril Somasekharan. I’ll always remember the glimmer of excitement in your eyes every time we talked about chemistry or designing a new type of nanoparticle. I am thankful for all that you taught me; I am a better wet lab scientist because of you. If I become a professor, I hope that I can teach with the same exuberance and joy that you taught me. I wish we had more time in the lab together. Hopefully, I can take you up on your offer to host me in Kerala.

I would like to thank Kelsey Kubelick. It’s funny that our introduction was me unknowingly trying to steal your desk. Sorry! I guess this set the stage for five years’ worth of my comical hijinks. I’ll always remember our time travelling in Japan and South Korea fondly. I wish we could have become better friends, but I know you like to keep work and

life separate. I'm not sure if you'll be able to maintain this arrangement in academia if you progress down the tenure track, but I'm rooting for you.

I would like to thank Kristina Hallam. You were a trusted friend both in and out of lab. I cherished our time together, whether it was screaming our lungs out in Mercedes Benz Stadium when Atlanta United won the MLS Cup or dancing to music in the wet lab during cleanup. You were there for me during the lowest points of my grad school career. I am grateful that you are a part of my life. I'll still keep sending you quality tweets from WeRateDogs, even though you're back in Dallas now.

I would like to thank Robin Hartman. Now that I'm in the position you were at the end of your year in Atlanta, I finally understand (and agree with) a lot of your thoughts on the whole graduate experience. I look forward to our in-game conversations about Texas football; we'll see if Tom Herman is still the head coach after the embargo on this dissertation is lifted. I hope that our paths will cross again in Austin.

I would like to thank Tim Sowers. I'm glad that fate brought us together and I was able to recruit you to the lab. I enjoyed our times together outside the lab, from the Ice Cream Festival to the MLS Cup Playoffs. I miss our lunchtime conversations and Game of Thrones discussions with Eleanor. I wish all the best to you and Liza. Sorry that my defense was double calendared with your wedding!

I would like to thank Yiying Zhu. The CLUE code that you wrote for volumetric acquisitions and ultrafast pulse-inversion imaging added a critical dimension to my small animal imaging studies. I fondly remember our trips to Atlanta United, to the Atlanta Braves and Zedd concert, and to Scotland for IUS. I look forward to seeing your academic

career grow wings and soar when you achieve your dream of becoming a professor. I hope that we will get the opportunity to work together again in the next stages of our careers!

There are many other lab members over the years that I would like to thank for the parts they played in my journey: Ashley Alva, Changhan Yoon, Ethan Smith, Fiona Splaine, Makenna Laffey, Hein de Hoop, Jaesok Yu, Jurjen Leer, Lingyi Zhao, and Yury Kabatskiy. I would also like to give a special thank you to Jinhwan Kim who made a critical assist in the adjuvant nanodroplet project in the 11th hour of my dissertation studies. To the next generation of the lab; Jeehyun Lee, David Qin, and Anthony Yu; I wish you the best of luck. The lab is a far different place now than it was when I joined nearly 7 years ago. It is up to you to either inhabit this new environment or to find your voices, become your own advocates, and change it into one that better suits you and your collective training.

Of course, I would like to thank my advisor, Stas Emelianov. I will always be grateful to you for the role you played in my transfer into the Emory MSTP, a community that profoundly changed my life. There are few advisors who would support a student designing a clinical trial from the ground up, but you gave me that opportunity, as well. Although I'm disappointed with how that project ended, I am thankful for the experience and knowledge gained during the process. I am also thankful for the intellectual freedom you granted me during my graduate studies, which is in stark contrast to how most graduate students are trained. I hope that the vision and creativity I honed during this time will pay dividends later in my career.

I would also like to thank Brandon Dixon for his mentorship and the role he played in shaping the studies I performed in the lymphatics. Thank you for introducing me to the

vibrant LE&RN community. The Gordon Research Conference in 2018 and Lymphatic Forum in 2019 were two of my favorite conferences that I attended as a graduate student. Thank you to Zhanna Nepiyushchikh and Fabrice Bernard for your gracious assistance in performing dissections and lymph node digestions. In addition, thank you to Anish Mukherjee and Matt Cribb for your input on my ongoing studies. To Anish in particular, I hope that we can get some compelling preliminary data in the rat tail model before I return to clinic. Furthermore, I would also like to thank members of the Thomas lab. Thank you to Susan Thomas for the use of your homogenizer in preliminary studies. Also, thank you to Meghan O'Melia for teaching me consistent techniques for performing comprehensive lymph node dissections. Additionally, thank you to Lauren Sestito for enlightening conversations on lymph node architecture and drainage.

Next, I would like to thank Brooks Lindsey. I am glad that you decided to become a professor at Georgia Tech and am proud to have played a small role in your faculty recruitment. I have enjoyed discussing US signal processing and talking shop about nanodroplets over the course of my dissertation studies. With our rapidly expanding ultrasound community at Tech, I am hopeful that we can make continued progress in discovering more about these still-mysterious contrast agents.

I would like to thank Melissa Gilbert-Ross. Your input on cancer biology and relevant animal models has added a fresh dimension to my ongoing work. My small-animal studies are markedly improved for your advice and expertise. Implementing and manipulating these small animal models was one of the most rewarding parts of my dissertation studies, and I am pleased to know that this work may have played a small role in pivoting other lab members away from xenografts in their own ongoing studies. I would

also like to thank Janna Mouw for her input on specific small-animal breast cancer models relevant to the molecular targeting aspect of these dissertation studies.

I would like to thank Paul García. There are few people on this Earth who implicitly understand the nuanced hardships of M.D.-Ph.D. training. On a path where one perpetually feels like a black sheep, it is nice to find someone who has walked the same road and sees the world through the same eyes. You have been a trusted mentor throughout my training, both in the research and clinical domains. I pray that I can achieve the same level of balance and success in my career as you have in yours. Hopefully, our paths will cross again at Columbia soon.

I would like to thank the program directors and administrators of the Emory MSTP. Bob Gross, I always leave our meetings feeling energized. I am forever grateful for your help during the one of the most challenging times of my graduate experience, and I am lucky to be able to say that I am the first person who you admitted in your role as program director. Mary Horton, you were truly the MSTP mom. I don't think I would have even been able to transfer here without your role in the entire process. Joanna Bonsall, I am amazed by your passion for clinical education and love our conversations about M.D.-Ph.D. training. I am looking forward to working closely with you as I re-enter the clinic. Andy Neish, I always appreciated you asking me how my week was going at CRC or Recruitment events. Thanks for always checking in. Anita Corbett, thanks for always giving me a kick in the butt when I need it. I'm glad that someone else shares my feelings about the Office of… Something in Particular. Ann Chahroudi, thanks for all the work you've put in to improve CRC. The clinic I spent with you at the Ponce de Leon Center was one of my favorites. Cathy Quiñones, thank you for always taking the time to listen to

me and assuage my concerns. And thank you for always helping me dust myself off and bounce back after I faceplanted throughout my training. Erica Weaver, thanks for all of the hard work you've put in on my fellowship grant, for recruitment, and for this Program. We wouldn't be going anywhere without you. Loan Huynh, thank you for always being able to answer the questions that Post-Award couldn't. Your warm greetings in OMESA always bring a smile to my face.

I would like to thank all of the Emory MSTP students who welcomed me with open arms and who have been my trusted friends and colleagues since I moved to Atlanta in 2015. To the senior BME M.D.-Ph.D. students: Dwight Chambers, Lizz Iffrig, Chris Johnson, Mario Martínez, Adam Prasanphanich, Erik Reinertsen, Caitlin Sok, and Vineet Tiruvadi; you were a constant source of knowledge and support. I hope I managed to be for the next generation just a fraction of the rock you were for me. You set the standard high. To my adopted entry cohort: Saumya Gurbani, Mari Peterson, Jessie Preslar, Myles McCrary, Matt Stern, David Trac, Arielle Valdez-Sinon, Daniel Whittingslow, and Aimée Vester; I am so thankful that you all are in my life. I couldn't have gotten through grad school without you to lean on when times were tough, and I'm sure the same will be true when I'm back on the wards. To all of the other students that I didn't mention by name, young and old, I could probably write an entire second dissertation just on the ways in which my life is better for having you all in it. Although this document is mainly about my scientific accomplishments over the past 5 years, the accomplishment during that same time of which I am most proud will forever be the work I did with the Student Association. Nothing made me happier than to see the joy and camaraderie amongst students at

Recruitment and social events. You sustained me when the sour aspects of academia did everything in their power to sap my joy and energy. I love you all.

I would like to thank all of the PRL staff for their support throughout my graduate studies. It has been a pleasure to work with you and get to know all of you. To Laura O'Farrell and Richard Noel, thank you for all of your assistance with performing and guidance on learning various animal procedures. I am grateful for your expertise and the knowledge that you have passed on to me. Also, I would like to thank Andrea Gibson for always answering my questions and consulting on mice that I was concerned about. I would like to thank all of the technicians and support staff, too: Chris Barrow, Ogeda Blue, Rebecca Graham, Nitasha Hairston, Raven Hughey, Brittany Hunt, Altair Rivas, Josh Scarbrough, Brian Shulman, Jessica Weems, and Kim Woodard. I have enjoyed our conversations in the animal facility over the years. You always kept me in good spirits through all of the long days and frustrating experimental results.

I would like to thank Andrew Shaw of the Optical Microscopy Core in the Petit Institute for Bioengineering and Bioscience. I have enjoyed our conversations at the microscope over the years. Thank you for your patience with me and for your constant assistance in learning the confocal systems and optimizing the images I acquired from them. Also, I would like to thank Matt Cooper, formerly of the Marder Group and the Center for the Science and Technology of Advanced Materials and Interfaces (STAMI). Thank you for teaching me how to use the fluorimeter and to debug its ancient software. I appreciated you delving into the science behind the instrument, and I enjoyed learning more about chemistry from you.

I would like to thank Kyla Ross and Mike Davis from the Department of Biomedical Engineering. To Kyla, I am immensely grateful for our individual meetings towards the end of my graduate studies. I am confident that the lessons you taught me will make me a more effective leader, a more compassionate physician, and a better person. I am excited for the next stage of your career at Georgia Tech, where you will be in a position to assist more students across campus and have a profound positive impact on campus culture. To Mike, I continue to be in awe of you. The knowledge you bring to every conversation and the grace with which you handle even the most challenging of situations is truly spectacular. I am grateful for your patience with me, for your assistance throughout my graduate studies, and for your advice on how to approach my uncertain future career. Emory and Georgia Tech are lucky to have you.

I would also like to thank many of my longtime friends. Thank you to Alejandro Bolívar-Cervoni, Braxton Shelley, and Evan Schwartz for constantly checking in on me. Thank you to Ankit Prasad, Dan Simpson, and Jacob Levitt for distracting me from work and keeping me sane with great group chats about Duke football and basketball. And thank you to all of my other childhood, school, and family friends who have touched base during this long journey of mine.

Of course, I would like to thank my family. To my paternal grandparents, Bernice and Joseph Yarmoska, thank you for your unwavering love and support throughout my childhood. Although neither of you were able to see me reach this point, I hope you are looking on from the next life proud of the man I am trying to become. Grandpa, your battle with cancer is what first set down the path of cancer research. Grandma, your tough-as-nails attitude is what gave me the confidence that I could take on any challenge and

succeed. To my maternal grandparents, Karl and Anneliese Maier, thank you for all of your love and support as well as all of the memories we have made over the years. Oma, after years of calling me “Dr. Dr. Bubbi,” this nickname will soon be accurate. Opa, thank you for being my guardian angel for the last two years of my graduate studies; I needed every last bit of your divine intervention to make it through. I carry your name with me proudly. To my uncle, Glenn Yarmoska, I appreciate you checking in on me all these years. The Subway gift cards you gave me the past two Christmases ended up being extremely clutch for keeping up with meals during my final dissertation writing push.

Last, but most certainly not least, I would like to thank my mom and dad. I love you both with all of my heart. There aren’t many parents on this Earth who would be okay with their son telling them he wanted to walk away from a free M.D. and move halfway across the country with his graduate mentor, all without a guarantee of being accepted by the dual-degree program on the other side. You not only were fine with this decision, but you flew to Texas to help me pack and drove with me to Atlanta to settle down in my new home. You have showered me with love and support since before I was even born. I am blessed to have you as parents. Dad, I often thought about you reminiscing about walking the tunnels at MIT as I walked the dark tunnels of Georgia Tech to and from my own experiments. I wish you could have been the first in our family to earn a doctorate, but fate had other plans. Thank you for the sacrifices you have made for me and our family over the years; they did not go unnoticed. Mom, thank you for always checking in on me… even if I didn’t always want to play twenty questions after many long days. I appreciated all of the care packages that you’ve sent over the years, and the lab has appreciated all of your holiday gifts. I can’t promise that my studies will bring me any closer to home, but I can

promise that you'll always be close to my heart. I could have fifty doctorates and I would still be your baby boy.

Research detailed within this dissertation was supported by the National Cancer Institute under grant numbers R01CA149740, R01CA158598, and F30CA216939; the Breast Cancer Research Foundation; the Emory Medical Scientist Training Program under grant T32GM008169; the Georgia Research Alliance; and the endowment of the Georgia Institute of Technology. The content is solely the responsibility of the author and does not necessarily represent the official views of these organizations. Use of trade names and commercial sources is for identification only.

TABLE OF CONTENTS

LIST OF TABLES

LIST OF FIGURES

LIST OF SYMBOLS AND ABBREVIATIONS

ADV	Acoustic droplet vaporization
B-mode	Brightness mode (i.e., traditional ultrasound imaging)
BP	Boiling point
CEUS	Contrast-enhanced ultrasound
CNR	Contrast-to-noise ratio
CTL(s)	Cytotoxic lymphocyte(s) (i.e., “CD8+” or “killer” T cells)
Cy3(CA)	Cyanine 3 (carboxylic acid)
Cy5	Cyanine 5
$\delta^{(2)}$ UFPI	(Second) differential ultrafast pulse inversion
$\delta^{(2)}$ US	(Second) differential ultrasound
DAPI	4′,6-diamidino-2-phenylindole
dB	Decibel
DC(s)	Dendritic cell(s)
DLS	Dynamic light scattering
DMF	Dimethylformamide
DOPE	1,2-dioleoyl-sn-glycero-3-phosphoethanolamine (i.e., 18:1 (Δ9-Cis) PE)
DOTAP	1,2-dioleoyl-3-trimethylammonium-propane chloride salt (i.e., 18:1 TAP)
DSPC	1,2-distearoyl-sn-glycero-3-phosphocholine (i.e., 18:0 PC)
DSPE-mPEG2000	1,2-distearoyl-sn-glycero-3-phosphoethanolamine-N-[methoxy(polyethylene glycol)-2000] ammonium salt (i.e., 18:0 PEG2000 PE)
EpCAM	Epithelial cell adhesion molecule (i.e., CD326)
EPR	Enhanced permeability and retention

Erbb2	Rodent receptor tyrosine-kinase-protein erbb-2 (i.e., mouse CD340)
FRET	Fluorescence (or Förster) Resonance Energy Transfer
GEMM	Genetically engineered mouse model
HER2	Human epidermal growth factor receptor 2 (i.e., human CD340)
IACUC	Institutional Animal Care and Use Committee
ICG	Indocyanine green
IP	Intraperitoneal
IV	Intravenous
LA	Left axillary (lymph node) (i.e., left proper axillary lymph node)
LI	Left inguinal (lymph node) (i.e., left subiliac lymph node)
LP	Left popliteal (lymph node)
Mφ(s)	Macrophage(s)
MMTV	Mouse mammary tumor virus
MRI	Magnetic resonance imaging
nD	Nanodroplet
Nd:YAG	Neodymium-doped yttrium aluminum garnet (a standard lasing medium)
ODV	Optical droplet vaporization
PA	Photoacoustic
PFCnD(s)	Perfluorocarbon nanodroplet(s)
PFH	Perfluorohexane
PFHnD(s)	Perfluorohexane nanodroplet(s)
pICnD(s)	Poly(I:C) perfluorocarbon nanodroplet(s)
poly(I:C)	Polyinosinic:polycytidylic acid
PRF	Pulse repetition frequency
PT	Primary tumor

RA	Right axillary (lymph node) (i.e., right proper axillary lymph node)
rcf	Relative centrifugal force
RI	Right inguinal (lymph node) (i.e., right subiliac lymph node)
RNA	Ribonucleic acid
RP	Right popliteal (lymph node)
QA	Quality assurance
SLN	Sentinel lymph node
SNR	Signal-to-noise ratio
TDLN(s)	Tumor-draining lymph node(s)
TEMED	N,N,N',N'-tetramethylethane-1,2-diamine
TFT	Trifluorotoluene (i.e., α,α,α-Trifluorotoluene or benzotrifluoride)
TGC	Time gain compensation
TLR	Toll-like receptor
UFPI	Ultrafast pulse-inversion
US	Ultrasound
US/PA	Ultrasound and photoacoustic
VEGF	Vascular endothelial growth factor (i.e., VEGF-A)
VEGF-C	Vascular endothelial growth factor C

SUMMARY

Gas microbubbles are the contrast agent of choice for ultrasound (US) imaging. These agents are excellent for highlighting vasculature on imaging. However, their relatively large (1-10 μm) size prevents them from efficient trafficking within extravascular spaces. Microbubbles cannot extravasate from leaky cancer neovessels into the tumor stroma, nor can they transport within lymphatics without appreciable mechanical stimulation. Perfluorocarbon nanodroplets (PFCnDs) are a phase-change class of US contrast agents that were designed to address the challenge of contrast-enhanced US imaging within extravascular locations. PFCnDs are structurally similar to microbubbles, but they contain a fluoroalkane core that is kept in the liquid state at physiological temperature. In the liquid-cored state, PFCnDs are stable at submicrometer sizes but they produce minimal imaging contrast. Upon a user-triggered input of energy, however, the fluoroalkane core can vaporize, transforming the PFCnDs into microbubbles *in situ*.

Here, we utilize optically triggered perfluorohexane nanodroplets (PFHnDs) with an encapsulated near-infrared dye that allow a pulsed laser to trigger the phase change. Because the phase change is triggered optically, these particles also provide photoacoustic (PA) contrast in addition to US contrast. Moreover, because the perfluorohexane core has a bulk boiling temperature above physiological temperature, these particles will repeatably vaporize and recondense in response to a series of laser pulses. This enables longitudinal imaging of a single PFHnD population, in contrast to traditional PFCnDs that are only capable of a single vaporization event.

In Aim 1, we optimized the synthesis of and imaging sequence for PFHnDs in order to improve their trafficking and detection, respectively, within extravascular spaces. We discovered that increasing the percentage of PEGylated lipids within lipid shelled PFHnDs reduces their average size and size variance over several hours post-synthesis. This discovery provides a facile method for achieving small, monodisperse PFCnDs and synergizes with downstream diagnostic and therapeutic syntheses that necessitate long incubation steps prior to particle use. We also implemented a novel imaging sequence based on pulse inversion that enhances the US contrast from PFHnDs relative to background, and we demonstrated this sequence both in phantoms and *in vivo*.

In Aim 2, we explored the use of optically triggered PFHnDs within the lymphatic system. We developed a post-processing algorithm to exploit the dual US/PA contrast of these particles along with the unique temporal dynamics of their repeated phase change. We acquired longitudinal volumetric images of PFHnDs trafficking through tumor-draining and naïve murine lymphatics, and we assessed various confounding factors for observing US/PA contrast enhancement. In parallel, we also developed a new class of adjuvant-carrying PFHnDs for use as an image-guided therapeutic vehicle in tumor-draining lymphatics. After characterizing these particles, we demonstrated their efficacy as a therapeutic in an *in vitro* model of antigen presenting cells.

In Aim 3, we attempted to tackle the "White Whale" of PFCnD research: demonstration of PFCnD extravasation from neovasculature into the primary tumor stroma. First, we developed a facile method of bioconjugation of PFHnDs to monoclonal antibodies for tumor surface markers, and we demonstrated the specificity of these targeted PFHnDs for tumor cells *in vitro*. Then, we proceeded to test these targeted PFHnDs *in vivo*,

utilizing syngeneic and transgenic models of primary breast cancer as model organisms. We implemented losartan microdosing in an attempt to reduce tumor solid stress and improve particle delivery. Ultimately, our proof-of-concept *in vivo* results were inconclusive, but they draw a compelling blueprint for future investigative efforts. In this vein, we also developed a new class of on-particle Fluorescence Resonance Energy Transfer (FRET) PFCnDs that can be used as a sensor for the intact status of particles on whole organ or histological fluorescence imaging. We characterized successful FRET sensitized emission from these particles and plan to further optimize them for future *in vivo* studies.

Finally, I reflect on the studies presented in this dissertation and offer my vision for ongoing and future work in each arena. These dissertation studies represent a novel contribution to the field of contrast-enhanced ultrasound research, as they develop and explore new avenues of extravascular applications for PFCnDs. Our findings have the potential to inspire new lines of investigation with PFCnDs and to push the envelope with regards to applications-based phase-change contrast agent research.

CHAPTER 1. INTRODUCTION

Contrast agents allow clinicians to highlight areas of disease and even to deliver therapeutics in conjunction with standard diagnostic imaging platforms. Ultrasound greatly benefits from the use of contrast agents, as endogenous ultrasound contrast between unique soft tissues is low compared to competing non-ionizing imaging paradigms. Gas microbubbles are the most ubiquitously utilized ultrasound contrast agent and have high echogenicity relative to background tissue. However, microbubbles have a limited lifetime due to gas diffusion from the core, and microbubbles' large size (1-10 μm) restricts them to the vasculature. Microbubbles will neither extravasate from blood vessels nor traffic through lymphatics in times permissive of clinical imaging. As such, their utility is highly limited in diseases where much of the pathology and markers of disease exist outside of the vascular space. Cancer is one constellation of diseases that exemplify these design constraints.

Amongst women in the United States, breast cancer is the most commonly diagnosed cancer and results in the second highest mortality rate.[1] Although the treatment paradigm for breast cancer has evolved in recent years, detection of metastases to regional lymph nodes remains a critical aspect of the clinical protocol and has strong implications for recurrence and survival in patients with early-stage breast cancer. Sentinel lymph node biopsy has emerged as a relatively low-morbidity option for the clinical evaluation of regional lymphatic metastases, but this procedure relies on radioisotopes and also carries a relatively high false-negative rate in detecting metastases. Alternative methods for sentinel

lymph node detection and diagnosis have been explored, but they are not without weaknesses and have yet to gain clinical traction.

In terms of primary or recurrent tumors, foci of rapidly dividing cancer cells will rapidly outgrow their supply of nutrients. To maintain a growth advantage, these tumor cells will secrete pro-angiogenic factors that induce blood vessels to supply the growing neoplasm. Due to their rapid synthesis, the neovessels induced in this process contain large gaps, or fenestrations, between endothelial cells. These “leaky” vessels can be exploited to deliver diagnostic or therapeutic agents to tumors via intravascular routes though the enhanced permeability and retention (EPR) effect.

A contrast agent with the ability to reach and to traffic through extravascular spaces has the potential to add tremendous value to image-guided diagnostic and therapeutic applications in breast cancer. To this end, we developed optically-triggered phase-change perfluorocarbon nanodroplets (PFCnDs) for use with ultrasound imaging. Perfluorocarbon nanodroplets can be functionalized to afford molecular specificity and loaded with therapeutic cargo for controlled delivery and release. This contrast-enhanced imaging approach can be used to detect sentinel lymph nodes and assess them for metastases via subcutaneous delivery. It can also probe primary or recurrent tumors following intravascular administration. As such, this platform can have a profound impact on the diagnosis and treatment of breast cancer and its nodal metastases. Therefore, the overall goal of this dissertation was to develop and validate this platform in murine models of metastatic breast cancer.

To develop and demonstrate this theranostic platform, the specific aims of this dissertation work were as follows:

1.1 Aim 1: Optimize the Synthesis and Detection of Laser-Activated Perfluorocarbon Nanodroplets for the Extravascular Space

We undertook efforts to reduce the size and size distribution of PFCnDs for improved extravascular trafficking. By increasing the percentage of PEGylated lipids within the phospholipid shell, we were able to achieve a stable size reduction without having to resort to more technically challenging, non-scalable synthesis methods. In parallel, we investigated methods to improve the ultrasonic detection of laser activated PFCnDs. We developed a novel pulse-inversion-based imaging sequence and leveraged the unique time-decaying ultrasound dynamics of perfluorohexane nanodroplets to improve the ability to detect these agents within hyperechoic background environments.

1.2 Aim 2: Apply Perfluorocarbon Nanodroplets to Imaging and Therapeutic Delivery in Tumor-Draining Lymphatics

We utilized the perfluorohexane nanodroplet platform developed in Aim 1 to image PFCnDs longitudinally in lymphatics over 24 hours. We compared naïve mice to those with orthotopic 4T1 tumors and assessed the path of drainage via histology of bilateral lymph nodes. Furthermore, we developed a new class of adjuvant-carrying nanodroplets for ultrasound image-guided immunotherapy in tumor-draining lymph nodes. We conducted proof-of-principle *in vitro* studies in antigen presenting cells and demonstrated that these particles can effectively elicit an immune response.

1.3 Aim 3: Assess Perfluorocarbon Nanodroplet Extravasation within Primary Breast Tumors

We pursued avenues to increase the extravasation of systemically delivered PFCnDs in primary breast tumors. First, we developed antibody functionalized PFCnDs and demonstrated their molecular specificity for extracellular tumor markers *in vitro*. Then, we utilized targeted PFCnDs in two murine models of primary breast cancer. We performed concomitant tumor neovascular modulation and assessed the results of particle delivery with ultrasound and photoacoustic imaging as well as histology.

1.4 Significance and Innovation

The accomplished work is significant in that it addresses fundamental challenges that have stymied the preclinical utilization of PFCnDs and presents their use in realistic small animal models of neoplastic disease. It demonstrates longitudinal imaging of PFCnDs *in vivo* with a single bolus delivery, which has yet to be reported in the literature. Additionally, this work lays the foundation for yet-unexplored avenues of applications-based research with PFCnDs in the cancer domain and beyond. This work is innovative in establishing several new classes of nanodroplets as well as in its use of genetically engineered mouse models and tumor microenvironment modulation strategies.

CHAPTER 2. BACKGROUND

2.1 Ultrasound Imaging

Ultrasound (US) imaging is a non-ionizing imaging modality with widespread clinical use, particularly in point-of-care settings. In brief, ultrasound imaging transmits sound waves into a tissue of interest and receives backscattered waves to create an image of the tissue with contrast proportional to changes in underlying tissue density. This technique does well when imaging soft tissue structures; however, it is not typically used to image structures with drastically different densities than soft tissue, such as the lungs and bone.

The sound waves transmitted in US imaging are above the human audible range (i.e., greater than 20 kHz). Waves with a center frequency 1 MHz and lower can be appreciably absorbed by the body, leading to thermal deposition, and sound waves in this range are typically reserved for therapeutic ablative procedures.[2] Sound waves above 1 MHz in frequency are mostly scattered by physiological tissues, and thus these are used for imaging purposes.

In US imaging, the transducer serves as both source and receiver for sound waves. Modern "phased array" transducers in US imaging systems contain an array of piezoelectric elements, each of which can convert electric potential energy into mechanical energy and vice versa.[3] When a voltage is applied to a piezoelectric element, it vibrates and generates an ultrasonic wave. Conversely, when an acoustic wave vibrates a piezoelectric element, it produces an electrical potential that can be recorded as a voltage.

A pulser can apply a voltage to the piezoelectric elements of the transducer, which generate an US wave that can propagate through biological tissue. When this longitudinal pressure wave encounters an interface between two different mediums, some percentage of the wave is transmitted into the new medium and the rest is reflected back towards the transducer. The reflection fraction, a, which is the ratio of reflected wave intensity or the incident wave intensity, can be defined as:

$$a = \frac{(Z_2 - Z_1)^2}{(Z_2 + Z_1)^2} \tag{1}$$

where Z_2 and Z_1 are the acoustic impedances at the two mediums making up a boundary.[4] Acoustic impedance, Z, is a material property that defines how much resistance an ultrasound wave encounters as it passes through tissue. It is defined as:

$$Z = \rho c \tag{2}$$

where ρ is the density of the medium and c is the speed of sound in the medium. In most soft tissues, the speed of sound is similar and is assumed to be a constant 1540 m/s. Therefore, the amount of reflected ultrasound at an interface is proportional to the difference in density between the two media at the boundary.[5]

Although differences in density lead to reflected waves, and thus imaging contrast, in US, too drastic of a difference can lead to the majority of the waves being reflected and none being transmitted. If no waves are transmitted, then an US image cannot be reconstructed past the highly reflective boundary. This manifests as a hypoechoic (i.e., dark) “acoustic shadow,” which tails underneath a hyperechoic (i.e., bright) surface. Both

low-density and high-density regions can create this effect;[6] thus, US imaging is not typically used to image the lungs or through bone. Similarly, this explains why a layer of coupling gel, with similar acoustic impedance to tissue, is necessary to ensure US waves are transmitted into and out of the body. An internal matching layer sits between the piezoelectric elements and external cladding of the transducer to ensure efficient transmission and receipt of US waves by the system.

To collect a standard "brightness mode," or "B-mode," US image, the pulser applies a voltage to the piezoelectric elements of the transducer. Variable time delays are applied across the elements to generate a parabolic, converging wavefront that is focused at a particular depth, centered along one of the elements of the transducer. After firing the US wave, the transducer receives and records all back-reflected waves for a period of time. The receive time is defined by the round trip of a sound wave for the maximum depth within the desired imaging plane. This process is repeated for each element across the face of the transducer for a single "line-by-line" image acquisition. A variable time gain compensation (TGC) is applied to received signals as a function of time in order to account for depth-dependent attenuation of sounds waves propagating within tissue.

The "delay-and-sum" method is typically employed to create an image from the collected "line-by-line" data.[7,8] To reconstruct the signal along the line of an US acquisition, a variable time delay is applied to the received signals at each element to account for the variable distance travelled from reflected signals from points in this line back to the transducer. After this delay is applied, the signals are summed together. This process amplifies coherent signals from the line of interest and suppresses incoherent signals from scatterers outside of this line. Next, one of several methods is employed in

order to extract the magnitude of the envelope of the complex summed US waveform. This receive beamforming process is repeated for each line of the line-by-line acquisition until the entire imaging plane is reconstructed. Finally, for visualization purposes, the reconstructed signal is typically normalized and displayed on a logarithmic (i.e., dB) scale.

2.1.1 Plane Wave Ultrasound Imaging

Plane wave US imaging is a variation of the workflow for B-mode imaging described above. In contrast to the line-by-line acquisition regime, plane wave US imaging uses a single planar wave transmit in contrast to the multiple converging wave transmits across the elements of the transducer. By reducing the number of transmit events, plane wave imaging can achieve up to two orders of magnitude increased temporal resolution in comparison to line-by-line over the same lateral field of view.[9] Plane wave imaging is consistently utilized for ultrafast (i.e., greater than 500 frames per second) US imaging applications.

Although plane wave US imaging can increase temporal resolution dramatically compared to traditional line-by-line acquisitions, this increase comes at a cost. Because of the lack of transmit focusing, the entire volume beneath the transducer is insonified with every transmit. As a result, appreciable coherent, off-axis received signals persist when reconstructing images with the delay-and-sum method. This leads to “side lobe” artifacts and overall reduced contrast-to-noise ratio (CNR) within reconstructed images when compared to equivalent line-by-line acquisitions over the same volume. To address this drawback, researchers developed the method of angular compounding.[10] In angular compounding, time delays are applied in order to transmit and receive a series of tilted

plane waves that are swept through angles relative to the transducer, where 0° defines a traditional plane wave parallel to the transducer face. Static structures remain spatially coherent upon reconstruction regardless of plane wave transmit angle, whereas off-axis signals are spatially variant. Therefore, when successive angularly swept plane wave acquisitions are compounded, or added prior to reconstruction, side lobe artifacts are suppressed in the resultant images. This enhancement comes at the cost of some of the temporal resolution benefit of plane wave US imaging, as multiple transmit-and-receive events become necessary to form the compounded images.

The enhanced temporal resolution afforded by plane wave US imaging is necessary to capture the transient ultrasound contrast created by perfluorohexane nanodroplets. As will be discussed in Section 2.4, these contrast agents only serve as ultrasound reflectors for milliseconds after an energy pulse. Therefore, this fast phenomenon requires an ultrafast regime to capture on US imaging. Plane wave US imaging allows for successful imaging of perfluorohexane nanodroplets without a reduction in the field of view, as would be necessary in a line-by-line acquisition approach.

2.2 Photoacoustic Imaging

Photoacoustic (PA) imaging is an adjunct to US imaging. It utilizes some of the same hardware and signal processing techniques as US imaging, but it produces fundamentally different images. PA imaging can be thought of as “lightning and thunder.” Upon exposure to a pulse of laser irradiation (the “lightning”), chromophores within the tissue absorb light. This absorption leads to localized heating and thermal expansion, which produces a pressure wave (the “thunder”). The laser-induced pressure waves can be recorded with an

ultrasound transducer and processed to form an image. Here, the contrast is proportional to the optical absorption of tissue, as opposed to changes in its density. Because of the similarity in hardware, a single imaging system can be used to acquire both US and PA (US/PA) images, which can be co-registered for a plane of interest.

Photoacoustic imaging is based on the photoacoustic effect, which is the formation of sound waves from a material irradiated by time-varying light. This phenomenon was first discovered by Alexander Graham Bell when he reported that a material produced sound waves after exposure to sunlight that was interrupted by a rotating slotted wheel.[11] Although the photoacoustic effect was discovered in the late nineteenth century, it wasn't until after the development of nanosecond pulsed lasers nearly a century later that photoacoustic imaging was born.[12-16]

When biological tissue is irradiated with a short (i.e., nanosecond) pulse of laser light, photons can be absorbed by local chromophores within the beam path. This process produces heat due to non-radiative relaxation of the chromophores. In turn, the heating leads to rapid thermal expansion of the surrounding tissue. This causes localized extension and compression of the tissue, which generates an acoustic wave.[17] The initial pressure, p_0, of the generated acoustic wave immediately after the laser pulse can be defined as follows:

$$p_0 = \mu_a F \Gamma \tag{3}$$

Here, μ_a is the absorption coefficient of the optical absorber, F is the local optical fluence from the illuminated light, and Γ is the Grüneisen parameter.[18] The Grüneisen parameter is a quantity that accounts for the volumetric thermal expansion of, speed of

longitudinal sound waves in, and heat capacity at constant pressure of the surrounding medium. Under the assumption of negligible shear stress induced by the photoacoustic effect induced by pulsed laser light, the Grüneisen parameter is a measure of the thermoelastic efficiency of the medium.[19]

After compensating for changes in local fluence or assuming a constant fluence, changes in the intensity of received PA signals are proportional to changes in optical absorption of local chromophores. A PA image is acquired and processed in an equivalent to a receive-only event on US. The receive time for a PA event is half that of an equivalent US event because the sound waves only need to complete a unidirectional trip towards the transducer.

The choice of wavelengths for pulsed laser irradiation in PA imaging is critical. There are many endogenous chromophores, such as hemoglobin and fat, that have unique optical absorption spectra. However, it is sometimes necessary to distinguish populations of photoabsorbers with similar absorption characteristics, such as oxy- and deoxyhemoglobin. In these cases, it is necessary to acquire multiple PA images with different excitation wavelengths and perform spectral unmixing based on the differences in predicted PA signals predicated on underlying spectral characteristics of the photoabsorbers of interest.[20,21]

2.3 Contrast-Enhanced Ultrasound/Photoacoustic Imaging

Ultrasound is widely utilized for soft tissue imaging. However, the most significant deficiency of this imaging modality is that image contrast amongst soft tissues is poor due to the abundant subwavelength sound scattering present in tissue.[22-24] This low contrast can

make it difficult to discern many organs or identify small lesions indicative of disease. As with other imaging modalities when endogenous contrast is poor, US imaging can utilize exogenous agents to improve imaging contrast.

The contrast agents utilized for clinical US imaging are gas microbubbles.[25] Microbubbles have a gas core, which is typically comprised of oxygen or perfluorocarbon, surrounded by a biocompatible protein or phospholipid shell. In practice, microbubbles are injected intravenously and imaged within the vasculature. Commercial microbubbles are typically naïve, but microbubbles functionalized with VEGFR2 antibody have received an IND from the FDA and are being tested for molecularly-specific imaging of solid tumors.[26,27] Microbubbles have multiple mechanisms for producing US contrast. First, microbubbles are excellent ultrasound reflectors due to their gas core and the resultant acoustic impedance mismatch experienced by incident ultrasound waves. Second, and perhaps more significant, microbubbles experience nonlinear oscillations when placed into an acoustic field.[28]

Researchers have exploited the nonlinear oscillations of microbubbles to create imaging systems and sequences for contrast-enhanced ultrasound (CEUS). By transmitting and receiving with independent transducers, it is possible to induce microbubble oscillations with low frequency US and to receive their harmonic oscillatory waves with a high frequency transducer.[29-31] In this "harmonic imaging" regime, the reflections at the transmit frequency are suppressed, although some biological tissue may produce harmonic reflections. In addition to this dual-transducer approach, a single-transducer method called "pulse inversion" also exploits the nonlinear oscillations of microbubbles for enhanced contrast.[32] Pulse inversion necessitates two successive transmit and receive events with

inverted waveforms, which are compounded to form a single CEUS image. The underlying logic is similar to adding two sine waves that are 180° out of phase; these two waves will completely cancel when added. However, the harmonic oscillations of microbubbles are higher frequency than the incident US wave, and they are independent of the transmit phase. Therefore, when pulse inversion frames are compounded, the harmonic microbubble oscillations persist and are amplified. Again, tissue harmonics may confound the imaging results, but the magnitude of tissue harmonics is generally low. Pulse inversion acquisition sequences are available on many commercial US systems.

Like US imaging, PA imaging can also benefit from the introduction of contrast agents. Unique contrast in PA imaging can be achieved through the use of exogenous optical absorbers. Spectral unmixing may also be used to differentiate endogenous from exogenous sources of PA contrast. However, in with exogenous absorbers it is also possible to design contrast agents to have unique absorption characteristics compared to biological tissue. Biological tissues have two "optical windows" between 650 and 1350 nm in which endogenous chromophores have minimal absorption.[33,34] By tuning the absorption of PA contrast agents into one of these two windows, it is possible to achieve high imaging contrast without resorting to spectroscopic PA imaging.

Because of the same underlying physical phenomenon of optical absorption, PA imaging shares many of its contrast agents with optical imaging. For example, plasmonic nanoparticles are featured prominently throughout preclinical PA imaging research.[35-37] Biocompatible dyes and dye constructs can also be used as exogenous PA contrast agents.[38-40] In particular, indocyanine green (ICG) has FDA approval and can already be used for contrast-enhanced photoacoustic imaging in the clinic. In order to develop more

clinically relevant PA contrast agents, researchers will need to balance the need for long-term biocompatibility and successful clearance with the need for strong and uniquely discernable optical absorption.

2.4 Perfluorocarbon Nanodroplets

Perfluorocarbon nanodroplets (PFCnDs) leverage beneficial aspects of both US and PA contrast agents. This class of particles was initially developed to address the shortcomings of microbubbles: chiefly, their relatively large average size (1+ μm) and short (minutes) circulation time. Kept as a liquid at physiological temperature by high Laplace pressure,[41] PFCnDs are small enough to extravasate or to rapidly traffic through lymphatics prior to user-controlled activation to produce US contrast. As such, PFCnDs may successfully reach and be functionalized to extravascular targets. Because of their size relative to US wavelength and smaller difference in acoustic impedance from tissue, PFCnDs produce minimal contrast in their nascent, liquid-cored state. However, when exposed to a burst of energy, typically acoustic, the perfluorocarbon core undergoes a phase change. This phase-change event effectively transforms the PFCnDs into microbubbles *in situ*,[42,43] which allows for traditional CEUS imaging. By encapsulating optical absorbers within PFCnDs, the phase-change event can be triggered with a pulse of laser light. This process, known as optical droplet vaporization (ODV), allows for both PA and US contrast to be generated by PFCnD vaporization.

Classically, the mechanism of phase-change induction in PFCnDs was thought to be a result of overcoming the Laplace pressure of the nanodroplet construct with the input energy pulse.[41,44] Laplace pressure scales inversely with the particle radius and would

explain the stability of PFCnDs in a liquid-cored state where the ambient temperature and pressure should normally dictate bulk perfluorocarbon vaporization. More recently, an alternate theory based on homgenous nucleation has been proposed and supported by experimental data.[45] The homogenous nucleation theory states that suppressed vaporization in the PFCnD core is the result of a kinetic barrier: namely, the energy necessary for the chemical potential gradient to overcome the Laplace pressure-volume work.[45] This occurs at the peak of the Gibbs free energy when plotted against radius of a vapor embryo within the perfluorocarbon core. When a vapor embryo of critical size forms, the entire perfluorocarbon core will rapidly vaporize.[46-48] Unlike the Laplace pressure theory, the homogenous nucleation theory accurately predicts the pressure necessary to condense microbubbles into nanodroplets[49] and the spontaneous vaporization of PFCnDs near the perfluorocarbon spinodal,[50,51] which occurs at 80-90% of its critical temperature.[52] In the context of these two prevailing theories, it remains to be seen if there are fundamental mechanistic differences in the phase changes induced by acoustic droplet vaporization (ADV) versus ODV.

The phase-change behavior of PFCnDs has previously been used to provide contrast in multimodal imaging[53,54] and to indicate cargo release *in vivo*.[55] However, the vast majority of previous studies with PFCnDs have relied upon a one-time, ADV event to produce contrast. With an acoustic trigger, it is impossible to selectively interrogate distinctly targeted PFCnD populations within a single imaging acquisition. In response to this limitation, our group has developed a new imaging technique using optically triggered PFCnDs. By utilizing PFCnDs with a relatively high-boiling-point core (e.g., perfluorohexane [56°C] vs. perfluoropentane [28°C]) and an encapsulated near-infrared

photoabsorber, we are able to selectively trigger PFCnD contrast via irradiation with pulsed near-infrared laser light well below the ANSI safety limit.[56-58] This regime allows for multiplexed imaging by permitting user-controlled triggering of distinct populations of contrast agents via tuning of the incident laser irradiation to match specific photoabsorbers within different groups of PFCnDs. Therefore, optically triggered PFCnDs have the potential to be used to interrogate multiple molecular targets to produce a true *in vivo* "optical biopsy."

Nanodroplets may also contain therapeutic cargo and thus be used for controlled drug delivery and release.[42,55,59] The current clinical protocol for treating many metastatic solid tumors involves the surgical resection of nodes, which may lead to chronic morbidities.[60] Conversely, diffuse metastases are typically treated with systemically delivered biologics and chemotherapeutics. In this case, the systemic route of administration leads to undesirable off-target effects, such as gastrointestinal symptoms, hair loss, paresthesias, and fatigue.[61] Targeted PFCnDs could provide a focal means of image-guided, user-controlled delivery of encapsulated therapeutics to localized areas of disease, triggered by near-infrared laser irradiation.

CHAPTER 3. OPTIMIZATION OF THE SYNTHESIS AND DETECTION OF LASER-ACTIVATED PERFLUOROCARBON NANODROPLETS

3.1 The Effect of Variable Shell PEGylation on Nanodroplet Size and Size Stability

This subsection was adapted from: Yarmoska, S. K., Yoon, H. & Emelianov, S. Y. Lipid Shell Composition Plays a Critical Role in the Stable Size Reduction of Perfluorocarbon Nanodroplets. *Ultrasound in medicine & biology* **45**, 1489-1499 (2019).

3.1.1 Abstract

Perfluorocarbon nanodroplets (PFCnDs) are phase-change contrast agents that have the potential to enable extravascular contrast-enhanced ultrasound and photoacoustic (US/PA) imaging. Producing consistently small, monodisperse PFCnDs remains a challenge without resorting to technically challenging methods. We investigated the impact of variable shell composition on PFCnD size and US/PA image properties. Our results suggest that increasing the molar percentage of PEGylated lipid reduces the size and size variance of PFCnDs. Furthermore, our imaging studies demonstrate that nanodroplets with more PEGylated lipids produce increased US/PA signal compared to those with the standard formulation. Finally, we highlight the ability of this approach to facilitate US/PA imaging in a murine model of breast cancer. These data indicate that, through a facile synthesis process, it is possible to produce monodisperse, small-sized PFCnDs. Novel in their simplicity, these methods may promote the use of PFCnDs among a broader user base to study a variety of extravascular phenomena.

3.1.2 Introduction

Ultrasound is a portable, cost-effective, non-ionizing imaging modality that is increasingly gaining clinical traction in point-of-care clinical settings. Ultrasound image contrast is determined by variations in underlying tissue density and the speed of sound, which define the acoustic impedance to incident sound waves.[5] Unfortunately, soft tissues have similar echogenicity,[22-24] and so it is difficult to distinguish some organs or to identify small lesions indicative of disease using standard "B-mode" ultrasound alone. To address this limitation, gas microbubbles were developed for use as exogenous ultrasound contrast agents.[62] The density and compressibility of these microbubbles allows them to oscillate within an applied acoustic field, leading to enhanced backscatter of incident waves to increase contrast in ultrasound imaging.[25,63]

Although a measureable portion of particles from standard microbubble formulations are submicrometer in size,[64,65] the fraction of these agents that produce perceptible echogenicity on ultrasound have diameters on the micrometer scale.[28,64,66] Therefore, these agents are practically restricted to use within the systemic vasculature. Their minutes-long stability within systemic vasculature notwithstanding,[66-68] microbubbles within the useable fraction are still too large to extravasate through "leaky" cancer neovasculature or to traffic within extravascular locations in times permissive of clinical imaging. In order for contrast agents to interact with tumor cells, metastases, and other sources of pathology, they must first reach and travel through extravascular spaces. Extravascular trafficking necessitates small contrast agent size. Gaps between endothelial cells in leaky tumor neovasculature have been reported to be between 380 to 780 nm,[69-71] and the xenograft models used to produce these estimates were likely biased towards the

larger side of what is observed clinically in human solid tumors.[72] Similarly, though particles larger than 100 nm will preferentially drain to lymphatics versus blood vessels, particles larger than this will also exhibit size-dependent reduction in lymphatic trafficking speed and uptake efficiency.[73-75]

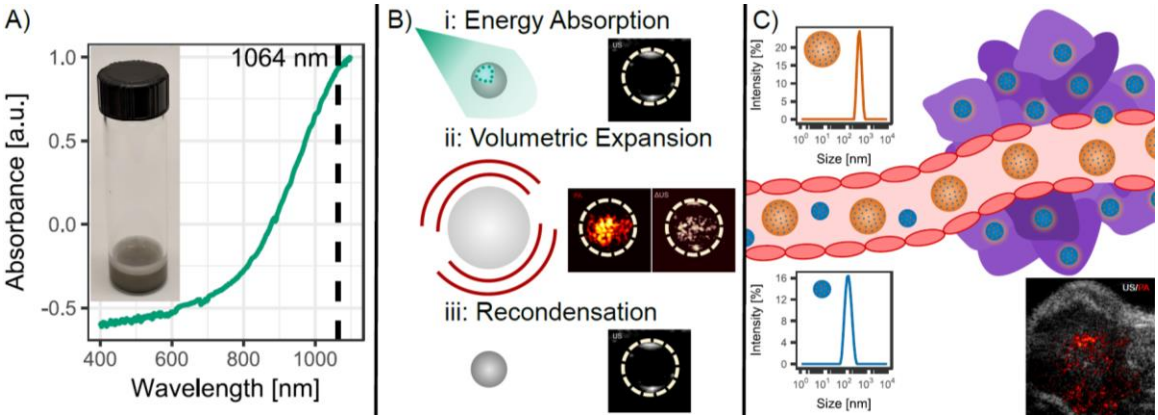

Figure 1: Schema for Perfluorohexane Nanodroplets. A) Absorption spectrum of the near-infrared photoabsorber encapsulated within PFCnDs; **B)** A schematic of optical droplet vaporization (ODV). First, a laser pulse is absorbed by encapsulated photoabsorbers within PFCnDs (i) to induce a phase change (ii). This mechanism can produce contrast through both US and photoacoustic (PA) imaging (ii, insets). "High-boiling point" perfluorocarbons, such as perfluorohexane (BP: 56°C), may recondense into the droplet state after the laser pulse ends (iii), allowing for repeatable contrast generation from the same PFCnD population (i-iii); **C)** Cartoon depicting extravascular imaging of a primary tumor with PFCnDs. Only PFCnDs smaller than the gaps between endothelial gaps in cancer neovasculature (blue) will be able to extravasate into the tumor stroma. Larger PFCnDs (red-orange) will be restricted to the vasculature.[76]

To achieve the nanoscale particle size necessary for successful extravascular imaging, perfluorocarbon nanodroplets (PFCnDs) were created as a new class of ultrasound contrast agent **(Figure 1A**, inset).[41,53] Nanodroplets are structurally similar to microbubbles; however, they contain a core composed of liquid perfluorocarbon instead of gas. This change allows PFCnDs to remain stable at the nanoscale. Because of their size relative to ultrasound wavelength and smaller difference in acoustic impedance from tissue,

PFCnDs produce minimal contrast in their nascent, liquid-core state. However, when exposed to a burst of energy, typically acoustic, the perfluorocarbon core undergoes a phase change. This phase-change event effectively transforms the PFCnDs into microbubbles *in situ*,[42,43] which allows for traditional contrast-enhanced ultrasound imaging.

The phase-change event can also be optically-triggered (**Figure 1B**, i) by incorporating a photoabsorber, such as a near-infrared dye, within the nanodroplet construct (**Figure 1A**). In this case, the initial pressure waves created from PFCnD vaporization events can be received ultrasonically to reconstruct a high-contrast photoacoustic image (**Figure 1B**, ii).[53,77] When using a "low-boiling point" perfluorocarbon (e.g., perfluoropentane; Boiling Point [BP]: 28°C), the PFCnD phase change is permanent.[77,78] Conversely, PFCnDs constructed with "high-boiling point" perfluorocarbons (e.g., perfluorohexane; BP: 56°C) will recondense into their original liquid state after exposure to an energy pulse (**Figure 1B**, iii).[58] The ability to repeatably induce a phase change in "high-boiling point" nanodroplets allows for more robust and longitudinal imaging studies with a single PFCnD population.[79]

Extravascular ultrasound imaging applications with PFCnDs are predicated on the ability to produce a small and monodisperse nanodroplet population. In solid tumors, for instance, only nanodroplets that are smaller than a tumor-specific pore cutoff size will be able to extravasate through gaps between neovascular endothelial cells into the tumor stroma (**Figure 1C**).[80] Using a monodisperse population of PFCnDs would allow for a higher percentage of the injected dose to reach the extravascular space, assuming the median size is below the pore cutoff. Additionally, the acoustic response from monodisperse PFCnDs would be relatively uniform, allowing for more accurate, image-

based estimates of *in vivo* nanodroplet concentration. Unfortunately, many facile synthesis methods (e.g., sonication, extrusion) produce nanodroplets closer to 500 nm than to 100 nm in size,[42,53-55] and these larger, polydisperse droplets may be ill-suited for extravascular use. Several methods have been employed to achieve a stable reduction in PFCnD size and particle dispersity: condensation synthesis, [41,81] size-separation,[82] and microfluidics.[83,84] Still, each of these methods is technically challenging and has its own weaknesses.

Condensation synthesis, which requires the formation of stable microbubbles, cannot be applied practically to "high-boiling point" perfluorocarbon formulations. Size-separation techniques have high variability in size reduction, low particle yields, and often require differential centrifugation, which adds time to the manufacturing process and is challenging to execute at scale. Microfluidic devices also have small sample yields and can be prohibitively expensive without local expertise in their fabrication. The ability to achieve PFCnD size reduction and monodispersity without these methods would facilitate their use amongst a broader cadre of researchers and would have the potential to place more emphasis on applications-based research with nanodroplets.

In the context of these lingering challenges, we investigated the impact of alterations in the nanodroplet shell composition on the size of PFCnDs. We restricted this analysis to lipid-shelled formulations because of their strong translational benefits: chiefly, their demonstrable biocompatibility and well-studied linker strategies for downstream functionalization. Previous research notes that the yield of and ultrasound signal produced by nanodroplets is increased by using a higher molar percentage of unsaturated phospholipids.[85] These same studies also describe that nanodroplets formed with 10% and 20% molar DSPE-mPEG2000 demonstrate a solid-liquid disordered phase existence,

which is structurally similar to the formulations displaying the most ideal yields and imaging properties.[85] Standard formulations for nanodroplets with acoustically-triggered vaporization have historically utilized no more than 10% molar PEGylated phospholipid.[41,57,81,86] However, literature from mixed-micelles, which have similar structure to the lipid shells of nanodroplets, suggests that increasing the molar concentration of PEGylated lipids up to 90% would confer stable size reduction,[87,88] potentially due to increased steric stabilization.

The objectives of this work were to assess the effect of varying the percentage of PEGylated phospholipids on the size and size distribution of lipid-shelled PFCnDs and to assess the impact of these changes on the ultrasound and photoacoustic contrast produced by the PFCnDs. Changes in the shell composition may have both direct and indirect, via size modulation, effects on the PFCnDs' acoustic response.

3.1.3 Materials and Methods

Nanodroplet Synthesis

Perfluorocarbon nanodroplets (PFCnDs) were synthesized using a sonication-based method, modified from one described by our group previously.[57,58] In this protocol, 2 µmol of phospholipids, consisting of a mixture of DSPC and DSPE-mPEG2000 (Avanti Polar Lipids, Inc.), were isolated from a chloroform suspension using a rotary evaporator (Rotavapor R-215, Büchi AG) with water bath, adhering to the "20/40/60 Rule." For PFCnDs used in imaging experiments, the evaporated chloroform suspension also contained 2 mg of near-infrared absorbing dye (Epolight™ 3072; Epolin, Inc.), which was

obtained from a 2 mg/mL chloroform suspension. After a minimum of 30 minutes in the Rotavapor, the resulting lipid cake was allowed to dry under vacuum overnight.

After drying, the lipids were resuspended in 1 mL of phosphate buffered saline. This solution was vortexed for 2 minutes and sonicated with 20 kHz ultrasound in a water bath sonicator (1510 Ultrasonic Cleaner; Branson Ultrasonics Corp.) at room temperature (25°C) in 5-minute increments until homogeneous. To this mixed micelle solution, we added 50 µL of perfluorohexane (FluoroMed, L.P.). The mixture was placed into an ice bath and positioned within a microtipped probe sonicator (QSonica). The ice-cold mixture was allowed to equilibrate for 5 minutes and then exposed to two rounds of probe sonication, one low intensity (1% power, 1 s on, 5 s off, 20 total pulses) and one high intensity (50% power, 1 s on, 10 s off, 5 total pulses), with 5 minutes in between sequences. Prior to size measurements or use in imaging, these PFCnDs were diluted 1:20 in phosphate buffered saline and exposed to 5 minutes of 20 kHz water bath sonication at room temperature to produce the final samples.

Size Characterization

Size characterization studies were performed on 1 mL samples of 1:1 phosphate buffered saline dilutions of the 1:20 dilution of PFCnDs described above. Size measurements were taken by a standard dynamic light scattering (DLS) instrument (Zetasizer Nano ZS; Malvern Instruments Ltd.) at various time points spanning from immediately post-synthesis to 6 hours post-synthesis. The quartz cuvette containing the 1 mL sample was inverted immediately prior to each measurement, and the cuvette remained within the 25°C temperature-buffered instrument holder between measurements. After a

60-second sample equilibration period, the DLS instrument obtained three measurements at each time point, each measurement an average of 10 individual measurements. The measurement sequence for each time point was executed over approximately eight minutes, including the equilibration step. Measurement data were exported as comma-separated values and displayed in R (R Core Team) using the ggplot2 data visualization package.

Absorption Characterization

The absorption of the near-infrared dye encapsulated within the PFCnDs was characterized by UV-Vis spectroscopy. A UV-Vis spectrophotometer (Evolution 220; Thermo Scientific) was used to measure the absorbance of 1:1000 PBS dilutions of both unloaded PFCnDs and PFCnDs containing the near-infrared dye. The spectrum of the unloaded PFCnDs was subtracted from that of the dye-loaded PFCnDs, and the resulting differential absorption spectrum was normalized for display purposes.

Ultrasound/Photoacoustic Imaging of Phantom

Ultrasound and photoacoustic (US/PA) imaging was performed using an integrated setup described elsewhere [89]. This system combines a custom ultrasound system (Vantage 256, Verasonics, Inc.) with a tunable nanosecond pulsed Nd:YAG laser (Phocus Mobile, Opotek, Inc.).

The Nd:YAG laser was used to produce pulses at the fundamental 1064 nm wavelength at a 10 Hz pulse repetition frequency (PRF). Within this imaging study, each laser pulse deposited 28 mJ of energy, resulting in a local fluence of approximately 13 mJ/cm^2. The laser pulses were delivered via optical fibers coupled to the imaging

transducer. These fibers were oriented such that the incident light intersected the imaging plane at 20±3 mm in the axial dimension.

The coupled Vantage 256 ultrasound system utilized an L11-4v (Verasonics, Inc.) linear array transducer, which has a −6 dB bandwidth ranging from 11 to 4 MHz. These imaging studies utilized a transmit center frequency of 5 MHz and a transmit voltage of 40V. Each ultrasound frame is the result of three angularly compounded plane waves. These plane waves span 6 degrees (-3°, 0°, 3°) and were acquired at 3 kHz for a resulting ultrasound imaging frame rate of 1 kHz.

Each imaging acquisition consisted of six packets of data. The last five packets were preceded by a single laser pulse. Each packet contains one photoacoustic image (receive only) followed by 50 ultrafast ultrasound frames, as described above. The resulting imaging sequence occurs over the course of 600 ms, as dictated by the 10 Hz laser PRF, with the resulting US/PA data acquired over the first 50 ms in each 100 ms packet.

Imaging data were processed offline in MATLAB (Mathworks). All images were linearly interpolated in two-dimensions by a factor of three for display purposes. Quantitative values from images were obtained from the raw (i.e., non-interpolated) data.

Imaging Phantom Setup

The base of the imaging phantoms were created from polyacrylamide in a process detailed by our lab previously.[58,89] In brief, 40% (w/v) acrylamide (OmniPur® Acrylamide Bis-acrylamide 29:1; MilliporeSigma) and 10% (w/v) ammonium persulfate (ACS Grade; VWR International) solutions were diluted to 10% and 0.002%, respectively, in degassed,

deionized water. To this solution, we added silica gel particles (40-63 μm particle size; MilliporeSigma) to achieve a final 1% (w/v) concentration of silica. A catalytic amount of TEMED (Proteomics Grade; AMRESCO Inc.) was added to initiate the crosslinking of aqueous acrylamide to solid polyacrylamide gel.

Two cylindrical inclusions were made in the polyacrylamide phantom. Viewed from the orientation of the imaging plane, these inclusions were 5 mm in diameter, separated by 20 mm, and located 20 mm at depth from the top surface of the polyacrylamide. Then, 1 mL of the 1:20 dilution of PFCnDs described previously was mixed into 10 mL of ultrasound gel (Sonigel; 3B Scientific) with a 1% (w/v) concentration of silica. After removing air bubbles from the gel mixture via 2 minutes of centrifugation at 1000 rcf, the 1:200 PFCnD gel mixture was added via syringe to fill one of the empty inclusions in the polyacrylamide gel. Each inclusion ultimately contained gel with one of the batches of PFCnDs to be analyzed by US/PA imaging, as detailed above.

Imaging data were processed offline in MATLAB (Mathworks). All images were linearly interpolated in two-dimensions by a factor of three for display purposes.

3.1.4 Results and Discussion

Nanodroplet Characterization

We synthesized batches of PFCnDs in one of two cohorts: nanodroplets with a 10:90 molar ratio of DSPC:DSPE-mPEG2000 and nanodroplets with a more standard 90:10 molar ratio, hereafter referenced by these defining numeric ratios. We then obtained average size measurements via dynamic light scattering (DLS) over the first six hours post-

synthesis (**Figure 2**). Initially, the standard formulation produced nanodroplets that were relatively large (median: 647 nm) and variable (Interquartile Range [IQR]: 484 nm) in size. Nonetheless, the minimum size observed (366 nm) was consistent with reported values within seminal PFCnD literature using sonication-based synthesis methods.[90] Over the first three hours post-synthesis, the average size of the 90:10 nanodroplets trended upward, potentially due to Ostwald ripening.[91] This hypothesis is further supported by a reduction in the inter-quartile range over time (137 nm by hour six). After the third hour post-synthesis, however, the median droplet size measurement began to decrease (624 nm by hour six). This observed phenomenon is likely due to the spontaneous vaporization of larger (i.e., 1+ µm) PFCnDs within the solution.[78]

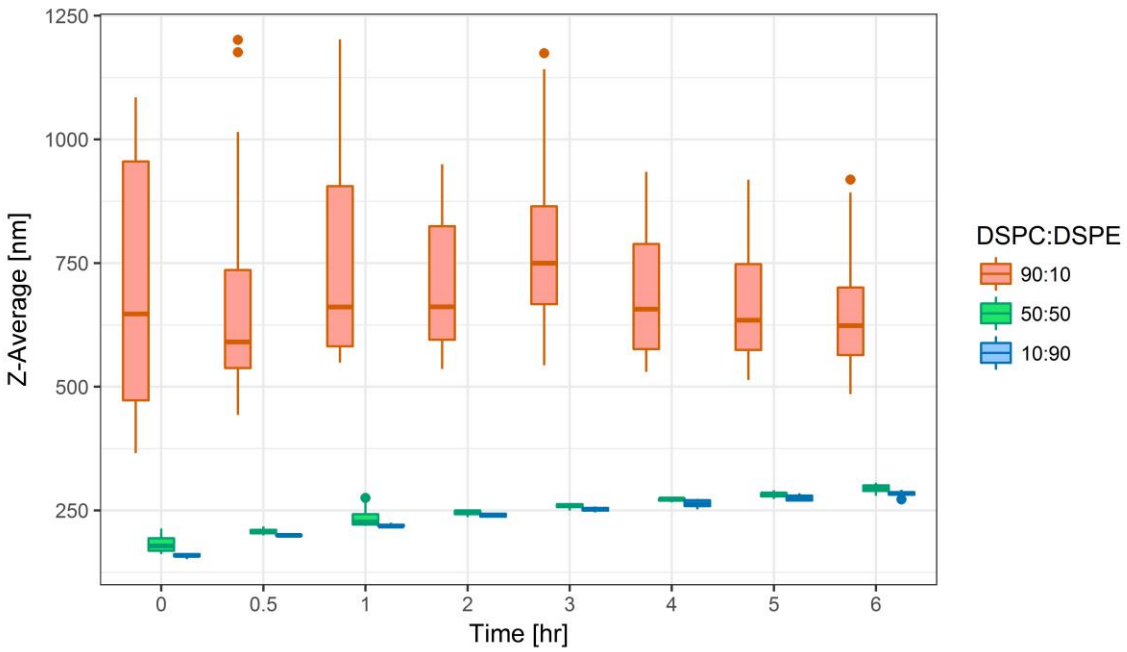

Figure 2: Average size data for PFCnDs as a function of time post-synthesis. Each box represents size data from four batches of lipid-shelled PFCnDs with shells containing a molar ratio of 90:10 (red-orange), 50:50 (green), or 10:90 (blue) DSPC:DSPE-mPEG2000. For each batch at each time point, the dynamic light scattering instrument yielded three Z-Average values for average particle size, each Z-Average an average of 10 successive

measurements. Samples were kept at room temperature (25°C) during and between measurements.[76]

By comparison, the initial size of 10:90 nanodroplets was smaller (median: 159 nm) and more consistent between batches (IQR: 5 nm). The low variance in size persisted for six hours post-synthesis, though the average size measurements did trend upward (median: 218 nm at 1 hour, 284 at 6 hours) similar to the 90:10 nanodroplets. Again, this phenomenon may potentially be due to Ostwald ripening of PFCnDs. Still, nanodroplets with an inverted molar ratio of PEGylated phospholipids remain small for an appreciable amount of time post-synthesis (median < 250 nm at 2 hours). This is a significant finding because downstream PFCnD modification protocols (e.g., bioconjugation) are time-consuming, and the nanodroplets will grow in size over this time. Many researchers only report initial size measurements from their nanodroplets, and these measurements may not accurately reflect the ultimate size of PFCnDs used in their *in vitro* and *in vivo* experiments.

We also investigated batches of PFCnDs with an "intermediate" molar ratio of DSPC:DSPE-mPEG2000 of 50:50. One might expect that the size data to fall halfway between the previous 90:10 and 10:90 batch data. Surprisingly, the intermediate nanodroplets behaved far more similarly to the 10:90 nanodroplets than to the 90:10 nanodroplets. These nanodroplets were initially slightly larger (median: 178 nm) and more variable (IQR: 25 nm) than 10:90 nanodroplets. However, such differences in the data distributions were small, and the size distributions were effectively the same after the first 2 hours post-synthesis. These data imply that the relationship between increased lipid shell PEGylation and reduced droplet size is nonlinear. It is possible that there is a critical concentration of PEG necessary to achieve sufficient steric stabilization such that

increasing PEGylation further will not have a demonstrable impact on reducing nanodroplet coalescence. Further study is necessary to fully characterize this relationship.

Much of the differences in size variance at each time point, detailed through the interquartile ranges described previously, can be explained by differences in the batch-to-batch variability of the different formulations tested. Both the 10:90 and 50:50 PFCnDs produced nearly identically sized particles batch-to-batch. However, the more traditional 90:10 PFCnDs were highly variable batch-to-batch, from 366 to 1085 nm immediately post-synthesis. More detailed descriptive statistics can be found in **APPENDIX A**. Supplemental Data for Nanodroplet Synthesis Studies It is clear that increasing the molar percentage of PEGylated lipid reduces the size of resulting PFCnDs as well as variance between synthesized batches.

This design approach is compatible with other shell modifications that could be implemented to further reduce the size and size variability of PFCnDs. Previous studies in the literature using "low-boiling point" perfluorocarbons have demonstrated an inverse relationship between the acyl chain length of phospholipids in the shell and the median sizes of resulting PFCnDs.[92] How these design choices are impacted by other factors, such as the addition of cholesterol or unsaturated lipids into the shell, remains an active area of research.

Phantom Imaging

In addition to these sizing studies, combined ultrasound and photoacoustic (US/PA) imaging was performed on PFCnDs with varying shell PEGylation. A tissue-mimicking phantom was constructed such that two circular inclusions containing diluted batches of

90:10 and 10:90 PFCnDs in scattering media were visible within a single US/PA imaging plane (**Figure 3A**). Optical fibers adjacent to the imaging transducer were oriented such that both inclusions could simultaneously be evenly illuminated, allowing a more fair comparison of the two droplet populations. Because PFCnDs were loaded with a near-infrared absorbing dye to trigger phase-change events, it was possible to analyze both ultrasound and photoacoustic contrast within the same imaging sequence.

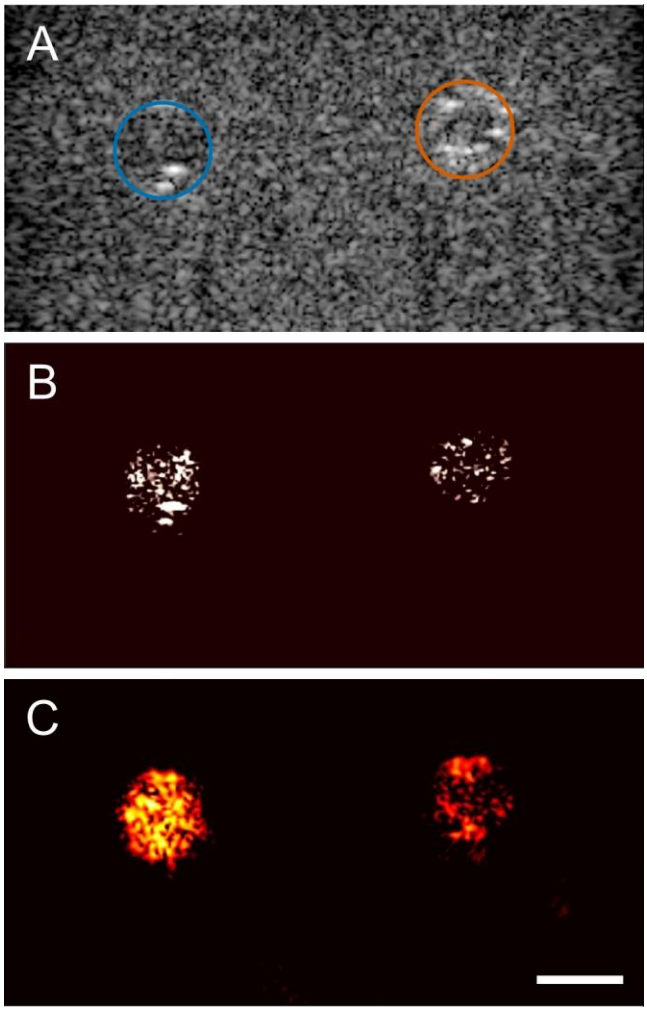

Figure 3: Dual inclusion tissue-mimicking polyacrylamide phantom. This phantom was doped with 1% (w/v) silica gel and containing two inclusions with 1:200 stock dilutions of "10:90" (left, blue circle; average size: 170 nm at 0 hours post-synthesis) and "90:10" (right, red-orange circle; average size: 470 nm at 0 hours post-synthesis) PFCnDs. **A)** Plane-wave B-mode ultrasound image prior to PFCnD laser activation. Three successive plane waves (at -3°, 0°, and 3°, respectively) were compounded to create each ultrasound image. This image is normalized, interpolated, and displayed using a 40 dB dynamic range. Scale bar is 5 mm; **B)** Absolute differential ultrasound image immediately post-laser pulse. Each differential ultrasound image was generated by taking the absolute value of the forward-looking difference of the linear ultrasound signal after compounding each unique ultrasound frame. This image is interpolated and displayed over a linear scale; **C)** Photoacoustic image immediately post-laser pulse. This image is normalized, interpolated, and displayed using a 22 dB dynamic range.[76]

The resulting imaging data were divided into six distinct packets: one without a pre-acquisition laser pulse and five with a pre-acquisition near-infrared laser pulse. Examining the differential ultrasound signal (**Figure 3B**) as a function of time reveals spikes in intensity within the inclusions immediately after the laser pulse (**Figure 4A**), which are characteristic of the repeatable vaporization-recondensation or "blinking" of perfluorohexane nanodroplets.[58] This differential signal returns to baseline for both inclusions after the first millisecond of ultrasound acquisitions.

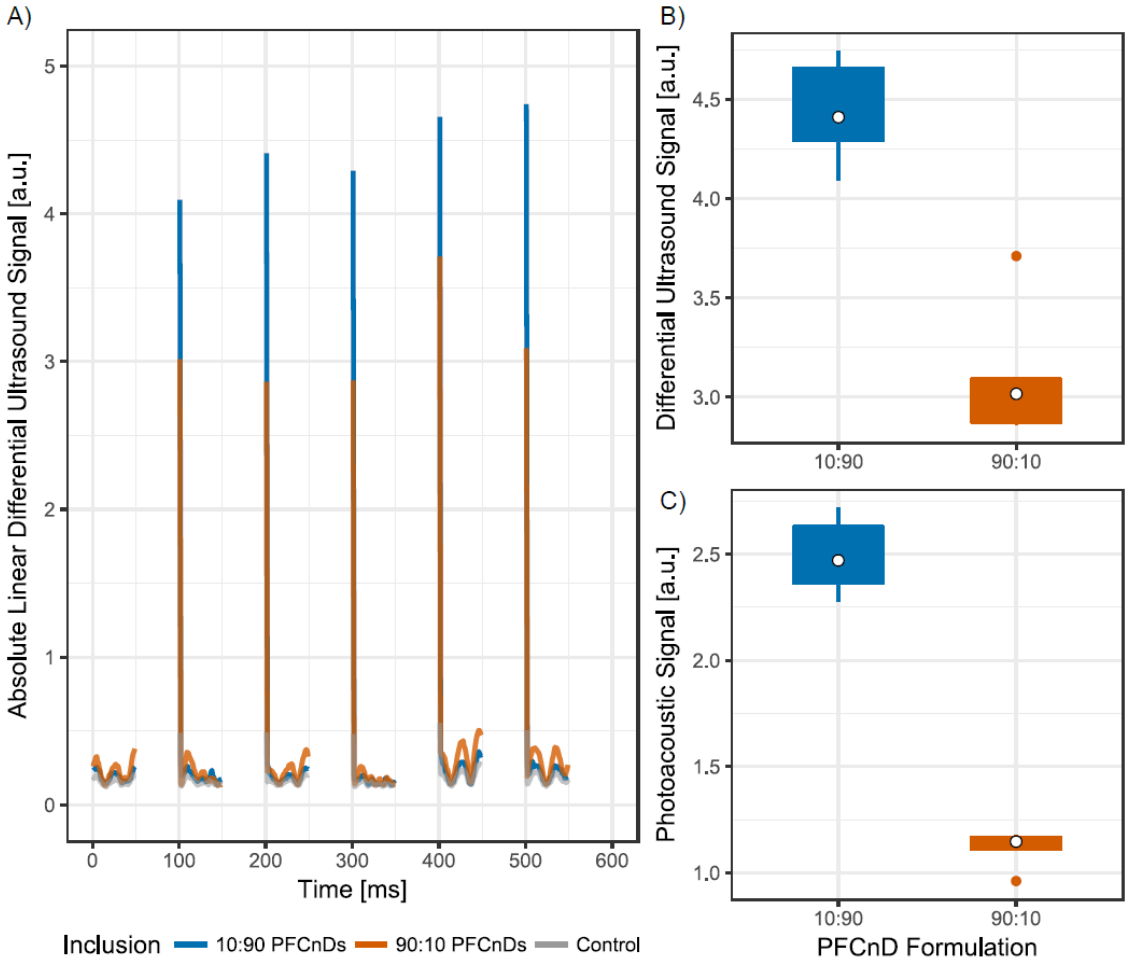

Figure 4: Nanodroplet US/PA analysis. A) Absolute linear differential ultrasound signal as a function of time for the phantom shown in Figure 3. The differential ultrasound signal was integrated across an area-equivalent region of interest containing the "10:90" PFCnDs (red-orange), the "90:10" PFCnDs (blue), and a control region centered within the polyacrylamide gel background in between the two inclusions (gray). Discontinuities within the graph correspond to times when no data are acquired by the US/PA imaging sequence; **B)** Absolute linear differential ultrasound signal post-laser pulse integrated across the "10:90" (blue) and "90:10" (red-orange) PFCnD inclusions; **C)** Linear photoacoustic signal integrated across the "10:90" (blue) and "90:10" (red-orange) PFCnD inclusions.

Analyzing the integrated differential ultrasound signal within each inclusion from the post-laser-pulse frames, the total signal from 10:90 PFCnDs is 1.5 times the total signal from 90:10 PFCnDs (**Figure 4B**). In plane-wave B-mode ultrasound, the backscattered signal (P_{US}) received from a region of interest containing PFCnDs is proportional to the total *en face* surface area of nanodroplets ($n_{PFCnDs} \cdot SA_{PFCnD}$) encountered by plane waves travelling through the region. That is to say,

$$P_{US} = P_{PFCnDs} \propto n_{PFCnDs} \cdot SA_{PFCnD} \tag{4}$$

Batches of both the 10:90 and 90:10 PFCnDs were synthesized with equivalent molar concentrations of perfluorocarbon and surfactant phospholipids. Assuming that the amount of surfactant is non-limiting, the number of droplets within each batch should be inversely proportional to the cube of the diameter of the PFCnDs because the total volume of perfluorocarbon (V_{PFC}) is constant between batches and,

$$V_{PFC} = n_{PFCnDs} \cdot V_{PFCnD} = n_{PFCnDs} \cdot (4/3)\pi(d/2)^3 \tag{5}$$

because the surface area of a droplet is proportional to the square of its diameter, combining Equations (4) and (5) would imply that the signal from PFCnDs in these experiments should be inversely proportional to the corresponding droplet diameter (d). Theoretically, this suggests that there should be approximately 2.8 times the signal from the inverted PFCnD inclusion than the standard PFCnD inclusion.

The 1.5-fold enhancement observed is much less than the theoretical one. Because the synthesis is sonication-based, it is likely that the total volume of perfluorocarbon is not

conserved, as some nanodroplets will be vaporized by the 20 kHz ultrasound during sonication, which would lead to a decrease in the observed contrast enhancement. Additionally, the quoted droplet diameters were for immediately post-synthesis PFCnDs, prior to incorporation into gel mixtures for imaging. It is possible that the nanodroplets continued to grow in size, as observed in **Figure 2**, after synthesis but prior to imaging. Since the size of 10:90 nanodroplets trends much larger relative to their initial size, this could reduce the size ratio used to predict theoretical signal enhancement.

As aforementioned, the laser-activated PFCnDs used for imaging also produce a photoacoustic signal, which can be visualized independently for contrast enhancement (**Figure 3C**). The photoacoustic signal produced from nanodroplets can be attributed to two distinct components.[53] The first component is due to the pressure wave created by the optical droplet vaporization (ODV) and the resulting volumetric expansion. Because the partial derivative of spherical volume in the radial direction is equivalent to surface area, the resulting pressure of this component follows the logic of the ultrasound signal enhancement detailed previously.

If volumetric expansion were the only component of the photoacoustic signal emitted by PFCnDs, then the signal enhancement for 10:90 nanodroplets should be equivalent across ultrasound and photoacoustic imaging. However, experimentally the photoacoustic signal enhancement is higher: 2.2 for photoacoustic signal (**Figure 4C**) versus 1.5 for differential ultrasound (**Figure 4B**). One potential explanation for this observation is the photoacoustic signal emitted from the encapsulated photoabsorber, which is the second component of laser-activated PFCnD photoacoustic signal.[53] A study in mixed micelles demonstrated that water-insoluble drugs have increased solubility in

DSPE compared to DSPC.[93] Similar logic would suggest that inverted nanodroplets, with an appreciably higher DSPE shell content, should solubilize more of the water-insoluble, near-infrared photoabsorber and may be preferable for encapsulating non-polar therapeutics when using PFCnDs for applications in controlled delivery and release.

In conclusion, we have investigated the effects of variable lipid shell composition on the particle and imaging characteristics of lipid-shelled, laser-activated PFCnDs. Our results suggest that increasing the molar concentration of PEGylated phospholipid compared to standard formulations reduces the size and size variability of nanodroplets. Additionally, our imaging studies demonstrate that nanodroplets from batches with an inverted molar ratio of lipids produce increased ultrasound and photoacoustic signal compared to batches of 90:10 nanodroplets, likely because of increased total surface area and dye encapsulation in 10:90 nanodroplets.

These data confirm that it is possible to produce small-sized, monodisperse PFCnDs without the need for more involved synthesis strategies. We also note that the strategy of increased shell PEGylation is not mutually exclusive with alternative approaches: it could potentially be combined with others (e.g., size separation, microfluidics, acyl chain elongation) to further tune PFCnD size or percent yield. Although these studies utilized nanodroplets for US/PA imaging, the dynamic contrast of these agents could potentially be used with optical coherence tomography,[94] magnetic resonance imaging,[95,96] and other techniques that can use microbubbles or perfluorocarbon for contrast generation. Moving forward, we anticipate that the shell-focused strategy for PFCnD synthesis will facilitate the use of PFCnDs amongst more investigators in a wide array of applications-based research endeavors.

3.2 Pulse-Inversion-Based Imaging for Enhanced Imaging Sensitivity to Optically-Activated Nanodroplets

Adapted, with permission, from: Zhu, Y.I., Yarmoska, S. K. & Emelianov, S. Y. Pulse-Inversion-Based Imaging for Repeatable Optically Activate Phase-Change Nanodroplets with Enhanced Sensitivity and Specificity. *Submitted*.

Yiying Zhu was responsible for image acquisition and processing. Steven Yarmoska was responsible for synthesis and all other primary data generation.

3.2.1 Abstract

Optically-activated perfluorohexane nanodroplets (PFHnDs) can vaporize, providing ultrasound contrast, and then stochastically recondense into liquid droplets. Their repeatable activation and random recondensation enables super-resolution imaging and longitudinal contrast-enhanced ultrasound. However, imaging sensitivity and specificity are critical for the detection of these small-sized contrast agents. To address this challenge, we introduced the method of ultrafast planar pulse-inversion ultrasound imaging together with the analysis of PFHnD echogenicity dynamics to improve the detection of optically-activated PFHnDs. We demonstrated this imaging method in a tissue mimicking phantom and in an *in vivo* mouse spleen to achieve PFHnD-specific imaging.

3.2.2 Introduction

An emerging class of ultrasound contrast agents, perfluorocarbon nanodroplets (PFCnDs), has been explored to overcome the size limitations of microbubbles. These nanodroplets are synthesized with a liquid perfluorocarbon core and are produced to be in

the submicrometer range. Traditional nanodroplets can undergo a one-time activation to form gas microbubbles *in situ*, providing ultrasound contrast after they reach extravascular targets.[97] Repeatable activated nanodroplets, optically triggered phase-change perfluorohexane nanodroplets (PFHnDs),[98] have been investigated to provide multiple activations per particle. Upon pulsed laser irradiation, photoabsorbers encapsulated within the PFHnDs cause localized heating, vaporizing the PFHnDs into gas bubbles. These vaporized PFHnDs temporarily behave like microbubbles, providing transient ultrasound contrast. Then, within microseconds, vaporized PFHnDs spontaneously recondense to their naïve droplet form, ready to be triggered again to serve as contrast agents. PFHnDs are theoretically small enough to escape leaky tumor neovasculature and can be targeted to extracellular markers that are not expressed on the endothelium. Also, optically-activated PFHnDs can produce photoacoustic contrast because of the mechanism used to trigger their phase change.[99] Additionally, the ability of PFHnDs to be repeatably triggered due to their high boiling point perfluorohexane core enables both ultrasound super resolution imaging[100] and longitudinal tracking by contrast-enhanced ultrasound.[101]

One of the greatest challenges in PFHnD-enabled contrast-enhanced ultrasound imaging is low imaging sensitivity and low specificity to PFHnDs. These PFHnDs are designed to be small for extravasation, which also introduces two major challenges in imaging them. First, the backscattered ultrasound signals from PFHnDs are weak compared to those of microbubbles, due to their relatively reduced cross-sectional area. This challenge demands a high imaging sensitivity to capture the presence of PFHnDs. Second, due to their extravascular location, PFHnDs are present in a hyperechoic tissue environment. Compared to traditional vascular imaging, in which the background is

relatively anechoic, extravascular imaging requires high imaging specificity to differentiate PFHnDs from enhanced background signal.

Fortunately, optically triggered PFHnDs exhibit unique ultrasound echogenicity due to their vaporization-recondensation behavior. First, nascent liquid-cored PFHnDs weakly scatter ultrasound, appearing hypoechoic in an ultrasound image. Immediately after optical activation, however, vaporized PFHnDs become hyperechoic under ultrasound, similar to traditional gas microbubbles. Ultrafast ultrasound imaging can capture the transient echogenicity associated with PFHnDs that shows an exponential decaying trend, which is distinctive from the background. Previously, we have found that the PFHnD echogenicity dynamics can be manipulated by the ultrasound imaging sequence.[102] Different phases of the imaging pulse lead to different responses from PFHnDs in ultrasound images, including changes in ultrasound signal intensity and echogenicity dynamics. Based on these observations, we moved forward to design a new imaging method that can image PFHnDs with high sensitivity and specificity.

Here, we present an imaging method utilizing ultrafast planar pulse-inversion ultrasound imaging together with PFHnD echogenicity dynamics to improve the detection of optically activated PFHnDs. This method includes the following three components. The first is a pulse-inversion imaging sequence with acquisition including both fundamental and second-harmonic signals. Specifically, we transmit interleaved pulses with opposite phases (i.e., pulse inversion imaging): a pulse with an initial rarefactional phase is immediately followed by a pulse with an initial compressional phase.[102] The summation of echoes from the inverted pulses helps to suppress linearly scattering background. Second, we perform differential imaging in the time domain (i.e., subtracting adjacent ultrasound

frames) in order to further suppress static background signals. Finally, a PFHnD map is created by image processing, resulting in an exponential decay constant map reconstructed from exponential fitting for each image pixel over time. We have demonstrated this imaging method in a tissue mimicking phantom and an *in vivo* mouse spleen to achieve PFHnD-specific imaging.

3.2.3 Materials and Methods

Synthesis of PFHnDs

The PFHnDs consisted of a perfluorohexane core, a stabilizing lipid shell, and an encapsulated dye, and they were synthesized following a protocol adapted from previous studies.[76,103] Briefly, 1 µmol of DSPC, 18:0 Cy5 PE, and DSPE-mPEG2000 (all from Avanti Polar Lipids, Inc.) were isolated in a 1:1:8 molar ratio along with 0.5 mg of near-infrared-absorbing dye (IR-1048; Sigma-Aldrich) from a chloroform solution using a rotary evaporator. After rotary evaporation produced an even cake of lipid and dye, the solid isolate was further dried under nitrogen flow in order to evaporate all residual chloroform.

Next, the solid reagents were hydrated with 1 mL of 7.40 pH PBS and agitated using a water bath sonicator to produce a solution of dye-loaded nanomicelles. This solution was centrifuged at 300 rcf for 1 minute in order to pellet excess near-infrared dye. Then, 900 µL of the nanomicelle-containing supernatant was combined with 100 µL of PBS and 50 µL of perfluorohexane. This solution was then probe sonicated (1s on, 15s off, 5 times) on ice in order to produce a stock solution of PFHnDs, which was stored refrigerated in amber glass prior to use.

Prior to their use for imaging, 100 µL of PFHnDs were diluted in 2 mL of PBS and bath sonicated for 5 minutes. This solution was then centrifugated at 3000 rcf for 5 minutes in order to pellet the PFHnDs. The supernatant was removed and the PFHnDs were reconstituted in 100 µL of sterile saline for imaging. This protocol produces PFHnDs with an average hydrodynamic diameter of 244 nm measured via dynamic light scattering (Zetasizer Nano ZS; Malvern Instruments Ltd.) and at a concentration of approximately 10^{10} PFHnDs/mL as assessed by nanoparticle tracking analysis (NanoSight NS300; Malvern Panalytical).

Tissue Mimicking Phantom

A tissue-mimicking phantom containing three hollow cylindrical inclusions was fabricated to demonstrate the imaging sequences. To construct this phantom, 150 mL of degassed water was mixed with 50 mL of 40% acrylamide (Thermo Fisher Scientific) and set to mix on a stir plate at 350 rpm. To this stirring solution, 2 mL of 10% (w/v) ammonium persulfate solution (Sigma-Aldrich, St. Louis, MO, USA) and 400 mg of silica particles (product number: 717185; Sigma-Aldrich) were added. Next, 250 µL of N, N, N′, N′-Tetramethylethylenediamine (Alfa Aesar, Thermo Fisher Scientific) was added to crosslink the acrylamide. The primed solution was allowed to continue stirring for 9 minutes before being quickly poured into a rectangular 58 x 58 x 78 mm mold. The resultant solution polymerized within 60 seconds of being transferred into this mold.

The three hollow inclusions were filled with ultrasound gel containing either 0.2% w/v silica particles, 1% v/v (PFHnDs to gel) of the as-prepared PFHnDs, or a mixture of both 0.2% w/v silica particles and 1% v/v of the as-prepared PFHnDs. In order to

homogenize the inclusion components, silica and/or PFHnDs were added to de-gassed ultrasound gel, vigorously mixed by hand, and then centrifugated at 1000 rcf for 2 minutes. The resultant homogenous gel solutions were backfilled into the hollow inclusions using 1 mL slip tip disposable syringes.

Mouse Preparation

All small animal experiments were conducted under the purview of Georgia Tech's Institutional Animal Care and Use Committee (GT IACUC; Protocol A16018). A five-month-old BALB/c mouse (Strain 028; Charles River Laboratories) was placed under general anesthesia with isoflurane (5% induction, 1.5-2% maintenance) prior to the following interventions.

The mouse was placed on a heating pad set to 38°C to help maintain its internal body temperature while under general anesthesia. The skin overlying the neck and spleen of the mouse was shaved and chemically depilated with calcium hydroxide lotion. The mouse was placed in the right lateral decubitus position and its spleen was imaged as detailed above.

After preliminary imaging, the skin of the mouse neck was disinfected and 50 uL of PFHnDs, prepared for imaging as described previously, were injected intravenously in the right jugular vein. After 20 minutes, the mouse was again placed in the right lateral decubitus position and its spleen was imaged a second time.

After post-injection imaging, the mouse was euthanized via a lethal intraperitoneal injection of Euthasol (150 mg/kg; Henry Schein Medical). Following cessation of

breathing, the mouse was exsanguinated via perfusion with 6.80 pH PBS and fixed by perfusion with 4% paraformaldehyde. After perfusion-fixation, the spleen of the mouse was resected, placed into an OCT-filled cryomold (both Sakura Finetek), and flash frozen under dry ice.

Mouse Spleen Histology

The flash-frozen spleen was sectioned longitudinally and frozen sections were stored at -80°C. Prior to confocal imaging, slides were thawed and rehydrated with 7.40 pH PBS. After incubation with DAPI (4',6-Diamidino-2-Phenylindole, Dihydrochloride; Invitrogen, Thermo Fisher Scientific), slides were again washed with PBS, mounted with antifade reagent (ProLong Gold Antifade Mountant; Invitrogen), and sealed.

Mounted sections were imaged on a Zeiss laser scanning microscope consisting of an LSM 700 scan head mounted on an AxioObserver Z1 inverted microscope stand with a motorized stage. Images were obtained with laser lines at 405 and 639 nm using a 20x / 0.8 N.A. Plan Apochromat objective lens with a working distance of 0.550 mm.

Imaging System and Imaging Sequences

The imaging was performed by an ultrasound linear array transducer CL15-7 (Advanced Technology Laboratories, Inc.) integrated with an optical fiber bundle (Nanjing Chunhui Science & Industrial Co., LTD). The imaging probe was acoustically coupled with the imaging object using clear ultrasound gel. The optical fiber bundle, connected to a pulsed laser system (Phocus Mobile; Opotek Inc.) operating at 1064 nm wavelength, was used to irradiate the phantom with 5-ns laser pulses at a pulse-repetition rate of 10 Hz. The

estimated fluence at the depth of 5 mm, measured by a laser power meter (Nova II; Ophir-Spiricon, LLC), was 60 mJ/cm^2 (± 5% allowance). To image, the ultrasound transducer was driven at a 7 MHz center frequency using a programmable research ultrasound imaging system (Vantage 256; Verasonics, Inc.). The full imaging window was 22.8 mm wide and 25 mm deep. Immediately following each laser pulse, one photoacoustic image was captured. Then, 0-degree planar ultrasound waves were transmitted at a pulse repetition frequency of 10 kHz for the phantom imaging and 8 kHz for mouse imaging. Two ultrasound imaging sequences were used for ultrafast plane-wave imaging. One, denoted as "N-sequence," had had an initial rarefactional phase followed by a compressional phase. The other one, referred to as "NP-sequence," transmits pulses with opposite phases (i.e., pulse inversion imaging): first pulse with an initial rarefactional phase followed by a compressional phase and second pulse with an initial compressional phase. The received waves were sampled at 56 MHz to include both fundamental and second harmonic components of the ultrasound echoes. All data were saved and processed offline in MATLAB (MathWorks).

Image Processing and Quantitative Analysis

To form contrast-enhanced ultrasound images, the received beamformed images were processed as follows. For the N-sequence, the 10 kHz images were subtracted from the adjacent frames to get a series of differential images. For the NP-sequence, adjacent two ultrasound frames were first summed to form a new series of background-suppressed images. This new set of images were subtracted from the adjacent ones to get a series of differential images.

We processed the first-frame images to compute the signal-to-noise ratio (SNR) and PFHnD detection rate to compare the imaging sensitivity from two different imaging sequences. Specifically, a PFHnD mask was obtained for each first-frame image by identifying the image pixels that had 6 dB higher signal than the averaged background noise signal within the inclusion. The SNR was calculated by dividing the average signal from the PFHnD mask by the average background noise signal. The PFHnD detection rate was defined as the ratio of the pixel number in the PFHnD mask divided by the total pixel number within the inclusion, with the assumption that the inclusion was filled with 100% PFHnDs.

The final PFHnD specific imaging was achieved by performing double differential ultrafast ultrasound imaging after one laser activation to identify PFHnD related decaying behavior. An exponential decay function was fit to the value of each image pixel as a function of time. A decay constant map was then constructed for one imaging sequence as a PFHnD indicator. The PFHnD map overlaying the conventional B-mode image resulted in final PFHnD specified imaging.

3.2.4 Results and Discussion

Tissue Mimicking Phantom Imaging

The first-frame images after optical activation for the silica-only inclusion and the inclusion containing both silica and PFHnDs are shown in **Figure 5** for both the N-sequence and NP-sequence. It is clear that the contrast from optically triggered PFHnDs is not separable from the scattering background under conventional imaging, but the inclusions containing PFHnDs are separable by differential imaging. In differential

imaging of the silica and PFHnD containing inclusion, the SNRs are 33.9 dB and 39.2 dB with detection rates of 20.5% and 67.9% for the N-sequence and NP-sequence, respectively. The NP-sequence detects about three times the number of PFHnDs with double the SNR compared to the N-sequence.

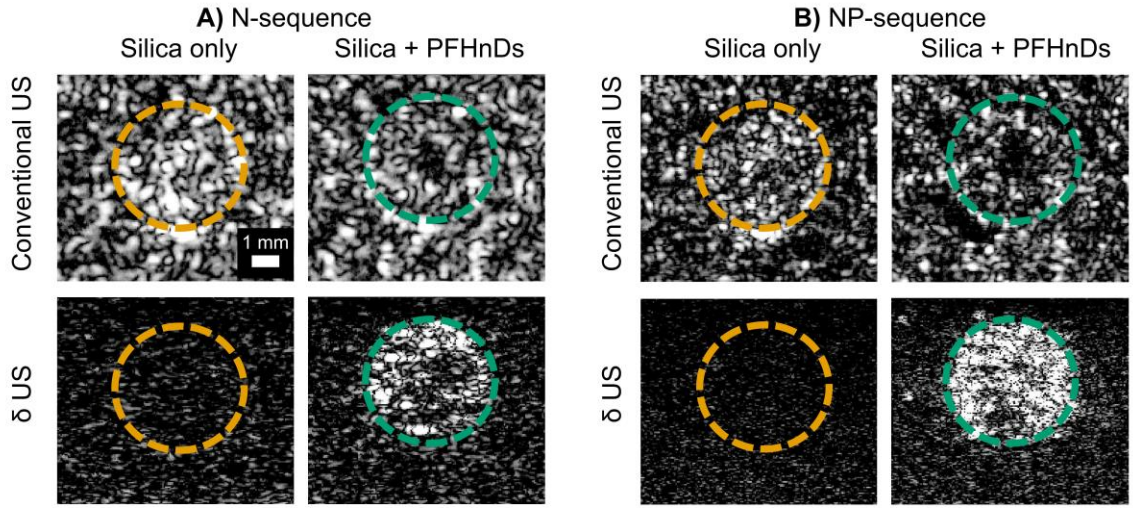

Figure 5: N-sequence versus NP-sequence US imaging of a phantom. First-frame conventional US images and differential US (δ US) images are shown for the N-sequence (**A**) and NP-sequence (**B**). Dashed contours indicate the silica-only inclusion (orange) and the inclusion filled with a mixture of silica and PFHnDs (green). The NP-sequence demonstrates a 5-dB SNR improvement and over triple the PFHnD detection rate of the N-sequence. Images are displayed on a 40-dB dynamic range.

The ultrafast differential ultrasound image series for PFHnDs after one optical activation imaged by the NP-sequence shows a unique disappearing behavior (**Figure 6**). Image pixels related to regions containing PFHnDs exhibit exponentially decaying ultrasound signals, with an example shown in **Figure 7A**. PFHnD maps for the PFHnD-only inclusion and silica-only inclusion are constructed from each ultrasound image series after one laser activation and displayed in **Figure 7B**.

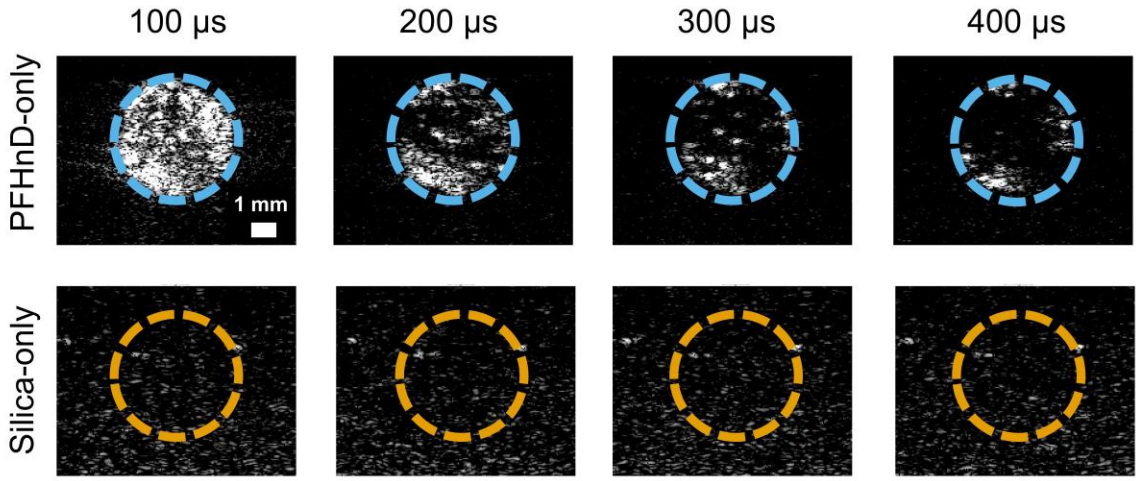

Figure 6: Decay in PFHnD signal post-lasing. An ultrafast differential US (δ US) image series after one optical activation for the PFHnD-only inclusion (top row) and the silica-only inclusion (bottom row) using the NP-sequence. Blue and orange contours indicate the PFHnD-only and silica-only inclusions, resspectively. PFHnDs show a characteristic signal enhancement followed by a rapid decay post-lasing, whereas the silica-only background is statically non-enhancing. All images are displayed on a 40-dB dynamic range.

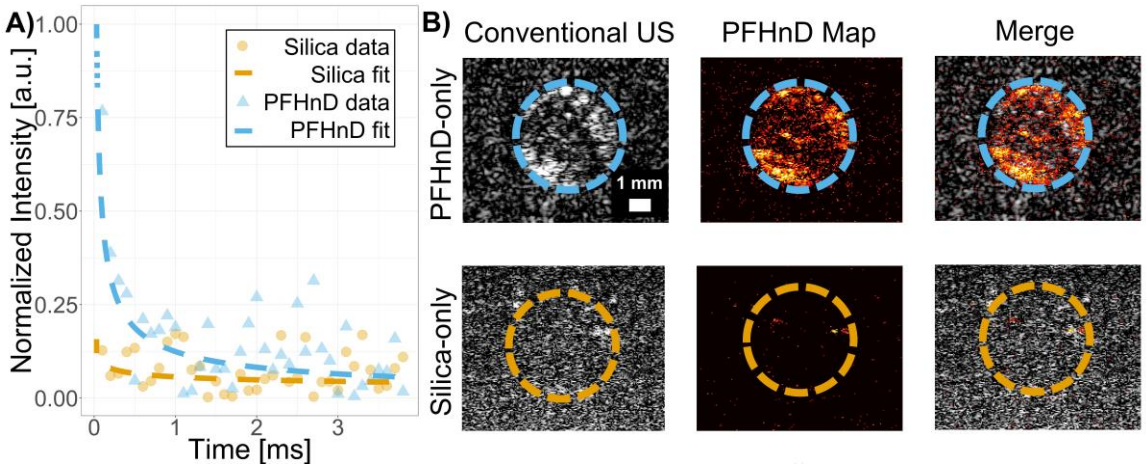

Figure 7: An example of US signal decay used for PFHnD mapping. A) Normalized intensity over time for representative image pixels from the PFHnD and silica inclusions displayed in Figure 6; **B)** Images of the PFHnD-only and silica-only inclusions from Figure 6. Blue and orange contours indicate the PFHnD-only and silica-only inclusions, respectively. The first column shows conventional US images. The second shows PFHnD maps reconstructed from exponential decay constants. The third column overlays these maps on the US images. B-mode images are displayed on a 40-dB dynamic range.

The unique ultrasound echogenicity decay associated with imaging PFHnDs, as shown in **Figure 7**, grants us opportunities to differentiate them from other scatters via differential imaging. Ideally, static linear scatters respond to successive ultrasound imaging pulses the same way. Therefore, their signals can be completely cancelled by subtracting adjacent ultrasound images. In contrast, the decaying signals from PFHnDs will have residual signal remaining after the subtraction of adjacent ultrasound frames. In our ideal tissue mimicking phantom, differential imaging could successfully separate PFHnDs from background silica. It is worth mentioning that this unique decaying behavior may relate to the acoustic interaction with the pulse inversion imaging sequence. More investigation is needed to understand the underlying physics of PFHnDs' recondensation process after optical triggering and PFHnDs' interaction with ultrasound when being imaged.

By performing differential imaging, either once or multiple times, optically triggered PFHnDs can be separated from background, yielding PFHnD contrast enhanced imaging. This differential imaging operation can also be easily implemented for real-time imaging. It is possible to threshold those images from differential imaging to create PFHnD masks. The additional exponential decay constant map we presented imposed one more parameter, the decay constant, to isolate PFHnD behavior. For example, in Figure 4, some hyperechoic regions in the PFHnD only inclusion are not detected by PFHnD map because those regions contain stable gas bubbles, which do not exhibit decaying echogenicity dynamics. The imaging application will ultimately dictate the most appropriate method for PFHnD contrast enhancement. For example, for real-time PFHnD particle trafficking tracking, real-time differential imaging may be more favorable. In contrast, PFHnD drug-loaded delivery may benefit from decay constant mapping to accurately specify PFHnDs

to correlate with drug delivery efficiency. In addition, other than providing ultrasound contrast, optically triggered PFHnDs also give photoacoustic signals upon laser activation. Photoacoustic imaging is another dimension to explore for optically triggered PFHnD related applications.

Murine Spleen Imaging

The *in* vivo imaging of PFHnDs introduces new challenges compared to the ideal phantom case. Here, ultrasound refection at the skin layer in the mouse results in residual signal after differential imaging (**Figure 8A**). By introducing second differential imaging (i.e., subtracting adjacent differential images the second time), these background signals are suppressed, as shown in **Figure 8B**, while retaining contrast in the spleen. The diffuse distribution of PFHnDs in the spleen 20 minutes after IV delivery, as shown in the second differential image, is confirmed by histology (**Figure 8F**). As demonstrated in this proof-of-concept *in vivo* experiment, the unique echogenicity decaying feature of PFHnDs may be retained after multiple differential operators, allowing improved discrimination versus other time-varying signals. It may also be possible to identify PFHnDs with one-time differential imaging by comparing pre-injection and post-injection images.

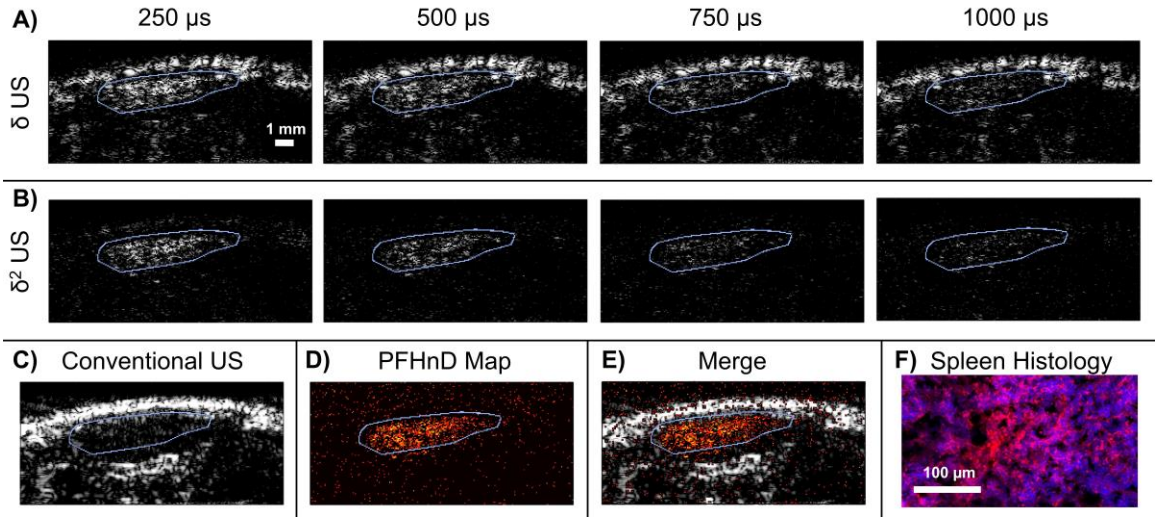

Figure 8: Results from the *in vivo* mouse spleen imaging experiment. Images were taken 20 minutes post-IV injection of PFHnDs. A blue contour indicates the spleen on images. **A)** Differential ultrafast US images (δ US) over time; **B)** second differential ultrafast US images (δ^2 US) over the same time; **C)** Corresponding conventional US image of the spleen; **D)** PFHnD map reconstructed from exponential decay constants derived from δ^2 US data; **E)** PFHnD map overlaid on the conventional US image; **F)** Histology of the mouse spleen. Blue signal is from DAPI-labeled cells and red signal is from Cy5, which tagged the IV-injected PFHnDs. B-mode images are presented on a 40-dB dynamic range.

In conclusion, we have demonstrated a new method leveraging pulse-inversion imaging and differential imaging of PFHnDs to increase sensitivity and take advantage of PFHnD echogenicity dynamics for specificity improvement. The pulse-inversion-based sequence we presented has higher imaging sensitivity by detecting about three times the number of PFHnDs with double the signal to noise ratio compared to conventional one-pulse imaging. This result has direct implications for background-free contrast-enhanced ultrasound imaging of PFHnDs and can be further developed for eventual use with molecular imaging involving PFHnDs.

CHAPTER 4. PERFLUOROCARBON NANODROPLETS FOR LYMPHATIC IMAGING AND THERAPEUTIC APPLICATIONS

4.1 Longitudinal Imaging of Perfluorohexane Nanodroplets Trafficking Within Regional Lymphatics in Breast Cancer

4.1.1 Abstract

Optically triggered perfluorocarbon nanodroplets (PFCnDs) are a phase-change class of ultrasound and photoacoustic (US/PA) contrast agent that are stable at submicrometer sizes. Upon laser irradiation, near-infrared dye encapsulated within the PFCnDs absorbs, causing a phase change of the fluoroalkane core to create microbubbles *in situ*. In this way, PFCnDs have the transport characteristics of a small particle while retaining the imaging contrast properties of a large particle. One biological system where the transport characteristics of PFCnDs are advantageous is the lymphatics. In contrast to traditional micrometer-sized gas microbubbles used with US imaging, the submicrometer size of these agents means that they are rapidly transported through the lymphatic vessels. This makes PFCnDs a more ideal US/PA contrast agent for use in analyzing transport and delivery within the lymphatic system. However, more common formulations of PFCnDs use low boiling point fluoroalkane cores, such as perfluoropentane, with bulk boiling points on the order of or below physiological temperature. These formulations will vaporize into stable microbubbles after a single input of energy, which impairs longitudinal imaging of a single injected bolus. It also hampers the implementation of PFCnDs in lymphatic imaging, because large-animal lymphatic trafficking times are variable and phase-changed

PFCnDs have unfavorable transport characteristics. In response to this limitation, we developed perfluorohexane nanodroplets (PFHnDs), which can repeatably vaporize and recondense at physiological temperatures in response to multiple laser pulses. This feature allows PFHnDs to retain the transport characteristics of their submicrometer liquid-cored state while supporting US/PA imaging at multiple timepoints. To demonstrate the utility of PFHnDs for longitudinal contrast-enhanced US/PA imaging, we imaged naïve and tumor-bearing mice longitudinally over 24 hours. We developed a computationally straightforward algorithm to leverage ultrafast US dynamics to highlight regions of PA contrast with a high probability of containing optically triggered PFHnDs. Our resulting imaging data show focal enhancement moving through ipsilateral lymphatics around the draining lymph node in both naïve and tumor-bearing animals. Histological data confirm the draining path of PFHnDs. We also explored confounding factors in the resulting US/PA contrast, and future studies will work to minimize these false-positive results. In total, these proof-of-concept data lay the foundation for using PFHnDs to longitudinally monitor transport and delivery in a variety of biological applications.

4.1.2 Introduction

The lymphatic system is critical in maintaining fluid homeostasis, mounting an effective immune response, and absorbing dietary lipids.[104] Dysregulation of the lymphatics can lead to lymphedema, for which curative clinical interventions are currently lacking.[105] Modulation of the lymphatics, both in terms of their flow and immune function, is also a hallmark of metastasis in most solid tumors.[106,107] Sentinel lymph node metastatic status offers important prognostic information to patients with breast cancer,[108] melanoma,[109] and other solid neoplastic diseases.[110,111] Furthermore, since the advent of

immunotherapy, tumor-draining lymph nodes (TDLNs) have gained increased interest as a control point for training the adaptive immune response on tumor antigens.[112] For these and other reasons, there is a renewed fervor to investigate both the basic science governing and therapeutic interventions within the lymphatic system.

Much of the basic and translational research within the lymphatic system involves analysis of flow and bulk transport through the lymphatics. To date, these analyses have been accomplished through the use of near-infrared tracers and histology.[113,114] While near-infrared tracers provide a facile means of tagging and tracking small molecules, their fluorescent imaging has limited depth penetration and resolution.[115] Histology is a gold-standard technique, but the use of histology precludes a true longitudinal analysis. Additionally, for preclinical research, the interim sacrifice of animals for histology may not be a viable strategy to assess transport longitudinally in large-animal models, where lymphatic structures are more individually variable.[116] To assess lymphatic transport and function, it may be necessary to employ other imaging techniques.

One such technique is ultrasound (US) imaging. Ultrasound is a non-ionizing imaging technique with clinical traction in point-of-care settings. Ultrasound can image at maximum depths of one to tens of centimeters, depending on transducer hardware. Additionally, with the integration of a pulsed laser light source, US systems can also perform photoacoustic (PA) imaging. Photoacoustic imaging relies on the photoacoustic effect, a phenomenon reminiscent of "lightning and thunder." Photons of input pulsed laser light ("lightning") are absorbed by chromophores. This causes localized heating and thermal expansion, which leads to a pressure wave ("thunder") that can be detected and formed into an image by conventional ultrasound hardware. Photoacoustic images are

ultrasound-like images with contrast based not on variations in tissue density but on variations in tissue optical absorption. Because US and PA images can be simultaneously acquired and co-registered, PA imaging provides complementary information to that afforded by traditional ultrasonography.

In order to analyze flow via imaging, a contrast agent is typically necessary for use as a tracer. In US, gas microbubbles are the clinically approved contrast agent of choice. These biocompatible agents produce excellent imaging contrast, but their relatively large (1+ μm) size makes them ill-suited for draining in the interstitium and lymphatics without mechanical assistance.[117] In PA imaging, dyes and plasmonic nanoparticles are the most prevalent exogenous contrast agents. These agents' small size means that they are rapidly transported through the lymphatics.[75] However, agents that are too small will be resorbed into the bloodstream,[75] and there are lingering concerns about the long-term biological clearance of larger plasmonic nanoparticles from the body. An ideal contrast agent for lymphatic imaging with US would leverage both the imaging contrast and biocompatibility of microbubbles and the transport characteristics of smaller particles.

Perfluorocarbon nanodroplets (PFCnDs) are a preclinical phase-change class of ultrasound and photoacoustic (US/PA) contrast agent that were developed to satisfy these design constraints.[41,53] Nanodroplets utilize the same biocompatible shell components as gas microbubbles, but they substitute the gas core material for one of fluoroalkane. The submicrometer size of PFCnDs keeps the fluoroalkane core in a liquid state at physiologic temperatures.[51] In this nascent liquid-cored state, PFCnDs produce imperceptible US contrast. However, when exposed to a pulse of acoustic or optical energy, the fluoroalkane core vaporizes.[53,86] This vaporization event effectively transforms the PFCnDs into

microbubbles *in situ*.[41] If the vaporization was triggered via laser irradiation, then this event also produces PA contrast.[53]

Traditional PFCnD formulations utilize a "low-boiling point" (e.g., perfluoropentane; BP: 28°C) perfluorocarbon core.[41,118,119] When these agents change phase *in situ*, the phase-change is permanent, as the resulting microbubbles are stable at physiologic temperatures. This precludes longitudinal imaging of a single injected bolus. It also stymies the implementation of PFCnDs in lymphatic imaging. Large-animal lymphatic architecture and trafficking times are variable, and phase-changed PFCnDs have unfavorable transport characteristics. To address these shortcomings, we propose the use of optically triggered perfluorohexane nanodroplets (PFHnDs).[58] These PFHnDs change phase in response to pulses of near-infrared laser light. However, because they have a core of perfluorohexane (BP: 56°C), PFHnDs will stochastically recondense into their original liquid-cored state after the laser pulse ends.[57] A single PFHnD can repeatedly change phase in response to a train of laser pulses, facilitating longitudinal imaging of these nanodroplets. Additionally, the optical trigger allows for the generation of PA contrast, which can be leveraged for enhanced imaging sensitivity compared to US-only acquisition.

The goal of these studies was to demonstrate the feasibility of longitudinal imaging with optically triggered PFHnDs. Here, we image these agents in tumor-draining and naïve murine lymphatics over 24 hours. Histology is utilized in order to confirm the draining path of the PFHnD bolus. Post-processing algorithms for the resulting contrast-enhanced US/PA data are implemented in order to improve the detection of PFHnD-generated signal, and confounding factors are discussed. Our proof-of-concept studies lay the foundation for

in vivo longitudinal imaging of phase-change US/PA contrast agents and may facilitate compelling image-guided applications-based research in the lymphatics.

4.1.3 Materials and Methods

Perfluorocarbon Nanodroplet Synthesis

One micromole (10^{-6} mol) of DSPC, 18:0 Cy5 PE, and DSPE-mPEG2000 (all from Avanti Polar Lipids, Inc.) in a 1:1:8 molar ratio was extracted from chloroform aliquots and added to a 10 mL pear-shaped flask (Aldrich). To this isolate, 0.5 mg of near-infrared-absorbing dye (IR-1048; Sigma-Aldrich) from a 5 mg/mL chloroform aliquot were added. An additional 200 µL of HPLC-grade chloroform were added to the flask to ensure the formation of an even lipid cake. The pear-shaped flask was covered in aluminum foil and placed into a rotary evaporator with a water bath (R-215, V700, and V-855 with B-491; Buchi) and water-cooled condenser and evaporated for 30 minutes, adhering to the "20/40/60" rule. After this, the solid isolate was further dried under nitrogen flow for a minimum of 20 minutes in order to evaporate all residual chloroform in the lipid cake.

Next, the solid reagents were hydrated with 1 mL of 7.40 pH PBS and homogenized using a water bath sonicator (1800 Series Ultrasonic Cleaner; Branson) for 5 minutes at room temperature to produce a solution of dye-loaded nanomicelles. This solution was centrifuged at 300 rcf for 1 minute in order to pellet excess near-infrared dye. Then, 900 µL of the nanomicelle-containing supernatant was combined with 100 µL of PBS and 50 µL of perfluorohexane (FluoroMed, L.P.) in a 2-dram glass scintillation vial (VWR). The glass vial was placed into an ice bath and allowed to rest for 5 minutes. Then, the solution was probe sonicated in the ice bath with a 1/8" microtip (QSonica) at 1% power (1s on,

15s off, 5 times) in order to produce a stock solution of PFCnDs, which was stored at 4°C in amber glass prior to use.

Prior to their use for imaging, 100 µL of PFCnDs were diluted in 2 mL of PBS and bath sonicated for 2 minutes. This solution was then centrifugated at 3000 rcf for 5 minutes in order to pellet the PFCnDs. The supernatant was removed and the PFCnDs were reconstituted in 200 µL of sterile saline for imaging. This protocol produces PFCnDs with an average hydrodynamic diameter of 225-258 nm measured via dynamic light scattering (Zetasizer Nano ZS; Malvern Instruments Ltd.) and at a concentration of approximately 10^{10} PFCnDs/mL as assessed by nanoparticle tracking analysis (NanoSight NS300; Malvern Panalytical).

All of the previously described synthesis steps were performed in darkness to minimize photobleaching of the Cy5 fluorophore.

4T1 Cell Line

4T1 triple negative breast carcinoma cells (ATCC), passage 11-16, were cultured in RPMI plus L-Glutamine (Corning) supplemented with 10% FBS (Corning) and 1% penicillin-streptomycin (Sigma-Aldrich). Cells were maintained within T-75 flasks (CELLSTAR; Greiner Bio One, VWR) at 37°C in a humidified incubator with 5% CO_2.

To passage cells, all media was aspirated from the T-75 flask and replaced by 5 mL of sterile PBS without calcium or magnesium (VWR). The PBS was swirled around the bottom of the flask a minimum of 15 times in order to wash any residual media from the cells. The PBS was then aspirated and replaced by 2 mL of 0.25% Trypsin/2.21 mM EDTA

in HBSS without sodium bicarbonate, calcium, or magnesium (Corning), enough volume to cover the entire bottom of the T-75. The flask was placed back into the incubator for 3 minutes and then removed. After gently agitating the flask and visually inspecting for signs of cell detachment, 8 mL of pre-warmed RPMI media, prepared as described above, was added to the flask to bring the total volume to 10 mL. This solution was used to wash the bottom of the flask five times, dislodging any residually adhering cells. Then, the solution was vigorously pipetted up-and-down five times in order to form a single-cell suspension. Lastly, 50 to 1000 µL of this solution was used to seed the new flask pre-filled with fresh warmed media to ultimately reach a total final volume of 20 mL.

Mice

All animal studies were conducted under the oversight of the Georgia Tech Institutional Animal Care and Use Committee (IACUC) under protocol A100281. Four-week-old female BALB/cJ mice were purchased from The Jackson Laboratory (Stock No.: 000651). Upon receipt, mice were allowed a minimum of five days to acclimate to the housing facility at the Georgia Institute of Technology. Mice were housed with their littermates, with a maximum of four mice per cage, until administration of perfluorohexane nanodroplets, at which point the dosed mouse would be housed in isolation prior to reaching the experimental endpoint. Cages within the housing facility contain 100% corn cobb bedding and enrichment in the form of a mouse igloo, wood gnawing block, and rodent nesting sheets (all Bio-Serv; Fisher Scientific). The facility operates on a 12-hour day-night cycle, with “daytime” occurring from 06:00-18:00 UTC-5. Mice had access to food and water *ad libitum* throughout all phases of the study.

Murine Anesthesia

In order to achieve general anesthesia, mice were placed into a non-primed induction chamber, which was then filled with 5% isoflurane in oxygen at a flow rate of 400 mL/min. After mice lost their righting reflex and their sympathetic response to isoflurance abated to yield a respiration rate of at most 100 breaths per minute (bpm), the isoflurane was lowered to 2%.

Once their respiration rate reduced to between 60-80 bpm, mice were transferred onto a temperature-controlled stage (Visualsonics) heated to 40°C. The isoflurane flow rate was raised to 600 mL/min for the initial transfer but was slowly lowered back to 400 mL/min during positioning on the stage. For procedures under general anesthesia scheduled to last longer than 30 minutes, sterile petrolatum ophthalmic ointment (Puralube; Dechra Phramaceuticals) was applied to the eyes of mice immediately post-transfer using a 6” wood-handled cotton-tip applicator (Puritan Medical).

Throughout general anesthesia sessions, the isoflurane was gradually lowered to between 1.25-1.5% maintenance in order to consistently maintain murine respiration between 60-80 bpm. If after two hours mice respired slower than 60 bpm, isoflurane was lowered to 1% or 0.75% as necessary to maintain the appropriate respiration rate.

After non-terminal procedures, mice were returned to pre-warmed cages and monitored until they regained consciousness and resumed normal behavior. A heat lamp was applied if this process did not occur within 15 minutes.

4T1 Syngeneic Model of Breast Cancer

Prior to inoculation, 4T1 cells were trypsinized (Corning), pelleted at 300 rcf for 5 minutes, and resuspended in sterile PBS without calcium (Corning) at a final concentration of 2×10^6 cells per mL. Cells were counted prior to pelleting using 10 µL of solution on a hemocytometer. The count from the central grid of the hemocytometer was used to estimate the number of cells in the pellet prior to resuspension. The final cell solution was stored on ice prior to inoculation.

Five- or six-week-old BALB/cJ mice were placed under general anesthesia per the previously detailed protocol. The skin overlying the right fourth mammary fat pad was shaved with an electric-powered shaver (BravMini+; Wahl). The area was then chemically depilated with Nair calcium hydroxide lotion (Church & Dwight). Nair was dabbed with a cotton-tipped applicator into the hair roots and allowed to sit on the skin for 60 seconds. After this, the Nair lotion was removed by sequential, unidirectional wiping with first moist and then dry gauze pads.

The shaved and depilated area was then disinfected with a 2% chlorhexidine gluconate solution (Dermachlor; Henry Schein Animal Health) applied with a gauze pad and allowed to air dry prior to further manipulation of the animal. Then, 50 µL of the 4T1 cell solution (10^5 cells) were injected subcutaneously in the anterolateral aspect of the right fourth mammary fat pad using a 31-Gauge diabetic syringe (Ultra Fine II™ U-100; BD). For non-tumor mice, a solution of sterile PBS was used as a sham inoculation.

US/PA System and Imaging Sequence

Imaging was performed using a linear array ultrasound transducer (CL15-7; Advanced Technology Laboratories, Inc.) integrated with a 2-to-1 optical fiber bundle

(CBGL-8-1/2-2500; Nanjing Chunhui Science & Industrial Co., LTD). The optical fiber bundle was connected to an Nd:YAG pulsed laser (Phocus Mobile; Opotek Inc.) operating at the fundamental 1064 nm wavelength. The split end of the fiber bundle was mechanically fixed to the transducer via a custom 3D-printed holder. These fiber outputs allowed for irradiation of imaged tissue, which was performed with 5-ns laser pulses at a pulse repetition frequency (prf) of 10 Hz. The estimated fluence at the depth of fiber intersection within the imaging plane (12-14 mm) was measured to be 85±5 mJ/cm^2 with a power meter (Nova II; Ophir-Spiricon, LLC). For US imaging, the transducer was driven at a 12.5 MHz center frequency using a programmable research US imaging system (Vantage 256; Verasonics, Inc.). The full imaging window in each plane was 22.8 mm wide and 25 mm deep. The imaging probe and optical fiber outputs were acoustically coupled with the subject using clear ultrasound gel (Sonigel; 3B Scientific).

For the imaging sequence at each imaging plane, a traditional line-by-line B-mode acquisition was first captured to record the underlying anatomy. Next, the tissue was irradiated with six successive laser pulses. A packet of US/PA data was acquired after each pulse. Each packet begins with 40 ultrafast pulse inversion (UFPI) frames at 8 kHz with alternating compressional or rarefactional phase as described in 3.2.3. After these "pre-laser" frames, the tissue is irradiated by a laser pulse. This pulse is immediately followed by a receive-only acquisition to capture PA signal and 40 "post-laser" UFPI frames at 8 kHz. Idle time fills the time between US/PA packets to synchronize with the 10 Hz prf of the pulsed laser. The first three US/PA packets use UFPI sequences with transmits that have an initial rarefactional phase, as described previously. The last three invert this order

and use transmits beginning with an initial compressional phase. All of the received waves were sampled at 56 MHz.

After all images in the US/PA imaging sequence at a plane were saved in system memory, a motor controller (Model ESP301; Newport Corporation) translated a motorized linear stage (Model UTS150PP; Newport Corporation) 0.3 mm in the direction perpendicular to the imaging. In this new imaging plane, the US/PA imaging sequence was again acquired and saved in memory. This process repeats to acquire 35 imaging planes, spanning a total distance of 10.2 mm, for each volumetric acquisition. After completing a volumetric acquisition, the software returns the motor stage to its original position at the first imaging plane.

All data were saved and processed offline in MATLAB (MathWorks). For displaying post-processed volumetric images, line-by-line B-mode and post-processed PA images at each imaging plane were linearly interpolated by a factor of 5 in two dimensions and saved as JPEGs. These co-registered JPEG stacks were imported into Amira (Thermo Fisher Scientific) and rendered in three-dimensional space. The B-mode layer was made translucent at $\alpha = 0.15$ to highlight the co-registered PA signal. Amira software adjusted the dynamic range of its display colormap in order to match the range of the post-processed PA signal for each individually rendered volume.

US/PA Imaging Protocol

Mice were placed under general anesthesia per the previously described protocol. If necessary, the skin overlying the abdomen, upper pelvis, and right back (hip to scapula) was shaved with an electric-powered shaver. These areas were then chemically depilated

with Nair calcium hydroxide lotion. For the first pre-injection imaging session, the Nair was left on the skin for a full 60 seconds. However, for downstream imaging timepoints where the mice had already been depilated, regions of regrown or residual hair in the imaged regions only received exposure of 30 seconds or less to the depilatory lotion. This protocol ensured no unnecessary irritation of the skin within the imaged regions.

After the mice were sufficiently depilated for imaging, a rectangular cut-out of hunter green felt (Walmart) was slid underneath mice and fixed to the imaging stage. The felt prevents reverberation artifacts in ultrafast imaging by attenuating plane waves reflected off the imaging stage and does not absorb residual 532-nm light from the laser source, which could produce potential photoacoustic artifacts. Once the felt was in place, mice were placed into the left lateral decubitus position, and their limbs were fixed to the imaging stage with adhesive tape (ZONAS® Porous Tape; Johnson & Johnson). Acoustic coupling gel (Sonigel; 3B Scientific), which was previously centrifugated for 5 minutes at 10,000 rcf to remove bubbles and UV-sterilized, was applied to the depilated skin surface using a 5-mL disposable slip-tip syringe (BD). The transducer was lowered until coupled with the gel, and real-time B-mode imaging on the Verasonics Vantage system was used to appropriately position the mouse. The 3-axis motor stage was used to translate the transducer through the imaging volume of interest. A 1-mL disposable slip-tip syringe (BD) was used to remove any bubbles remaining in the gel from this imaging volume.

Following initial positioning, acoustic coupling gel was used to couple the laser fiber bundles to the mouse skin surface. The motor stage was again translated through the volume of interest both to ensure no additional bubbles entered the volume and to ensure gel coupling of the fibers throughout the entire motion of the transducer setup through the

imaging volume. Bubbles were removed and more gel was added as necessary. Once quality coupling of the transducer and fibers was assured, two sequential US/PA volumes were acquired by the system. The first was a volume beginning cranially and ending caudally after the ipsilateral inguinal lymph node. The second volume started with the inguinal lymph node and proceeded caudally to the primary tumor or mid-4th mammary fat pad (naïve mice).

After volumetric US/PA acquisitions, a quality assurance (QA) code was executed in MATLAB (MathWorks) to quickly assess B-mode, PA, ultrafast pulse-inversion US, and initial differential US images across the imaging volume. If the QA code suggested issues in US coupling, laser light illumination, or malpositioning, then these issues were addressed, and the corresponding volume was reacquired.

Once high-quality volumetric scans were acquired in the left lateral decubitus position, the imaging stage was moved from under the transducer and excess gel was removed from the mice. Tape was removed from the four limbs of the mice, and they were repositioned and re-taped in the supine position. The imaging stage was re-positioned under the transducer 180° rotated compared to before, and additional gel was added to couple the transducer. After bubbles were removed from the imaging volume, more gel was again added to couple the laser fiber bundles. Following the same positioning workflow as before, two sequential US/PA volumes were acquired by the system. The first began caudally near the primary tumor and ended cranially. The second volume proceeded cranially in a non-overlapping fashion (i.e., 0.3 mm cranial to the final plane in the first acquisition).

Each volumetric acquisition takes approximately 8 minutes to acquire and save the data. The entire imaging workflow, from induction of anesthesia to regaining of consciousness or euthanasia, requires between 120 to 150 minutes, on average, to execute.

Perfluorocarbon Nanodroplet Injection

Mice were manually restrained without general anesthesia by scruffing. Then, the skin overlying the right fourth mammary fat pad was disinfected with a 70% isopropyl alcohol swab (BD). Next, a 31-Gauge diabetic syringe was used to perform a subcutaneous injection of 100 µL of 10^{10} particles/mL solution of perfluorocarbon nanodroplets in the anterolateral aspect of the right fourth mammary fat pad, superior to any primary tumors. Mice were immediately returned to the animal housing facility after the injection procedure and before any downstream imaging. A cage change was performed for each injected mouse during the injection protocol in order to encourage movement to circulate fluid from the injected bolus prior to post-injection imaging.

If mice displayed overly aggressive behavior during the manual restraint attempt (i.e., attempted biting or jumping out of cage), mice were sedated with "twilight" isoflurane exposure, which entails 5% isoflurane exposure at 400 mL/min flow rate until the loss of righting reflex, to facilitate injection.

Euthanasia

Mice were sacrificed via a primary lethal intraperitoneal injection of Euthasol (150 mg/kg; Henry Schein Medical) contralateral to the primary tumor. After cessation of breathing, mice were exsanguinated during the perfusion-fixation procedure, which served as secondary euthanasia. In brief, a transverse incision through the skin and underlying

fascia was made immediately inferior to the sternum. Vertical incisions were made superiorly on either side of the primary incision, transecting the ribs in the process, in order to expose the diaphragm. The diaphragm was transected laterally, and the rib cage was separated and reflected superiorly, exposing the heart. A 27-Gauge butterfly needle (Surflo Winged Infusion Set; Terumo) was inserted into the left ventricle of the ideally still-beating heart and the right auricle was lanced vertically in order to convert the circulatory system into an open circuit. At this stage, 20 mL of 6.90 pH PBS was pumped through the circulatory system at a rate of 5 mL/min using a syringe pump (Legato 200; KD Scientific) attached to the butterfly needle setup. Next, the PBS syringe was replaced by one with a solution of 4% paraformaldehyde (reagent grade; Sigma-Aldrich) in 6.90 pH PBS, and 20-25 mL of this solution was pumped through the mice at a rate of 5 mL/min. Successful perfusion-fixation was confirmed by palpation of the mouse extremities to assess rigor.

After perfusion-fixation, both the ipsi- and contralateral popliteal, inguinal, and proper axillary lymph nodes were resected. These nodes were placed into OCT-filled cryomolds (both Sakura Finetek), flash frozen under dry ice, and stored at -80°C to be sectioned for downstream histological analysis.

Lymph Node Histology

Prior to confocal imaging, slides were thawed, DAPI-stained, and sealed. All of these steps were performed in darkness to minimize photobleaching of fluorophores within the sections. First, frozen slides were thawed at room temperature for 20 minutes. Next, slides were rehydrated with 7.40 pH PBS for another 20 minutes. After this, excess PBS was tapped off slides, and the hydrated tissues were incubated with a 1:25000 (1:1000, then

10:250) PBS dilution of DAPI (4',6-Diamidino-2-Phenylindole, Dihydrochloride; Invitrogen, Thermo Fisher Scientific) from an aliquot of 5 mg/mL in dimethylformamide (DMF). After 10-12 minutes of DAPI incubation, the DAPI solution was tapped off slides. Then, the slides were washed three times with PBS, allowing PBS to hydrate the sample for 5 minutes before being tapped off for the next wash. After the last wash, slides were mounted with antifade reagent (ProLong Gold Antifade Mountant; Invitrogen). Two to three drops of mountant were dropped evenly across the slide, in between tissue, and a glass coverslip (VWR) was slowly and evenly pressed down over the slide to distribute the mountant across the glass without disrupting the tissue. Lastly, clear nail polish was twice applied to all four edges of the coverslip to seal it to the slide, allowing at least 30 minutes for the first application to dry before adding the second. Mounted and sealed slides were stored in the dark at 4°C, at minimum overnight, until their scheduled time to be imaged on the confocal.

Mounted sections were imaged on a Zeiss laser scanning microscope consisting of an LSM 700 scan head mounted on an AxioObserver Z1 inverted microscope stand with a motorized stage. Images were obtained with laser lines at 405 and 639 nm using a 20x / 0.8 N.A. Plan Apochromat objective lens with a working distance of 0.550 mm. Tiled confocal images were rendered as JPEGs using Zen Black software (Carl Zeiss AG). The dynamic range of the Cy5 channel was set as the minimal level to suppress all signal in the right popliteal lymph node.

Statistical Analysis

Statistical analyses were performed in R (R Core Team). A two-way ANOVA with repeated measures was performed on the data to assess the effects of measurement timepoint and animal model on the masked PA signal.

4.1.4 Results and Discussion

We elected to use BALB/c mice as a model small animal for our longitudinal studies of the lymphatic drainage of optically triggered PFHnDs. These mice have relatively static lymphatic organization,[120] and the background supports various syngeneic models of cancer, including the 4T1 model of metastatic triple-negative breast cancer.[121] The 4T1 syngeneic model is actively used in the scientific community for studies of cancer-induced lymphangiogenesis and lymphatic metastasis.[106,122-124] Thus, this animal model is a logical starting point for our proof-of-concept studies.

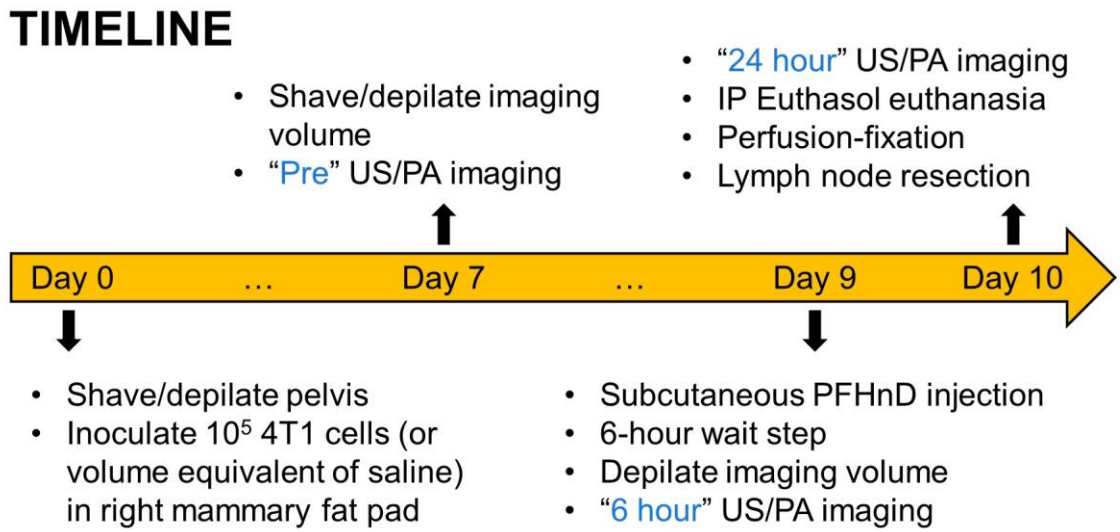

Figure 9: Schema for the inoculation and US/PA imaging of lymphatics in BALB/c mice.

The animal imaging protocol used for these imaging studies is shown in **Figure 9**. The timing and technique of our tumor inoculation is based on methods established by a prominent group of lymphatic researchers.[122] It does not produce overt lymphatic metastases over the course of our longitudinal US/PA imaging, but it should induce lymphovascular remodelling in the tumor-draining lymph node (TDLN).[122] We perform three sessions of US/PA imaging per mouse: one prior to PFHnD injection to establish a baseline, another 6 hours after PFHnD injection, and a final session at 24 hours prior to the experimental endpoint.

Each US/PA imaging volume is the result of sequential 2D acquisitions across the imaging span. Representative images from one such 2D plane can be seen in **Figure 10**. First, the US/PA imaging sequence acquires a traditional line-by-line B-mode US image (**Figure 10A**) in order to visualize the underlying anatomy. Next, after an emitted laser pulse, the sequence receives the generated PA signal, which can be reconstructed into a PA image (**Figure 10B**). Absorption at the skin surface and within other endogenous structures, as well as imaging artifacts, can produce PA signals that confound the signal produced by optically triggered PFHnDs. To more specifically isolate signal from the PFHnDs, it is necessary to leverage the transient US contrast generated by these repeatably vaporizable agents. In 3.2, we demonstrated the ability of an ultrafast pulse inversion (UFPI) sequence to enhance US signal from PFHnDs relative to background. We implement the same paradigm here, as well. By performing differential imaging (i.e., taking the first difference of the imaging data with respect to time), we can highlight the rapidly decaying ultrasound contrast produced by recondensing PFHnDs vaporized by the preceding laser pulse. To maintain methodological consistency with the previous study, we

utilize the second differential (i.e., first difference of the first difference) UFPI (δ^2 UFPI) data to analyze the dynamics of recondensing PFHnDs. Qualitatively, the differential UFPI (δ UFPI) and δ^2 UFPI data are similar (see **APPENDIX B**, **Figure 27**), and either could theoretically be used for analysis.

The first image in the δ^2 UFPI time series in our representative 2D dataset can be seen in **Figure 10C**. Although a region of draining PFHnDs, highlighted by the dashed yellow box, is easily perceived within this plane, there are also areas of nonspecific enhancement from an endogenous hyperechoic structure and the animal imaging stage. To better reject areas of nonspecific enhancement, it is necessary to examine the temporal dynamics of these signals. The absolute value of the median δ^2 UFPI signal from the boxed region of interest in **Figure 10C** is shown in **Figure 10D** as a function of time. This signal displays a high-magnitude exponential decay that is commonly observed from optically-triggered PFHnDs upon recondensation.[76,102,103]

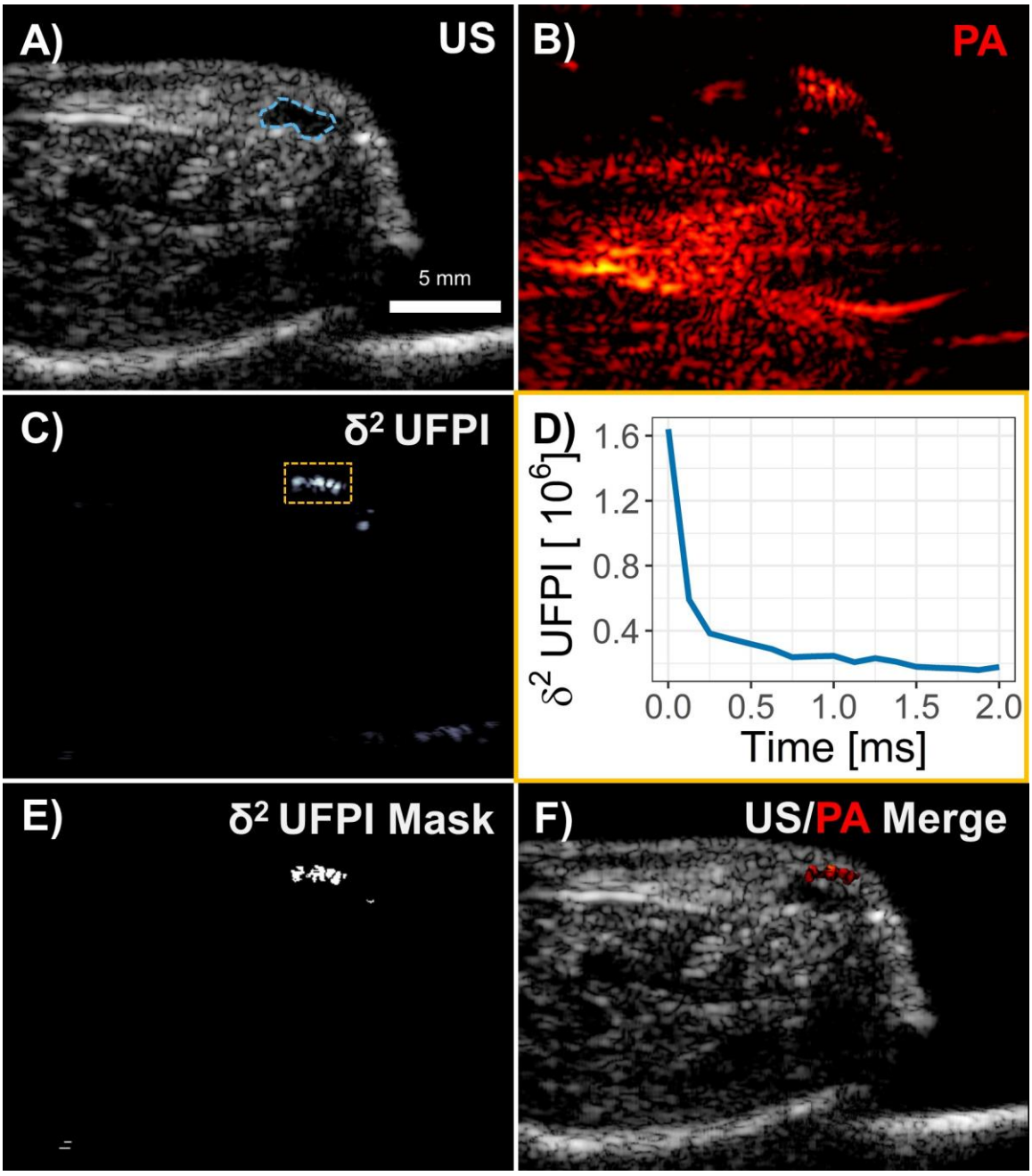

Figure 10: Representative 2D US/PA imaging data from a tumor-draining lymph node. A) Traditional B-mode imaging of the tumor-draining lymph node (light blue outline), displayed on a 40 dB dynamic range; **B)** The corresponding PA image, displayed on a 40 dB dynamic range; **C)** The second differential ultrafast pulse inversion (δ^2 UFPI) image acquired immediately post-laser pulse, displayed on a 20 dB dynamic range; **D)** A plot of the median linear δ^2 UFPI signal within the region of interest highlighted in **C)** by the dashed yellow box; **E)** The mask based on the δ^2 UFPI that will be applied to the PA data for display; **F)** Final merged US/PA image with the δ^2 UFPI masked PA data. Scale bar is 5 mm.

To date, both internally and in conference presentations, our group has explored a variety of post-processing options based on this exponential decay phenomenon for highlighting optically triggered PFHnDs. Many of these methods have involved fitting the linear time-series data to an exponential decay function and thresholding the data based on the resulting model coefficients. However, these methods are computationally intensive and scale poorly to the amount of data collected in these longitudinal studies. In order to efficiently process these data, we applied a pixelwise threshold to the δ^2 UFPI data with logical masking based on quantitative measures intended to approximate an exponential decay fit. These criteria are listed below in **Table 1**.

Table 1: Criteria for Thresholding δ^2 UFPI Imaging Data

Logical Mask Criteria
• $20\log_{10}(\delta^2\ \mathrm{UFPI}[1]) - 20\log_{10}\big(max(\delta^2\ \mathrm{UFPI})\big) \geq -20$ • $\delta^2\ \mathrm{UFPI}[1] > \delta^2\ \mathrm{UFPI}[2]$ • $\delta^2\ \mathrm{UFPI}[2] > \delta^2\ \mathrm{UFPI}[20]$ • $\delta^2\ \mathrm{UFPI}[1] > 2 \times \delta^2\ \mathrm{UFPI}[20]$

Applying these criteria to the pixelwise δ^2 UFPI data generates a logical mask at each plane, like the one shown in **Figure 10E**. After adjusting for variable time delay in the Verasonics Vantage receive-only acquisition relative to the laser Q-switch, the δ^2 UFPI mask is applied to the corresponding PA frame to generate a masked PA image (**Figure 10F**), whose retained contrast has a higher probability of corresponding to optically triggered PFHnDs. We perform this post-processing algorithm for all six laser pulses at each frame and then take the median result for the final masked PA image at the frame. When performed on each plane across the volume, this workflow generates volumetric imaging data like that shown in **Figure 11** for a representative syngeneic 4T1 mouse.

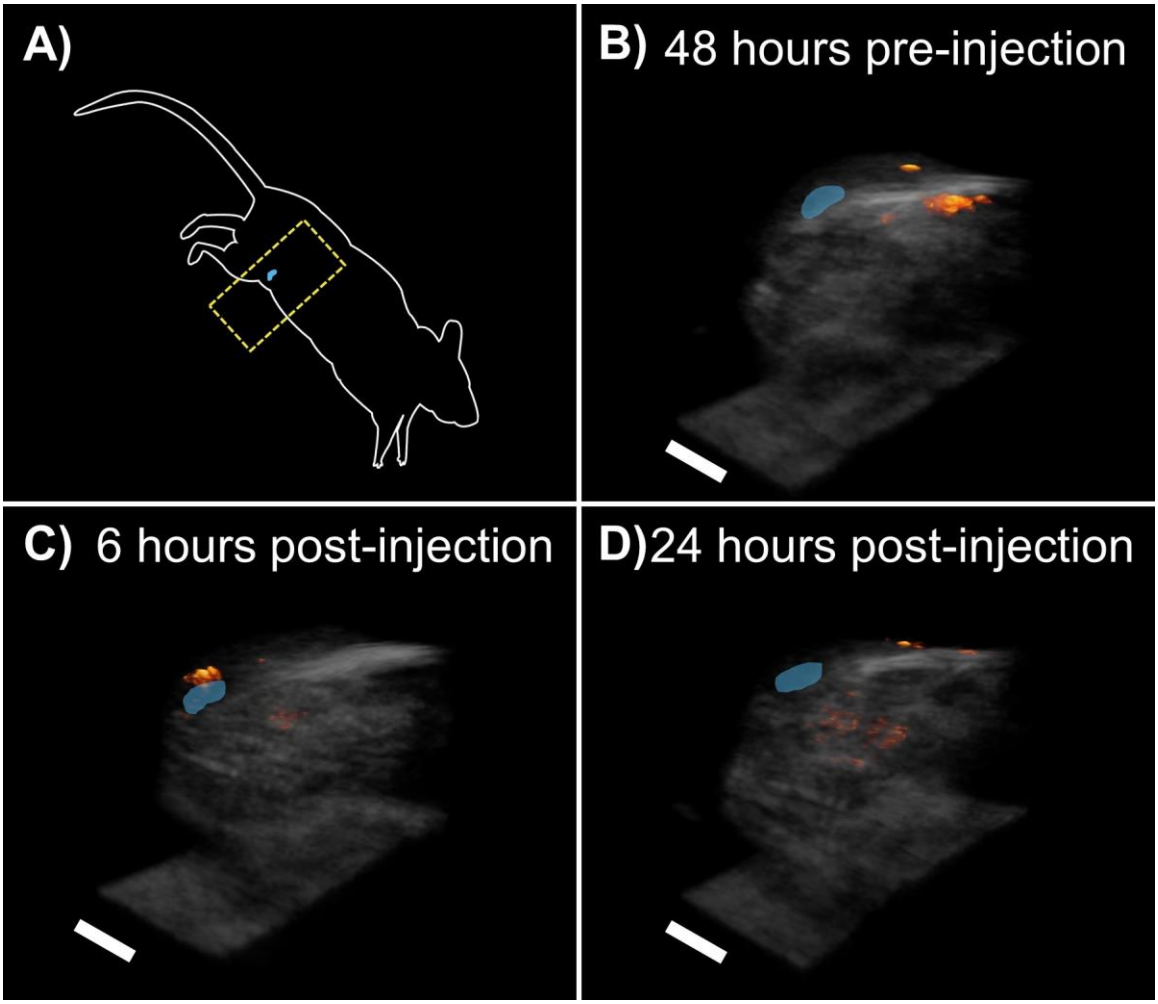

Figure 11: Processed US/PA volumes from a 4T1 syngeneic mouse. This mouse received a 100 µL subcutaneous injection of PFHnDs at 0 hours. **A)** Cartoon showing the left lateral decubitus position of the mouse for imaging. The yellow dashed lines approximate the volumes shown. Lymph nodes are false colored in light blue; **B)** Masked PA signal (red-orange) overlaid with the corresponding US volume 48 hours before PFHnD injection; **C)** Masked PA signal overlaid with US obtained 6 hours after PFHnD injection; **D)** Masked PA signal overlaid with US obtained 24 hours after PFHnD injection. Scale bars are approximately 5 mm.

The left lateral decubitus position of the mouse for the imaging volumes shown is displayed in **Figure 11A**, with the approximate region of interest boxed in dashed yellow lines. At baseline (**Figure 11B**), there is some nonspecific enhancement, but none adjacent to the TDLN. However, 6 hours after ipsilateral peritumoral injection of PFHnDs (**Figure 11C**), a large bolus of PA enhancement can be seen immediately adjacent to this lymph node. By 24 hours post-injection (**Figure 11D**), this bolus has cleared the region. Histology obtained after the 24-hour imaging timepoint (**Figure 12**) confirms that PFHnDs drained to the tumor-draining right inguinal (RI) lymph node and that they even reached the downstream right axillary (RA) lymph node. No enhancement from Cy5 included within the PFHnD construct was observed within the upstream right popliteal (RP) lymph node, which drains unidirectionally towards the RI lymph node.

The enhancement observed from Cy5-doped PFHnDs on histology of the RI and RA lymph nodes is focal and largely restricted to the exterior region of the nodes. Previous research has demonstrated that the vast majority of transport through lymph nodes occurs through the "peripheral pathway" through the subcapsular sinus and medulla, which sit on the periphery of the node.[125] Additionally, while the PFHnDs used in this study are small in their relationship to traditional US contrast agents, they are still relatively large in a biological sense. Therefore, it is unsurprising that only a small percentage of injected PFHnDs would be able to traverse the conduit network into the more central regions of the nodes. The number of retained functional PFHnDs in the RI TDLN may be below the detection threshold of our US/PA system, and more upstream locations in the lymphatic drainage pathway (i.e., near the RA) should be imaged at later timepoints in future studies.

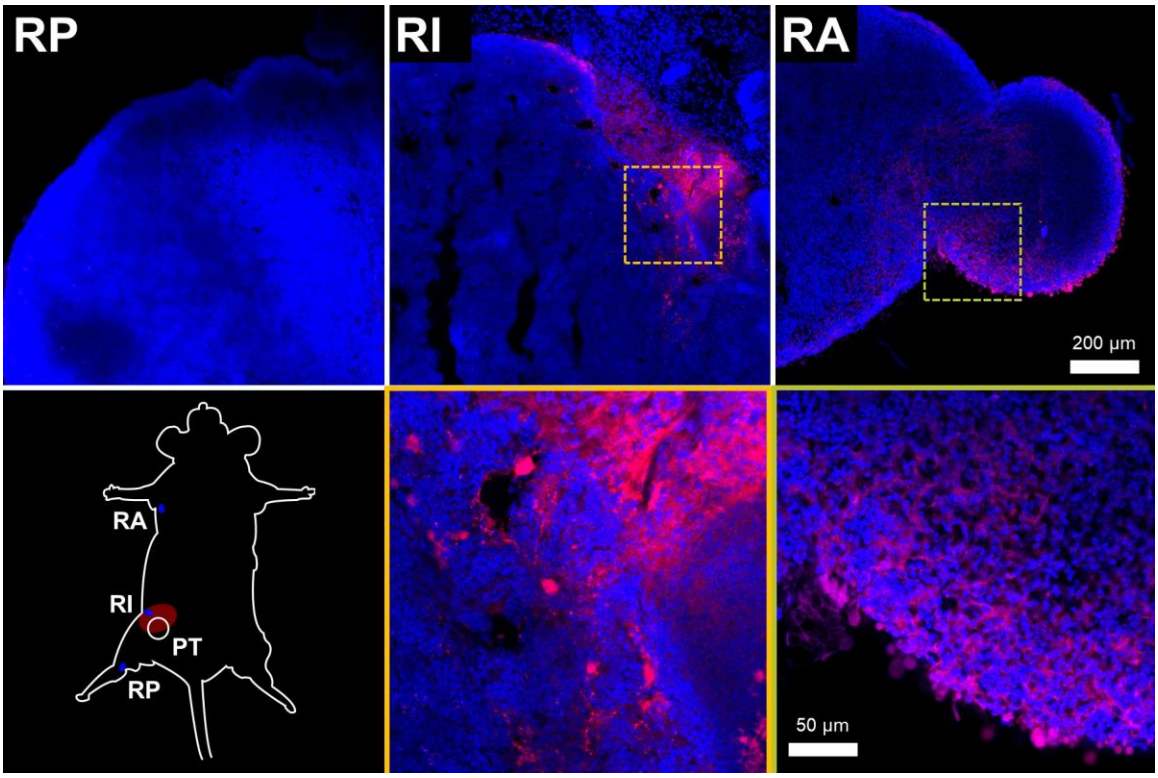

Figure 12: Representative fluorescent histology of draining PFCnDs in 4T1 syngeneic mice. Mice have a primary tumor (PT) in the right fourth mammary fat pad. Histology sections were obtained from the right popliteal (RP), right inguinal (RI), and right axillary (RA) lymph nodes post-perfusion at 24 hours post-injection. Sections are stained with DAPI (blue). PFCnDs (Cy5; red) can be seen on the periphery of the RI and RA lymph nodes, ipsilateral to the peritumoral injection site (red in lower left inset cartoon). All signal from the Cy5 channel is displayed on the same dynamic range. Yellow and green insets show magnified regions from the RI and RA lymph nodes, respectively. Scale bar for top row is 200 µm. Scale bar for bottom row insets is 50 µm.

Returning to the initial US/PA imaging volume, it is odd that there are still a few regions of focal enhancement after post-processing the data. In particular, the large region of enhancement at the cranial edge of the volume is suspicious, as it is deep to the skin surface and unlikely an artifact. Upon further investigation, it appears the large and focal enhancement in this region may be due to absorption from bowel contents. We subsequently performed volumetric US/PA imaging of resected large intestines from mice fed standard (**Figure 13A**) and non-fluorescent (**Figure 13B**) diets, and both showed

similar focal enhancement in regions containing fecal matter. Although absorption measurements of homogenized feces from mice on standard (**Figure 13C**) and non-fluorescent (**Figure 13D**) diets do not reveal high absorption at 1064 nm, the optical density of absorbers within the feces is likely high enough to create the photoacoustic effect on display within *in vivo* volumes containing the abdomen.

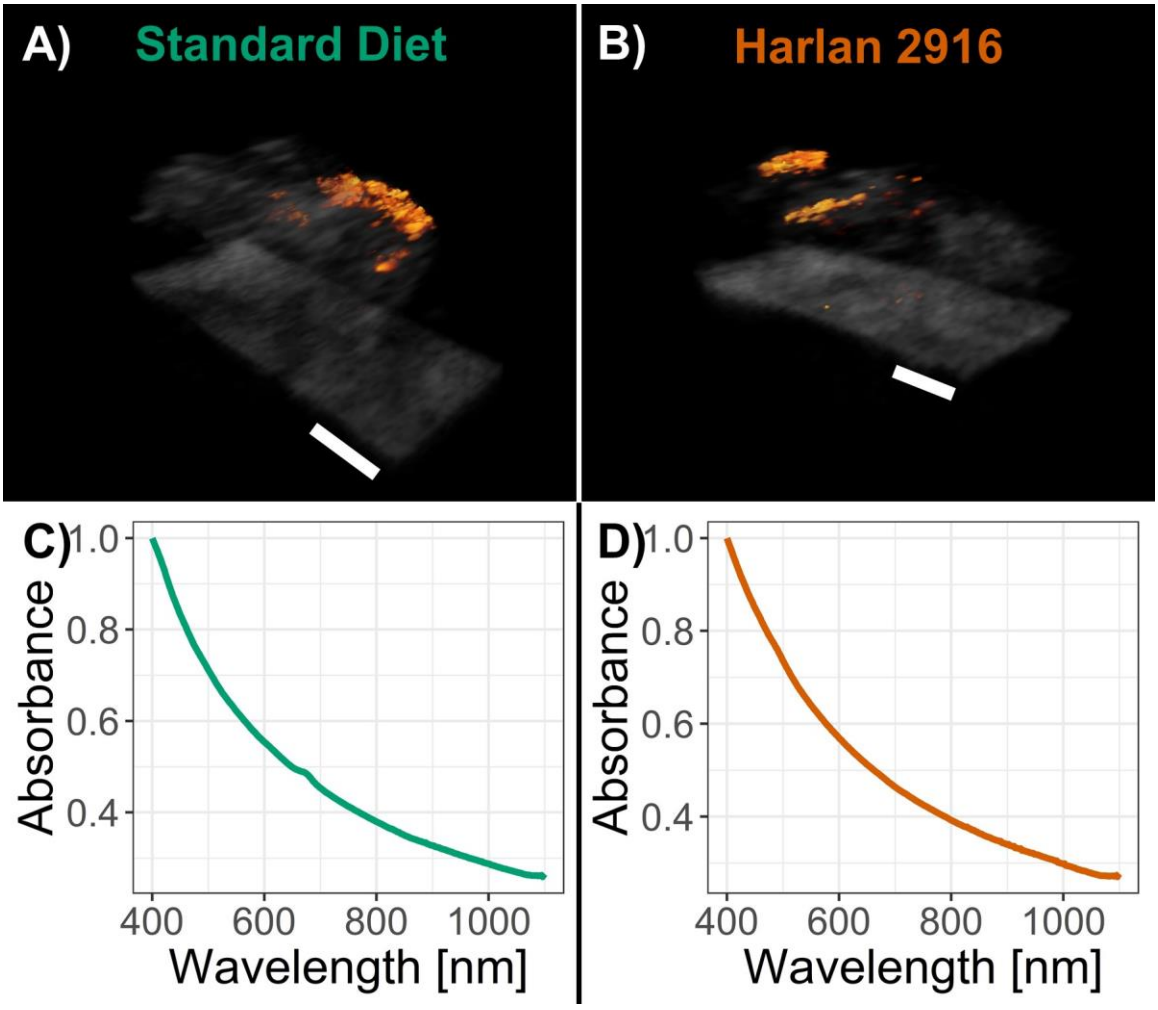

Figure 13: US/PA imaging of *ex vivo* murine intestines post-perfusion. *Ex vivo* large intestines show appreciable enhancement from post-processed PA images in mice fed both standard (**A**) and non-fluorescent (**B**) diets. Absorbance measurements were also obtained on homogenized murine fecal pellets from mice fed standard (**C**) and non-fluorescent (**D**) diets. Although the spectra are dominated by scattering, the high density of absorbers within the pellets may explain the confounding enhancement on US/PA imaging of the abdomen. Scale bars are approximately 5 mm.

Similar volumes from other 4T1 syngeneic mice that we imaged under this same protocol can be found in **APPENDIX B**. Supplemental Data for Imaging of Perfluorocarbon Nanodroplets Trafficking in Lymphatics. In addition to tumor-inoculated mice, we also imaged naïve BALB/c mice using the same protocol. A representative series of US/PA volumes from one of these naïve mice is shown in **Figure 14**. Again, at baseline (**Figure 14B**), there is some focal contrast enhancement in the abdomen, possibly due to feces in the large intestine. However, there is minimal enhancement surrounding the RI lymph node. Conversely, there is large focal enhancement near the draining RI lymph node (**Figure 14C**) 6 hours after PFHnDs are injected subcutaneously over the ipsilateral fourth mammary fat pad. By 24 hours post-injection (**Figure 14D**), most of this enhancement has dissipated, although some small regions of contrast remain caudal to the lymph node and upstream of it within the imaged volume. Due to the presence of minor artifacts throughout the longitudinally collected volumes, it is impossible to say with certainty whether these are also artifacts or whether they correspond to small foci of PFHnDs within regional lymphatics.

Similar to the 4T1 inoculated case, histology from naïve mice collected after the 24-hour timepoint (**Figure 15**) shows enhancement from the Cy5 fluorophore incorporated within PFHnDs retained within the ipsilateral RI and RA lymph nodes downstream of the injection site. No PFHnD-related fluorescence is noted in the upstream RP lymph node or in contralateral left popliteal or inguinal lymph nodes. US/PA volumes from other naïve mice imaged under this protocol, which qualitatively resemble the representative ones displayed here, can be found in **APPENDIX B**. Supplemental Data for Imaging of Perfluorocarbon Nanodroplets Trafficking in Lymphatics.

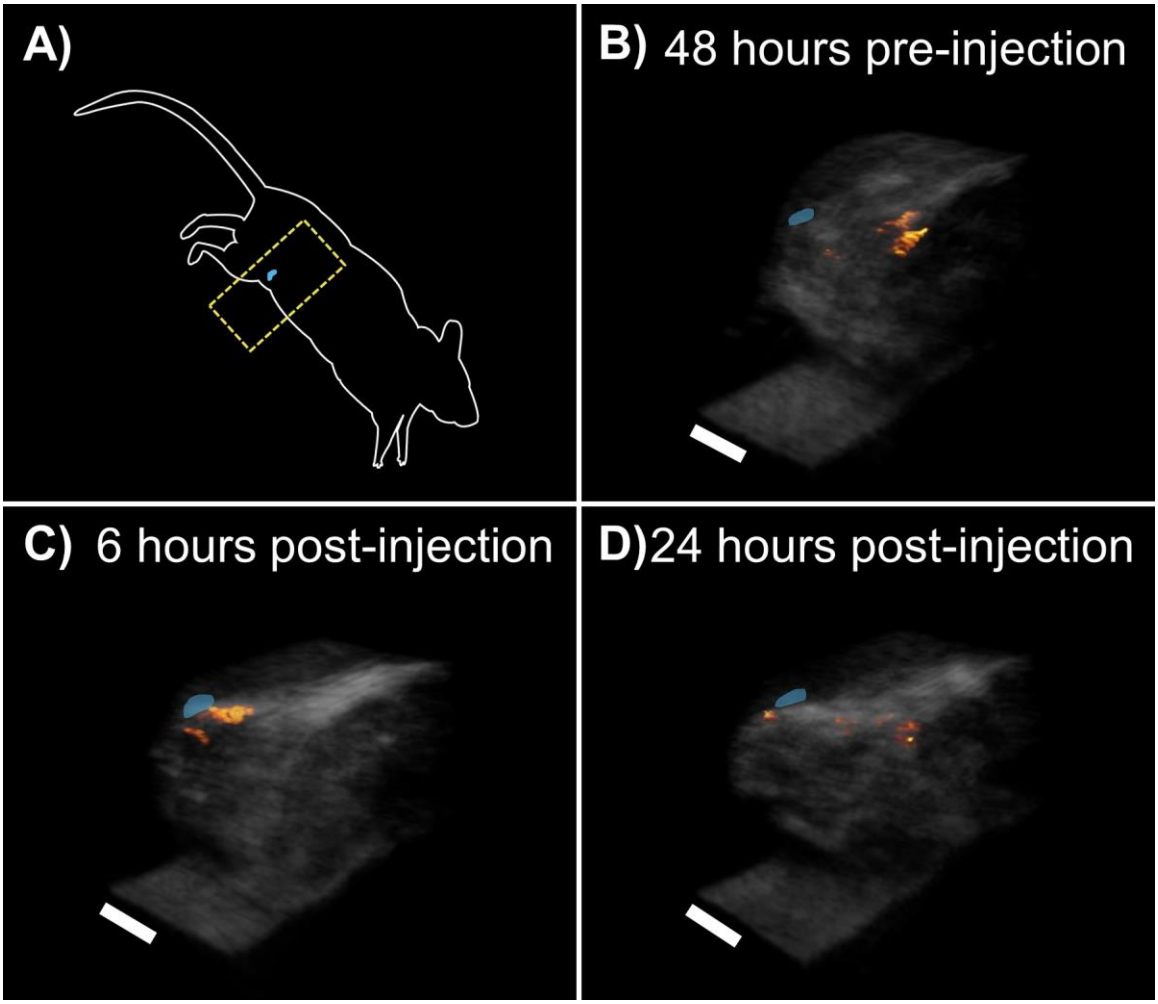

Figure 14: Processed US/PA volumes from a naïve BALB/c mouse. This mouse received a 100 µL subcutaneous injection of PFHnDs at 0 hours. **A)** Cartoon showing the left lateral decubitus position of the mouse for imaging. The yellow dashed lines approximate the volumes shown. Lymph nodes are false colored in light blue; **B)** Masked PA signal (red-orange) overlaid with the corresponding US volume 48 hours before PFHnD injection; **C)** Masked PA signal overlaid with US obtained 6 hours after PFHnD injection; **D)** Masked PA signal overlaid with US obtained 24 hours after PFHnD injection. Scale bars are approximately 5 mm.

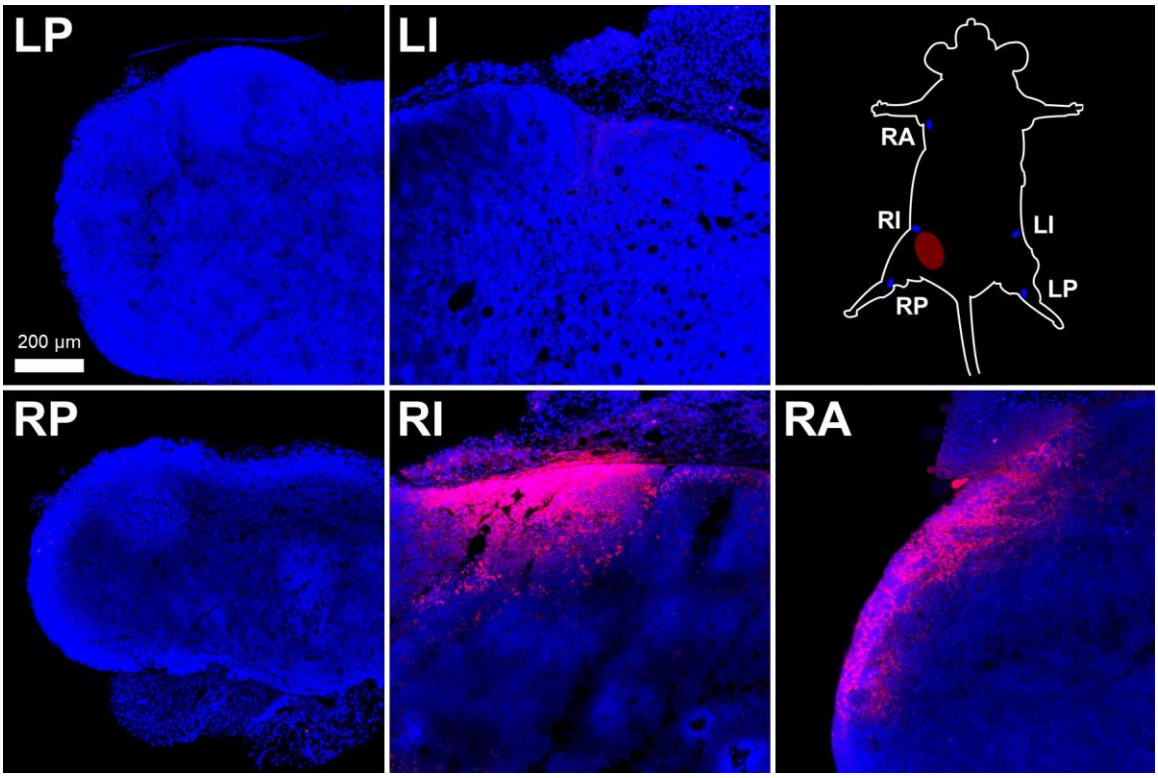

Figure 15: Representative fluorescent histology of draining PFCnDs in naïve BALB/c mice. Sections were taken from the left popliteal (LP), right popliteal (RP), left inguinal (LI), right inguinal (RI), and right axillary (RA) lymph nodes post-perfusion at 24 hours post-injection. Sections are stained with DAPI (blue). PFCnDs (Cy5; red) can be seen focally on the periphery of the RI and RA lymph nodes, ipsilateral to the injection site (red in upper right inset cartoon). All signal from the Cy5 channel is displayed on the same dynamic range. Scale bar is 200 µm.

Quantitative masked PA data from planes centered at the draining lymph nodes in all imaged mice are shown in **Figure 16**. The data were manually curated to exclude the third of each imaging plane containing the dorsal aspect of the mouse. This step represents an attempt to exclude surface artifacts and to focus on signal from PFHnDs draining through regional lymphatics near the RI lymph node. Masked PA signal in the remaining volumes centered around the RI lymph node (15 planes, 4.2 mm) was integrated, producing a single value of total PA signal at each timepoint for each mouse. This quantitative analysis shows an increase in the magnitude and variance of the total PA signal at 6 hours

compared to preliminary imaging, which then generally decreases back to baseline by 24 hours. However, a two-way ANOVA with repeated measures did not find significant differences in the masked PA signal as a function of time ($p=0.101$) or animal model ($p=0.319$), nor did it find a difference in the temporal behavior of PA signal as a function of animal model ($p=0.339$). The effect as a function of time is trending towards significance, and it is likely that a larger sample would be sensitive to changes, particularly at the 6-hour timepoint. A higher statistically powered sample size and more precise, artifact-free processing will be necessary to generate a better estimate of how PFHnD drainage varies by time and small animal model.

One might expect to observe differences between the trafficking of PFHnDs in naïve and tumor-draining lymphatics. In breast cancer, metastasis is partially mediated by the production of vascular endothelial growth factor C (VEGF-C), which induces lymphangiogenesis.[126] 4T1 cells have been previously shown to produce VEGF-C in this syngeneic model of breast cancer.[127] Still, the VEGF-C induced lymphangiogenesis in murine models of breast cancer has been observed within intratumoral lymphatics.[126] Our observations of bulk PFHnD transport may imply that this effect does not extend to extratumoral lymphatics. However, our imaging approach may also be insensitive to subtle changes in trafficking that would be better investigated at shorter timepoints and possibly with an intratumoral, not peritumoral, bolus. In any case, further refinement of our imaging technique and post-processing will be necessary to examine smaller and more sparse distributions of PFHnDs with sufficient confidence.

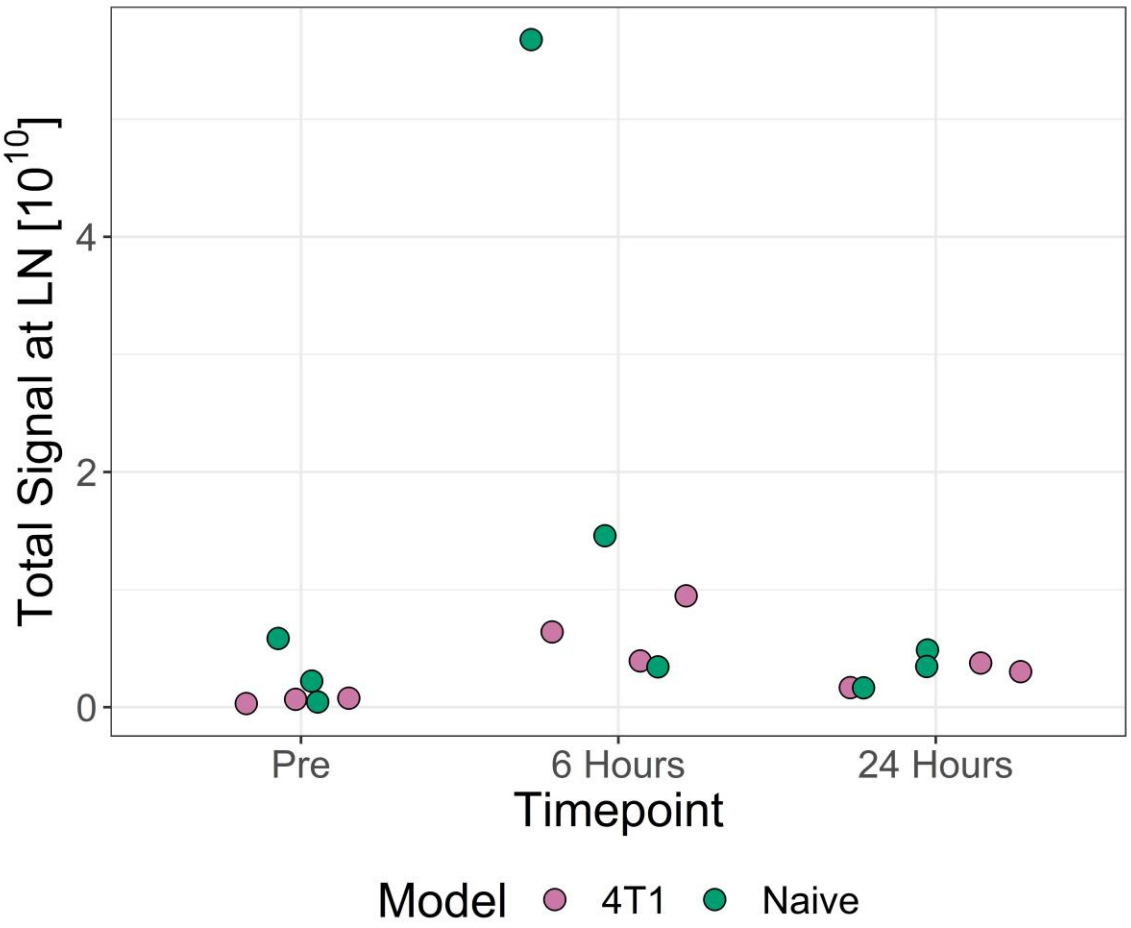

Figure 16: Curated total masked PA signal at the draining lymph node in imaged mice. Volumes centered around the draining lymph node were analyzed, and the dorsal third aspect of each plane was excluded. Data show an increase in signal in the region at 6 hours that generally dissipated by 24 hours. Two-way ANOVA with repeated measures did not find significant differences between animal models (p=0.319) or timepoints (p=0.101), but the timepoint data are trending towards significance.

Residual PA signal after post-processing represents a large confounding factor precluding more precise quantitative analysis of these results. As previously discussed, some of this confounding signal is due to endogenous strong absorbers, such as feces in the large intestines. Other residual signal is likely the result of the threshold-based post-processing technique failing to appropriately reject all other nonspecific signal. The

imaging sequences and processing techniques to best isolate the transient enhancement from optically triggered PFHnDs are still active areas of research.

In conclusion, we have generated evidence of the ability to track PFHnDs longitudinally *in vivo*. We developed an imaging sequence and post-processing techniques to leverage both the US and PA imaging data in order to highlight areas with increased probability of containing optically triggered PFHnDs. Using tumor-draining and naïve murine lymphatics as a test case, we imaged subcutaneously delivered PFHnDs over a period of 24 hours. Our US/PA imaging results show focal enhancement around the draining lymph node at 6 hours, with enhancement becoming weaker and more diffuse by 24 hours. Histological data obtained at 24 hours suggests that PFHnDs may have drained to even more distal lymphatics, and future imaging studies should include more cranial lymphatics to assess the complete extent of drainage. These studies lay the foundation for additional US/PA research in the lymphatics and for other biological applications that require longitudinal monitoring of transport and delivery.

4.2 Adjuvant-Containing Perfluorohexane Nanodroplets for Image-Guided Immunotherapy

4.2.1 Abstract

Immunotherapy has fundamentally changed the treatment approach to a variety of solid tumors. By harnessing the adaptive immune system to combat tumor growth, immunotherapeutics, such as checkpoint inhibitors, offer an avenue for treatment that has the potential for fewer off-target effects than traditional exogenous agents and approaches. Still, systemically administered immunotherapeutics can produce off-target effects in the

form of autoimmunity. To address this limitation, researchers have explored methods for the focal delivery of immunotherapeutics, including nanoparticle formulations. Imaging of these nanoparticles is critical to monitor their successful delivery to either primary tumors or tumor-draining lymph nodes. Many immunotherapeutic nanoparticles have not been developed with the ability for imaging with platforms that can scale from small to large animal imaging in translational studies. Ultrasound is one such scalable, non-ionizing imaging modality that has gained increasing utilization in point-of-care settings. However, gas microbubbles, the traditional contrast agents for use with ultrasound, have unfavourable transport characteristics in the extravascular space and are thus ill-suited for use as an immunotherapeutic vehicle. Perfluorocarbon nanodroplets are an emerging, phase-change contrast agent for ultrasound and photoacoustic imaging that have improved transport characteristics due to their submicrometer size prior to user activation for imaging. Here, we develop and present a class of perfluorocarbon nanodroplets for focal adjuvant delivery and demonstrate their ability to stimulate antigen presenting cells *in vitro*. These studies lay the foundation for the future advancement of ultrasound image-guided immunotherapy into the preclinical arena.

4.2.2 Introduction

The implementation of checkpoint inhibitors has revolutionized the treatment of solid tumors,[128-137] and the researchers who contributed seminal work to this approach were jointly awarded the Nobel Prize in Medicine in 2018.[138] Prior to the use of checkpoint inhibition as a therapeutic strategy, cancer patients relied solely upon exogenous methods for tumor destruction: surgical resection, radiotherapy, or cytotoxic chemotherapeutic and biologic agents. Checkpoint inhibitors disrupt a "molecular brake" imposed by certain solid

tumors on cytotoxic T lymphocytes (CTLs), allowing the body to mount an adaptive immune response to tumor antigens.[139] Checkpoint-based immunotherapeutic methods have shown clinical efficacy in patients with lung,[136] genitourinary,[129,131,132,137] and other cancers.[128,133-135]

Checkpoint inhibition and other immunomodulatory approaches in cancer seek to leverage the molecular specificity of the adaptive immune response to avoid the morbidities associated with exogenous cytotoxic and otherwise destructive methods. However, systemically administered immunotherapeutics still produce off-target effects (i.e., autoimmunity) by upregulating T cells outside the tumor microenvironment. One avenue for avoiding these side effects is to focally deliver the immunotherapeutic payload, either directly into the primary tumor or to tumor-draining lymph nodes (TDLNs).[140] By only upregulating tumor-resident T cells or T cells within a TLDN, this greatly increases the probability that CTLs train on tumor antigen instead of autoantigens.

Other groups have previously used an array of vehicles, from metallic nanoparticles to liposomes,[112,141-143] to focally deliver immunotherapeutics. Many of these approaches lack the ability to confirm delivery *in vivo* via concomitant imaging. Confirmation of appropriate local delivery without the need for *ex vivo* techniques, such as biopsy, will be highly desired for any downstream clinical scale-up of these approaches. Current formulations with the potential for image tracking, such as gold and iron oxide nanoparticles, are not without challenges. Gold nanoparticles, compatible with optical and photoacoustic (PA) imaging, have lingering concerns over their long-term biocompatibility and clearance that have stymied their implementation for any *in vivo* clinical application. Conversely, iron oxide nanoparticles are commonly paired with magnetic resonance

imaging (MRI), a paradigm that has clinically flourished with widespread use. However, MRI is a non-portable technique that is often not available in resource-limited and point-of-care settings, and its use incurs a large expense on both the patient and provider.

Ultrasound is a cost-effective, portable imaging paradigm with widespread implementation in both academic and community clinical settings. Contrast-enhanced ultrasound typically utilizes microbubbles, which are gas-cored, micrometer-sized constructs, that can be functionalized for molecular-specific diagnosis or therapeutic delivery.[25] Previous groups have adapted microbubbles to deliver genetic material as part of an ultrasound-guided therapeutic regime.[144,145] However, microbubbles have short (i.e., minutes-long) biostability and are thus ill-suited to imaging endocytosed vehicle and the ensuing cell-mediated transport of immunotherapeutic. Perfluorocarbon nanodroplets (PFCnDs) are an emerging class of phase-change contrast agents for use with ultrasound and photoacoustic imaging.[41,53,90,101] These PFCnDs utilize the same biocompatible shell components as microbubbles but replace the gas core with one of liquid fluoroalkane. In response to a pulse of either acoustic or optical energy, the fluoroalkane core vaporizes to effectively create a microbubble *in situ*. Our group has previously demonstrated that PFCnDs are biologically stable for at least 72 hours when trafficking within antigen presenting cells (APCs) and that they can be imaged within TDLNs at this timepoint.[146]

Here, we present a new class of immunotherapeutic PFCnDs: poly(I:C) perfluorocarbon nanodroplets (pICnDs). These pICnDs are coated with polyinosinic:polycytidylic acid (commonly abbreviated poly(I:C)), a molecule that is structurally similar to double-stranded RNA. When endocytosed by APCs, poly(I:C) stimulates intracellular TLR3 receptors within endosomes.[147] Within certain APCs, such

as dendritic cells (DCs) and macrophages (Mφs), TLR3 agonism leads to signalling cascades that mobilize adaptive immune cells, enact a T_H1 response, and ultimately result in cell-mediated immunity.[148] The CTL response associated with cell-mediated immunity has been shown to have robust anti-tumor activity.[149,150] The T_H1 response leads to upregulation of APC endocytosis, which can prime TDLN APCs to ingest locally metastatic tumor cells and present their antigens to T cells. This can train T cells to attack cancer cells, indirectly eliciting a CTL response. In addition, T_H1 cells can directly induce a CTL response through the production of cytokines, such as IL-2.[151] Furthermore, T_H1 cells may also directly kill cancer cells through the production of cytokines that initiate cell death.[149] Depending on the PD-L1 status of the tumor, poly(I:C) can serve as either a standalone immunotherapeutic or as a complement to checkpoint inhibition.

The overarching goals of these studies are to characterize these pICnDs, their imaging response, and their ability to elicit an immune response from APCs. To this end, we utilized RAW 264.7 Mφs as a model organism for evaluating the APC response. RAW 264.7 Mφs are an established *in vitro* platform for probing Mφ cell signaling. Moreover, due to the variety of syngeneic models available on a BALB/c background, these BALB/c-originating Mφs are a logical starting point for downstream preclinical scale-up of this image-guided therapeutic platform. The studies that follow demonstrate the ability of pICnDs to stimulate APCs, which could ultimately initiate widespread anti-tumor activity if pICnDs are focally delivered to either primary tumors or TDLNs.

4.2.3 Materials and Methods

Poly(I:C) Perfluorocarbon Nanodroplet Synthesis

One micromole (10^{-6} mol) of DSPC, 18:1 TAP (DOTAP), and 18:1 (Δ9-Cis) PE (DOPE) (all from Avanti Polar Lipids, Inc.) in a 2:9:9 molar ratio was extracted from chloroform aliquots and added to a 10 mL pear-shaped flask (Aldrich). To this isolate, 0.5 mg of near-infrared-absorbing dye (IR-1048; Sigma-Aldrich) from a 5 mg/mL chloroform aliquot were added. An additional 325 µL of HPLC-grade chloroform were added to the flask to ensure the formation of an even lipid cake. The pear-shaped flask was placed into a rotary evaporator with a water bath (R-215, V700, and V-855 with B-491; Buchi) and water-cooled condenser and evaporated for 30 minutes, adhering to the "20/40/60" rule. After this, the solid isolate was further dried under nitrogen flow for a minimum of 20 minutes in order to evaporate all residual chloroform in the lipid cake.

Next, the solid reagents were hydrated with 1 mL of 7.40 pH PBS and homogenized using a water bath sonicator (1800 Series Ultrasonic Cleaner; Branson) for 5 minutes at room temperature to produce a solution of dye-loaded nanomicelles. This solution was centrifuged at 300 rcf for 1 minute in order to pellet excess near-infrared dye. Then, 900 µL of the nanomicelle-containing supernatant was combined with 100 µL of PBS and 50 µL of perfluorohexane (FluoroMed, L.P.) in a 2-dram glass scintillation vial (VWR). The glass vial was placed into an ice bath and allowed to rest for 5 minutes. Then, the solution was probe sonicated in the ice bath with a 1/8" microtip (QSonica) at 1% power (1s on, 15s off, 5 times) in order to produce a stock solution of PFCnDs, which was stored at 4°C in amber glass prior to use.

Lyophilized polyinosinic-polycytidylic acid (poly(I:C)) (Sigma-Aldrich) was dissolved in sterile 7.40 pH PBS without calcium or magnesium (VWR) at a concentration of 10 mg/mL and frozen at -20°C in 100 µL aliquots. Before adjuvant loading, poly(I:C)

from aliquot was reannealed to ensure appropriate reconstitution. To achieve this, frozen aliquots were taken from -20°C and placed into a 60°C water bath for 20 minutes to thaw the solution and denature poly(I:C) strands. Then, the aliquots were removed from the bath and left to rest at room temperature for 20 minutes to allow for poly(I:C) strands to reanneal.

To coat PFCnDs with adjuvant, the stock solution was first reconstituted by vortex pulsing the solution 10 times and then by water bath sonicating the stock for 1 minute at room temperature. From this reconstituted solution, 100 µL of PFCnDs were diluted in 2 mL of PBS and bath sonicated for 2 minutes. This solution was then centrifugated at 3000 rcf for 5 minutes in a low-adhesion microcentrifuge tube (2 mL; USA Scientific) in order to pellet the PFCnDs. The supernatant was removed and the PFCnDs were reconstituted in 1 mL of 3.00 pH PBS in order to protonate DOPE groups on the shell. Of this positively charged PFCnD solution, 200 µL were added to a sterile low adhesion microcentrifuge tube with either 100 µL of 10 mg/mL poly(I:C) or 100 µL of sterile 7.40 pH PBS without calcium or magnesium (negative control). The tubes containing the PFCnDs were then placed into an ice bath on a shaker plate for thirty minutes to allow for anion exchange on the positively charged phospholipid surface of the PFCnD shell.

After the thirty minutes, an additional 700 µL of sterile 7.40 pH PBS was added to each microcentrifuge tube, and the tubes were again spun down at 3000 rcf for 5 minutes to pellet the PFCnDs. The supernatant was removed and the PFCnDs were reconstituted in 1 mL of phenol-free DMEM plus 4.5 g/L glucose, L-glutamine, and HEPES (Gibco, Thermo Fisher Scientific) supplemented with 10% FBS (Corning) and 1% penicillin-streptomycin (Sigma-Aldrich).

Zeta Potential Measurements

Nanodroplets were prepared as described in the synthesis section above. After the thirty-minute incubation step, 700 µL of 7.40 pH PBS were added to each sample to bring the total volume to 1.0 mL. Measurements of zeta potential were obtained by a standard DLS instrument (Zetasizer Nano ZS; Malvern Instruments Ltd.) using a folded capillary zeta cell (DTS1070; Malvern Instruments Ltd.). Samples were diluted 1:100 in 7.40 pH PBS prior to being loaded into the capillary cell. Each reported measurement is the average of ten successive zeta potential measurements, and three measurements were obtained for each sample.

RAW 264.7 Cell Line

RAW 264.7 BALB/c macrophages (ATCC), passage 7-8, were cultured in DMEM plus 4.5 g/L glucose, L-glutamine, and sodium pyruvate (Corning) supplemented with 10% FBS (Corning) and 1% penicillin-streptomycin (Sigma-Aldrich). Cells were maintained within T-75 flasks (CELLSTAR; Greiner Bio One, VWR) at 37°C in a humidified incubator with 5% CO_2.

To passage cells, the media was aspirated and replaced with 5 mL of fresh, 37°C - warmed media. A sterile cell scraper with 25-cm handle (bioWORLD) was used to physically dislodge adherent cells from the bottom of the flask using serial, downward, squeegee-like strokes. After rinsing the scraper in the cell-rich media, an additional 5 mL of warmed media was added to the flask. Using a motorized pipette, the 10 mL of cell-rich media was first used to wash the base of the flask five times to dislodge any remaining adherent cells and then used to pipette the solution up-and-down vigorously five times in

order to form a single cell suspension. Finally, 50 to 1000 µL of this solution was used to seed the new flask pre-filled with fresh warmed media to ultimately reach a total final volume of 20 mL.

RAW 264.7 cells resuspended from frozen aliquot were passed a minimum of one time in flask prior to being used to seed 96-well plates for *in vitro* experiments.

Poly(I:C) Perfluorocarbon Nanodroplet Griess Assay

Starting with RAW 264.7 cells in a T-75 flask, the media was aspirated and replaced by 5 mL of sterile PBS without calcium or magnesium (VWR). The PBS was swirled around the bottom of the flask a minimum of 15 times in order to wash any residual phenol-containing media from the cells. This PBS was aspirated and replaced with 5 mL of pre-warmed phenol-free DMEM plus 4.5 g/L glucose, L-glutamine, and HEPES (Gibco, Thermo Fisher Scientific) supplemented with 10% FBS (Corning) and 1% penicillin-streptomycin (Sigma-Aldrich). Cells were manually scraped and formed into a single-cell suspension, as detailed above, utilizing this phenol-free media. Next, the cells were pelleted at 400 rcf for 5 minutes and resuspended in phenol-free DMEM at a final concentration of 5×10^5 cells per mL.

From this cell suspension, 100 µL (5×10^4 cells) were added to wells of a sterile 96 well TC-treated black microplate (Cellstar, product number 655090; Greiner Bio-One), which was placed into an incubator for 24 hours. After the 24-hour period, 100 µL of particle-containing media were added to each well of RAW 264.7 cells. The four particle incubation conditions were as follows: pICnDs, blank pICnDs (no adjuvant), free poly(I:C), and phenol-free DMEM. Nanodroplets were prepared for incubation as detailed

previously. The free adjuvant solution was prepared by adding 100 µL of reannealed 10 mg/mL poly(I:C) to 900 µL of phenol-free media, which results in a 500 µg/mL concentration of poly(I:C) per well. After bringing all well volumes to 200 µL, the 96-well plate was returned to the incubator for 12 hours.

After the first 12 hours of particle incubation, the 96-well plate was removed from the incubator, and half of the wells were lased using a custom well-plate lasing system.[152,153] This system integrates a 10 Hz nanosecond pulsed Nd:YAG laser (Vibrant; Opotek, Inc.) with a three-axis motorized stage (three 100mm Precision Ball Screw Positioner Table/Linear Actuator Stage 404XR; Parker Hannifin Corporation) and power meter (Nova II; Ophir Photonics) in order to lase individual wells of the 96-well plate in a controlled manner. The system is driven by LabVIEW 2016 software (National Instruments) that can control the number and intensity of laser pulses per well, modulating the energy via an external Q-switch delay triggered to the laser via a coupled function generator (AFG3022C; Tektronix, Inc.). The well-plate lasing system was used to lase half of the wells with 10 pulses of 1064-nm laser light at 10 Hz. Each laser pulse was 20±1 mJ with a beam profile approximately matched to the cross-section of the well, yielding an optical fluence of roughly 62.5 mJ/cm^2. The lid of the 96-well plate was removed during the lasing procedure. The plate spent no more than 10 minutes outside of the incubator for the duration of this lasing step, and it was returned to the incubator immediately at the conclusion of lasing.

Another 12 hours after the lasing step, the 96-well plate was again removed from the incubator. At this time, 100 uL of supernatant was removed from each well and placed into the corresponding well of a non-sterile 96 well TC-treated black microplate. A

volume-matched ladder of sodium nitrite (50 µM by twos to 0.78 µM and then 0 µM) in phenol-free DMEM was created in triplicate in the first three columns of this non-sterile well plate. A 40 mg/mL solution of modified Griess reagent (product number G4410; Sigma-Aldrich) was created in deionized water, and 100 µL of this solution was added to each sample well in the new 96-well plate. The preceding transfer and incubation steps were performed in darkness as to minimize light exposure to the colorimetric Griess reagent.

After allowing the Griess reagent to incubate with the samples for 10 minutes in darkness, the well-plate was placed into a microplate reader (Synergy HT; BioTek Instruments) for quantitative absorbance measurements. Using the standard plate reader software (Gen5; BioTek Instruments), an absorbance spectrum from 500 to 650 nm in 2-nm steps was acquired for each sample well. These spectra were exported to an Excel spreadsheet and processed in MATLAB (MathWorks). For each well, the absorbance at baseline (650 nm) was subtracted from the absorbance at the peak of the modified Griess reagent (546 nm). These adjusted absorbance values were arranged in a matrix and exported in a plain Excel spreadsheet. Processed data were ultimately plotted in R (R Core Team) using the ggplot2 data visualization package. A linear regression of the ladder data was used to convert absorbance data to moles of nitrite detected.

Statistical Analysis

Statistical analyses were performed in R (R Core Team). A two-way ANOVA was performed on the data to assess the factors of particle incubation and lasing on nitrite production, as assessed by adjusted absorbance. For factors with a significant impact on

the adjusted absorbance, a *post hoc* Tukey's test was performed to assess all pairwise differences in the adjusted absorbance means for groups within the factor.

4.2.4 Results and Discussion

The conserved TLR3 domain recognizes double-stranded RNA because this antigen is typically of viral origin in a biological setting. When internalized by Mφs or DCs, pI:C leads to a T_H1 response via TLR3 agonism.[147] This is because pI:C is structurally similar to double-stranded RNA and can thus serve as a double-stranded RNA mimic. Because of this structural similarity, particle design modifications developed for the delivery of genetic material should also prove efficacious for delivering pI:C. Liposomes and other gas-filled, ultrasound responsive agents have previously been used for gene delivery.[154-156] In these formulations, cationic lipids were utilized within the shell to load genetic material onto the particle surface via electrostatic interaction between the cationic particle exterior and the highly anionic phosphate backbone of DNA or RNA.

In the poly(I:C) perfluorocarbon nanodroplets (pICnDs) presented here, we based our formulation on that of cationic liposomes. We elected to use DOTAP (1,2-dioleoyl-3-trimethylammonium-propane) as our cationic lipid and DOPE (1,2-dioleoyl-sn-glycero-3-phosphoethanolamine) as a "helper" lipid.[157] Under acidic conditions, the head group of DOPE is also protonated, and both DOPE and DOTAP can participate in electrostatic interactions with phosphate groups in poly(I:C) during adjuvant incubation. To test whether this formation allowed for adherence of poly(I:C) to the nanodroplet surface, we performed zeta potential measurements of particles resuspended in 7.40 pH PBS following incubation with either poly(I:C) adjuvant or a volume equivalent of 7.40 pH PBS under

acidic conditions. Zeta potential is proportional to the surface charge of particles in solution.[158] After incubation and resuspension, the zeta potential of pICnDs was -11.16 mV as compared to the -4.54 mV measured from "blank" nDs incubated without adjuvant (**Table 2**). The more negative zeta potential of pICnDs indicates that poly(I:C) is appropriately adhering to the particles' surface, as its phosphate backbone makes poly(I:C) molecules anionic.

Table 2: Zeta Measurements for Loaded and Unloaded pICnDs

Sample	Zeta Potential [mV] (μ±σ)	Zeta Deviation [mV] (μ±σ)	Mobility [μmcm/Vs] (μ±σ)	Conductivity [mS/cm] (μ±σ)
Blank nDs	-4.54±0.47	0.00±0.00	-0.3577±0.0373	15.0±0.4
pICnDs	-11.16±1.72	0.00±0.00	-0.8788±0.1357	14.8±0.3

After obtaining preliminary evidence of adjuvant adherence to the nanodroplet surface in our pICnD formulation, we proceeded to conduct a functional *in vitro* assay of our immunotherapeutic particles. We elected to use BALB/c-derived RAW 264.7 Mφs as a model APC line. This cell line was utilized to demonstrate canonical TLR3 agonism by poly(I:C).[147] Additionally, there are a variety of syngeneic models of cancer that utilize a BALB/c background, which would increase the import of these *in vitro* results for downstream *in vivo* immunotherapeutic studies. Cells were seeded in a 96-well plate and incubated for 24 hours to give them sufficient time to recover from the stress of passaging and re-enter a log growth phase. Following this seeding period, wells were incubated with either pICnDs, PBS-incubated "blank" nDs, free poly(I:C) (positive control), or media (negative control).

Twelve hours after particle incubation with RAW 264.7 Mφs, cells were irradiated with pulse near-infrared laser light at 1064 nm using a custom well-plate lasing system.

The wait step prior to laser irradiation gives sufficient time for free particles to be endocytosed by Mφs within the wells. For lased wells, the lasing sequence was designed to mimic the effect of an acute US/PA imaging session. Here, the concern is not thermal deposition from the laser but mechanical effects from the repeated vaporization and recondensation of intracellular PFHnDs. During vaporization, PFHnDs expand between 3-5 times in diameter,[119,159] which corresponds to a two or three order-of-magnitude volumetric expansion. It is possible that repeated vaporization and recondensation of PFCnDs may impact either positively impact Mφ response to adjuvant by mechanically releasing adjuvant from the pICnD surface or negatively impact Mφ response to adjuvant by damaging its internal organelles.

Another twelve hours after true or sham laser irradiation, supernatant from the wells was isolated for a Griess assay. This is an established assay that utilizes a colorimetric reagent that detects the presence of nitrite ions in solution.[160-162] Nitrite is a stable breakdown product of nitric oxide,[163] and it can be used as a surrogate for nitric oxide production.[164] Macrophages produce nitric oxide in response to TLR agonism,[165] and nitric oxide from activated Mφs produces a variety of downstream effects, from antimicrobial activity to adaptive immune modulation.[166,167] The results of the Griess assay for our *in vitro* studies of RAW 264.7 Mφs are shown in **Figure 17** below.

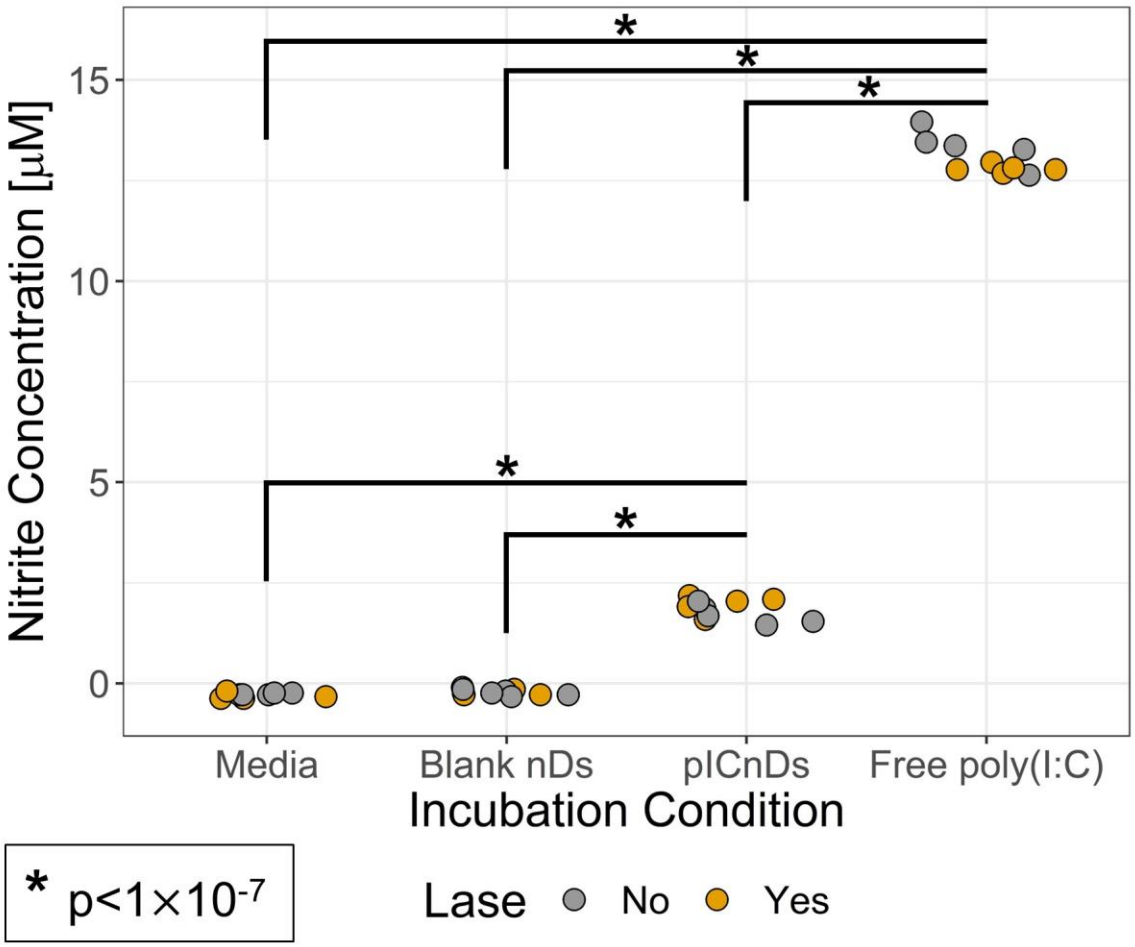

Figure 17: *In vitro* Griess assay of RAW 264.7 macrophages. Nitrite is a stable breakdown product of nitric oxide, which is produced by macrophages after adjuvant stimulation. The production nitrite in wells incubated with media or naïve PFCnDs is marginal, whereas nitrite production is elevated in wells incubated with pICnDs and free pI:C: adjuvant. Two-way ANOVA was performed with *post hoc* Tukey's test between incubation conditions. * $p<1\times10^{-7}$.

A two-way ANOVA revealed significant differences between incubation conditions but not between lasing conditions. In terms of the particle incubations, wells incubated with media or unloaded "blank" nDs produced minimal nitrite, with responses below the working range of the modified Griess reagent. Wells incubated with pICnDs displayed a significantly increased nitrite production compared to these negative controls. However, the average nitrite production from pICnD-incubated wells, 1.8 μM, was nearly an order-of-magnitude lower than that observed from free adjuvant incubation, 13.1 μM. It is worth noting that the selected free adjuvant incubation, 500 μg/mL, is well in excess of what is reported in the literature for positive controls.[160,168] Thus, the levels of nitrite observed likely represent the maximal potential response of RAW 264.7 Mφs to poly(I:C) stimulation. Still, more work is necessary to optimize the loading and delivery of adjuvant to APCs via pICnDs.

Ongoing studies will seek to improve the loading efficiency of poly(I:C) to cationic nDs in order to improve Mφ activation. We will explore increasing the molar percentage of cationic lipids within the shell, altering the pH of adjuvant incubation, and using a different subset of helper lipids. Of note, the helper lipid DOPE has been used in gene delivery to facilitate endosomal escape by destabilizing the endosomal membrane.[157,169,170] Although this phenomenon is beneficial for traditional gene delivery, poly(I:C) produces its effects at TLR3, which is located within the endosome. Endosomal escape may account for some of the attenuated nitrite production observed in pICnD wells in our *in vitro* study, but further work is necessary to characterize this effect. The PEGylated lipid within the preliminary pICnD formulation already affords some steric stabilization to the nDs.[76] As

such, it is possible that future iterations of pICnDs can replace DOPE with additional cationic lipid without destabilizing the construct.

In conclusion, we have developed a new class of PFCnDs capable of focally delivering adjuvant. These particles have the potential to facilitate US/PA image-guided immunotherapy. Our preliminary studies support the ability to adhere poly(I:C) to the cationic shell surface of PFCnDs, and *in vitro* studies show that these particles are capable of eliciting an immune response from APCs. We have shown that this response is unaffected by the mechanical effects induced by the repeated laser-activated vaporization and recondensation of PFCnDs, which is necessary for contrast-enhanced US/PA imaging of these contrast agents. Future studies will optimize the ability of these particles to retain and deliver adjuvant, increasing the probability of eliciting and effective immune response *in vivo*. The *in vivo* implementation of adjuvant-delivering particles will require additional optimization, as it is dependent upon the complex interplay between innate and adaptive immune cells that *in vitro* methods, such as co-culture, do not always faithfully recapitulate. Nonetheless, the proof-of-concept studies presented here lay the groundwork for a timely and bold new direction in therapeutic contrast-enhanced US research.

CHAPTER 5. ASSESSING PERFLUOROCARBON NANODROPLET EXTRAVASATION WITHIN PRIMARY BREAST TUMORS

5.1 Antibody-Functionalized Perfluorohexane Nanodroplets for Molecularly Specific Ultrasound Imaging in Cancer

5.1.1 Abstract

The molecular makeup of solid tumors plays an integral role in their diagnosis, prognosis, and therapy. Standard-of-care methods for sampling tissue for histological analysis of molecular markers, such as biopsy, may be contraindicated based on anatomical location or patient comorbidities and can be subject to sampling error. Molecular imaging techniques provide one avenue for real-time, non-invasive analysis of entire lesions as either an adjunct to or replacement for these techniques. Ultrasound is one such non-invasive, non-ionizing imaging modality that can provide molecular information through the use of functionalized contrast agents. However, gas microbubbles, which are the standard contrast agents used clinically with ultrasound, are too large to extravasate through fenestrations in leaky tumor vasculature to bind cancer markers when delivered systemically. Perfluorocarbon nanodroplets (PFCnDs) are a phase-change class of ultrasound contrast agents that are submicrometer sized prior to on-demand user activation into microbubbles *in situ*. These PFCnDs are small enough to extravasate after intravascular delivery, and these agents can be functionalized to afford molecular specificity. In this proof-of-principle study, we demonstrate one such functionalization

strategy: the conjugation of monoclonal antibodies to the PFCnD surface via thiol chemistry. After synthesizing targeted PFCnDs through this methodology, we then apply these PFCnDs to an assay of cancer cells *in vitro*. We demonstrate that PFCnDs targeted to breast cancer markers preferentially adhere to the surface of cancer cells that express this marker and that it is the molecularly specific binding of the antibodies that is responsible for this interaction. This study builds the foundation for the use of targeted PFCnDs in whole-organism studies of solid tumors.

5.1.2 Introduction

Diagnosis of solid tumors, such as breast cancer, typically involves histological analysis of samples obtained via biopsy. After sectioning the sample, a pathologist can assess the tissue morphology and molecular makeup in order to diagnose and sub-type the potential tumor. Different tumor subtypes dictate different courses of treatment for the patient. In breast cancer, for example, tumor subtypes are delineated by the relative expression of three cellular receptors: estrogen receptor (ER), progesterone receptor (PR), and human epidermal growth factor receptor 2 (HER2). Each of these receptors has a corresponding treatment that will affect cells overexpressing them; for example, tamoxifen, a selective estrogen receptor modulator, is often prescribed to ER-positive patients.

Molecular markers play a role throughout the clinical work-up: from diagnosis to therapy. However, the biopsy process used to sample tissue for molecular analysis is not without drawbacks. Biopsy is prone to sampling error and has the potential for morbidity due to the presence of nearby arteries, lymphatic vessels, and nerves in common locations for solid tumors. Therefore, non-invasive methods of assessing the molecular composition

of tumors are of high clinical interest. Imaging techniques, such as ultrasound, have the potential to be used to assist or potentially even supplant biopsy. However, an exogenous contrast agent with molecular specificity is necessary to facilitate molecular-specific imaging.

Molecular targeting provides a means by which contrast agents, such as PFCnDs, can attain disease-state specificity. Several groups have reported surface coating of liposomes and perfluorocarbon-based particles with targeting ligands.[171-174] In this study, we seek to demonstrate disease-state specificity by conjugating PFCnDs to monoclonal antibodies (mAbs). Our *in vitro* assay demonstrates that conjugation to mAbs for extracellular cellular moieties causes PFCnDs to focally adhere to cancer cells and that this interaction is molecularly specific.

5.1.3 Materials and Methods

Targeted Perfluorocarbon Nanodroplet Synthesis

Prior to synthesis of the nanodroplet stock solution, monoclonal antibodies to either HER2 (ab16901 lot # GR3215414-5; abcam) or Gamma-sarcoglycan (H-60 lot # SC515128; Santa Cruz Biotechnology) were modified with Traut's reagent (2-iminothiolane hydrochloride; Sigma-Aldrich) to create sulfhydryl groups from primary amine groups on the antibodies. Maleimide groups on the surface of the nanodroplets from stock can then react with these sulfhydryl groups to tether monoclonal antibodies to the nanodroplet surface. One microliter of a 1:20 PBS dilution of 2 mg/mL Traut's reagent in PBS was added to each of three antibody aliquots (10 µL; 1 mg/mL) after thawing them at

room temperature. These aliquots were allowed to incubate for one hour at room temperature, during which time the stock solution of nanodroplets was synthesized.

One micromole (10^{-6} mol) of DSPC, DSPE-PEG2000 Maleimide, and DSPE-mPEG2000 (all from Avanti Polar Lipids, Inc) in a 1:2:7 molar ratio was extracted from chloroform aliquots and added to a 10 mL pear-shaped flask (Aldrich). To this isolate, 330 µg of DiI (Invitrogen) from a 3 mg/mL chloroform aliquot were added. The pear-shaped flask was covered in aluminum foil and placed into a rotary evaporator with a water bath (R-215, V700, and V-855 with B-491; Buchi) and water-cooled condenser and evaporated for 30 minutes, adhering to the "20/40/60" rule. After this, the solid isolate was further dried under nitrogen flow for a minimum of 20 minutes in order to evaporate all residual chloroform in the lipid cake.

Next, the solid reagents were hydrated with 1 mL of 7.40 pH PBS and homogenized using a water bath sonicator (1800 Series Ultrasonic Cleaner; Branson) for 5 minutes at room temperature to produce a solution of dye-loaded nanomicelles. This solution was centrifuged at 300 rcf for 1 minute in order to pellet excess DiI. Then, 900 µL of the nanomicelle-containing supernatant was combined with 100 µL of PBS and 50 µL of perfluorohexane (FluoroMed, L.P.) in a 2-dram glass scintillation vial (VWR). The glass vial was placed into an ice bath and allowed to rest for 5 minutes. Then, the solution was probe sonicated in the ice bath with a 1/8" microtip (QSonica) at 1% power (1s on, 15s off, 5 times) in order to produce the stock solution of PFCnDs, which was stored at 4°C in amber glass prior to incubation with antibodies.

After the one-hour Traut's reagent incubation, 1 µL of a 1:10 PBS dilution of a quenching solution of 1 mg/mL glycine (Invitrogen UltraPure; Thermo Fisher Scientific) in PBS was added to each of the three antibody aliquots. The quenched antibody solutions were allowed to rest for 5-10 minutes prior to incubation with nanodroplets.

Prior to antibody incubation, 100 µL of the PFCnD stock solution was diluted in 1 mL of PBS and bath sonicated for 2 minutes. All three quenched antibody aliquots (12 µL each; 36 µL total) were added to this diluted nanodroplet stock and left to incubate in the dark within an ice bath on a shaker plate for two hours, replacing ice in the water bath at the one-hour mark. After the two-hour incubation, 1 µL of 1-butanethiol (Acros Organics; Thermo Fisher Scientific) was added to the solution to quench all unreacted maleimide groups. This quenched solution was allowed to rest for 5-10 minutes prior to resuspension.

After quenching, the targeted PFCnD solution was centrifugated at 3000 rcf for 5 minutes in order to pellet the PFCnDs. The supernatant was removed and the PFCnDs were reconstituted in 1 mL of sterile PBS. This solution was then diluted 1:10 in pre-warmed DMEM media, described below, for incubation with cells.

SK-BR-3 Cell Line

SK-BR-3 HER2+ breast adenocarcinoma cells (ATCC), passage 5-10, were cultured in DMEM plus 4.5 g/L glucose, L-glutamine, and sodium pyruvate (Corning) supplemented with 10% FBS (Corning) and 1% penicillin-streptomycin (Sigma-Aldrich). Cells were maintained within T-75 flasks (CELLSTAR; Greiner Bio One, VWR) at 37°C in a humidified incubator with 5% CO_2.

To passage cells, all media was aspirated from the T-75 flask and replaced by 5 mL of sterile PBS without calcium or magnesium (VWR). The PBS was swirled around the bottom of the flask a minimum of 15 times in order to wash any residual media from the cells. The PBS was then aspirated and replaced by 2 mL of 0.25% Trypsin/2.21 mM EDTA in HBSS without sodium bicarbonate, calcium, or magnesium (Corning), enough volume to cover the entire bottom of the T-75. The flask was placed back into the incubator for 3 minutes and then removed. After gently agitating the flask and visually inspecting for signs of cell detachment, 8 mL of pre-warmed DMEM media, prepared as described above, was added to the flask to bring the total volume to 10 mL. This solution was used to wash the bottom of the flask five times, dislodging any residually adhering cells. Then, the solution was vigorously pipetted up-and-down five times in order to form a single-cell suspension. Lastly, 50 to 1000 µL of this solution was used to seed the new flask pre-filled with fresh warmed media to ultimately reach a total final volume of 20 mL.

MDA-MB-231 Cell Line

MDA-MB-231 triple-negative breast adenocarcinoma cells (ATCC), passage 10-15, were cultured in DMEM plus 4.5 g/L glucose, L-glutamine, and sodium pyruvate (Corning) supplemented with 10% FBS (Corning) and 1% penicillin-streptomycin (Sigma-Aldrich). Cells were maintained within T-75 flasks (CELLSTAR; Greiner Bio One, VWR) at 37°C in a humidified incubator with 5% CO_2.

To passage cells, all media was aspirated from the T-75 flask and replaced by 5 mL of sterile PBS without calcium or magnesium (VWR). The PBS was swirled around the bottom of the flask a minimum of 15 times in order to wash any residual media from the

cells. The PBS was then aspirated and replaced by 2 mL of 0.25% Trypsin/2.21 mM EDTA in HBSS without sodium bicarbonate, calcium, or magnesium (Corning), enough volume to cover the entire bottom of the T-75. The flask was placed back into the incubator for 3 minutes and then removed. After gently agitating the flask and visually inspecting for signs of cell detachment, 8 mL of pre-warmed DMEM media, prepared as described above, was added to the flask to bring the total volume to 10 mL. This solution was used to wash the bottom of the flask five times, dislodging any residually adhering cells. Then, the solution was vigorously pipetted up-and-down five times in order to form a single-cell suspension. Lastly, 50 to 1000 µL of this solution was used to seed the new flask pre-filled with fresh warmed media to ultimately reach a total final volume of 20 mL.

In vitro *Cell Targeting Assay*

Cells, either SK-BR-3 or MDA-MB-231, were trypsinized as detailed previously, pelleted at 300 rcf for 5 minutes, and resuspended in fresh, pre-warmed media at a concentration of 5×10^3 cells per mL. Then, 3 mL of media (1.5×10^4 cells) were added to each well of a sterile, glass-bottomed 6-well plate (Chemglass). The seeded 6-well plate was kept in the incubator for 2-3 days prior to the start of the assay.

On the day of the assay, DiI-labelled, maleimide functionalized PFCnDs were synthesized as described above. These PFCnDs were either targeted (anti-HER2), mistargeted (anti-Gamma-sarcoglycan), or untargeted (1-butanethiol backfill only). The media in each well was aspirated and replaced with 2 mL of PFCnD-containing media. The 6-well plate was then returned to the cell incubator for 2 hours, with brief, manual agitation

of the plate every 10 minutes to prevent the negatively buoyant PFCnDs from completely sinking during this time.

After the 2-hour incubation with PFCnDs, the wells were washed to remove unbound PFCnDs. The media in each well was aspirated and replaced by fresh, pre-warmed, PFCnD-free media a total of three times. Next, 1.5 µL of 10 mM Green CMFDA Dye (CellTracker™; Invitrogen) in DMSO was added to each well and allowed to incubate for 45 minutes. After incubation with this dye, the well plate was immediately imaged under confocal microscopy.

Confocal imaging was performed within the Optical Microscopy Core in the Petit Institute for Bioengineering and Bioscience at Georgia Tech. Cells were imaged on a Zeiss laser scanning microscope consisting of an LSM 700 scan head mounted on an AxioObserver Z1 inverted microscope stand with a motorized stage. Images were obtained with laser lines at 488 and 555 nm using a 10x / 0.3 N.A. Plan Apochromat objective lens with a working distance of 5.20 mm.

5.1.4 Results and Discussion

The use of Traut's reagent is common to create sulfhydryl groups from primary amine groups on antibodies. Sulfhydryl groups can then be used for antibody conjugation via a thiol chemistry-based approach. Here, we utilize a maleimide linker on the PFCnD shell in order to achieve bioconjugation of antibodies to the nanodroplet surface. However, antibodies have primary amine groups throughout their structure. As such, it is possible that antibodies can be attached to PFCnDs in an orientation where the antigen-binding sites are not outwardly facing. It is also possible, even with appropriate directional conjugation,

that the Traut's reagent may convert additional primary amines to sulfhydryl groups within the antigen-binding site itself. Depending on the resulting conformational change induced such a substitution, the Traut's reagent may inadvertently inactivate some antibodies in solution. As such, it is important to assess this synthesis strategy to ensure that it affords sufficient functional antibody attachment to be used in downstream *in vivo* studies that require a molecularly specific agent.

Prior to any *in vitro* assays, the PFCnDs in this protocol were coarsely assessed for successful bioconjugation via average size measurements using DLS. **Figure 18** shows the size measurements of PFCnDs before and after incubation with thiolated antibodies. The large increase in hydrodynamic diameter from 268 to 423 nm, far more than would be expected from Ostwald ripening alone,[76] suggests that the Traut's reagent bioconjugation protocol successfully attaches antibodies to the PFCnDs' surface. After this coarse assessment, we proceeded to a more relevant *in vitro* assay to assess the binding of bioconjugated PFCnDs to their intended molecular targets.

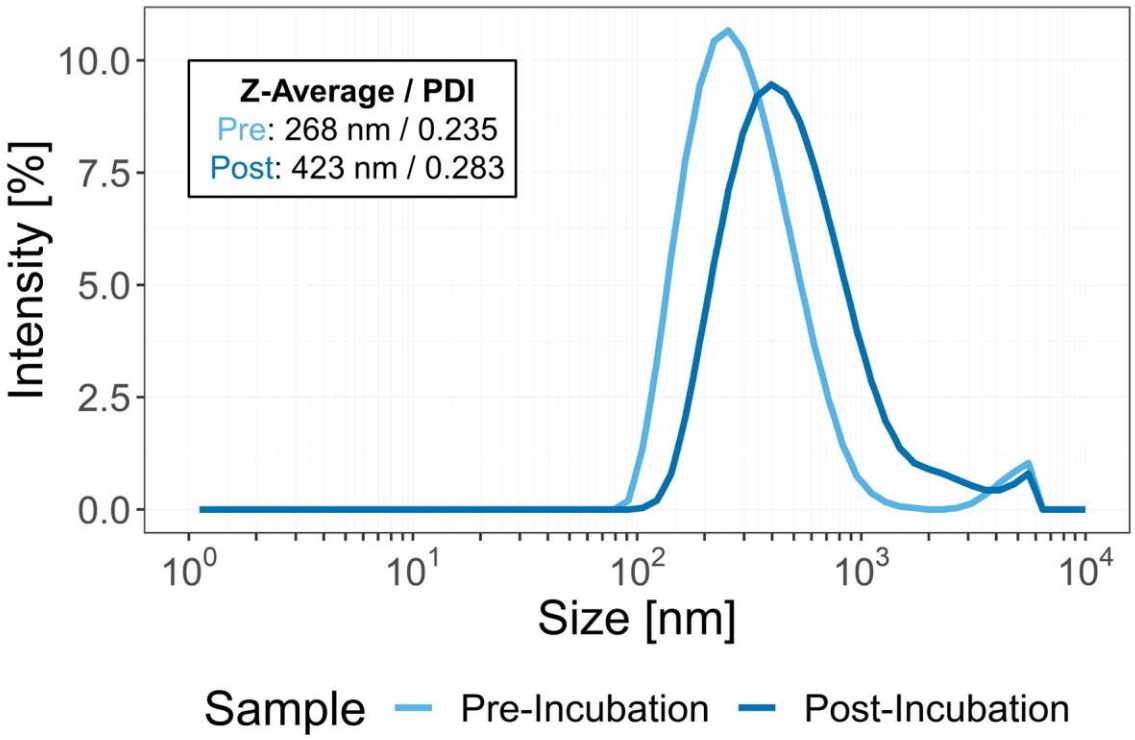

Figure 18: Average PFCnD size data before and after anti-HER2 antibody incubation. Data demonstrate an increase in Z-Average in excess of what would be expected from Ostwald ripening over the incubation time period, suggesting successful antibody conjugation.

We hypothesize that targeted PFCnDs will focally adhere to cancer cells as a result of the molecularly specific binding of bioconjugated antibodies on the nanodroplet shell to their corresponding extracellular targets on the cancer cell surface. This molecular interaction is necessary to accumulate PFCnDs within tumors to permit diagnostic contrast-enhanced US/PA imaging with these agents. As such, we performed a controlled *in vitro* assessment of this binding by incubating cancer cells of different receptor status with fluorescently labelled PFCnDs and assessing their binding via confocal imaging. Representative data from this assay can be seen in **Figure 19**.

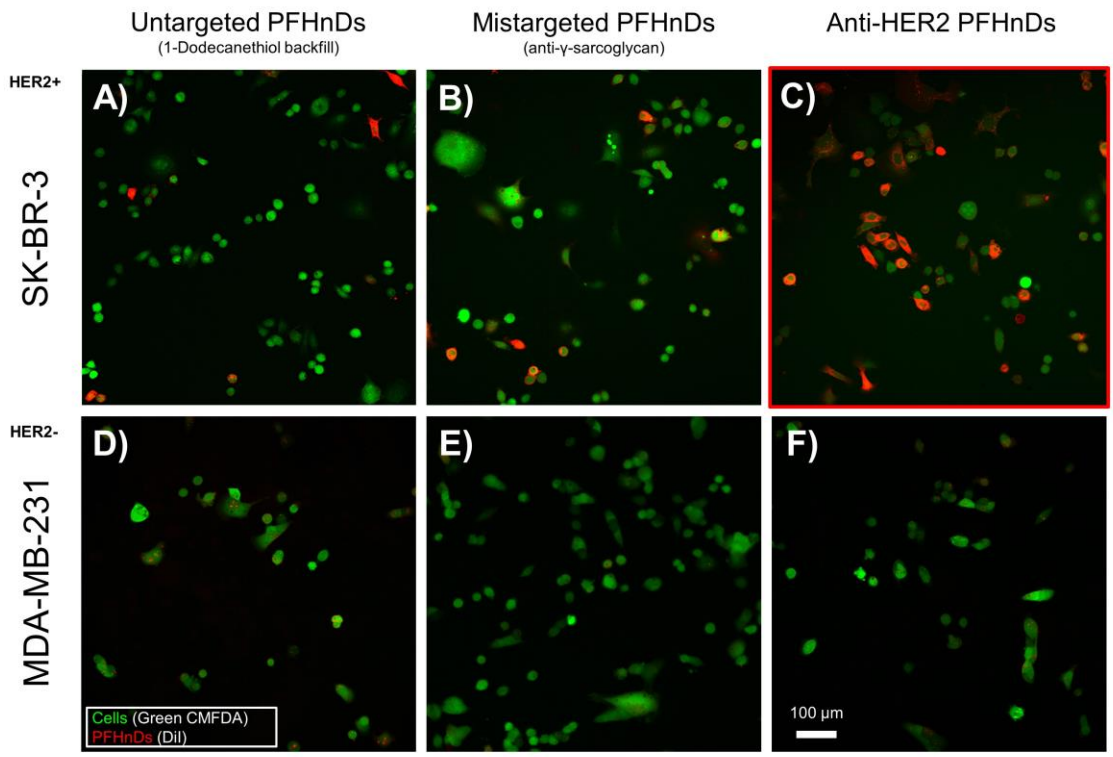

Figure 19: Representative confocal images from the *in vitro* PFHnD targeting assay. HER2-positive SK-BR-3 cells (**A**, **B**, **C**) or HER2-negative MDA-MB-231 cells (**D**, **E**, **F**) incubated with untargeted (**A**, **D**), mistargeted (**B**, **E**), or targeted (**C**, **F**) PFHnDs. After washing, only **C)** shows appreciable enhancement from PFHnD fluorescent signal.

As mentioned, human breast cancer is often classified by the expression levels of ER, PR, and HER2 within tumor tissue samples. Of these three classically assessed receptors, only HER2 is constitutively present on the extracellular membrane where it can interact with extracellular contrast agents. For this reason, we elected to conduct our *in vitro* assay of breast cancer cells with HER2 as the molecular target of interest. We utilized two established cell lines of HER2-positive (SK-BR-3) and HER2-negative (MDA-MB-231) breast cancer.

To adequately assess the impact of binding from the PFCnDs' perspective, we employed three distinct control populations. First, as a negative control, we incubated

maleimide-group containing PFCnDs without antibodies and only performed a 1-butanethiol backfill to cap all maleimide groups. Second, we performed a mistargeted control by incubating PFCnDs with Traut's reagent functionalized monoclonal antibodies to Gamma-sarcoglycan. Gamma-sarcoglycan is expressed within the cell membranes of striated muscle,[175] and therefore, it should not be expressed in breast cancer cells of epithelial origin. Lastly, we included PFCnDs incubated with Traut's reagent functionalized monoclonal antibodies to HER2, our target of interest. After incubating cells with particles in these groups, the media in the wells was aspirated and replaced with PFCnD-free media three times in order to wash out unbound PFCnDs remaining in solution prior to imaging.

As shown in the representative data, the highest focal retention of PFCnD fluorescent signal was observed for the molecularly appropriate targeted group (**Figure 19C**). For cells with the appropriate HER2 target, untargeted (**Figure 19A**) and mistargeted (**Figure 19B**) PFCnDs only exhibited minor residual adhesion to cells. Given the homogenously colored appearance of isolated cells in each of the SK-BR-3 incubation wells, it is also possible that some of the retained fluorescence may be due to the nonspecific transfer of DiI from PFCnDs into the cell membranes of cancer cells upon contact,[176,177] although this phenomenon is rare.

Similar to the negative controls in the HER2-positive cell case, the HER2-negative cell conditions show minimal (**Figure 19D**) or absent (**Figure 19E**, **Figure 19F**) PFCnD fluorescent signal after washing wells. This is an important finding, as along with the mistargeted PFCnD control data it precludes the possibility of an unknown surface protein interaction that could lead to confounding appreciable accumulation of targeted PFCnDs

at the cancer cell surface. Taken together, these *in vitro* data suggest that PFCnDs targeted to extracellular cell markers will focally adhere to these markers due to the molecularly specific interaction of bioconjugated antibodies on the particle surface. The results are encouraging for the advancement of PFCnDs towards *in vivo* molecular US/PA imaging.

In conclusion, we have developed a facile method of bioconjugating antibodies to the surface of PFCnDs. We have then utilized this method to demonstrate that HER2 targeted PFCnDs focally adhere to HER2-positive breast cancer cells *in vitro* and that this interaction is molecularly specific. Our ongoing research efforts with these particles will move towards applying them to the molecularly specific imaging of HER2-positive tumors *in vivo*. More generally, these methods open up the possibility for the molecularly-specific imaging of a wide array of surface markers, both epithelial and endothelial, with US/PA imaging.

5.2 Imaging of Intravascularly Delivered Perfluorohexane Nanodroplets in Primary Breast Tumors

5.2.1 Abstract

To accommodate their growing metabolic demands, many solid tumors recruit blood vessels via the secretion of pro-angiogenic cytokines. The resulting aberrant angiogenesis produces neovasculature that is torturous and “leaky,” with large gaps between endothelial cells. These endothelial fenestrations provide an opportunity, however, for the delivery of diagnostic or therapeutic particles that are small enough to be transported through them. Many preclinical researchers have utilized the combination of fenestrated vasculature and impaired lymphatic outflow to deliver particles to primary

tumors through what is known as the enhanced permeability and retention effect. The ability to image particles delivered to tumors is critical for providing real-time diagnoses and confirming therapeutic delivery. In ultrasound imaging, the diagnostic contrast agent used clinically is gas microbubbles. Unfortunately, microbubbles are too large to extravasate from through fenestrations into the tumor stroma when they are delivered systemically. In response to this limitation, perfluorocarbon nanodroplets (PFCnDs) were developed. PFCnDs are submicrometer agents that can be triggered to vaporize into microbubbles *in situ*, affording ultrasound and photoacoustic contrast in the process. The overarching goal was to be able to deliver the submicrometer form of PFCnDs intravascularly, allow them to be transported into the tumor stroma, and then trigger them for extravascular contrast-enhanced ultrasound imaging. However, researchers have yet to show that PFCnDs extravasate in a realistic small animal model of primary cancer. To this end, we investigated the use of PFCnDs for ultrasound and photoacoustic (US/PA) imaging in two immunocompetent, orthotopic models of primary breast cancer. We also implemented a drug regimen to attempt to increase PFHnD delivery in these models. Our preliminary results, while inconclusive, lay the groundwork to obtain results that will be scalable to human neoplastic disease.

5.2.2 Introduction

All neoplastic diseases are the result of genetic mutations that result in a pro-growth phenotype within cells. This occurs either by the upregulation of growth pathways (proto-oncogenes) or by the disruption of pathways that keep aberrant growth in check (tumor-suppressor genes). If this rampant growth occurred in isolation, then all neoplastic growths would be self-limited, as their metabolic demands would rapidly outpace the local

availability of metabolic resources. However, the metabolic demands of the tumor, specifically the ensuing local hypoxia, create a selective pressure for the secretion of pro-angiogenic cytokines.[178] This induces local angiogenesis to supply oxygen and other nutrients to support the continued growth and eventual metastasis of the neoplasm.

Tumor vessels grow through the same mechanisms of angiogenesis as in embryonic development: sprouting or intussusception from existing vascular networks.[179] Circulating endothelial precursor cells may also play a role in tumor angiogenesis.[180,181] A diverse array of molecular pathways contribute towards the formation of cancer neovasculature. Chief among these are members of the vascular endothelial growth factor (VEGF) and angiopoietin (Ang) pathways.[178] The molecular regulators of angiogenesis are not as well coordinated in tumor angiogenesis as in physiological angiogenesis. Consequently, tumor neovasculature is structurally abnormal as compared to physiological vasculature. Tumor blood vessels are often tortuous and dilated with excessive communicating shunts. This disorganization leads to localized chaotic blood flow,[182] which results in hypoxic and acidic regions within tumors.[183] Additionally, the underlying structure of tumor blood vessels is abnormal. Tumor neovessels are "leaky."[69,70,184] The vascular walls are porous, owing to endothelial fenestrae, vesicles, and transcellular holes in addition to widened interendothelial junctions.[178] The endothelial pore size in leaky tumor neovasculature has been reported to be between 380 to 780 nm;[69-71] however, these estimates were likely biased towards the larger side of what is observed clinically in human solid tumors.[72]

The hyperpermeability of tumor neovasculature coupled with defective lymphatic drainage in neoplastic tissue can result in the penetration and retention of both nanoparticles and small molecules into the tumor stroma.[71,185,186] This phenomenon is

referred to as the enhanced permeability and retention (EPR) effect, and it has been championed by biomedical researchers for decades as a mechanism to passively target diagnostic and therapeutic agents to tumors following intravascular administration.[72,187] Although EPR shows promise in preclinical xenograft models,[188] vascular leakiness has been shown to be heterogeneous across time and space as well as in response to treatment.[189] Therefore, translational efforts should employ adjunct strategies, such as active targeting and pharmacological vascular remodeling, to achieve appreciable delivery through EPR.[72,190-192]

For years, researchers in the ultrasound contrast agent community have promised that PFCnDs could be used as extravascular contrast agents in tumors due to their size and the EPR effect.[59,77,118,119,193] However, little meaningful progress has been made towards rigorously proving that this phenomenon occurs. Several groups have shown signal enhancement in primary tumors inoculated non-orthotopically in the flank,[194] but these tumor models bear no resemblance to known human disease.

The goal of these studies was to investigate the potential for PFCnD extravasation in a realistic model of breast cancer. We performed US/PA imaging before, immediately after, and 24 hours after intravenous PFCnD administration. We then compared the results of US/PA imaging to histology. Additionally, we utilized a regimen of angiotensin receptor blocker microdosing in an attempt to decrease tumor solid stress and improve particle delivery. These efforts represent a critical reframing of the biological application that has justified the development of phase-change US agents for the last two decades, and they highlight lingering challenges in ongoing efforts to conclusively demonstrate PFCnD extravasation.

5.2.3 Materials and Methods

Targeted Perfluorocarbon Nanodroplet Synthesis

Prior to synthesis of the nanodroplet stock solution, monoclonal antibodies to Erbb2 (ab16901 lot # GR3215414-5 or GR3283213-2; abcam) or polyclonal antibodies to EpCAM (ab71916 lot # GR3292991-1; abcam) were modified with Traut's reagent (2-iminothiolane hydrochloride; Sigma-Aldrich) to create sulfhydryl groups from primary amine groups on the antibodies. Maleimide groups on the surface of the nanodroplets from stock can then react with these sulfhydryl groups to tether monoclonal antibodies to the nanodroplet surface. One microliter of a 1:20 PBS dilution of 2 mg/mL Traut's reagent in PBS was added to each of three antibody aliquots (10 µL; 1 mg/mL) after thawing them at room temperature. These aliquots were allowed to incubate for one hour at room temperature, during which time the stock solution of nanodroplets was synthesized.

One micromole (10^{-6} mol) of DSPC, 18:0 Cy5 PE, DSPE-PEG2000 Maleimide, and DSPE-mPEG2000 (all from Avanti Polar Lipids, Inc) in a 2:2:5:11 molar ratio was extracted from chloroform aliquots and added to a 10 mL pear-shaped flask (Aldrich). To this isolate, 0.5 mg of near-infrared-absorbing dye (IR-1048; Sigma-Aldrich) from a 5 mg/mL chloroform aliquot were added. An additional 400 µL of HPLC-grade chloroform were added to the flask to ensure the formation of an even lipid cake. The pear-shaped flask was covered in aluminum foil and placed into a rotary evaporator with a water bath (R-215, V700, and V-855 with B-491; Buchi) and water-cooled condenser and evaporated for 30 minutes, adhering to the "20/40/60" rule. After this, the solid isolate was further dried

under nitrogen flow for a minimum of 20 minutes in order to evaporate all residual chloroform in the lipid cake.

Next, the solid reagents were hydrated with 1 mL of 7.40 pH PBS and homogenized using a water bath sonicator (1800 Series Ultrasonic Cleaner; Branson) for 5 minutes at room temperature to produce a solution of dye-loaded nanomicelles. This solution was centrifuged at 300 rcf for 1 minute in order to pellet excess near-infrared dye. Then, 900 µL of the nanomicelle-containing supernatant was combined with 100 µL of PBS and 50 µL of perfluorohexane (FluoroMed, L.P.) in a 2-dram glass scintillation vial (VWR). The glass vial was placed into an ice bath and allowed to rest for 5 minutes. Then, the solution was probe sonicated in the ice bath with a 1/8" microtip (QSonica) at 1% power (1s on, 15s off, 5 times) in order to produce the stock solution of PFCnDs, which was stored at 4°C in amber glass prior to incubation with antibodies.

After the one-hour Traut's reagent incubation, 1 µL of a 1:10 PBS dilution of a quenching solution of 1 mg/mL glycine (Invitrogen UltraPure; Thermo Fisher Scientific) in PBS was added to each of the three antibody aliquots. The quenched antibody solutions were allowed to rest for 5-10 minutes prior to incubation with nanodroplets.

Prior to antibody incubation, 100 µL of the PFCnD stock solution was diluted in 1 mL of PBS and bath sonicated for 2 minutes. All three quenched antibody aliquots (12 µL each; 36 µL total) were added to this diluted nanodroplet stock and left to incubate in the dark within an ice bath on a shaker plate for two hours, replacing ice in the water bath at the one-hour mark. After the two-hour incubation, 1 µL of 1-butanethiol (Acros Organics;

Thermo Fisher Scientific) was added to the solution to quench all unreacted maleimide groups. This quenched solution was allowed to rest for 5-10 minutes prior to resuspension.

After quenching, the targeted PFCnD solution was centrifugated at 3000 rcf for 5 minutes in order to pellet the PFCnDs. The supernatant was removed and the PFCnDs were reconstituted in 150-300 μL of sterile saline for imaging. This protocol produces PFCnDs with a hydrodynamic diameter of 400-600 nm measured via dynamic light scattering (Zetasizer Nano ZS; Malvern Instruments Ltd.).

4T1 Cell Line

4T1 triple negative breast carcinoma cells (ATCC), passage 11-16, were cultured in RPMI plus L-Glutamine (Corning) supplemented with 10% FBS (Corning) and 1% penicillin-streptomycin (Sigma-Aldrich). Cells were maintained within T-75 flasks (CELLSTAR; Greiner Bio One, VWR) at 37°C in a humidified incubator with 5% CO_2.

To passage cells, all media was aspirated from the T-75 flask and replaced by 5 mL of sterile PBS without calcium or magnesium (VWR). The PBS was swirled around the bottom of the flask a minimum of 15 times in order to wash any residual media from the cells. The PBS was then aspirated and replaced by 2 mL of 0.25% Trypsin/2.21 mM EDTA in HBSS without sodium bicarbonate, calcium, or magnesium (Corning), enough volume to cover the entire bottom of the T-75. The flask was placed back into the incubator for 3 minutes and then removed. After gently agitating the flask and visually inspecting for signs of cell detachment, 8 mL of pre-warmed RPMI media, prepared as described above, was added to the flask to bring the total volume to 10 mL. This solution was used to wash the bottom of the flask five times, dislodging any residually adhering cells. Then, the solution

was vigorously pipetted up-and-down five times in order to form a single-cell suspension. Lastly, 50 to 1000 µL of this solution was used to seed the new flask pre-filled with fresh warmed media to ultimately reach a total final volume of 20 mL.

Mice

All animal studies were conducted under the oversight of the Georgia Tech Institutional Animal Care and Use Committee (IACUC) under protocol A100281. Three-to-four-week-old female transgenic mice (Stock No.: 002376) and four-week-old female BALB/cJ mice (Stock No.: 000651) were purchased from The Jackson Laboratory. Upon receipt, mice were allowed a minimum of five days to acclimate to the housing facility at the Georgia Institute of Technology. Mice were housed with their littermates, with a maximum of five mice per cage, until administration of perfluorohexane nanodroplets, at which point the dosed mouse would be housed in isolation prior to reaching the experimental endpoint. Cages within the housing facility contain 100% corn cobb bedding and enrichment in the form of a mouse igloo, wood gnawing block, and rodent nesting sheets (all Bio-Serv; Fisher Scientific). The facility operates on a 12-hour day-night cycle, with "daytime" occurring from 06:00-18:00 UTC-5. Mice had access to food and water *ad libitum* throughout all phases of the study.

MMTVneu Genetically Engineered Mouse Model

This is a genetically engineered mouse model (GEMM) of neu overexpression (FVB/N-Tg(MMTVneu)202Mul/J; The Jackson Laboratory).[195,196] This model results in the expression of unactivated neu (Erbb2) protein under the direction of the MMTV long terminal repeat, which leads to the spontaneous development of mammary tumors. Tumors

first appear around four months of age, with a median incidence of 205 days. These tumors are focal in the mammary gland, and tumors overexpress HER2.

Mice in this GEMM were purchased from the vendor at 3-to-4 weeks of age. At 6-to-7 weeks of age, mice were placed under general anesthesia and their ears were punched for longitudinal identification. During this anesthesia session, and monthly thereafter, the entire mammary crests of the mice were shaved and chemically depilated, as described previously, in order to facilitate tumor screening. Weekly thereafter, mice were manually restrained via scruffing in order to visually inspect and palpate the mammary crests to monitor for the development of tumors.

Murine Anesthesia

In order to achieve general anesthesia, mice were placed into a non-primed induction chamber, which was then filled with 5% isoflurane in oxygen at a flow rate of 400 mL/min. After mice lost their righting reflex and their sympathetic response to isoflurance abated to yield a respiration rate of at most 100 breaths per minute (bpm), the isoflurane was lowered to 2%.

Once their respiration rate reduced to between 60-80 bpm, mice were transferred onto a temperature-controlled stage (Visualsonics) heated to 40°C. The isoflurane flow rate was raised to 600 mL/min for the initial transfer but was slowly lowered back to 400 mL/min during positioning on the stage. For procedures under general anesthesia scheduled to last longer than 30 minutes, sterile petrolatum ophthalmic ointment (Puralube; Dechra Phramaceuticals) was applied to the eyes of mice immediately post-transfer using a 6” wood-handled cotton-tip applicator (Puritan Medical).

Throughout general anesthesia sessions, the isoflurane was gradually lowered to between 1.25-1.5% maintenance in order to consistently maintain murine respiration between 60-80 bpm. If after two hours mice respired slower than 60 bpm, isoflurane was lowered to 1% or 0.75% as necessary to maintain the appropriate respiration rate.

After non-terminal procedures, mice were returned to pre-warmed cages and monitored until they regained consciousness and resumed normal behavior. A heat lamp was applied if this process did not occur within 15 minutes.

4T1 Syngeneic Model of Breast Cancer

Prior to inoculation, 4T1 cells were trypsinized (Corning), pelleted at 300 rcf for 5 minutes, and resuspended in sterile PBS without calcium (Corning) at a final concentration of 2×10^6 cells per mL. Cells were counted prior to pelleting using 10 µL of solution on a hemocytometer. The count from the central grid of the hemocytometer was used to estimate the number of cells in the pellet prior to resuspension. The final cell solution was stored on ice prior to inoculation.

Five- or six-week-old BALB/cJ mice were placed under general anesthesia per the previously detailed protocol. The skin overlying the right fourth mammary fat pad was shaved with an electric-powered shaver (BravMini+; Wahl). The area was then chemically depilated with Nair calcium hydroxide lotion (Church & Dwight). Nair was dabbed with a cotton-tipped applicator into the hair roots and allowed to sit on the skin for 60 seconds. After this, the Nair lotion was removed by sequential, unidirectional wiping with first moist and then dry gauze pads.

The shaved and depilated area was then disinfected with a 2% chlorhexidine gluconate solution (Dermachlor; Henry Schein Animal Health) applied with a gauze pad and allowed to air dry prior to further manipulation of the animal. Then, 50 µL of the 4T1 cell solution (10^5 cells) were injected subcutaneously in the anterolateral aspect of the right fourth mammary fat pad using a 31-Gauge diabetic syringe (Ultra Fine II™ U-100; BD).

Losartan Potassium Microdosing

Lyophilized solid losartan potassium (99% by TLC; BioVision) was dissolved 8 mg/mL in non-sterile PBS (VWR). The resulting solution was drawn up into a 10-mL Leur lock syringe, taken into a sterile biohood, and sterile-filtered through a 0.20 um polyethersulfone membrane (Part Number 431229; Corning). The resulting sterile losartan solution was divided into 1 mL aliquots and stored at -20°C prior to use. All of the previous steps were performed in darkness to protect the light-sensitive losartan.

Frozen aliquots were thawed in darkness at room temperature for a minimum of 30 minutes prior to injection. In a sterile biohood, a 40 mg/kg dose of the 8 mg/mL solution was drawn into a sterile 30-Gauge diabetic syringe. Mice were placed under general anesthesia as detailed previously. After being placed into the supine position, the mice received the 40 mg/kg dose of losartan via an intraperitoneal injection contralateral to the side of the tumor side. The general anesthesia session for each losartan injection lasted no more than 5 minutes, unless accompanied by concomitant US/PA imaging.

US/PA System and Imaging Sequence

Imaging was performed using a linear array ultrasound transducer (CL15-7; Advanced Technology Laboratories, Inc.) integrated with a 2-to-1 optical fiber bundle (CBGL-8-1/2-2500; Nanjing Chunhui Science & Industrial Co., LTD). The optical fiber bundle was connected to an Nd:YAG pulsed laser (Phocus Mobile; Opotek Inc.) operating at the fundamental 1064 nm wavelength. The split end of the fiber bundle was mechanically fixed to the transducer via a custom 3D-printed holder. These fiber outputs allowed for irradiation of imaged tissue, which was performed with 5-ns laser pulses at a pulse repetition frequency (prf) of 10 Hz. The estimated fluence at the depth of fiber intersection within the imaging plane (12-14 mm) was measured to be 85±5 mJ/cm^2 with a power meter (Nova II; Ophir-Spiricon, LLC). For US imaging, the transducer was driven at a 12.5 MHz center frequency using a programmable research US imaging system (Vantage 256; Verasonics, Inc.). The full imaging window in each plane was 22.8 mm wide and 25 mm deep. The imaging probe and optical fiber outputs were acoustically coupled with the subject using clear ultrasound gel (Sonigel; 3B Scientific).

For the imaging sequence at each imaging plane, a traditional line-by-line B-mode acquisition was first captured to record the underlying anatomy. Next, the tissue was irradiated with six successive laser pulses. A packet of US/PA data was acquired after each pulse. Each packet begins with 40 ultrafast pulse inversion (UFPI) frames at 8 kHz with alternating compressional or rarefactional phase as described in 3.2.3. After these “pre-laser” frames, the tissue is irradiated by a laser pulse. This pulse is immediately followed by a receive-only acquisition to capture PA signal and 40 “post-laser” UFPI frames at 8 kHz. Idle time fills the time between US/PA packets to synchronize with the 10 Hz prf of the pulsed laser. The first three US/PA packets use UFPI sequences with transmits that

have an initial rarefactional phase, as described previously. The last three invert this order and use transmits beginning with an initial compressional phase. All of the received waves were sampled at 56 MHz.

After all images in the US/PA imaging sequence at a plane were saved in system memory, a motor controller (Model ESP301; Newport Corporation) translated a motorized linear stage (Model UTS150PP; Newport Corporation) 0.3 mm in the direction perpendicular to the imaging. In this new imaging plane, the US/PA imaging sequence was again acquired and saved in memory. This process repeats to acquire 35 imaging planes, spanning a total distance of 10.2 mm, for each volumetric acquisition. After completing a volumetric acquisition, the software returns the motor stage to its original position at the first imaging plane.

All data were saved and processed offline in MATLAB (MathWorks). For displaying post-processed volumetric images, line-by-line B-mode and post-processed PA images at each imaging plane were linearly interpolated by a factor of 5 in two dimensions and saved as JPEGs. These co-registered JPEG stacks were imported into Amira (Thermo Fisher Scientific) and rendered in three-dimensional space. The B-mode layer was made translucent at $\alpha = 0.15$ to highlight the co-registered PA signal. Amira software adjusted the dynamic range of its display colormap in order to match the range of the post-processed PA signal for each individually rendered volume.

US/PA Imaging Protocol

Mice were placed under general anesthesia per the previously described protocol. If necessary, the skin surrounding the primary tumor was shaved with an electric-powered

shaver. The area was then chemically depilated with Nair calcium hydroxide lotion. For the first pre-injection imaging session, the Nair was left on the skin for a full 60 seconds. However, for downstream imaging timepoints where the mice had already been depilated, regions of regrown or residual hair in the imaged regions only received exposure of 30 seconds or less to the depilatory lotion. This protocol ensured no unnecessary irritation of the skin within the imaged regions.

After the mice were sufficiently depilated for imaging, a rectangular cut-out of hunter green felt (Walmart) was slid underneath mice and fixed to the imaging stage. Once the felt was in place, mice were placed into the anatomically appropriate position for viewing the primary tumor, and their limbs were fixed to the imaging stage with adhesive tape (ZONAS® Porous Tape; Johnson & Johnson). Acoustic coupling gel (Sonigel; 3B Scientific), which was previously centrifugated for 5 minutes at 10,000 rcf to remove bubbles and UV-sterilized, was applied to the depilated skin surface using a 5-mL disposable slip-tip syringe (BD). The transducer was lowered until coupled with the gel, and real-time B-mode imaging on the Verasonics Vantage system was used to appropriately position the mouse. The 3-axis motor stage was used to translate the transducer through the imaging volume of interest. A 1-mL disposable slip-tip syringe (BD) was used to remove any bubbles remaining in the gel from this imaging volume.

Following initial positioning, acoustic coupling gel was used to couple the laser fiber bundles to the mouse skin surface. The motor stage was again translated through the volume of interest both to ensure no additional bubbles entered the volume and to ensure gel coupling of the fibers throughout the entire motion of the transducer setup through the imaging volume. Bubbles were removed and more gel was added as necessary. Once

quality coupling of the transducer and fibers was assured, US/PA volumes were acquired by the system.

After volumetric US/PA acquisitions, a quality assurance (QA) code was executed in MATLAB (MathWorks) to quickly assess B-mode, PA, ultrafast pulse-inversion US, and initial differential US images across the imaging volume. If the QA code suggested issues in US coupling, laser light illumination, or malpositioning, then these issues were addressed, and the corresponding volume was reacquired.

Each volumetric acquisition takes approximately 8 minutes to acquire and save the data. The entire imaging workflow, from induction of anesthesia to regaining of consciousness or euthanasia, requires between 90 to 120 minutes, on average, to execute.

Perfluorocarbon Nanodroplet Injection

Mice were placed under general anesthesia per the previously described protocol. When transferred to the temperature-controlled stage, mice were placed in the supine position. An electric-powered shaver was used to shave the skin overlying the neck down to the manubrium. This area was then chemically depilated with Nair calcium hydroxide lotion, which was dabbed with a cotton-tipped applicator into the hair roots and allowed to sit on the skin for 60 seconds prior to removal via sequential, unidirectional wiping with first moist and then dry gauze pads.

After preparing the skin, the mice were optimally positioned for injection into the jugular vein. Mice were moved from the center to the upper edge of the temperature-controlled stage. A 1-mL disposable syringe was placed underneath the mouse at the level

of the scapula. Then, the breathing tube was positioned such that the mouse head hangs off and slightly below the stage. The result of these manipulations is the mouse positioned with its neck in extension and its shoulders abducted and extended.

After positioning the mice, the depilated skin on the neck was disinfected with a 70% isopropyl alcohol swab. A 30-Gauge diabetic syringe was filled with 70 µL of a 10^{10} particles/mL solution of perfluorocarbon nanodroplets. Then, this needle was inserted suprasternally in the medial aspect of the pectoral muscle at an approximate angle of 30° from the skin surface and pointed towards the ipsilateral mouse ear. The needle was inserted into the mouse such that the needle tip enters the widest part of the jugular vein, which appears as the darkest aspect of the vein as seen through the skin. To confirm needle positioning, the entire syringe was elevated no more than 1 mm in order to better visualize the needle. After the needle was positioned correctly, the syringe plunger was slightly withdrawn to generate a flash of blood in order to confirm placement of the needle tip within the jugular vein. Once a flash was generated, the syringe plunger was slowly depressed in a sawtooth motion in order to deliver the full 70 µL volume intravascularly while confirming placement of the needle tip throughout the course of the injection via flashes on pullback.

Euthanasia

Mice were sacrificed via a primary lethal intraperitoneal injection of Euthasol (150 mg/kg; Henry Schein Medical) contralateral to the primary tumor. After cessation of breathing, mice were exsanguinated during the perfusion-fixation procedure, which served as secondary euthanasia. In brief, a transverse incision through the skin and underlying

fascia was made immediately inferior to the sternum. Vertical incisions were made superiorly on either side of the primary incision, transecting the ribs in the process, in order to expose the diaphragm. The diaphragm was transected laterally, and the rib cage was separated and reflected superiorly, exposing the heart. A 27-Gauge butterfly needle (Surflo Winged Infusion Set; Terumo) was inserted into the left ventricle of the ideally still-beating heart and the right auricle was lanced vertically in order to convert the circulatory system into an open circuit. At this stage, 20 mL of 6.90 pH PBS was pumped through the circulatory system at a rate of 5 mL/min using a syringe pump (Legato 200; KD Scientific) attached to the butterfly needle setup. Next, the PBS syringe was replaced by one with a solution of 4% paraformaldehyde (reagent grade; Sigma-Aldrich) in 6.90 pH PBS, and 20-25 mL of this solution was pumped through the mice at a rate of 5 mL/min. Successful perfusion-fixation was confirmed by palpation of the mouse extremities to assess rigor.

After perfusion-fixation, both the primary tumor and spleen were resected. These specimens were placed into OCT-filled cryomolds (both Sakura Finetek), flash frozen under dry ice, and stored at -80°C to be sectioned for downstream histological analysis.

Histology

Prior to confocal imaging, slides were thawed, DAPI-stained, and sealed. All of these steps were performed in darkness to minimize photobleaching of fluorophores within the sections. First, frozen slides were thawed at room temperature for 20 minutes. Next, slides were rehydrated with 7.40 pH PBS for another 20 minutes. After this, excess PBS was tapped off slides, and the hydrated tissues were incubated with a 1:25000 (1:1000, then 10:250) PBS dilution of DAPI (4',6-Diamidino-2-Phenylindole, Dihydrochloride;

Invitrogen, Thermo Fisher Scientific) from an aliquot of 5 mg/mL in dimethylformamide (DMF). After 10-12 minutes of DAPI incubation, the DAPI solution was tapped off slides. Then, the slides were washed three times with PBS, allowing PBS to hydrate the sample for 5 minutes before being tapped off for the next wash. After the last wash, slides were mounted with antifade reagent (ProLong Gold Antifade Mountant; Invitrogen). Two to three drops of mountant were dropped evenly across the slide, in between tissue, and a glass coverslip (VWR) was slowly and evenly pressed down over the slide to distribute the mountant across the glass without disrupting the tissue. Lastly, clear nail polish was twice applied to all four edges of the coverslip to seal it to the slide, allowing at least 30 minutes for the first application to dry before adding the second. Mounted and sealed slides were stored in the dark at 4°C, at minimum overnight, until their scheduled time to be imaged on the confocal.

Mounted sections were imaged on a Zeiss laser scanning microscope consisting of an LSM 700 scan head mounted on an AxioObserver Z1 inverted microscope stand with a motorized stage. Images were obtained with laser lines at 405 and 639 nm using a 20x / 0.8 N.A. Plan Apochromat objective lens with a working distance of 0.550 mm. Tiled confocal images were rendered as JPEGs using Zen Black software (Carl Zeiss AG). The dynamic range of the Cy5 channel was set as the minimal level to suppress all signal from the spleen in a saline injected MMTVneu mouse.

5.2.4 Results and Discussion

The MMTVneu GEMM of HER2-overexpressing breast cancer is a logical choice for investigating the IV delivery of PFCnDs to primary tumors. Breast cancer is a highly

prevalent cancer of significant public health relevance,[1] and HER2 is overexpressed in approximately 13% of cases.[197] This spontaneous model of HER2-overexpressing breast cancer is also compatible with the targeted PFHnDs developed in 5.1. Previous nanoparticle delivery studies in small animal models have only shown appreciable primary tumor retention after vascular delivery when specific molecular targeting is implemented.[198-201] Thus, we elected to exclusively use targeted PFHnDs for our primary tumor studies.

To investigate PFHnD extravasation in the MMTVneu model, we performed volumetric US/PA imaging of the primary tumor using a similar workflow and equivalent data processing to what was detailed in 4.1.4. We performed baseline imaging 48 hours prior to injection, imaging immediately after IV injection of targeted PFHnDs, and terminal imaging 24-hour after IV injection, at which point we perfused the mouse and resected its primary tumor and spleen for histological processing. Volumetric US/PA data for an MMTVneu mouse imaged under this protocol can be seen below in **Figure 20**.

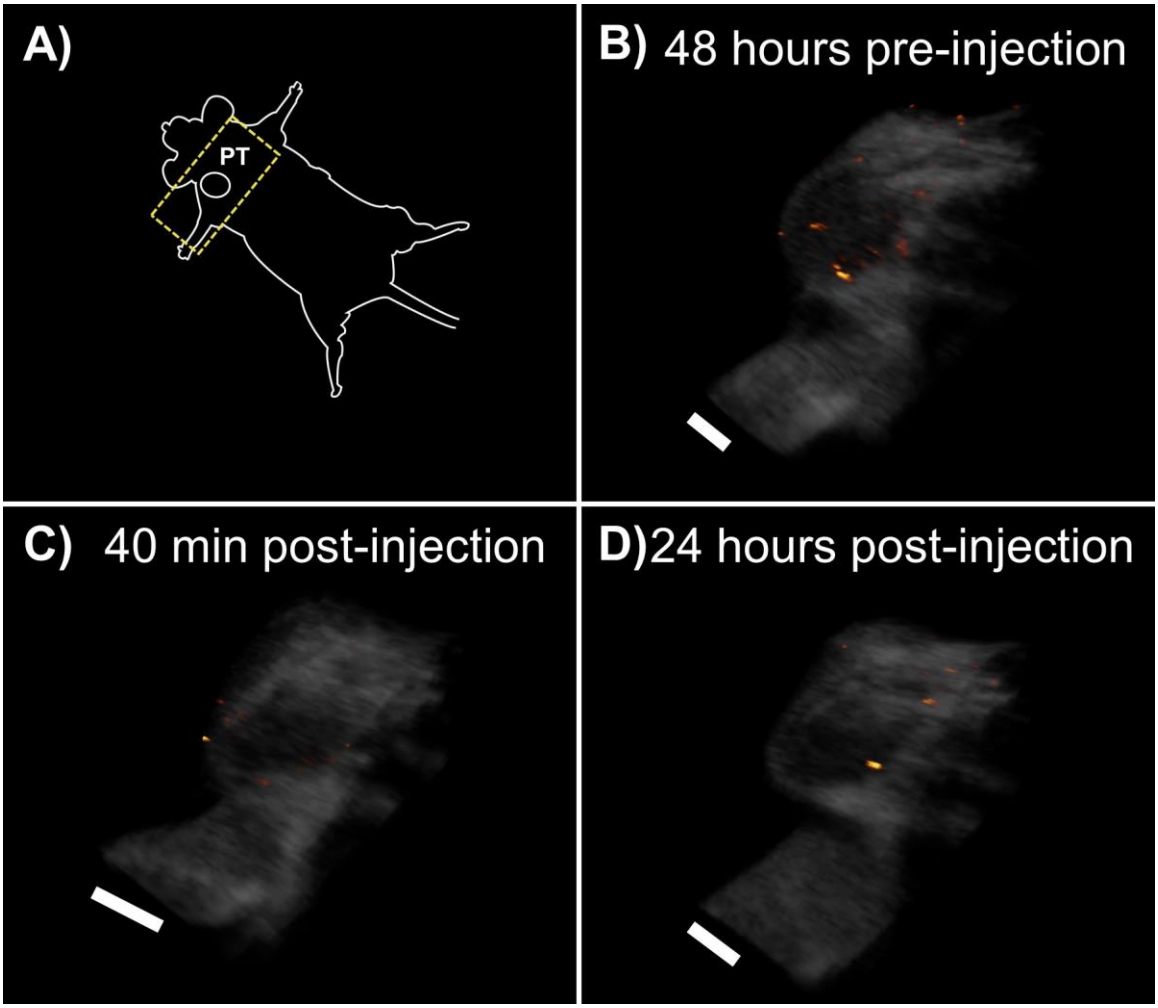

Figure 20: US/PA imaging volumes from an MMTVneu mouse injected with targeted PFHnDs. This mouse received an IV injection of anti-HER2 PFHnDs. **A)** Cartoon showing the primary tumor (PT) location and supine position of the mouse for imaging. The yellow dashed lines approximate the volumes shown; **B)** Masked PA signal (red-orange) overlaid with the corresponding US volume 48 hours before targeted PFHnD injection; **C)** Masked PA signal overlaid with US obtained 40 minutes after targeted PFHnD injection; **D)** Masked PA signal overlaid with US obtained 24 hours after targeted PFHnD injection. All volumes show minimal PA enhancement. Scale bars are approximately 5 mm.

Unfortunately, the primary tumor volumes obtained after image processing show no enhancement within the tumor stroma and only minimal masked PA signal in focal spots on the tumor surface. Because this sparse enhancement is at the level of the skin and can also be seen at baseline, it is likely an artifact nonspecific to any injected PFHnDs. To

further analyze the delivery within this mouse, we performed confocal imaging of histological sections of the primary tumor and spleen. The injected PFHnDs were doped with a Cy5 fluorophore, which should produce enhancement on confocal imaging. The results from this mouse can be seen in **Figure 21**.

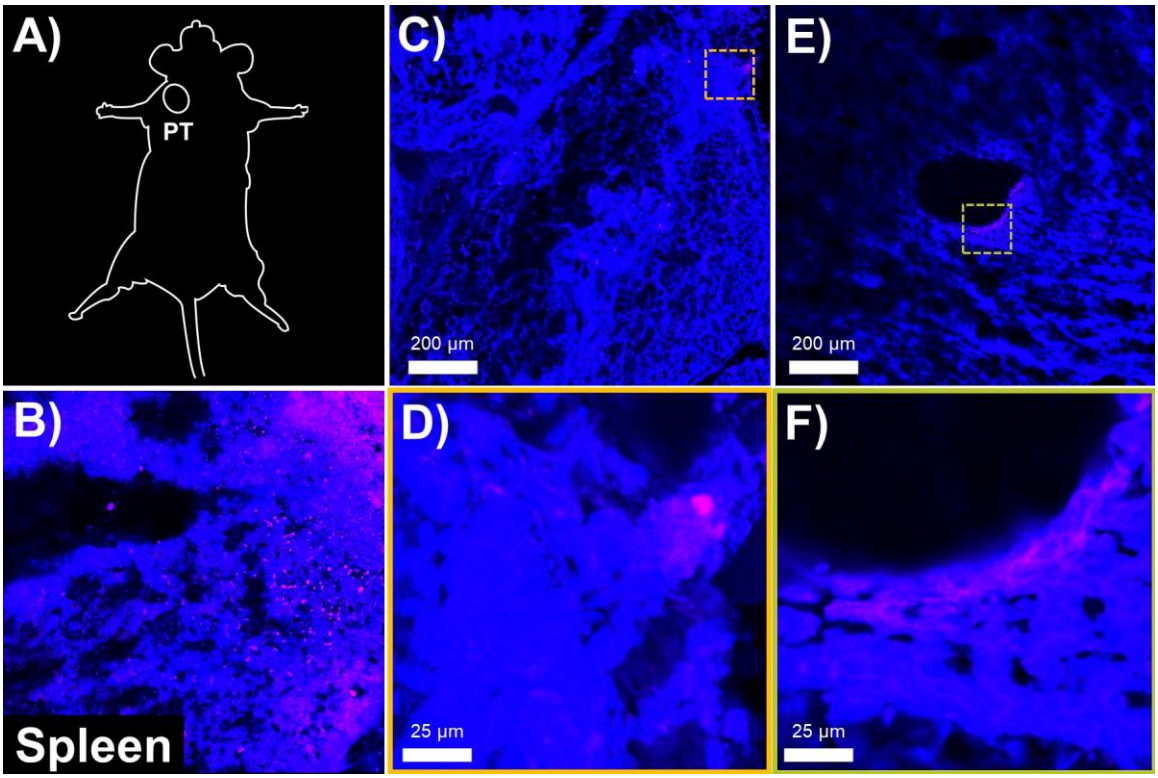

Figure 21: Representative histology from an MMTVneu mouse 24 hours after IV injection of HER2-targeted PFHnDs. This mouse received no pre-treatment. Sections were stained with DAPI (blue). **A)** Cartoon diagram of primary tumor location in the right first mammary fat pad; **B)** Section of the spleen showing focal enhancement from the Cy5 channel (red; absent); **C)** Section of the primary tumor with sparse enhancement from the Cy5 channel; **D)** Inset of the region in **C)** denoted with a yellow dashed line. The focal enhancement could correspond to Cy5-tagged PFHnDs; **E)** Second view of a primary tumor section showing minimal Cy5 enhancement; **F)** Inset of the region in **E)** denoted with a green dashed line. Enhancement from background connective tissue underscores the low SNR of the Cy5 channel. Scale bar for **B**), **C**), and **E**) is 200 µm; 25 µm for insets.

The spleen of this mouse shows focal, low-intensity enhancement from the Cy5 channel (**Figure 21B**). This may indicate successful IV delivery, as the spleen is one of the

major reticuloendothelial organs responsible for clearing PFHnDs from circulation. However, because of the low SNR of the Cy5 channel, it is also possible that this signal is a false positive due to noise. The dynamic range of the Cy5 channel was set in relation to the results of a saline-injected control mouse (see **APPENDIX D**, **Figure 39**). Sections of the primary tumor are largely devoid of Cy5 signal (**Figure 21C**), although there are sparse foci of signal that may correspond to retained PFHnDs (**Figure 21D**). The primary tumor tissue displays some perivascular Cy5 enhancement (**Figure 21E**). However, upon closer inspection (**Figure 21F**), this appears to be nonspecific enhancement from endothelial connective tissue.

It is apparent that strategies in addition to particle targeting will need to be employed in order to successfully increase delivery to the primary tumor stroma. One complementary approach to particle modification is modulation of the tumor microenvironment. Previous studies have shown that administering a subclinical dose of angiotensin receptor blocker (i.e., too low a dose to reduce systemic blood pressure) leads to a reduction of tumor solid stress through collagen remodelling within primary tumor neovasculature.[190-192] By reducing an unfavourable pressure gradient for particles attempting to traverse into the stroma, this microdosing regimen increases the efficiency of nanoparticle delivery.[190]

For all downstream small animal experiments investigating PFCnD extravasation, we implemented a 7-day losartan potassium microdosing regimen prior to IV delivery of PFHnDs (see **APPENDIX D**, **Figure 37**). To increase the throughput of our tumor extravasation studies, we elected to pursue imaging in the 4T1 syngeneic mouse model of breast cancer in addition to the MMTVneu model. The MMTVneu model has a median incidence of 205 days, whereas 4T1 tumors can be generated on-demand and imaged

within a week of inoculation. However, 4T1 tumors are triple-negative, meaning that HER2 targeting will be ineffective in this model. As such, for 4T1 studies we implemented PFHnDs targeted against epithelial cell adhesion molecule (EpCAM). EpCAM is a cell-cell adhesion molecule that is typically expressed in the basolateral membrane of normal epithelial cells.[202] In many cancers of epithelial cell origin, EpCAM is upregulated.[203] The 4T1 cell line demonstrates high EpCAM expression throughout the entire cell membrane within primary tumor cells,[204] and it has been used previously as a molecular target for US/PA nanoparticle targeting of 4T1 cells.[205]

The volumetric imaging results for a successful IV injection of anti-EpCAM PFHnDs in a losartan microdosed 4T1 syngeneic mouse can be seen in **Figure 22**. Prior to injection (**Figure 22B**), there is only sparse residual PA enhancement on the skin overlying the tumor surface. However, immediately after injection (**Figure 22C**), a "Y-shaped" region of PA enhancement can be seen converging at the tumor, which is suggestive of PFHnDs in a large feeding vessel. **Figure 22D** shows an alternate view of this volume, where the curvature of the primary tumor in the mouse pelvis is more evident. Still, there is no obvious PA enhancement within the tumor, suggesting that particles have not appreciably accumulated within the stroma during this early timepoint. Unfortunately, this mouse expired shortly after the post-injection imaging session, and so 24-hour US/PA imaging could not be performed. After veterinary consultation, our working hypothesis is that the PFHnD injection within this mouse was too concentrated.

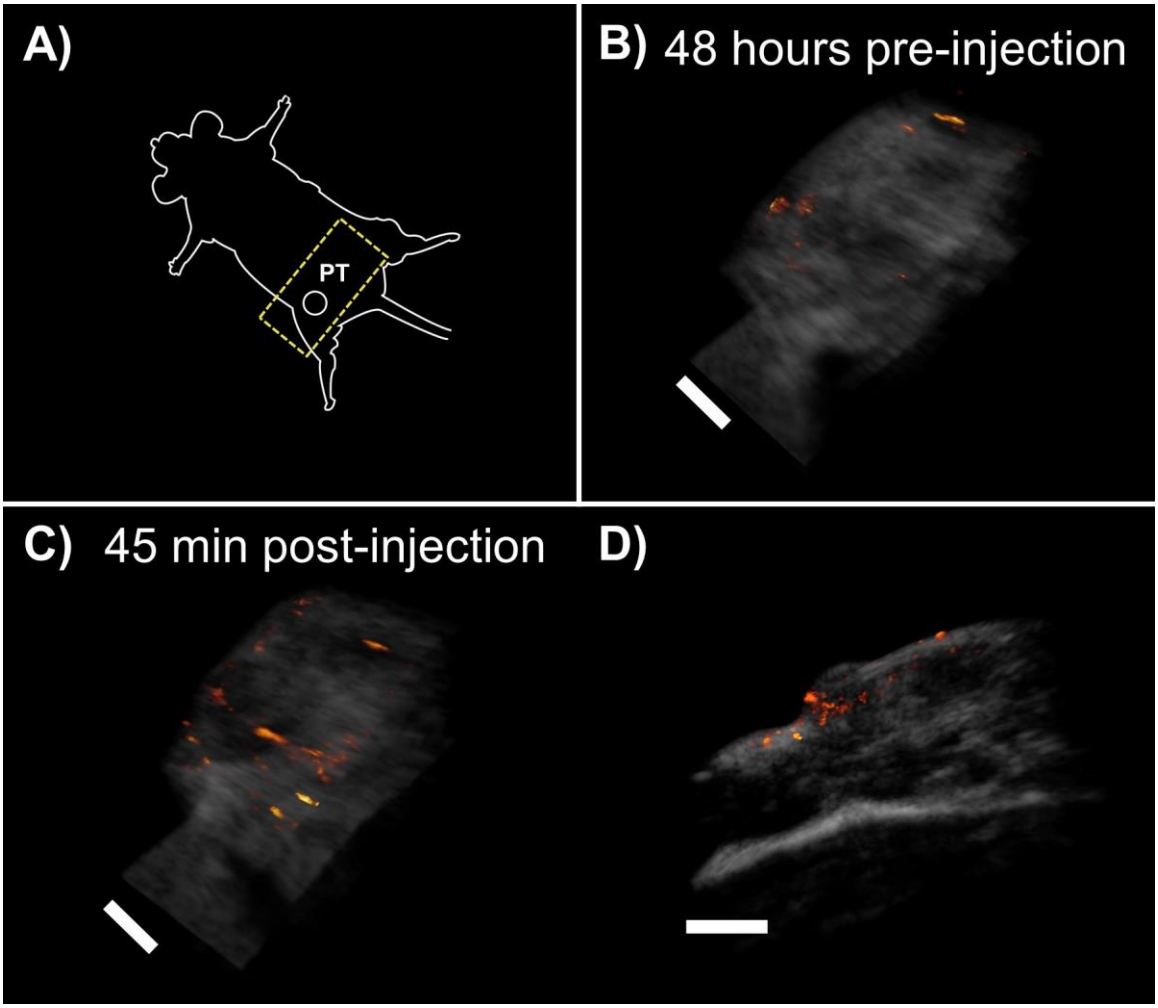

Figure 22: US/PA imaging volumes from a targeted PFHnD injected 4T1 syngeneic mouse. This mouse was microdosed with 40 mg/kg losartan for 7 days prior to IV injection with anti-EpCAM PFHnDs. **A)** Cartoon showing the primary tumor (PT) location and supine of the mouse for imaging. The yellow dashed lines approximate the volumes shown; **B)** Masked PA signal (red-orange) overlaid with the corresponding US volume 48 hours before targeted PFHnD injection; **C)** Masked PA signal overlaid with US obtained 45 minutes after targeted PFHnD injection along with an alternate view (**D**). These post-injection volumes show subepidermal enhancement in a channel running towards the tumor, possibly corresponding to a feeding vessel. This mouse expired 2 hours after post-injection imaging. Scale bars are approximately 5 mm.

Figure 23 shows histology obtained from non-perfused tissue that was immediately resected and flash frozen after the 4T1 mouse from **Figure 22** expired. Again, PFHnDs were doped with Cy5 fluorophore. The representative section of the spleen in **Figure 23B**

shows high enhancement from the Cy5 channel surrounding structures that resemble follicles in what should thus be the periarteriolar lymphoid sheaths. It is unclear whether the circular lesions noted throughout the spleen are due to PFHnD bioeffects or artifacts of the sample preparation. Though the spleen histology confirms successful systemic administration of the PFHnD bolus, the primary tumor histology lacks appreciable Cy5 enhancement (**Figure 23C**). Given the short timepoint of organ collection, it remains unclear whether this lack of tumor enhancement is due to lack of sufficient time for particle accumulation or inability of particles to traffic into the tumor stroma through endothelial fenestra in tumor neovessels.

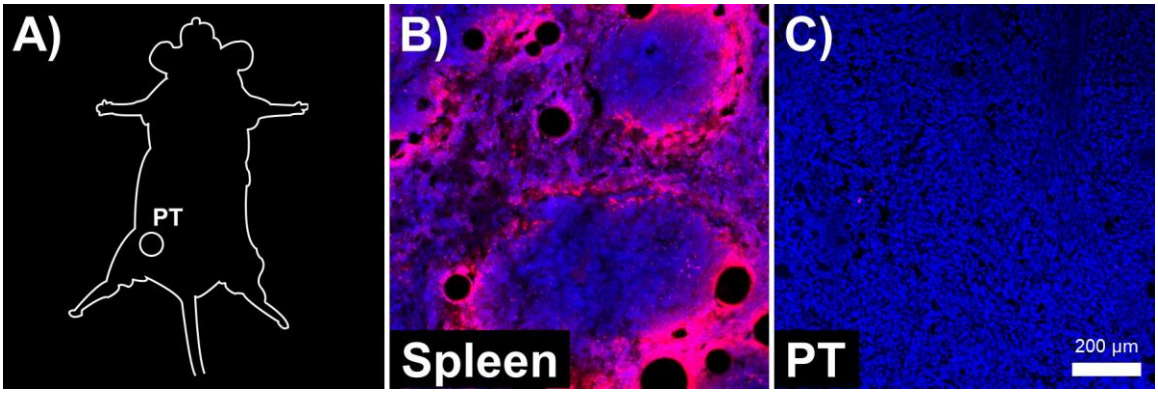

Figure 23: Representative histology from a 4T1 syngeneic mouse 2 hours after IV injection of EpCAM-targeted PFHnDs. This mouse received 7 days of 40 mg/kg losartan microdosing prior to PFHnD injection. Sections were stained with DAPI (blue). **A)** Cartoon diagram of the primary tumor location in the right fourth mammary fat pad; **B)** Section of the spleen showing strong enhancement in the Cy5 channel surrounding structures resembling follicles. The full dynamic range was used for displaying the Cy5 channel; **C)** Section of the primary tumor showing minimal enhancement from the Cy5 channel. Scale bar is 200 µm.

Data from other unsuccessful attempts to generate appreciable PFHnD extravasation, likely due to poor delivery, can be found in **APPENDIX D**. Supplemental Data for Nanodroplet Extravasation Studies. Ongoing studies will seek to achieve more consistent

IV delivery of PFHnDs and to optimize the injected dose. It is also likely that to promote extravasation, we will need to redouble efforts to reduce the average diameter of targeted particles. After bioconjugation, the targeted PFHnDs used in these preliminary studies ranged from 400 to 600 nm in average diameter, as measured by DLS. This size range may be too large to extravasate, even with reduction of tumor solid stress. Estimates of the pore cutoff size in 4T1 tumors, for example, are on the order of 250 nm.[206]

For the time being, PFCnD extravasation remains the "White Whale." Nonetheless, the animal models and drug regimens that we have implemented here chart a path forward towards addressing this experimental challenge in a good-faith way that will have clear translational potential, unlike the efforts in non-orthotopic graft models that have predated our preliminary studies. We hope that with further refinements in PFHnD synthesis, detection, and imaging along with greater experience in these animal models, we will continue to make progress in this defining experimental application within the field of phase-change contrast agent research.

5.3 On-Particle Fluorescence Resonance Energy Transfer to Assess Tissue for Intact Perfluorocarbon Nanodroplets

5.3.1 Abstract

Perfluorocarbon nanodroplets (PFCnDs) are a class of phase-change contrast agents for use in contrast-enhanced ultrasound and photoacoustic (US/PA) imaging. These agents were initially designed to overcome the chief barrier preventing gas microbubbles, the main contrast agent in US, from being used for contrast-enhanced imaging in the extravascular space: the relatively large (i.e., 1 μm+) size of these particles. Prior to user-

initiated activation into microbubbles *in situ*, PFCnDs are stable at submicrometer sizes. Therefore, contrast-enhanced US/PA imaging marries the biological diffusion characteristics of a small particle with the imaging contrast enhancement afforded by a large particle. Amongst researchers in imaging science, the hope was that these combined properties would facilitate the use of PFCnDs for contrast-enhanced imaging of primary solid tumors. An intravascular bolus of submicrometer PFCnDs could theoretically extravasate through fenestra in tumor neovasculature prior to activation for imaging within the tumor stroma. However, despite two decades of research, researchers have failed to conclusively demonstrate that PFCnDs accumulate in the tumor stroma in a realistic model of orthotopic neoplastic disease. One of the many challenges in this endeavor is conclusively proving that intact PFCnDs are spatially located in the intravascular space. Histology is the gold standard interrogating the tumor microarchitecture, and fluorescent tags can be incorporated into PFCnDs to visualize them on histology. Unfortunately, fluorescent tags are a secondary marker of PFCnDs, at best. Confocal microscopy of a fluorescent tag cannot differentiate intact PFCnDs from either digested PFCnD components or residual *in situ* nanomicelles. In response to this challenge, we have developed a new class of dual-labelled PFCnDs that exhibit on-particle fluorescence resonance energy transfer. Because the donor and acceptor fluorophore are spatially isolated within different layers of the nanodroplet, these particles should only exhibit resonance transfer in an intact state. As such, FRET signal on confocal microscopy can be used as a sensitive marker of intact PFCnDs on histology. Here, we demonstrate successful resonance transfer in dual-labelled particles compared to matched controls. These

characterization studies pave the way for the implementation of this dual-labelled PFCnD platform in the assessment of PFCnD biodistribution in models of cancer and beyond.

5.3.2 Introduction

Gas microbubbles are the clinically approved and predominantly used contrast agents for contrast-enhanced ultrasound imaging. Although microbubbles are strong US reflectors, and thus efficient US contrast agents, their relatively large (i.e., 1 μm+) size effectively prohibits their use in extravascular imaging. Microbubbles are too large to extravasate through endothelial fenestrations in cancer neovasculature, and they are too large to traffic within lymphatic vessels or the interstitium in times permissive of clinical imaging. In response to the size restrictions of microbubbles in these biological applications, perfluorocarbon nanodroplets (PFCnDs) were developed.[41,42,53,59,77,78,81,86,118] Perfluorocarbon nanodroplets are structurally similar to gas microbubbles, but they contain a fluoroalkane core that is maintained in a liquid state at physiological temperatures.[51,118] As such, PFCnDs are stable in the liquid-cored state at submicrometer sizes, which affords them enhanced biological stability and superior transport characteristics compared to microbubbles. Liquid-cored PFCnDs do not produce perceptible enhancement on US imaging. However, when exposed to a pulse of acoustic or optical energy, the core of the PFCnD undergoes a phase transition to the vapor state, effectively creating microbubbles *in situ*.[41,53] These vaporized PFCnDs provide contrast in a similar manner to traditional microbubbles. Further, if the phase transition was initiated by a laser pulse, then the initial vaporization event of the particles also generates contrast on photoacoustic imaging.[53] Optically-activated PFCnDs have been used for super-resolution[57,100] and molecular contrast-enhanced ultrasound and photoacoustic (US/PA) imaging,[57,146] and they have been

used to highlight transport phenomena within lymphatics,[58,77,146] post-blood-brain-barrier brain,[207,208] and the reticuloendothelial system.[53,77,103,146] Still, the "White Whale" of PFCnD research remains the imaging of nanodroplet extravasation in primary tumors.

Historically, PFCnDs were developed to facilitate US imaging of intravascularly delivered particle accumulation within the tumor stroma. After systemic administration, the submicrometer size of PFCnDs should theoretically allow them to extravasate through the relatively large inter-endothelial cell gaps in cancer neovessels. However, despite over two decades of active investigation, imaging researchers have yet to conclusively to demonstrate the aforementioned paradigm in a realistic, orthotopic model of primary cancer. Recently, one group demonstrated retention of fluorescent signal within a primary tumor in the mouse flank 48-hours.[194] However, this study demonstrates critical flaws that have continued to propagate within PFCnD extravasation research to date. First, it utilizes a contrived animal model, a nude glioblastoma multiforme flank xenograft, that does not recapitulate the presentation of known human neoplastic disease. Glioblastoma multiforme is innately hypervascular,[209] but it almost never metastasizes outside of the central nervous system.[210] Second, this study relies on fluorescent signal from a secondary tag to serve as a proxy reporter of PFCnD accumulation. Although fluorescence on histology is a gold standard for assessing PFCnD biodistribution, it can fall victim to inherent confounding. Because the fluorescent tag on the PFCnDs is a secondary marker, it can report false positive results. This is because the read-out of fluorescence is agnostic to the underlying structure of the particle containing the fluorescent tag. Fluorophores contained within intact PFCnDs, digested or non-functional PFCnDs, perfluorocarbon-less residual nanomicelles, and free fluorophores all appear equivalent on both IVIS imaging and confocal imaging of

tissue sections. Even super resolution microscopy does not have sufficient spatial resolution to distinguish amongst these functionally unique, submicrometer entities.

To address the absence of a gold standard to identify intact PFCnDs, we propose a novel dual-labelled PFCnD construct. This particle contains two fluorophores in unique spatial locations: one within the hydrophobic layer of the phospholipid shell and the other within the fluoroalkane core. The spectral characteristics of these two fluorophores are such that they can exhibit on-particle fluorescence resonance energy transfer (FRET). When a fluorophore absorbs a photon, it enters an excited energy state, after which it returns back to the "ground" state and emits a photon in return. However, due to energy lost as heat during this process, the emitted photon has a longer, "red-shifted" wavelength. [Consider E=hv eqn] If another fluorophore in close proximity has an absorption spectrum containing this second photon, then the photon could be absorbed by this second fluorophore. The fluorescent process would then begin again, resulting in the emission of an even further red-shifted photon. This describes the process of FRET sensitized emission.[211]

Because the two fluorophores in our construct occupy unique locations within the particle, we should only observe FRET sensitized emission if the particle is intact. All FRET phenomena are highly dependent upon close spatial proximity of the "donor" and "acceptor" fluorophores. The "Förster distance" at which efficient FRET is possible is defined by the spectral overlap of the donor and acceptor molecules as well as their molecular orientation,[212] and this distance is typically on the order of 1-10 nanometers.[213] In our construct, the acceptor fluorophore is soluble within the fluoroalkane core. Any construct without fluoroalkane, such as a nanomicelle or digested PFCnD, would not be

capable of sensitized emission. Therefore, the FRET sensitized emission is an indirect functional marker of intact particle status.

Here, we present proof-of-principle studies that characterize the developed FRET nanodroplets. We demonstrate the on-particle sensitized emission phenomenon and compare these nanodroplets to a control complement. These results lay the groundwork for ongoing efforts to use on-particle FRET nanodroplets to characterize particle distribution within histological sections and whole organ preparation.

5.3.3 Materials and Methods

SQ650 Dye Synthesis

The squarylium dye, SQ650, was synthesized by Vadakkancheril S. Jisha, Ph.D. In brief, squaric acid (0.34 g, 6 mmol) and 2,3,3-trimethylindolenine (1.9 g, 5.9 mmol) were heated under reflux for 3 hours in a mixture of 60 ml of n-butanol/toluene (4:1, v:v) containing 1.5 ml of quinoline. Water was removed azeotropically using a Dean-Stark trap. The reaction mixture was then cooled to room temperature. The precipitated crude products were separated by filtration and washed with n-hexane. The product was further characterized by ^{1}H NMR and ^{13}C NMR.

Fluorescent Nanodroplet Synthesis

One micromole (10^{-6} mol) of DSPC and DSPE-mPEG2000 (both from Avanti Polar Lipids, Inc.) in a 1:9 molar ratio was extracted from chloroform aliquots and added to a 10 mL pear-shaped flask (Aldrich). For Cy3-positive batches, 30 µL of Cy3 carboxylic acid (Lumiprobe) from a 1 mg/mL chloroform aliquot were added. An additional 400 µL

of HPLC-grade chloroform were added to the flask to ensure the formation of an even lipid cake. The pear-shaped flask was covered in aluminum foil and placed into a rotary evaporator with a water bath (R-215, V700, and V-855 with B-491; Buchi) and water-cooled condenser and evaporated for 30 minutes, adhering to the "20/40/60" rule. After this, the solid isolate was further dried under nitrogen flow for a minimum of 20 minutes in order to evaporate all residual chloroform in the lipid cake.

Next, the solid reagents were hydrated with 1 mL of 7.40 pH PBS and homogenized using a water bath sonicator (1800 Series Ultrasonic Cleaner; Branson) for 5 minutes at room temperature to produce a solution of dye-loaded nanomicelles. This solution was centrifuged at 300 rcf for 1 minute and 900 µL of the nanomicelle-containing supernatant was combined with 100 µL of PBS in a 2-dram glass scintillation vial (VWR). To this solution, 50 µL of either pure perfluorohexane (FluoroMed, L.P.) or, for SQ650-positive batches, a 1:1 homogenized mixture of perfluorohexane (PFH) to trifluorotoluene (TFT) was added. To make the 1:1 PFH:TFT mixture, 10 mg of SQ650 dye was dissolved in 1 mL of α,α,α,-trifluorotoluene (Sigma-Aldrich). An equal volume (1 mL) of PFH was added to this solution, and the mixture was vortexed until homogenous prior to use.

The glass vial containing the 50-µL fluoroalkane bolus and nanomicelles was placed into an ice bath and allowed to rest for 5 minutes. Then, this solution was probe sonicated in the ice bath with a 1/8" microtip (QSonica) at 1% power (1s on, 15s off, 5 times) in order to produce a stock solution of fluorescent PFCnDs, which was stored at 4°C in amber glass prior to use.

Prior to their use, 100 µL of the fluorescent PFCnD stock were diluted in 2 mL of PBS and bath sonicated for 2 minutes. This solution was then centrifugated at 3000 rcf for 5 minutes in order to pellet the fluorescent PFCnDs. The supernatant was removed and the PFCnDs were reconstituted in 1 mL of PBS.

All of the previously described synthesis steps were performed in darkness to minimize photobleaching of the fluorophores.

Fluorimetry

Fluorimetry was performed using a Fluorolog-3 Model FL3-21 spectrofluorometer (Horiba Instruments Incorporated) housed within the Center for the Science and Technology of Advanced Materials and Interfaces (STAMI) at the Georgia Institute of Technology. After allowing the Peltier cooling element for the detector to reach -20°C, 1 mL of fluorescent PFCnD sample, prepared as described previously, was added to a four-walled glass cuvette and diluted with 2 mL of PBS. Measurements of free fluorophores were performed with chloroform as both solvent and diluent.

FluorEssence software was used to optimize the acquisition parameters and correct the measured fluorescent spectrum. Slit widths on the spectrofluorometer were adjusted to achieve a minimum count per second rate of 10^5 at the detector. Typically, the slit widths at excitation and detection wavelengths were set equally between 3 and 5 nm.

Samples were excited at either 540 nm or 640 nm, as denoted in the results, and emission spectra began acquiring at a minimum of 20 nm red-shifted from the excitation center wavelength.

OPJ files containing the fluorescent spectra were downloaded for offline analysis. Files were opened in Origin Viewer (OriginLab), tabular spectra were converted into CSV format, and these spectra were ultimately plotted for display in R (R Core Team) using the ggplot2 data visualization package.

5.3.4 Results and Discussion

One of the canonical donor-acceptor pairs for FRET sensitized emission is Cyanine 3 (Cy3) and Cyanine 5 (Cy5). For our on-particle FRET nanodroplets, we have elected to replace the acceptor Cy5 with the squarylium dye, SQ650. This class of dye has demonstrated biocompatibility for image-guided *in vivo* applications, such as photodynamic therapy.[214,215] The SQ650 dye has similar absorption and fluorescent emission characteristics to Cy5 and is thus a reasonable substitute to couple with Cy3 for these FRET nanodroplets (see **APPENDIX E**, **Figure 47**).

In order for the FRET sensitized emission in these particles to be a true reporter of their intact state, the donor and acceptor must occupy two spatially unique locations within the particle that will not associate upon particle destruction. Within PFCnDs, the two main components that occupy distinct locations are the fluoroalkane core and the amphipathic surfactant shell. Fluoroalkanes have poor solubility in both hydrophobic and hydrophilic materials, and thus they should not associate with shell components upon particle destruction. In order to incorporate a fluorophore within the shell of phospholipid shelled PFCnDs, the most logical design choice is to increase its hydrophobicity such that it preferentially associates with the hydrophobic fatty acid tails. Cyanine 3 carboxylic acid (Cy3CA) is non-reactive and hydrophobic, making it an ideal candidate to incorporate into

the lipid shell of PFCnDs. Being dissolved into phospholipid does not affect the ability of Cy3CA to fluoresce (**Figure 24**).

To incorporate a second fluorophore into the fluoroalkane core of PFCnDs is a more challenging proposition. Previous studies have shown that dyes must be highly fluorinated relative to their total mass (50%+ wt% F) in order to be soluble in fluoroalkanes.[216,217] The SQ650 dye is not fluorinated, though ongoing efforts are working to modify the indolyl groups with linear fluoroalkanes in order to reach the critical percentage weight of fluorine to achieve standalone solubility. In the interim, a double emulsion is necessary in order to achieve a PFCnD construct with core-soluble SQ650. Trifluorotoluene (TFT) is a hydrofluorocarbon in which SQ650 is readily soluble. When mechanically homogenized with perfluorohexane (PFH), TFT forms a stable emulsion that can serve as a proxy for the pure typically PFH used in PFHnD synthesis. Additionally, the TFT:PFH emulsion does not compromise the ability of SQ650 to fluoresce, as shown in **Figure 24**.

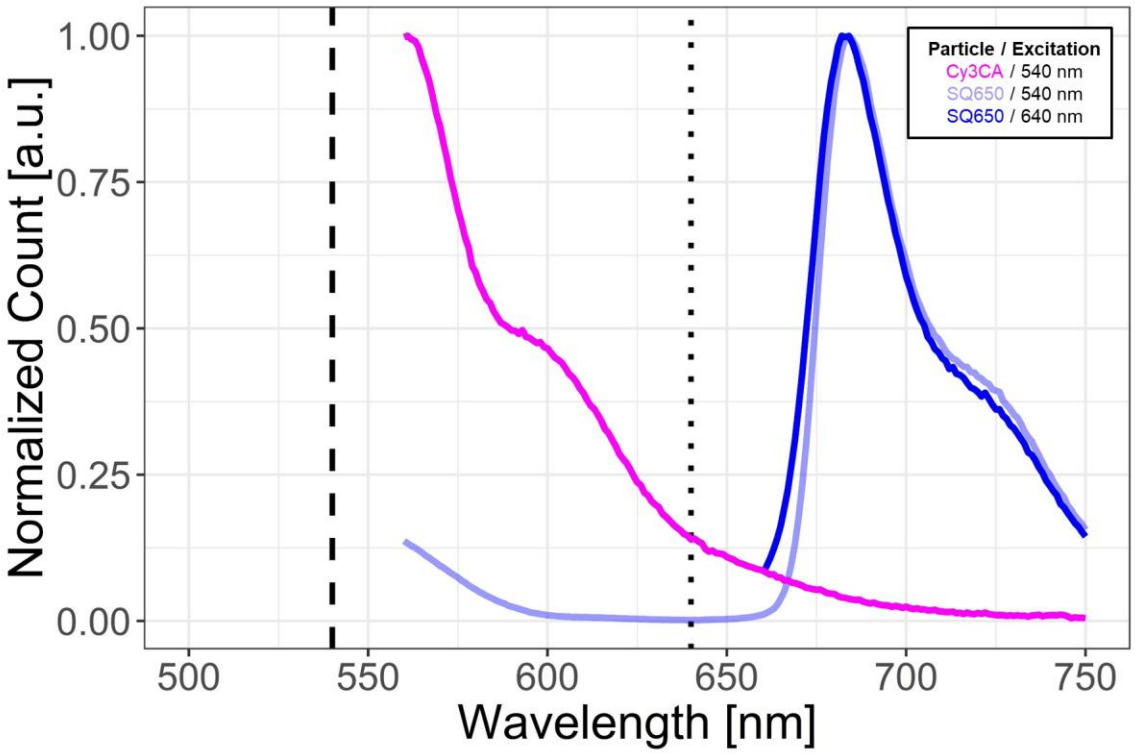

Figure 24: Fluorimetry of individual fluorophores used in FRET particles. Cyanine 3 carboxylic acid (Cy3CA) containing nanomicelles (pink) dilute in PBS were measured using 3-nm excitation and emission slit widths. Free SQ650 dye in a 1:1 (v:v) emulsion of trifluorotoluene and perfluorohexane was measured using 5-nm excitation and emission slit widths. Excitation wavelengths for each measurement were as noted in the legend. The excitation lines at 540 and 640 nm are noted on the fluorescence spectrum with dashed and dotted lines, respectively. Each spectrum was normalized to its own maximum value.

A major potential source of confounding in a FRET sensitized emission setup is nonspecific activation of the acceptor fluorophore from the donor excitation wavelength. The SQ650 dye only marginally absorbs within the region of wavelengths that would be used to excite the Cy3CA donor. Nonetheless, because of the high local fluences generated by confocal microscopy, it is still prudent to assess nonspecific donor activation for this FRET implementation. Indeed, fluorimetry of SQ650 within a 1:1 TFT:PFH emulsion exhibits qualitative nonspecific activation when excited at 540 nm (**Figure 24**). However,

it is important to note that fluorimetry of free dye in bulk emulsion is likely not indicative of the response of dye within the proposed nanodroplet construct.

To perform a more fair assessment of the nonspecific activation of SQ650, we obtained fluorimetry measurements on PFCnDs containing SQ650 in the core of the construct. Using the same PFCnD population, we recorded fluorescence emission spectra after both specific (640 nm) and nonspecific (540 nm) excitation. As displayed in **Figure 25**, nonspecific activation is approximately an order of magnitude weaker than specific activation from excitation within the main absorbance spectrum of SQ650.

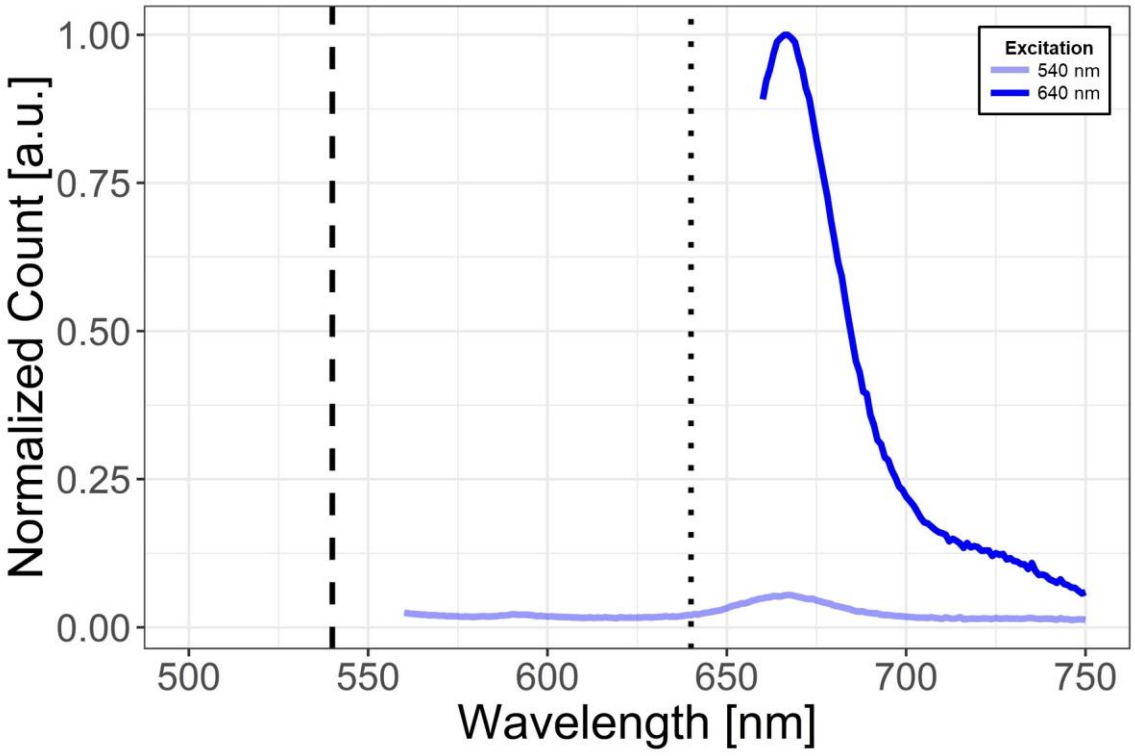

Figure 25: Fluorimetry of SQ650-containing nanodroplets. Nanodroplets were diluted in PBS and excited for measurements as noted in the legend. The excitation lines at 540 and 640 nm are noted on the fluorescence spectrum with dashed and dotted lines, respectively. Both measurements were performed on the same sample using 5-nm excitation and emission slit widths. The spectra were normalized to the maximum value from the 640-nm excitation spectrum.

Next, we assessed the fluorescence emission spectrum of PFCnDs containing both Cy3CA in the particle shell and SQ650 in the core (**Figure 26A**). First, we assessed excitation at 540 nm, well within the donor excitation spectrum of Cy3CA. The resulting emission spectrum displays the characteristic shouldered emission spectrum of Cy3CA, meaning that the excitation of the donor is not fully quenched by the encapsulated SQ650 acceptor. However, this emission spectrum does contain the characteristic emission peak of SQ650. In comparison to the emission observed upon excitation by 640 nm, the 540-nm induced SQ650 emission is roughly one-third that observed on specific activation of the acceptor. Although we cannot rule out some nonspecific activation of the acceptor, this ratio of peak acceptor emission signal, versus the ratio observed in **Figure 25**, implies that some FRET sensitized emission is occurring within the dual-labelled PFCnDs.

We also compared the emission spectrum of FRET nanodroplets to spectra of single-fluorophore and no-fluorophore controls (**Figure 26B**). The Cy3CA-only PFCnDs do not display a peak in the region of the SQ650 acceptor, ruling out any nonspecific contributions from the emission of the donor in the dual-fluorophore PFCnD results. Additionally, the SQ650-only PFCnDs display a lower peak fluorescence emission than the dual-fluorophore PFCnDs when excited at 540 nm, providing further evidence of sensitized emission from the dual-fluorophore particles. Lastly, PFCnDs without any encapsulated fluorophores emit only marginal signal upon fluorimetry.

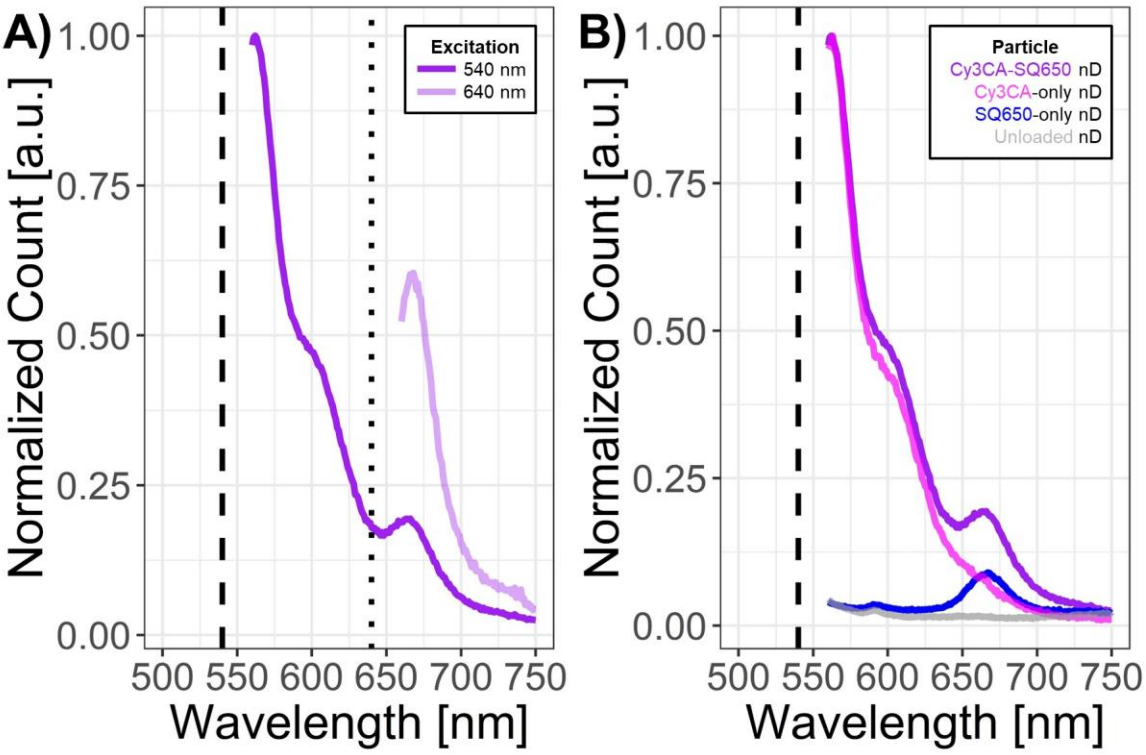

Figure 26: Fluorimetry of FRET nanodroplets and controls. A) Fluorescence spectrum from Cy3CA and SQ650-containing nanodroplets diluted in PBS and excited with 540-nm (purple) and 640-nm (light purple) light. The excitation lines at 540 and 640 nm are noted on the fluorescence spectrum with dashed and dotted lines, respectively. The dual-fluorophore particles display evidence of resonance transfer; **B)** Fluorescence spectra of FRET nanodroplets as well as single and no-fluorophore nanodroplet controls. The excitation line at 540 is noted on the spectra with a dashed line. All spectra were acquired with 5-nm excitation and emission slit widths and were normalized to the maximum value from the FRET nanodroplet spectrum, except for the Cy3CA nanodroplet spectrum, which was acquired using 3-nm excitation and emission slit widths and self-normalized.

The dual-labelled PFCnDs reported here demonstrate sensitized emission upon donor excitation. However, more work is necessary to enhance this phenomenon so that it is reliable enough to be utilized in applications involving confocal and gross fluorescence imaging. It is possible that the double emulsion necessary to synthesize the PFCnDs presented here is restricting donor fluorophores from absorbing photons emitted from acceptor fluorophores. Efforts to solubilize SQ650 in PFH via fluoroalkane conjugation will allow the creation of dual-labelled PFCnDs via a single emulsion synthesis method.

This will allow for a greater amount of SQ650 acceptor fluorophore to be dissolved within the core of these PFCnDs, and the use of pure PFH in the core will impose less spatial restriction on the acceptor fluorophores. Sensitized emission will only occur within the Förster distance of the donor-acceptor pair, which should restrict this phenomenon to the outer core of the PFCnDs near the surfactant shell. Upon ideal donor synthesis, additional optimization of the donor-acceptor ratio will also be necessary to assure quality sensitized emission.

The class of on-particle FRET PFCnDs presented within this study could eventually be used to report on the intact state of the nanodroplets in tissue for both tumor delivery as well as other applications that require knowledge of functional biodistribution and clearance. FRET sensitized emission could be detected in whole organs *in vivo* or *ex vivo* via IVIS or fluorescence tomographic imaging, given an appropriate filter set. Many commercial confocal systems also include spectral unmixing software to facilitate high resolution FRET measurements on histology sections, as well.[218,219] Knowledge of intact particle distribution is critical for successfully developing US/PA image-guided diagnostic and therapeutic approaches using PFCnDs, the *in vivo* characteristics of which remain largely understudied. This class of dual-labelled PFCnDs provide a compelling avenue for addressing this critical gap in the field of phase-change contrast agent development.

CHAPTER 6. CONCLUSIONS AND FUTURE DIRECTIONS

6.1 Optimization of Synthesis and Detection

In Aim 1, we developed a new approach to synthesize small, monodisperse PFHnDs. By increasing the amount of PEGylated lipid within the phospholipid shell of PFHnDs, we were able to achieve a stable size reduction over time courses relevant to incubation steps that are necessary for the diagnostic and therapeutic functionalization of these particles. In phantom studies, we determined that increased PEGylation also increases the observed US/PA contrast as compared to equivalent stock dilutions of PFHnDs from a more traditional low-PEG formulation. Furthermore, we implemented a new imaging sequence based on ultrafast pulse inversion imaging to enhance the detection of US contrast created by optically triggered PFHnDs. We then demonstrated the advantages of this sequence relative to traditional ultrafast plane wave imaging both in phantoms and *in vivo* in a murine spleen.

From our synthesis studies, it remains unclear if the ratio of lipids in the stock, either per particle or per injected bolus, is equivalent to the initial bulk ratio. Providing quantitative evidence for this is further complicated by the fact that mass spectrometry techniques are confounded by the ionized solvents necessary to form stable lipid particles. Additionally, our data showed a non-linear effect of shell PEGylation on size reduction, but we did not completely characterize this phenomenon or establish a critical point where this effect begins to wane appreciably. Moreover, it would be interesting to see if combining this strategy with increased acyl chain length has a synergistic effect on PFCnD size reduction without compromising the ability to vaporize the agent to create US/PA

contrast. There are many potential avenues for further investigation into synthesis optimization based on shell composition alone.

Critically, it will be necessary to develop phantoms or setups that better recapitulate the biological environment in order to truly assess the impact of design changes on PFCnD size and stability for downstream preclinical applications. Although PFCnDs are constantly touted for their increased stability relative to microbubbles, particle stability still appears to be an issue *in vivo*. Spontaneous vaporization of PFCnDs *in vivo* is an underreported phenomenon in the field of US contrast agent development. The majority of optimization studies are performed *in vitro*, and the *in vivo* environment presents a host of additional challenges to particle size and stability, such as protein adsorption, opsonization, biological breakdown, and clearance.

From our imaging sequence studies, it will be necessary to compare the imaging contrast afforded by our pulse inversion sequence to sequences that take advantage of enhanced frame rates and/or angular compounding. It is possible that an optimal imaging sequence may need to include both pulse inversion and angular compounding, but the temporal resolution necessary to capture PFHnD dynamics places a stringent restriction on the minimum necessary frame rate for these sequences to be effective. Moreover, from the *in vivo* studies presented in this dissertation, it is obvious that there are a host of confounding phenomenon that can mimic the temporal dynamics and enhancement expected from PFHnDs. More work is necessary to integrate the US and PA effects of optically triggered PFHnDs to better isolate these agents from background, especially in sparse concentrations. Specific *in vivo* detection of PFCnDs remains an active area of research.

6.2 Lymphatic Imaging and Therapeutic Applications

In Aim 2, we utilized the PFHnDs developed in 3.1 to investigate lymphatic drainage in both naïve and tumor-bearing mice. During this process, we developed a computationally simple post-processing algorithm in order to leverage the unique US and PA contrast enhancement of optically triggered PFHnDs to highlight regions with a high probability of containing these agents. Our *in vivo* studies highlighted the ability to track PFHnDs draining through regional lymphatics longitudinally over the course of 24 hours. Histology obtained at 24 hours confirmed the draining path of the PFHnDs ipsilateral to the initial subcutaneous injection site. To our knowledge, this study is the first report of the longitudinal imaging of a single injected bolus of a phase-change US/PA agent. Additionally, we developed a new class of adjuvant-carrying PFHnDs that could be implemented for US/PA image-guided immunotherapy and demonstrated the ability of these particles to stimulate antigen presenting cells *in vitro*.

In terms of the *in vivo* detection of these agents, imaging sensitivity remains a great challenge. Confounding signal from the skin and deep structures, such as the large intestines, presents a huge challenge to specifically identifying optically triggered PFHnDs. One potential long-term solution to this is the development of more efficient photoabsorbers. We have observed contrast enhancement in our experimental workflow using PFHnDs without encapsulated near-infrared dye (see **APPENDIX B**, **Figure 33** and **Figure 34**), suggesting that either our optical fluence is high enough to induce perfluorohexane vaporization alone or that the observed enhancement is not due to particle vaporization. The study of submicrometer PFHnD laser interaction is complicated by the diffraction limit of optical imaging methods, so it is impossible to know which hypothesis

is more likely. However, in the former case, a more efficient absorber would allow the use of a lower fluence in US/PA imaging, which could minimize confounding enhancement from endogenous absorption. Sono-photoacoustic imaging,[82,220,221] which synchronizes the laser pulse with the rarefactive phase of a focused ultrasound pulse, may be another avenue to achieve contrast enhancement from optically-triggered PFHnDs with a lower fluence and less endogenous enhancement.

More immediately, future work related to the presented longitudinal data will focus on optimizing data processing. The masked PA data shown were the result of a median filter applied to the enhancement results from all six laser pulses acquired at each plane. This step was intended to suppress nonspecific signal that may be decorrelated. However, given the persistence of obviously correlated endogenous absorption, it may be necessary to use other techniques, such as compounding, to enhance exogenous signal from PFHnDs relative to background. Additionally, it will be necessary to acquire saline-injected controls in order to better characterize confounding signal from endogenous sources and dye-independent PFHnD absorption.

Furthermore, these longitudinal *in vivo* studies have revealed bioeffects from the subcutaneous administration of PFCnDs that are yet unreported in the literature. Hours after injection, we observed a reflective bolus near the initial injection site in all mice imaged within 4.1 (see **APPENDIX B**, **Figure 28**). The cause of this phenomenon is unknown. Possible explanations are spontaneous vaporization of injected particles, aggregation of injected particles, diffusion of oxygen into the fluoroalkane core of particles, or side effects from a local inflammatory response. More investigation is necessary to elucidate the mechanism of this consistently observed effect.

For the adjuvant-containing pICnDs, the immediate future will bring further optimization and enhanced characterization. The shell composition of these particles likely requires optimization in order to bind the maximum amount of poly(I:C) without compromising membrane stability. The current level of adjuvant binding, as assessed by our *in vitro* Griess assay, is unlikely to be sufficient to generate an effective T_H1 response *in vivo*. A fluorescent-tagged poly(I:C) can be used during incubation to provide a more quantitative assessment of adjuvant binding than zeta potential measurements. Additionally, once the formulation is finalized, it will be necessary to perform an ELISA for IL-12 to ensure that pICnDs are appropriately stimulating APCs to enact a T_H1, and not T_H2, response.

The scale up of pICnDs to an *in vivo* setting will introduce a host of additional challenges. First, delivery of sufficient adjuvant to the TDLN, without inciting excessive nonspecific inflammation, will need to be confirmed. Then, it will be necessary to assess the cellular response of the TDLN. Ultimately, we will need to demonstrate that pICnD delivery induces the activation of a critical amount of CTLs. Characterizing this cellular response will require an appreciable amount of lymph node cell isolation and characterization via flow cytometry. Only after an appropriate cellular response at the draining node is documented will we be able to probe the whether this immunotherapeutic approach is able to incite CTLs to train on tumor antigens to attenuate solid tumor growth and metastatic spread.

6.3 Extravasation Within Primary Breast Tumors

In Aim 3, we first engineered targeted PFHnDs via bioconjugation of thiolated antibodies to maleimide groups incorporated into the nanodroplet lipid shell surface. We demonstrated that this bioconjugation technique affords PFHnDs specificity for their appropriate molecular target *in vitro*. Next, we attempted to image targeted PFHnD extravasation *in vivo* in two immunocompetent, orthotopic small animal models of primary breast cancer. We also implemented an angiotensin receptor blocker microdosing regimen in order to reduce primary tumor solid stress, which should improve intravascular particle delivery. These approaches pave the way for successful and translatable results for the US/PA imaging of extravasated PFCnDs in the future. Lastly, we created a new class of PFHnDs that display on-particle FRET sensitized emission. These particles can provide a functional reporter of intact particle state, which can serve as a "gold standard" assay for PFHnD particle extravasation assessment. Altogether, these developments and approaches provide novel contributions to the field of phase-change contrast agent research.

The preliminary *in vivo* results presented in this dissertation reveal a multitude of areas for future work on this application. First, it will be necessary to improve the consistency of IV delivery via improved jugular injection technique and to determine the maximum tolerated dose of PFCnDs. Extravasation studies in other agents estimate that only 1% of the injected dose of IV particles will reach the tumor stroma.[222] Thus, the optimal injected dose will be a balance between safety and imaging sensitivity. As alluded to in 6.2, the sensitivity of US/PA imaging to optically triggered PFHnDs is still an active area of research. Improvements in the system, sequence, and post-processing should help balance the delicate calculus of considerations in determining the optimal injected dose.

Our approach to tumor microenvironment modulation may help increase the low delivery efficiency to primary tumors. However, we still need to characterize the effect of this regimen at the molecular level via histological analysis of primary tumor vasculature. The researchers who first reported this microdosing strategy performed a lectin injection and assessed tumor vessels for CD31 and lectin co-staining as a marker of perfusion.[191] Because those perfusion assessments were performed in xenograft models, it is unclear if the effects will directly translate when implemented in syngeneic models or GEMMs. It is likely that the losartan microdosing regimen will need to be altered to account for variability in the natural history of these different small animal models.

Additional work will likely be necessary to improve the probability of successful PFHnD extravasation. The targeted particles used for IV delivery within our preliminary *in vivo* studies ranged from 400 to 600 nm in average diameter. This is well above the empirically determined pore cutoff size for the 4T1 syngeneic model,[206] and it may also be too large for analogous GEMMs. From our *in vitro* studies in 5.1, we observed a large size increase after conjugation of monoclonal antibodies. This may be because of the physical size of the antibodies themselves, but it may also be due to other nonspecific phenomena, such as increased particle aggregation. The optimal resuspension protocol for bioconjugated PFHnDs may be different than that for naïve PFHnDs. If the antibody size is indeed the primary issue at hand, then alterative targeting moieties may need to be improved in order to achieve further size reduction of the targeted construct. The Functional and Molecular Imaging Research Laboratory at Dartmouth College has developed a currently unpublished directional method for creating targeted PFHnDs using purified antigen-binding fragments instead of the full monoclonal antibody. Their

approach, though highly labor-intensive, may be the best option for achieving molecular specificity to cancer markers while retaining small PFCnD size. It is worth noting, however, that directional methods based on those used for gold nanoparticles utilize a PEGylated bifunctional linker.[223] To avoid an unnecessary particle size increase by using a PEGylated element to connect the particle and fragment, it will likely be necessary to synthesize a small molecule linker with both requisite functional groups.

In terms of the various particles displayed in Aim 3, future work will continue the optimization of these agents. With targeted PFHnDs, we have demonstrated specificity for monoclonal-HER2-antibody targeted PFHnDs to HER2-positive cells *in vitro*; however, we have not performed this analysis for polyclonal-EpCAM-antibody targeted PFHnDs to 4T1 cells *in vitro*. It is possible that the polyclonal nature of the antibody clone we selected does not afford sufficient specificity to these cells. In this case, it will be necessary to find a monoclonal antibody to mouse EpCAM or to select an alternative molecular target, assuming we want to continue *in vivo* efforts in the high-throughput syngeneic 4T1 model.

For the on-particle FRET PFHnDs, additional development will be necessary to advance the platform. A fluoroalkane-soluble SQ650 dye will be especially critical. This will allow for the creation of dual-labelled PFCnDs from a single-emulsion method with enhanced acceptor fluorophore signal in each particle. Additionally, it will strengthen the assertion that the platform is sensitive to intact particle status. Unmodified SQ650 is soluble in organic solvents. As such, it may migrate to the hydrophobic shell layer of the dual-labelled particle formulation presented in this dissertation, despite physical isolation of the donor and acceptor fluorophores using the dual emulsion method. Upon creation and characterization of a fluoroalkane-soluble SQ650 dye in this construct, it will also be

necessary to characterize the loss of sensitized emission upon particle destruction. This feature of the construct is crucial to the assertion that FRET is a marker of intact status. Boiling samples of PFHnDs is one potential way of destroying the particles without destroying the fluorophores themselves.

Characterization of sensitized emission from *ex vivo* samples will be the last necessary step prior to the implementation of FRET PFHnDs in preclinical applications research. The spleen is a logical organ to assess via histology, as it is one of the primary reticuloendothelial organs responsible for clearing IV delivered PFCnDs. Spleen sections should provide samples with high concentrations of FRET PFCnDs to optimize the detection of FRET signal via spectral unmixing on confocal microscopy, which is not a trivial step for imaging intermolecular FRET pairs.

6.4 General

Perfluorocarbon nanodroplets are an intriguing class of contrast agents with a high upside for applications-based research. For these agents to gain traction, however, much more fundamental knowledge about their governing physics and behavior *in vivo* is necessary. Improved knowledge of the interactions between PFCnDs, ultrasound, and incident near-infrared photons will allow for the design of more biologically stable and imaging-responsive particles. Much of the current applications-based research conducted with PFCnDs involves intravascular studies that have already been performed, or could have been performed just as efficiently, with gas microbubbles. From an experimental design perspective, this is a logical and safe approach to research. Perfluorocarbon nanodroplets also have increased vascular circulation time as compared to microbubbles,[224]

so there is a minor upside to the direct substitution. However, if researchers are content to relegate applications of PFCnDs to the vascular domain, then the platform will surely fail to gain any traction outside of the ultrasound community. The extravascular capabilities of PFCnDs are what will ultimately set these agents apart and allow them to meaningfully expand the footprint of ultrasound utility. The studies presented in this dissertation are a beginning, not an end. It will require an appreciable concerted effort from a team of diverse and dedicated researchers to transform the visions set forth by these preliminary studies into fully executed realities. If this commitment is made, then I look forward to seeing the progress the field makes in the years to come.

APPENDIX A. SUPPLEMENTAL DATA FOR NANODROPLET SYNTHESIS STUDIES

Table 3: Z-Average [nm] versus time for 90:10 PFCnDs

Time [hr]	Minimum	First Quartile	Median	Third Quartile	Maximum
0	366	472	647	956	1085
0.5	443	538	591	736	1201
1	549	582	661	905	1202
2	536	595	662	825	950
3	544	667	750	865	1174
4	530	576	657	788	934
5	514	574	635	748	918
6	485	564	624	701	919

Table 4: Z-Average [nm] versus time for 50:50 PFCnDs

Time [hr]	Minimum	First Quartile	Median	Third Quartile	Maximum
0	162	169	178	194	213
0.5	199	204	208	211	218
1	219	221	227	242	275
2	236	242	248	250	252
3	250	257	260	263	265
4	266	270	273	274	277
5	273	278	284	285	291
6	280	289	295	300	306

Table 5: Z-Average [nm] versus time for 10:90 PFCnDs

Time [hr]	Minimum	First Quartile	Median	Third Quartile	Maximum
0	151	157	159	162	164
0.5	197	199	200	201	203
1	217	218	218	221	225
2	236	237	240	243	244
3	246	250	252	255	258
4	252	259	263	271	273
5	268	270	274	280	285
6	272	282	284	287	292

APPENDIX B. SUPPLEMENTAL DATA FOR IMAGING OF PERFLUOROCARBON NANODROPLETS TRAFFICKING IN LYMPHATICS

δ UFPI vs δ^2 UFPI Imaging

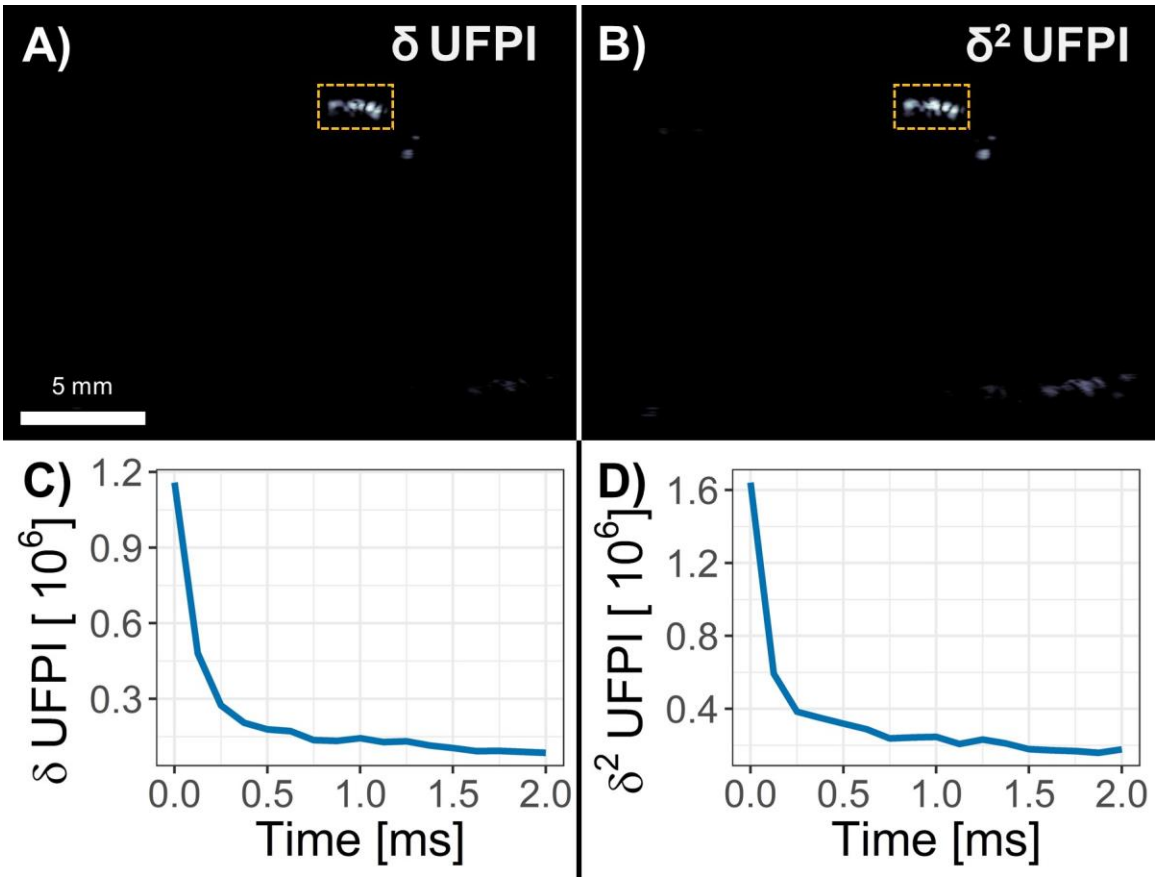

Figure 27: δ UFPI and δ^2 UFPI Images for a PFHnD-containing region of interest. Images correspond to the plane from **Figure 10**. The δ UFPI (**A**) and δ^2 UFPI (**B**) images are qualitatively similar. Further examining the region of interest (yellow-dashed box), the median linear signals as a function of time also display comparable temporal dynamics for both δ UFPI (**C**) and δ^2 UFPI (**D**) processing.

Representative Post-Injection Bolus

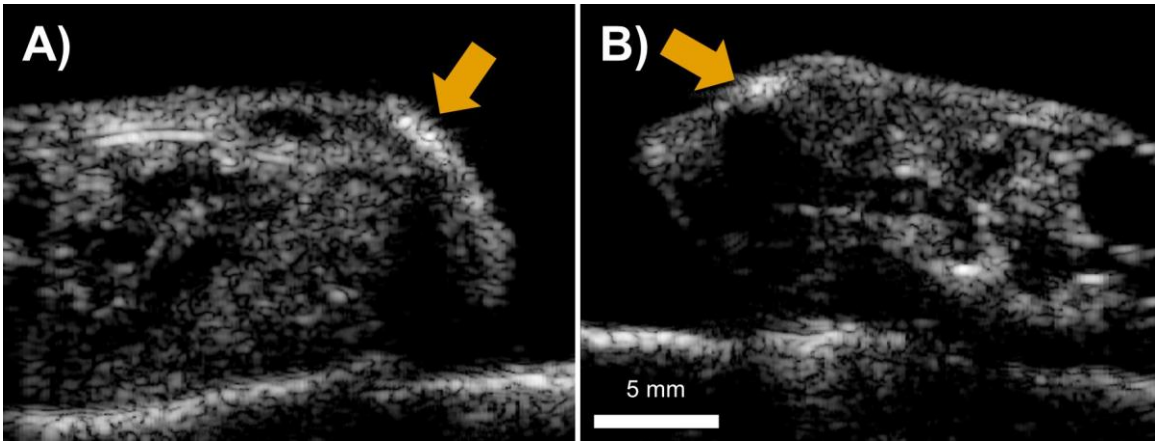

Figure 28: Representative B-mode images showing the development of injection-site boluses *in vivo*. Representative images (4T1 mouse 2; 6-hour timepoint) in left lateral decubitus (**A**) and supine (**B**) views show the formation of a reflective bolus (orange arrows) near the initial injection site. This is a consistently observed result hours after subcutaneous PFHnD administration. It remains unclear if this observation corresponds to spontaneous vaporization of PFHnDs, pooling of bulk perfluorohexane from broken-down PFHnDs, an inflammatory reaction, or another unknown phenomenon. Scale bar is 5 mm.

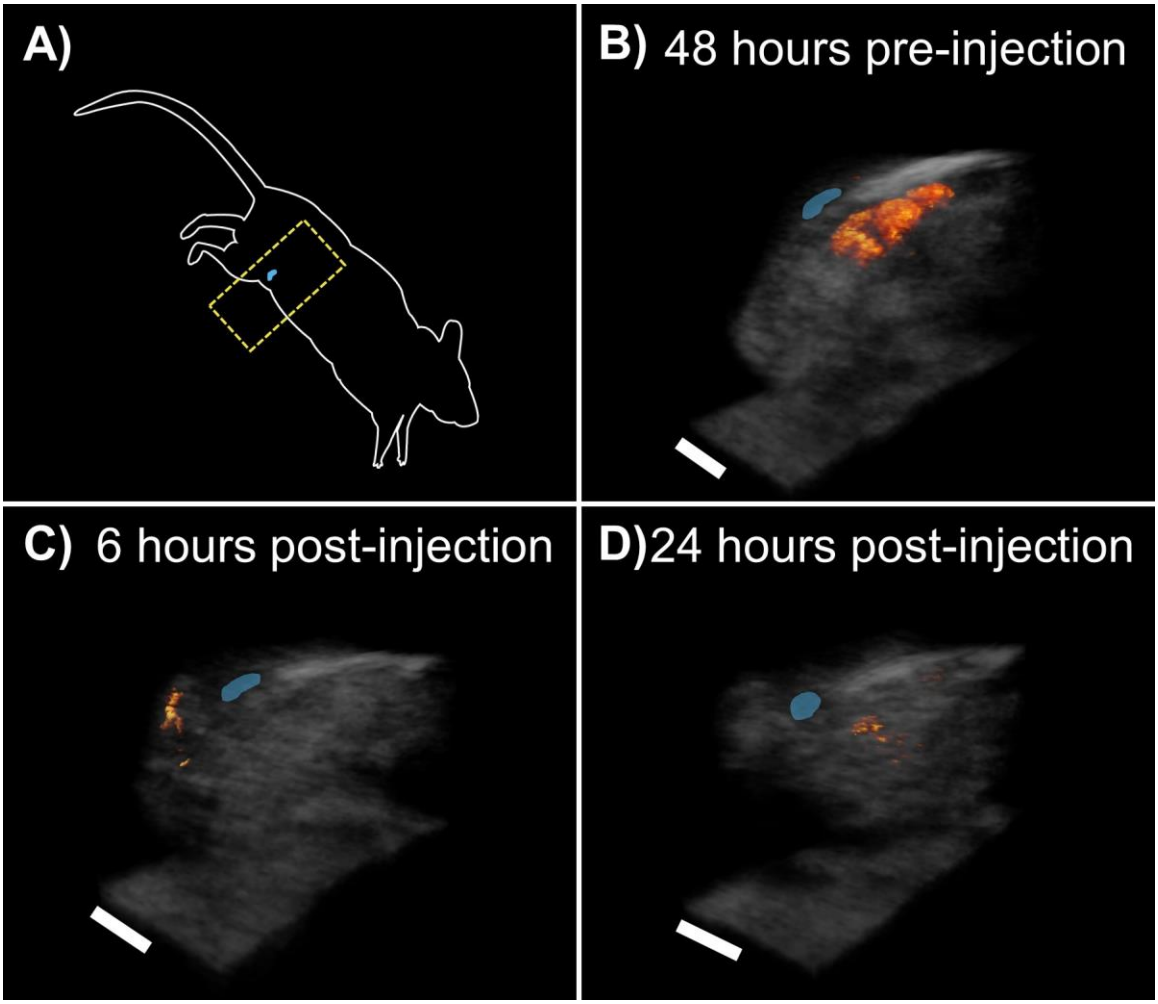

Figure 29: Processed US/PA volumes from 4T1 syngeneic mouse 2. This mouse received a 100 µL subcutaneous injection of PFHnDs at 0 hours and had a primary tumor in the right fourth mammary fat pad. **A)** Cartoon showing the left lateral decubitus position of the mouse for imaging. The yellow dashed lines approximate the volumes shown. Lymph nodes are false colored in light blue; **B)** Masked PA signal (red-orange) overlaid with the corresponding US volume 48 hours before PFHnD injection; **C)** Masked PA signal overlaid with US obtained 6 hours after PFHnD injection; **D)** Masked PA signal overlaid with US obtained 24 hours after PFHnD injection. Scale bars are approximately 5 mm.

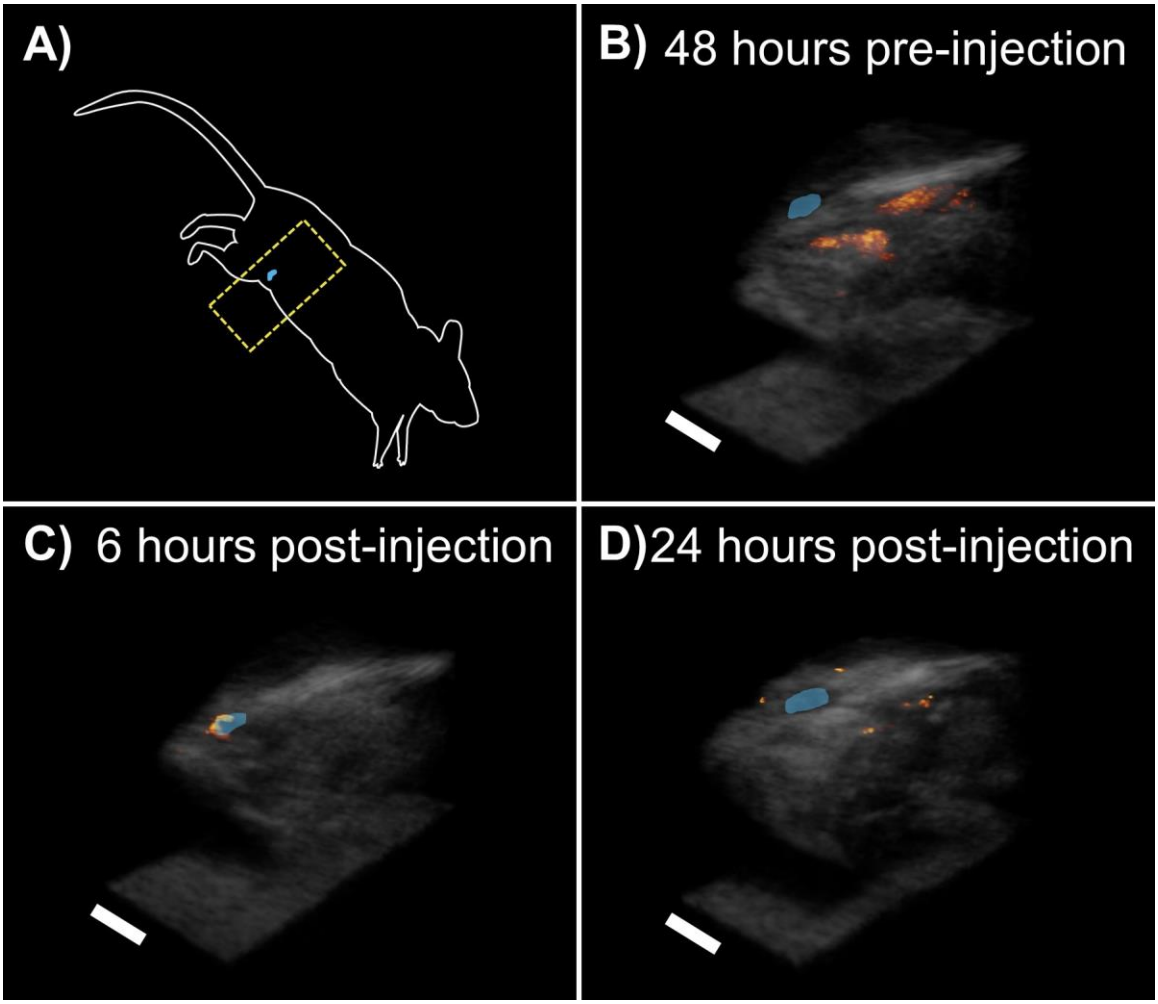

Figure 30: Processed US/PA volumes from 4T1 syngeneic mouse 3. This mouse received a 100 µL subcutaneous injection of PFHnDs at 0 hours and had a primary tumor in the right fourth mammary fat pad. **A)** Cartoon showing the left lateral decubitus position of the mouse for imaging. The yellow dashed lines approximate the volumes shown. Lymph nodes are false colored in light blue; **B)** Masked PA signal (red-orange) overlaid with the corresponding US volume 48 hours before PFHnD injection; **C)** Masked PA signal overlaid with US obtained 6 hours after PFHnD injection; **D)** Masked PA signal overlaid with US obtained 24 hours after PFHnD injection. Scale bars are approximately 5 mm.

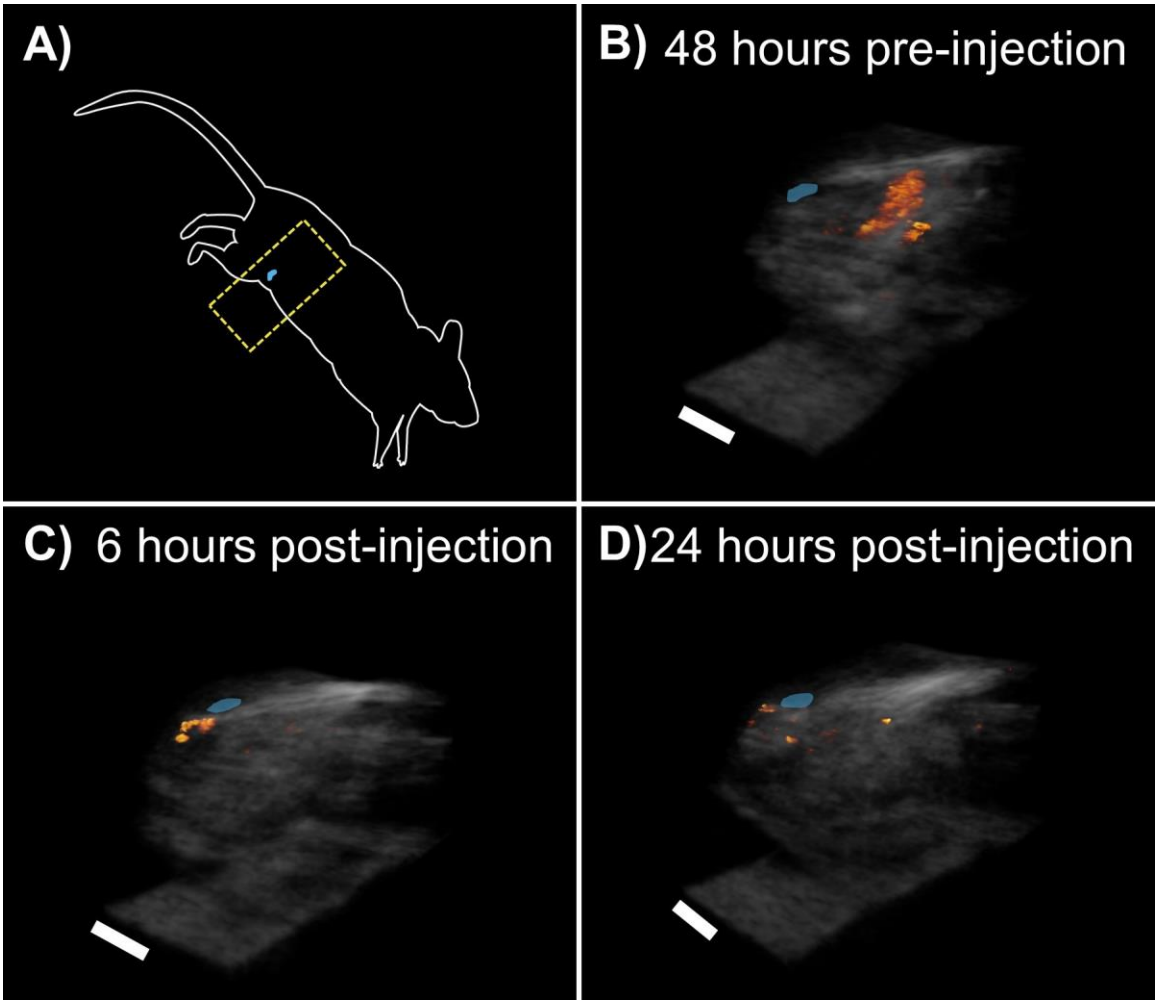

Figure 31: Processed US/PA volumes from BALB/c mouse 2. This mouse received a 100 µL subcutaneous injection of PFHnDs at 0 hours. **A)** Cartoon showing the left lateral decubitus position of the mouse for imaging. The yellow dashed lines approximate the volumes shown. Lymph nodes are false colored in light blue; **B)** Masked PA signal (red-orange) overlaid with the corresponding US volume 48 hours before PFHnD injection; **C)** Masked PA signal overlaid with US obtained 6 hours after PFHnD injection; **D)** Masked PA signal overlaid with US obtained 24 hours after PFHnD injection. Scale bars are approximately 5 mm.

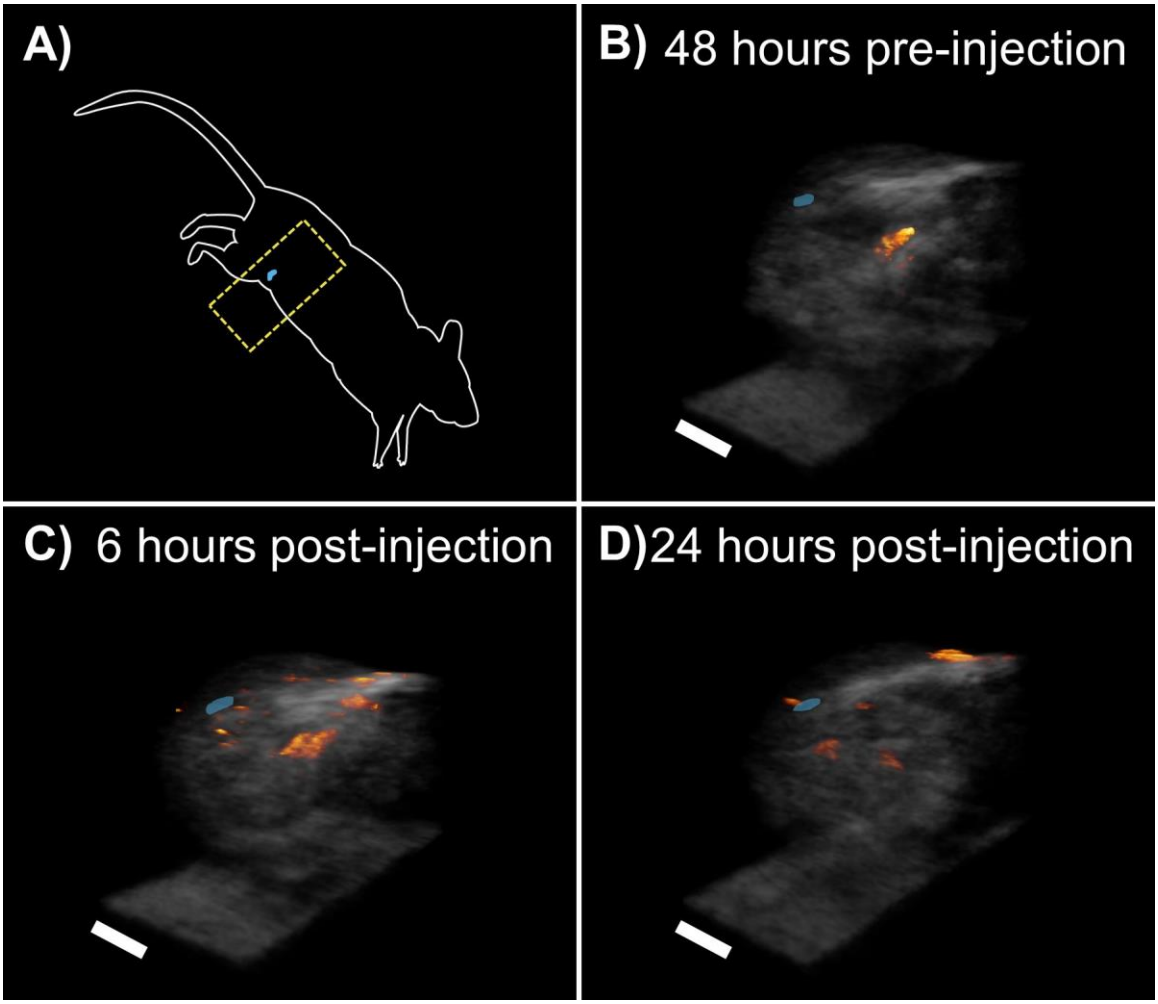

Figure 32: Processed US/PA volumes from BALB/c mouse 3. This mouse received a 100 µL subcutaneous injection of PFHnDs at 0 hours. **A)** Cartoon showing the left lateral decubitus position of the mouse for imaging. The yellow dashed lines approximate the volumes shown. Lymph nodes are false colored in light blue; **B)** Masked PA signal (red-orange) overlaid with the corresponding US volume 48 hours before PFHnD injection; **C)** Masked PA signal overlaid with US obtained 6 hours after PFHnD injection; **D)** Masked PA signal overlaid with US obtained 24 hours after PFHnD injection. Scale bars are approximately 5 mm.

Control Particle Image Volumes

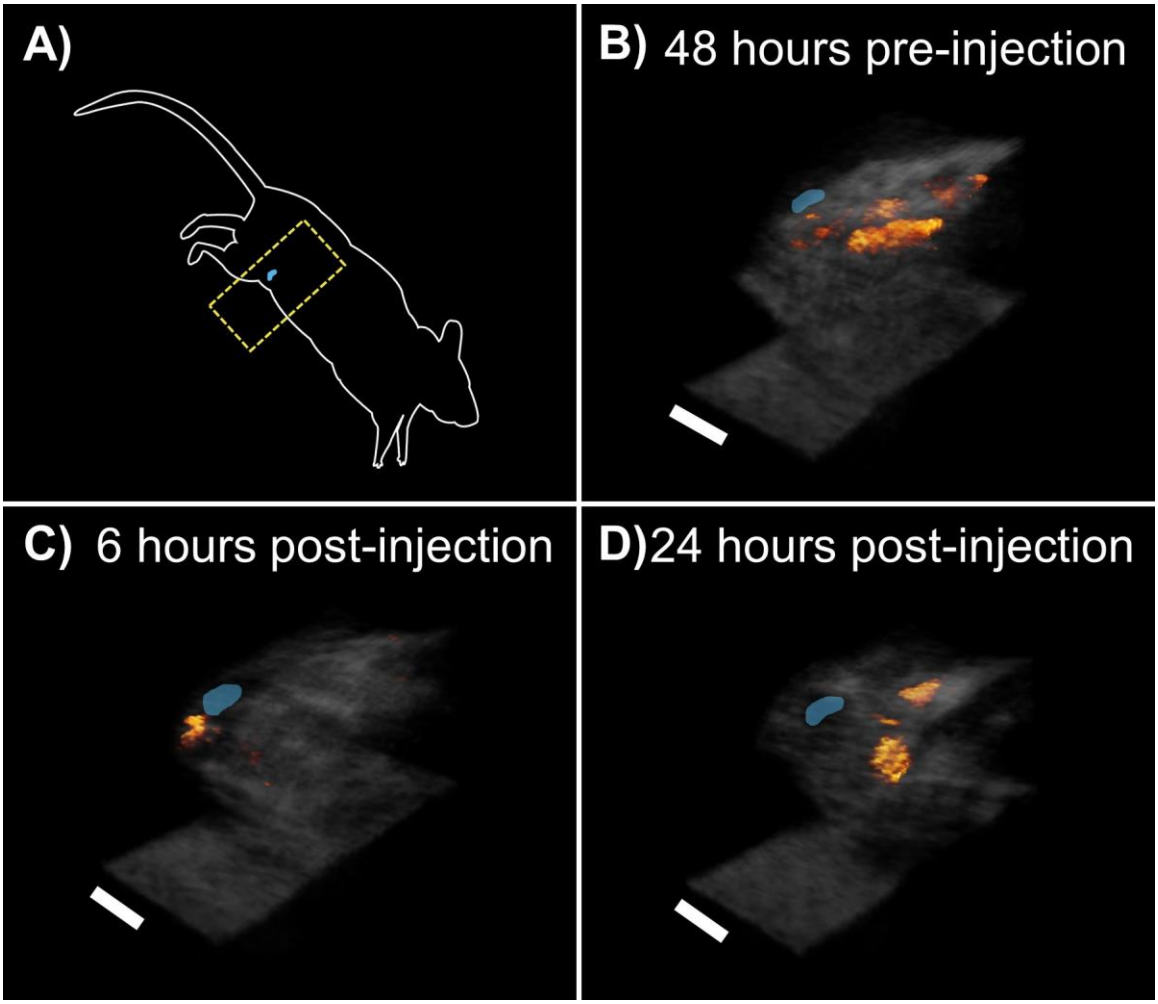

Figure 33: Processed US/PA volumes from a 4T1 syngeneic control. This mouse received a 100 µL subcutaneous injection of PFHnDs without IR1048 dye at 0 hours and had a primary tumor in the right fourth mammary fat pad. **A)** Cartoon showing the left lateral decubitus position of the mouse for imaging. The yellow dashed lines approximate the volumes shown. Lymph nodes are false colored in light blue; **B)** Masked PA signal (red-orange) overlaid with the corresponding US volume 48 hours before PFHnD injection; **C)** Masked PA signal overlaid with US obtained 6 hours after PFHnD injection; **D)** Masked PA signal overlaid with US obtained 24 hours after PFHnD injection. Scale bars are approximately 5 mm.

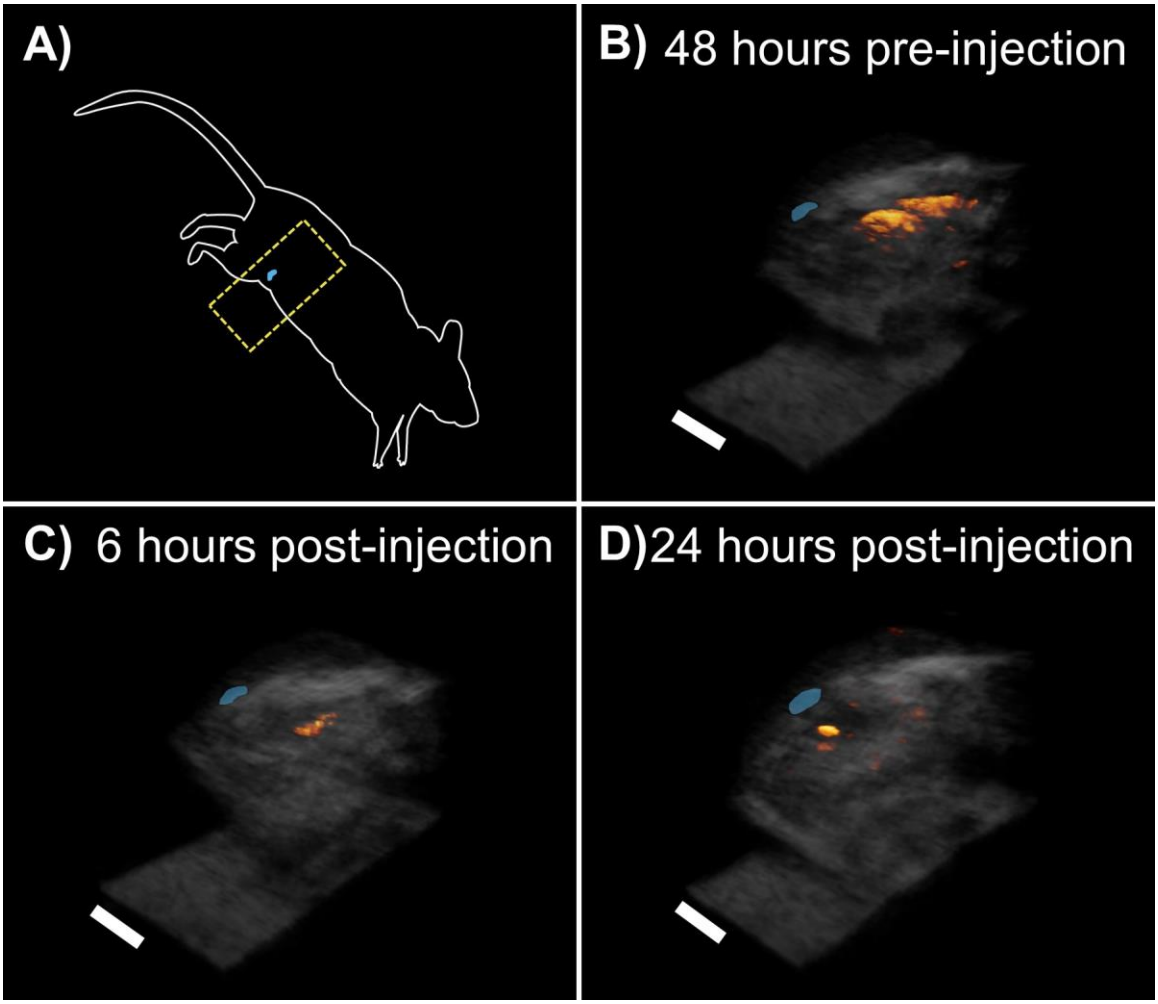

Figure 34: Processed US/PA volumes from a BALB/c control. This mouse received a 100 µL subcutaneous injection of PFHnDs without IR1048 dye at 0 hours. **A)** Cartoon showing the left lateral decubitus position of the mouse for imaging. The yellow dashed lines approximate the volumes shown. Lymph nodes are false colored in light blue; **B)** Masked PA signal (red-orange) overlaid with the corresponding US volume 48 hours before PFHnD injection; **C)** Masked PA signal overlaid with US obtained 6 hours after PFHnD injection; **D)** Masked PA signal overlaid with US obtained 24 hours after PFHnD injection. Scale bars are approximately 5 mm.

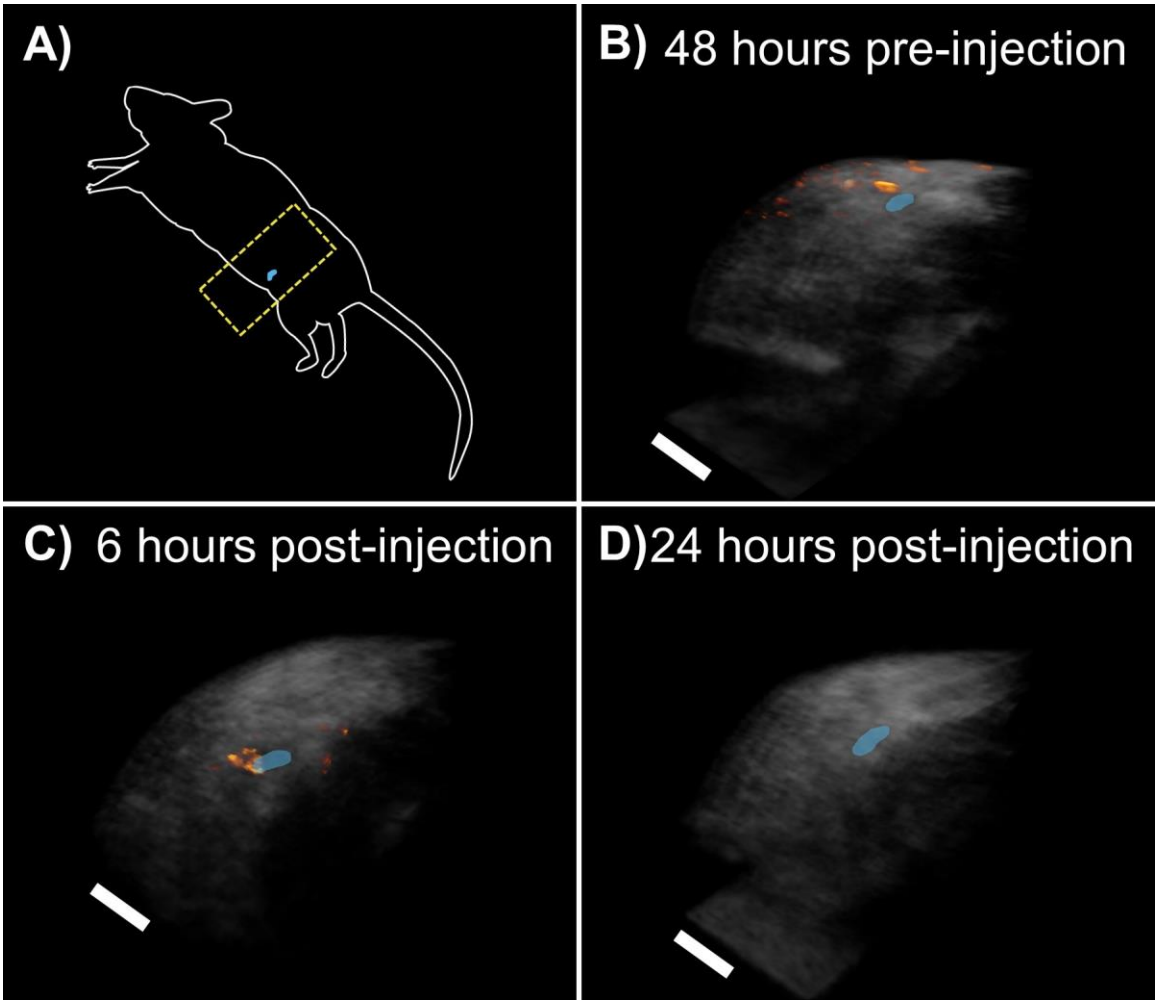

Figure 35: Processed SLN US/PA volumes from an MMTVneu mouse. This mouse received a 150 µL subcutaneous injection of anti-HER2 targeted PFHnDs at 0 hours and had a primary tumor in the left fourth mammary fat pad. **A)** Cartoon showing the right lateral decubitus position of the mouse for imaging. The yellow dashed lines approximate the volumes shown. Lymph nodes are false colored in light blue; **B)** Masked PA signal (red-orange) overlaid with the corresponding US volume 48 hours before PFHnD injection; **C)** Masked PA signal overlaid with US obtained 6 hours after PFHnD injection; **D)** Masked PA signal (absent) overlaid with US obtained 24 hours after PFHnD injection. Scale bars are approximately 5 mm.

APPENDIX C. SUPPLEMENTAL DATA FOR POLY(I:C) NANODROPLET STUDIES

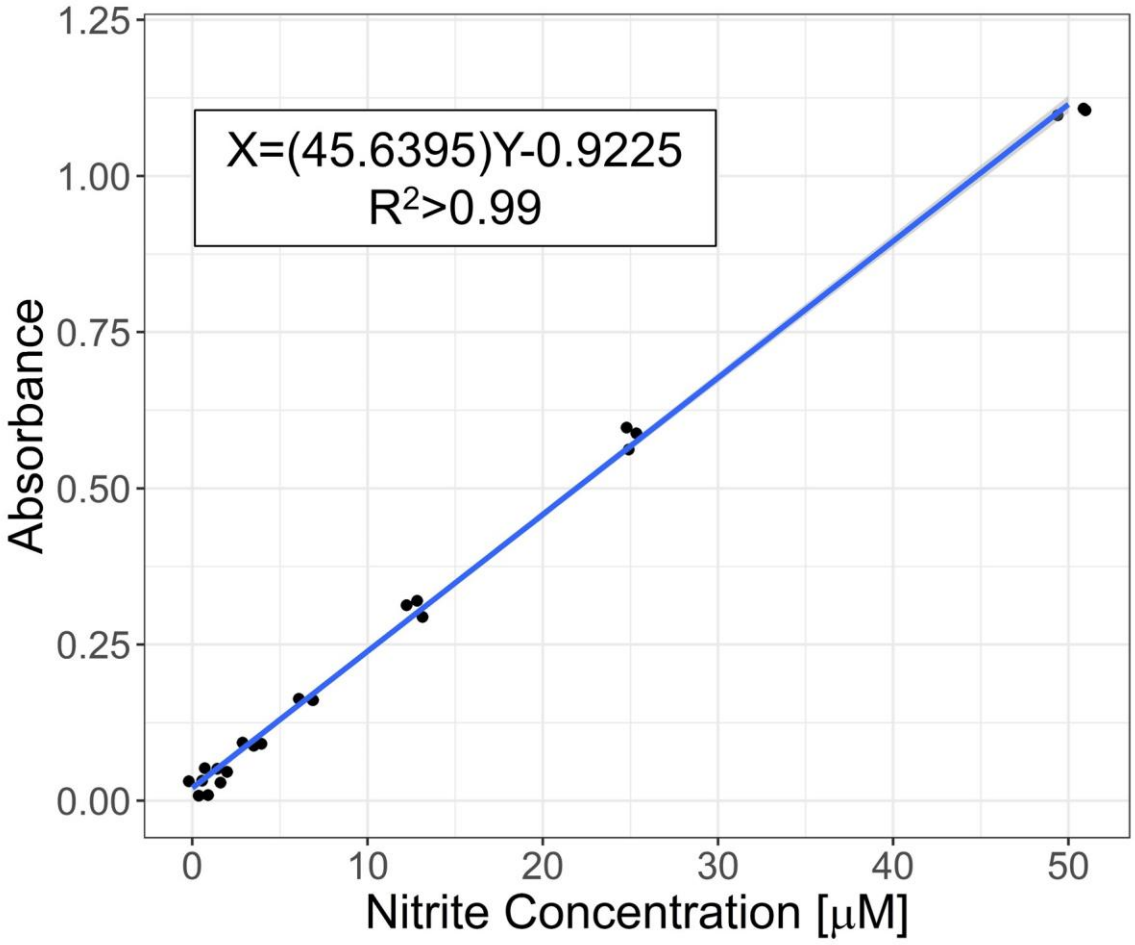

Figure 36: Sodium nitrite ladder used for the *in vitro* Griess assay. The working range of the modified Griess reagent is 0.43 to 65 μM. A linear regression (inset) of the ladder data was used to convert absorbance (Y) to nitrite concentration (X) for cell-containing wells. The linear regression (blue line) with 95% confidence interval (gray ribbon) is plotted against the raw data (black dots). Horizontal jitter was applied to the raw data for improved visualization.

APPENDIX D. SUPPLEMENTAL DATA FOR NANODROPLET EXTRAVASATION STUDIES

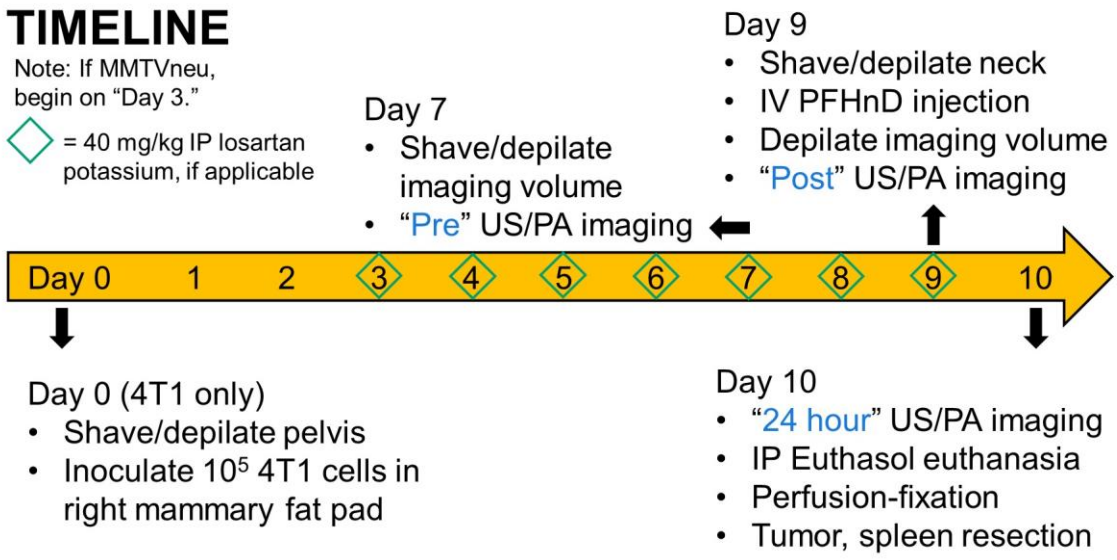

Figure 37: Schema for *in vivo* primary tumor studies of PFHnD extravasation.

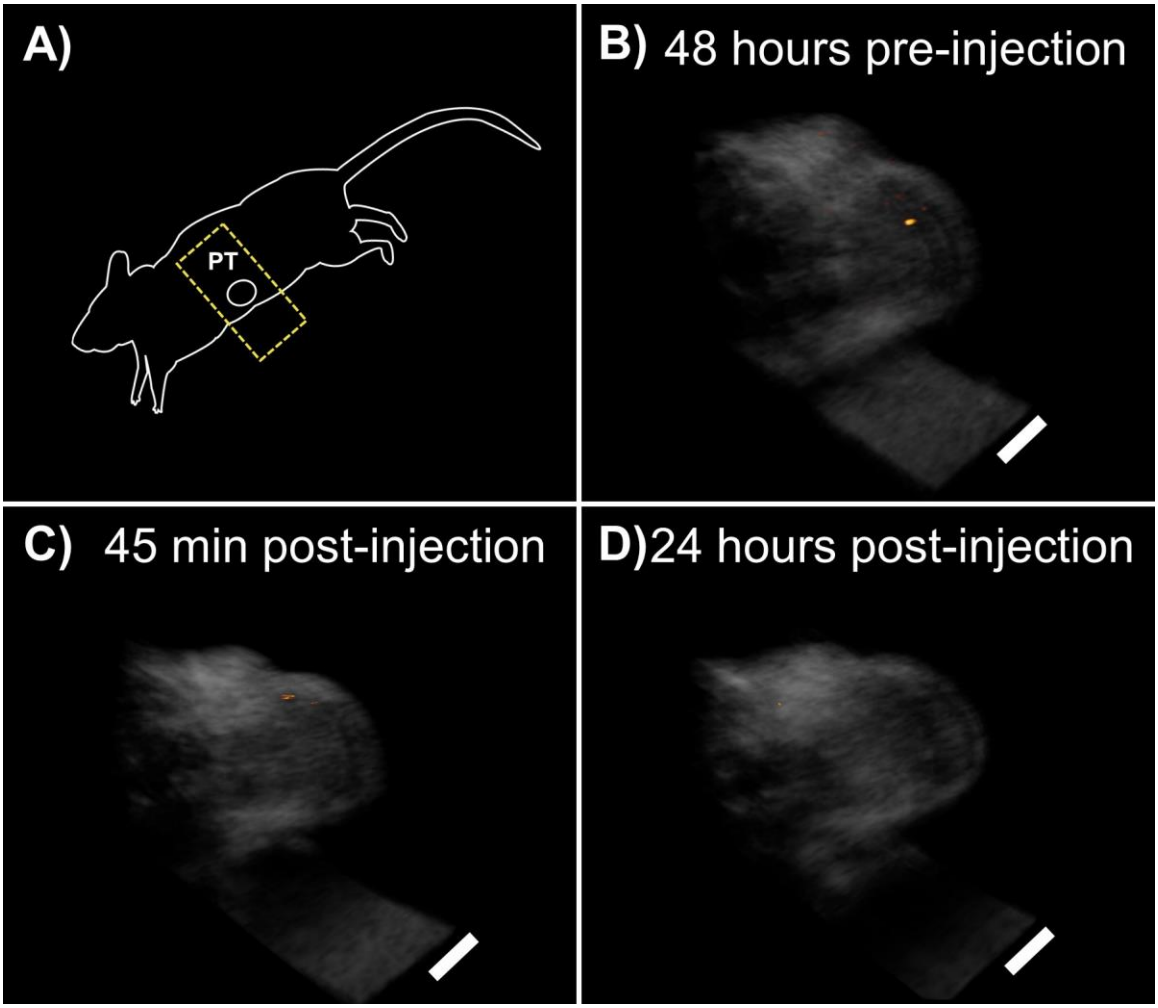

Figure 38: US/PA imaging volumes from a saline injected MMTVneu mouse. This mouse was not microdosed with losartan. **A)** Cartoon showing the right lateral decubitus position of the mouse for imaging. The yellow dashed lines approximate the volumes shown; **B)** Masked PA signal (red-orange) overlaid with the corresponding US volume 48 hours before saline injection; **C)** Masked PA signal overlaid with US obtained immediately after saline injection; **D)** Masked PA signal overlaid with US obtained 24 hours after PFHnD injection. All volumes show minimal PA enhancement. Scale bars are approximately 5 mm.

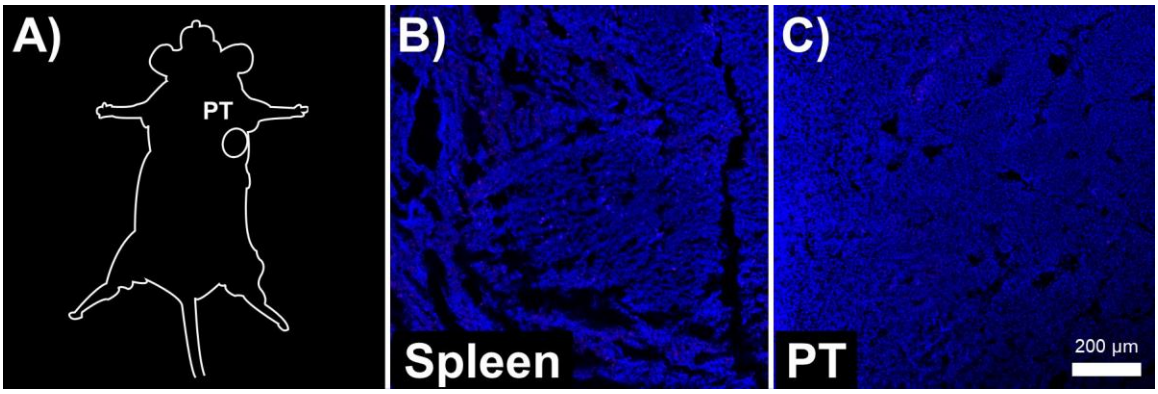

Figure 39: Representative histology from an MMTVneu mouse 24 hours post-saline injection. Mouse received a volume equivalent IV injection of saline instead of PFHnDs. Sections were stained with DAPI (blue). **A)** Cartoon showing the location of the primary tumor; **B)** Section of the spleen showing no appreciable enhancement from Cy5 tagged PFHnDs (red; absent); **C)** Section of the primary tumor showing no appreciable enhancement from Cy5. These sections were used to establish the dynamic range for Cy5 for all other spleen and primary tumor fluorescent images. Scale bar is 200 µm.

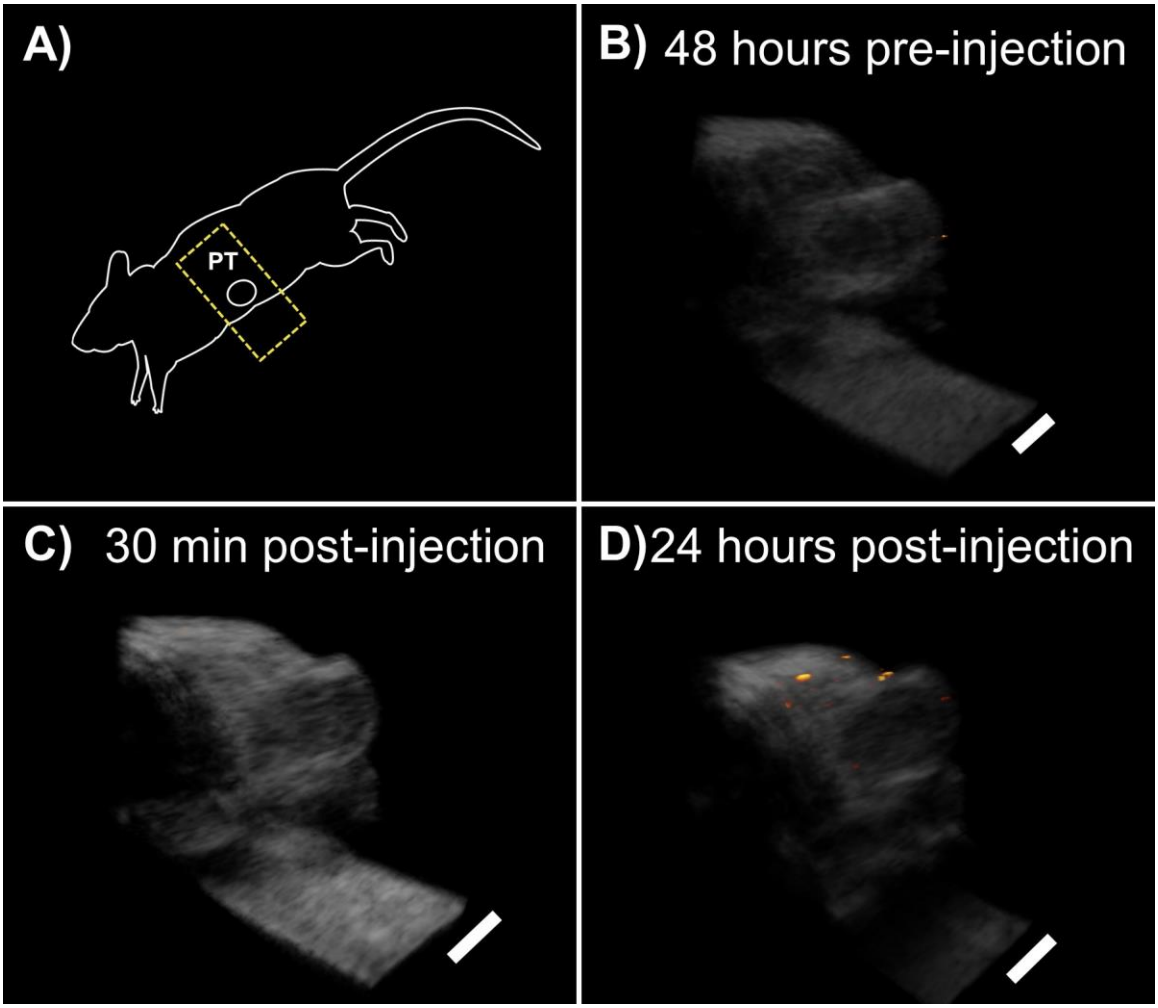

Figure 40: US/PA imaging volumes from a targeted PFHnD injected MMTVneu mouse. This mouse was microdosed with 40 mg/kg losartan for 7 days prior to IV injection with anti-HER2 PFHnDs. **A)** Cartoon showing the right lateral decubitus position of the mouse for imaging. The yellow dashed lines approximate the volumes shown; **B)** Masked PA signal (red-orange) overlaid with the corresponding US volume 48 hours before targeted PFHnD injection; **C)** Masked PA signal overlaid with US obtained 30 minutes after targeted PFHnD injection; **D)** Masked PA signal overlaid with US obtained 24 hours after targeted PFHnD injection. All volumes show minimal PA enhancement. Scale bars are approximately 5 mm.

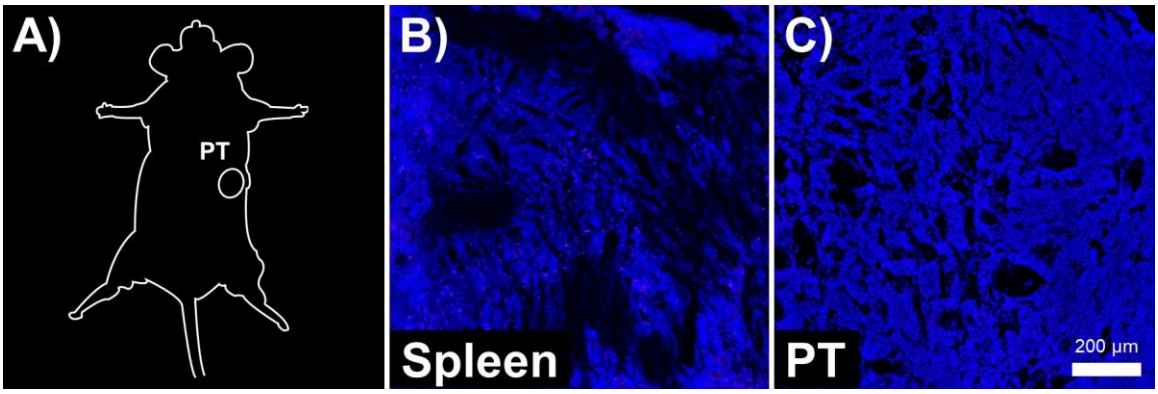

Figure 41: Representative histology from an MMTVneu mouse 24 hours post-PFCnD injection. Mouse was microdosed with 40 mg/kg losartan prior to IV injection of anti-HER2 targeted PFHnDs. Sections were stained with DAPI (blue). **A)** Cartoon showing the location of the primary tumor; **B)** Section of the spleen showing no appreciable enhancement from Cy5 tagged PFHnDs (red; absent); **C)** Section of the primary tumor showing no appreciable enhancement from Cy5 tagged PFHnDs. Scale bar is 200 µm.

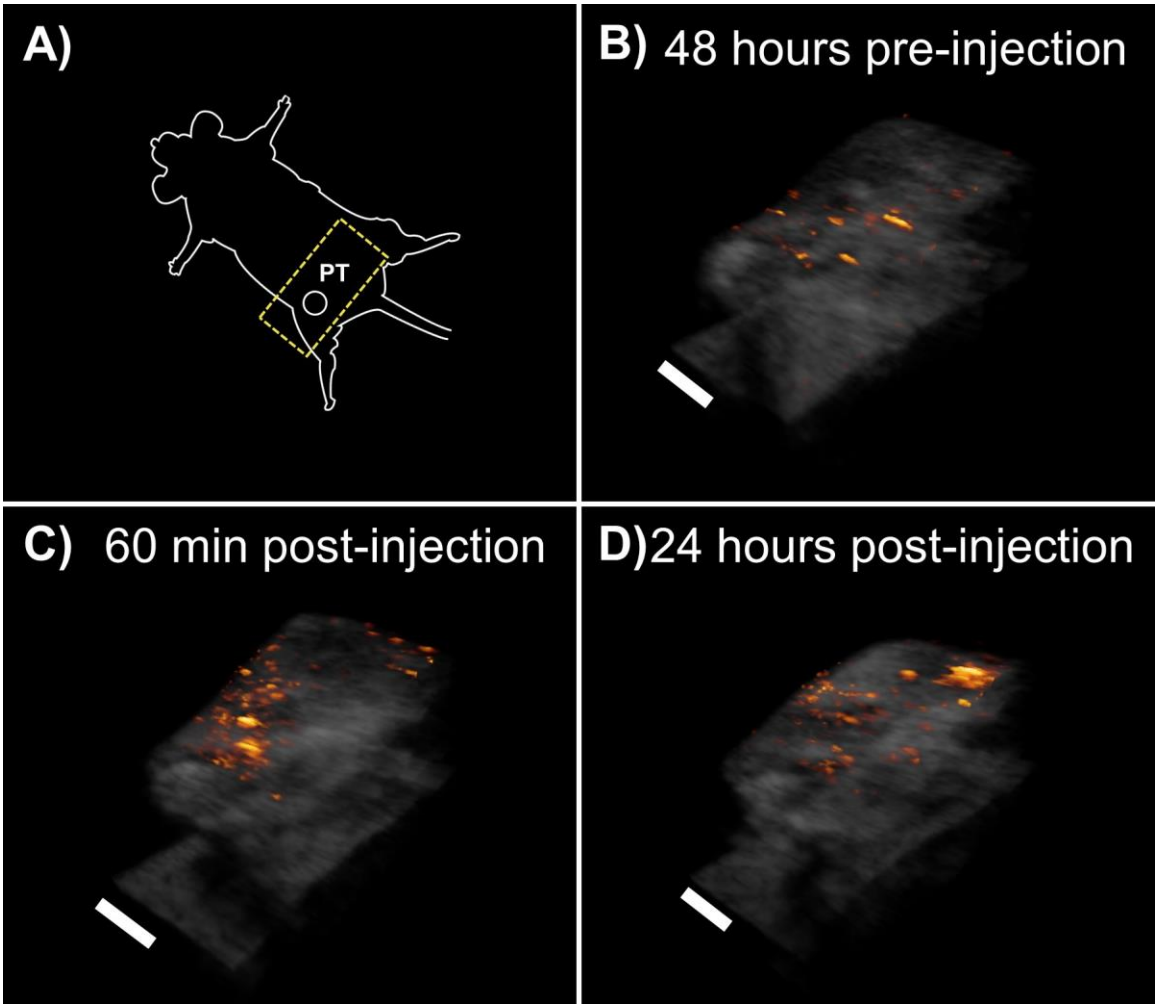

Figure 42: US/PA imaging volumes from a targeted PFHnD injected 4T1 syngeneic mouse. This mouse was microdosed with 40 mg/kg losartan for 7 days prior to IV injection with anti-EpCAM PFHnDs. **A)** Cartoon showing the supine position of the mouse for imaging. The yellow dashed lines approximate the volumes shown; **B)** Masked PA signal (red-orange) overlaid with the corresponding US volume 48 hours before targeted PFHnD injection; **C)** Masked PA signal overlaid with US obtained 60 minutes after targeted PFHnD injection; **D)** Masked PA signal overlaid with US obtained 24 hours after targeted PFHnD injection. All volumes show static PA enhancement at the skin surface, which is likely artifact. Scale bars are approximately 5 mm.

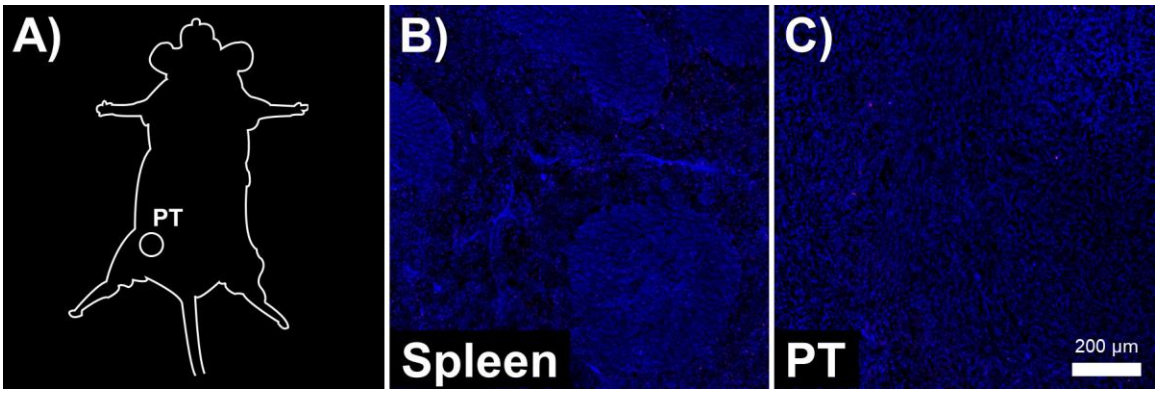

Figure 43: Representative histology from a 4T1 syngeneic mouse 24 hours post-PFCnD injection. Mouse was microdosed with 40 mg/kg losartan prior to IV injection of anti-EpCAM targeted PFHnDs. There was flash confirmation of the IV injection, but it is possible that this was a hematoma. Sections were stained with DAPI (blue). **A)** Cartoon showing the location of the primary tumor; **B)** Section of the spleen showing no appreciable enhancement from Cy5 tagged PFHnDs (red; absent); **C)** Section of the primary tumor showing no appreciable enhancement from Cy5 tagged PFHnDs. Scale bar is 200 µm.

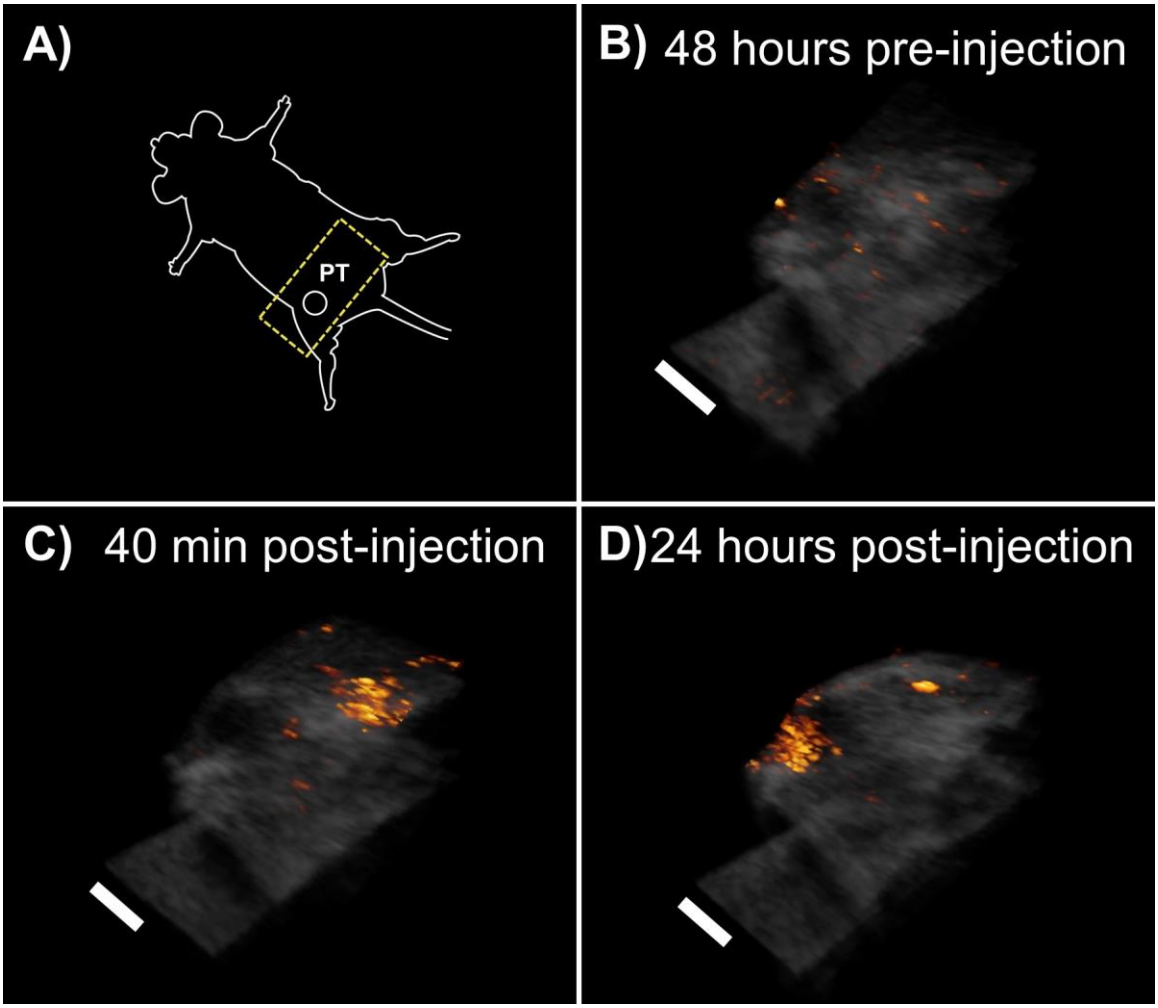

Figure 44: US/PA imaging volumes from another targeted PFHnD injected 4T1 syngeneic mouse. This mouse was microdosed with 40 mg/kg losartan for 7 days prior to IV injection with anti-EpCAM PFHnDs. **A)** Cartoon showing the supine position of the mouse for imaging. The yellow dashed lines approximate the volumes shown; **B)** Masked PA signal (red-orange) overlaid with the corresponding US volume 48 hours before targeted PFHnD injection; **C)** Masked PA signal overlaid with US obtained 40 minutes after targeted PFHnD injection; **D)** Masked PA signal overlaid with US obtained 24 hours after targeted PFHnD injection. Post-injection volumes show strong PA enhancement at the skin surface medial (40 min) and lateral (24 hour) to the primary tumor. This is likely artifact. Scale bars are approximately 5 mm.

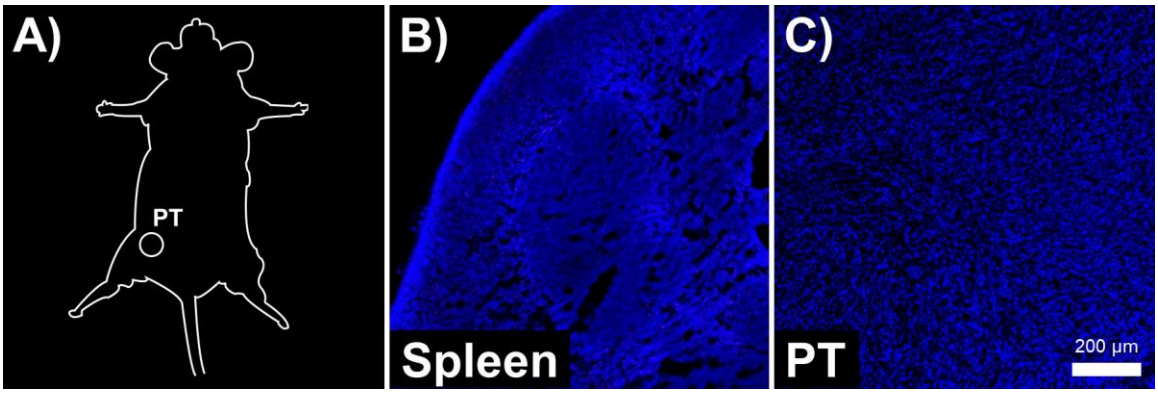

Figure 45: Representative histology from another 4T1 syngeneic mouse 24 hours post-PFCnD injection. Mouse was microdosed with 40 mg/kg losartan prior to IV injection of anti-EpCAM targeted PFHnDs. There was no flash confirmation of the IV injection, calling the delivery into question. Sections were stained with DAPI (blue). **A)** Cartoon showing the location of the primary tumor; **B)** Section of the spleen showing no appreciable enhancement from Cy5 tagged PFHnDs (red; absent); **C)** Section of the primary tumor showing no appreciable enhancement from Cy5 tagged PFHnDs. Scale bar is 200 µm.

APPENDIX E. SUPPLEMENTAL DATA FOR DUAL FLUOROPHORE NANODROPLETS

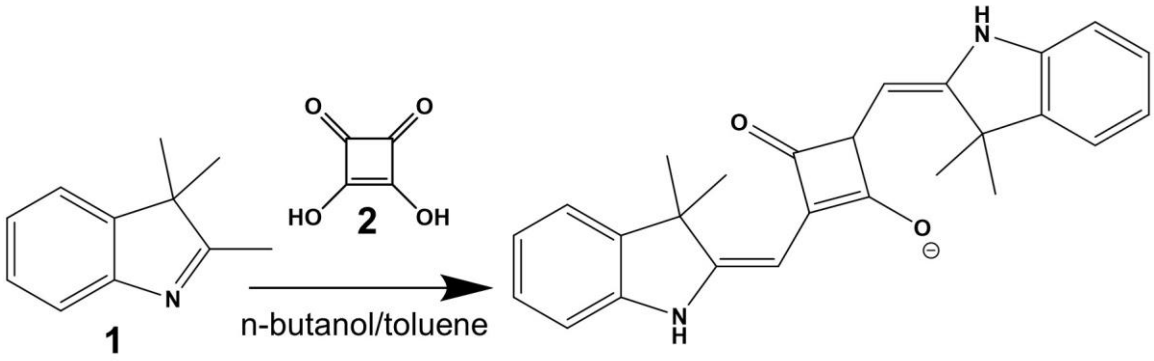

Figure 46: Schema of SQ650 synthesis. Squaric acid (**2**) and 2,3,3-trimethylindolenine (**1**) were heated under reflux in a mixture of 4:1 (v:v) n-butanol:toluene containing quinoline, as described in 5.3.3. Figure provided by Vadakkancheril S. Jisha, Ph.D.

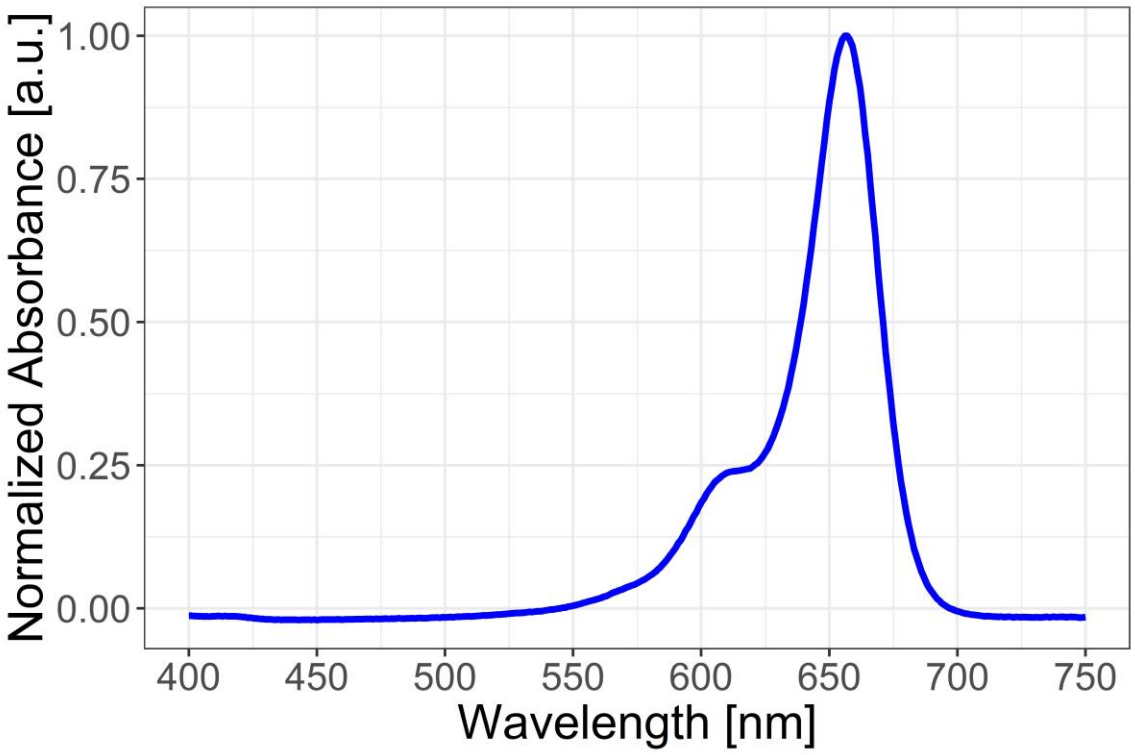

Figure 47: Absorbance spectrum of free SQ650 in chloroform. A qualitative amount of SQ650 dye was used. The spectrum and its peak at 656 nm compare favorably with Cy5 (649 nm peak).

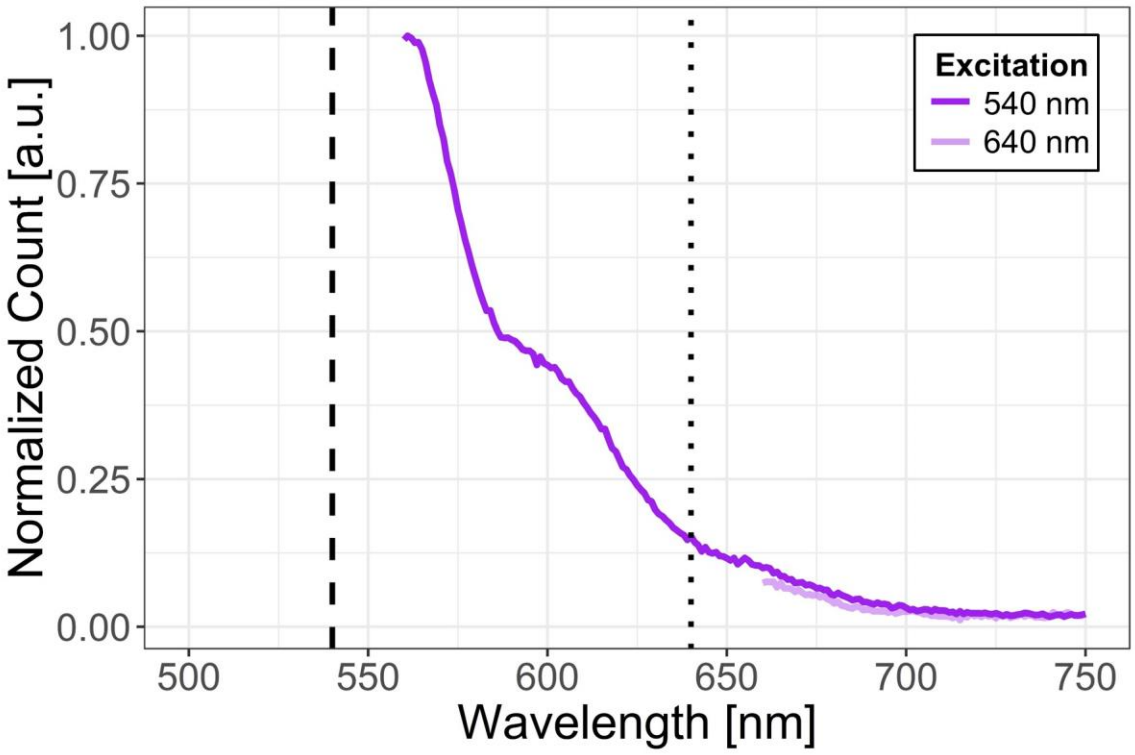

Figure 48: Fluorimetry of FRET nanodroplets made with 2:1 PFH:TFT. The original fluoroalkane emulsion stock contained 25 mg/mL SQ650. Although the PFCnD precursor stock contained SQ650 in the fluoroalkane phase, the resulting nanodroplets do not exhibit an SQ650 emission peak with either 640-nm (light purple) or 540-nm (purple) excitation. Spectra were acquired with 3-nm excitation and emission slit widths and were normalized to the maximum value from the 540-nm excitation spectrum

REFERENCES

1 Group, U. S. C. S. W. *United States Cancer Statistics: 1999-2012 Incidence and Mortality Web-based Report*, <https://nccd.cdc.gov/uscs/> (2015).

2 ter Haar, G. & Coussios, C. High intensity focused ultrasound: physical principles and devices. *International journal of hyperthermia* **23**, 89-104 (2007).

3 Gallego-Juarez, J. Piezoelectric ceramics and ultrasonic transducers. *Journal of Physics E: Scientific Instruments* **22**, 804 (1989).

4 Bushberg, J. T. & Boone, J. M. *The essential physics of medical imaging*. (Lippincott Williams & Wilkins, 2011).

5 Szabo, T. L. *Diagnostic ultrasound imaging: inside out*. (Academic Press, 2004).

6 Sommer, F. G. & Taylor, K. Differentiation of acoustic shadowing due to calculi and gas collections. *Radiology* **135**, 399-403 (1980).

7 Karaman, M., Li, P.-C. & O'Donnell, M. Synthetic aperture imaging for small scale systems. *IEEE transactions on ultrasonics, ferroelectrics, and frequency control* **42**, 429-442 (1995).

8 Thomenius, K. E. in *1996 IEEE Ultrasonics Symposium. Proceedings.* 1615-1622 (IEEE).

9 Tanter, M. & Fink, M. Ultrafast imaging in biomedical ultrasound. *IEEE transactions on ultrasonics, ferroelectrics, and frequency control* **61**, 102-119 (2014).

10 Montaldo, G., Tanter, M., Bercoff, J., Benech, N. & Fink, M. Coherent plane-wave compounding for very high frame rate ultrasonography and transient elastography. *IEEE transactions on ultrasonics, ferroelectrics, and frequency control* **56**, 489-506 (2009).

11 Bell, A. G. LXVIII. Upon the production of sound by radiant energy. *The London, Edinburgh, and Dublin Philosophical Magazine and Journal of Science* **11**, 510-528 (1881).

12 Oraevsky, A. A., Jacques, S. L., Esenaliev, R. O. & Tittel, F. K. in *Laser-Tissue Interaction V; and Ultraviolet Radiation Hazards.* 122-128 (International Society for Optics and Photonics).

13 Beard, P. C., Perennes, F. & Mills, T. N. Transduction mechanisms of the Fabry-Perot polymer film sensing concept for wideband ultrasound detection. *ieee*

transactions on ultrasonics, ferroelectrics, and frequency control **46**, 1575-1582 (1999).

14 O'donnell, M., Hamilton, J. D., Vossler, G. & Brooks, C. (Google Patents, 1998).

15 Hsu, E. *et al.* Bone marrow metastasis in astrocytic gliomata. *Journal of Neuro-oncology* **37**, 285-293 (1998).

16 Kim, C., Erpelding, T. N., Jankovic, L., Pashley, M. D. & Wang, L. V. Deeply penetrating in vivo photoacoustic imaging using a clinical ultrasound array system. *Biomedical optics express* **1**, 278-284 (2010).

17 Hu, C. L. Spherical model of an acoustical wave generated by rapid laser heating in a liquid. *The Journal of the Acoustical Society of America* **46**, 728-736 (1969).

18 Oraevsky, A. A., Jacques, S. L. & Tittel, F. K. Measurement of tissue optical properties by time-resolved detection of laser-induced transient stress. *Applied optics* **36**, 402-415 (1997).

19 Oraevsky, A. A. & Karabutov, A. A. Optoacoustic tomography. *Biomedical photonics handbook* **34**, 1-34 (2003).

20 Tzoumas, S. & Ntziachristos, V. Spectral unmixing techniques for optoacoustic imaging of tissue pathophysiology. *Philosophical Transactions of the Royal Society A: Mathematical, Physical and Engineering Sciences* **375**, 20170262 (2017).

21 Luke, G. P., Nam, S. Y. & Emelianov, S. Y. Optical wavelength selection for improved spectroscopic photoacoustic imaging. *Photoacoustics* **1**, 36-42 (2013).

22 Chivers, R. The scattering of ultrasound by human tissues—Some theoretical models. *Ultrasound in medicine & biology* **3**, 1-13 (1977).

23 Senapati, N., Lele, P. & Woodin, A. in *1972 Ultrasonics Symposium.* 59-63 (IEEE).

24 Stakutis, V., Morse, R., Dill, M. & Beyer, R. Attenuation of ultrasound in aqueous suspensions. *The Journal of the Acoustical Society of America* **27**, 539-546 (1955).

25 Stride, E. & Saffari, N. Microbubble ultrasound contrast agents: a review. *Proceedings of the Institution of Mechanical Engineers, Part H: Journal of Engineering in Medicine* **217**, 429-447 (2003).

26 Pochon, S. *et al.* BR55: a lipopeptide-based VEGFR2-targeted ultrasound contrast agent for molecular imaging of angiogenesis. *Investigative radiology* **45**, 89-95 (2010).

27 Willmann, J. K. *et al.* Ultrasound molecular imaging with BR55 in patients with breast and ovarian lesions: first-in-human results. *Journal of Clinical Oncology* **35**, 2133 (2017).

28 Helfield, B. L. & Goertz, D. E. Nonlinear resonance behavior and linear shell estimates for Definity™ and MicroMarker™ assessed with acoustic microbubble spectroscopy. *The Journal of the Acoustical Society of America* **133**, 1158-1168 (2013).

29 Miller, D. Ultrasonic detection of resonant cavitation bubbles in a flow tube by their second-harmonic emissions. *Ultrasonics* **19**, 217-224 (1981).

30 Kim, J., Lindsey, B. D., Li, S., Dayton, P. A. & Jiang, X. in *Health Monitoring of Structural and Biological Systems 2017*. 101700T (International Society for Optics and Photonics).

31 Martin, K. H. *et al.* Dual-frequency piezoelectric transducers for contrast enhanced ultrasound imaging. *Sensors* **14**, 20825-20842 (2014).

32 Simpson, D. H., Chin, C. T. & Burns, P. N. Pulse inversion Doppler: a new method for detecting nonlinear echoes from microbubble contrast agents. *IEEE transactions on ultrasonics, ferroelectrics, and frequency control* **46**, 372-382 (1999).

33 Smith, A. M., Mancini, M. C. & Nie, S. Bioimaging: second window for in vivo imaging. *Nature nanotechnology* **4**, 710 (2009).

34 Weissleder, R. A clearer vision for in vivo imaging. *Nature biotechnology* **19**, 316-317 (2001).

35 Ku, G. *et al.* Copper sulfide nanoparticles as a new class of photoacoustic contrast agent for deep tissue imaging at 1064 nm. *ACS nano* **6**, 7489-7496 (2012).

36 Luke, G. P. *et al.* Silica-coated gold nanoplates as stable photoacoustic contrast agents for sentinel lymph node imaging. *Nanotechnology* **24**, 455101 (2013).

37 Song, K. H., Kim, C., Cobley, C. M., Xia, Y. & Wang, L. V. Near-infrared gold nanocages as a new class of tracers for photoacoustic sentinel lymph node mapping on a rat model. *Nano letters* **9**, 183-188 (2009).

38 Sreejith, S. *et al.* Near-infrared squaraine dye encapsulated micelles for in vivo fluorescence and photoacoustic bimodal imaging. *ACS nano* **9**, 5695-5704 (2015).

39 Yao, J., Maslov, K. I., Hu, S. & Wang, L. V. Evans blue dye-enhanced capillary-resolution photoacoustic microscopy in vivo. *Journal of biomedical optics* **14**, 054049 (2009).

40 Wang, X. *et al.* Noninvasive photoacoustic angiography of animal brains in vivo with near-infrared light and an optical contrast agent. *Optics letters* **29**, 730-732 (2004).

41 Sheeran, P. S., Luois, S. H., Mullin, L. B., Matsunaga, T. O. & Dayton, P. A. Design of ultrasonically-activatable nanoparticles using low boiling point perfluorocarbons. *Biomaterials* **33**, 3262-3269 (2012).

42 Rapoport, N. Phase-shift, stimuli-responsive perfluorocarbon nanodroplets for drug delivery to cancer. *Wiley Interdisciplinary Reviews: Nanomedicine and Nanobiotechnology* **4**, 492-510 (2012).

43 Sheeran, P. S. & Dayton, P. A. Phase-change contrast agents for imaging and therapy. *Current pharmaceutical design* **18**, 2152-2165 (2012).

44 Rapoport, N. Y., Kennedy, A. M., Shea, J. E., Scaife, C. L. & Nam, K.-H. Controlled and targeted tumor chemotherapy by ultrasound-activated nanoemulsions/microbubbles. *Journal of Controlled Release* **138**, 268-276 (2009).

45 Sheeran, P. S. *et al.* Methods of generating submicrometer phase-shift perfluorocarbon droplets for applications in medical ultrasonography. *IEEE transactions on ultrasonics, ferroelectrics, and frequency control* **64**, 252-263 (2016).

46 Kripfgans, O. D., Fabiilli, M. L., Carson, P. L. & Fowlkes, J. B. On the acoustic vaporization of micrometer-sized droplets. *The Journal of the Acoustical Society of America* **116**, 272-281 (2004).

47 Doinikov, A. A., Sheeran, P. S., Bouakaz, A. & Dayton, P. A. Vaporization dynamics of volatile perfluorocarbon droplets: a theoretical model and in vitro validation. *Medical physics* **41**, 102901 (2014).

48 Shpak, O. *et al.* Ultrafast dynamics of the acoustic vaporization of phase-change microdroplets. *The Journal of the Acoustical Society of America* **134**, 1610-1621 (2013).

49 Mountford, P. A., Sirsi, S. R. & Borden, M. A. Condensation phase diagrams for lipid-coated perfluorobutane microbubbles. *Langmuir* **30**, 6209-6218 (2014).

50 Sheeran, P. S. *et al.* More than bubbles: creating phase-shift droplets from commercially available ultrasound contrast agents. *Ultrasound in medicine & biology* **43**, 531-540 (2017).

51 Mountford, P. A., Thomas, A. N. & Borden, M. A. Thermal activation of superheated lipid-coated perfluorocarbon drops. *Langmuir* **31**, 4627-4634 (2015).

52 Eberhart, J. The thermodynamic and the kinetic limits of superheat of a liquid. *Journal of Colloid and Interface science* **56**, 262-269 (1976).

53 Wilson, K., Homan, K. & Emelianov, S. Biomedical photoacoustics beyond thermal expansion using triggered nanodroplet vaporization for contrast-enhanced imaging. *Nature communications* **3**, 618 (2012).

54 Hannah, A., Luke, G., Wilson, K., Homan, K. & Emelianov, S. Indocyanine green-loaded photoacoustic nanodroplets: dual contrast nanoconstructs for enhanced photoacoustic and ultrasound imaging. *ACS nano* **8**, 250-259 (2013).

55 Rapoport, N. *et al.* Ultrasound-mediated tumor imaging and nanotherapy using drug loaded, block copolymer stabilized perfluorocarbon nanoemulsions. *Journal of Controlled Release* **153**, 4-15 (2011).

56 ANSftSUo, L. American national standard for the safe use of lasers. *American National Standards Institute. ANSIZ136. New York, NY: American National Standards Institute* (2007).

57 Luke, G. P., Hannah, A. S. & Emelianov, S. Y. Super-resolution ultrasound imaging in vivo with transient laser-activated nanodroplets. *Nano letters* **16**, 2556-2559 (2016).

58 Hannah, A. S., Luke, G. P. & Emelianov, S. Y. Blinking Phase-Change Nanocapsules Enable Background-Free Ultrasound Imaging. *Theranostics* **6**, 1866-1876, doi:10.7150/thno.14961 (2016).

59 Rapoport, N. in *Therapeutic Ultrasound* 221-241 (Springer, 2016).

60 Fleissig, A. *et al.* Post-operative arm morbidity and quality of life. Results of the ALMANAC randomised trial comparing sentinel node biopsy with standard axillary treatment in the management of patients with early breast cancer. *Breast cancer research and treatment* **95**, 279-293 (2006).

61 Cella, D., Peterman, A., Hudgens, S., Webster, K. & Socinski, M. A. Measuring the side effects of taxane therapy in oncology. *Cancer* **98**, 822-831 (2003).

62 Goldberg, B. B., Liu, J.-B. & Forsberg, F. Ultrasound contrast agents: a review. *Ultrasound in medicine & biology* **20**, 319-333 (1994).

63 Kogan, P., Gessner, R. C. & Dayton, P. A. Microbubbles in imaging: applications beyond ultrasound. *Bubble Science, Engineering & Technology* **2**, 3-8 (2010).

64 Gorce, J.-M., Arditi, M. & Schneider, M. Influence of bubble size distribution on the echogenicity of ultrasound contrast agents: A study of SonoVue™. *Investigative radiology* **35**, 661-671 (2000).

65 Goertz, D. E., de Jong, N. & van der Steen, A. F. Attenuation and size distribution measurements of Definity™ and manipulated Definity™ populations. *Ultrasound in medicine & biology* **33**, 1376-1388 (2007).

66 Wilson, S. R. & Burns, P. N. Microbubble-enhanced US in body imaging: what role? *Radiology* **257**, 24-39 (2010).

67 Kabalnov, A. *et al.* Dissolution of multicomponent microbubbles in the bloodstream: 2. Experiment. *Ultrasound in medicine & biology* **24**, 751-760 (1998).

68 Kwan, J. J. & Borden, M. A. Lipid monolayer collapse and microbubble stability. *Advances in colloid and interface science* **183**, 82-99 (2012).

69 Hobbs, S. K. *et al.* Regulation of transport pathways in tumor vessels: role of tumor type and microenvironment. *Proceedings of the National Academy of Sciences* **95**, 4607-4612 (1998).

70 Hashizume, H. *et al.* Openings between defective endothelial cells explain tumor vessel leakiness. *The American journal of pathology* **156**, 1363-1380 (2000).

71 Barua, S. & Mitragotri, S. Challenges associated with penetration of nanoparticles across cell and tissue barriers: a review of current status and future prospects. *Nano today* **9**, 223-243 (2014).

72 Prabhakar, U. *et al.* (AACR, 2013).

73 Strand, S. & Bergqvist, L. Radiolabeled colloids and macromolecules in the lymphatic system. *Critical reviews in therapeutic drug carrier systems* **6**, 211-238 (1989).

74 Swartz, M. A., Berk, D. A. & Jain, R. K. Transport in lymphatic capillaries. I. Macroscopic measurements using residence time distribution theory. *American Journal of Physiology-Heart and Circulatory Physiology* **270**, H324-H329 (1996).

75 Swartz, M. A. The physiology of the lymphatic system. *Advanced drug delivery reviews* **50**, 3-20 (2001).

76 Yarmoska, S. K., Yoon, H. & Emelianov, S. Y. Lipid Shell Composition Plays a Critical Role in the Stable Size Reduction of Perfluorocarbon Nanodroplets. *Ultrasound in medicine & biology* **45**, 1489-1499 (2019).

77 Santiesteban, D. Y., Dumani, D. S., Profili, D. & Emelianov, S. Y. Copper sulfide perfluorocarbon nanodroplets as clinically relevant photoacoustic/ultrasound imaging agents. *Nano letters* **17**, 5984-5989 (2017).

78 Kripfgans, O. D., Fowlkes, J. B., Miller, D. L., Eldevik, O. P. & Carson, P. L. Acoustic droplet vaporization for therapeutic and diagnostic applications. *Ultrasound in medicine & biology* **26**, 1177-1189 (2000).

79 Yoon, H. *et al.* Contrast-enhanced ultrasound imaging in vivo with laser-activated nanodroplets. *Medical Physics* (2017).

80 Mei, K.-C., Bai, J., Lorrio, S., Wang, J. T.-W. & Al-Jamal, K. T. Investigating the effect of tumor vascularization on magnetic targeting in vivo using retrospective design of experiment. *Biomaterials* **106**, 276-285 (2016).

81 Sheeran, P. S., Luois, S., Dayton, P. A. & Matsunaga, T. O. Formulation and acoustic studies of a new phase-shift agent for diagnostic and therapeutic ultrasound. *Langmuir* **27**, 10412-10420 (2011).

82 Arnal, B. *et al.* Sono-photoacoustic imaging of gold nanoemulsions: Part I. Exposure thresholds. *Photoacoustics* **3**, 3-10 (2015).

83 Martz, T. D., Bardin, D., Sheeran, P. S., Lee, A. P. & Dayton, P. A. Microfluidic generation of acoustically active nanodroplets. *Small* **8**, 1876-1879 (2012).

84 Seo, M. & Matsuura, N. Monodisperse, Submicrometer Droplets via Condensation of Microfluidic-Generated Gas Bubbles. *Small* **8**, 2704-2714 (2012).

85 Chattaraj, R., Goldscheitter, G. M., Yildirim, A. & Goodwin, A. P. Phase behavior of mixed lipid monolayers on perfluorocarbon nanoemulsions and its effect on acoustic contrast. *RSC Advances* **6**, 111318-111325 (2016).

86 Dayton, P. A. *et al.* Application of ultrasound to selectively localize nanodroplets for targeted imaging and therapy. *Molecular imaging* **5**, 7290.2006. 00019 (2006).

87 Weissig, V., Whiteman, K. R. & Torchilin, V. P. Accumulation of protein-loaded long-circulating micelles and liposomes in subcutaneous Lewis lung carcinoma in mice. *Pharmaceutical research* **15**, 1552-1556 (1998).

88 Ashok, B., Arleth, L., Hjelm, R. P., Rubinstein, I. & Önyüksel, H. In vitro characterization of PEGylated phospholipid micelles for improved drug solubilization: effects of PEG chain length and PC incorporation. *Journal of pharmaceutical sciences* **93**, 2476-2487 (2004).

89 Yoon, H. & Emelianov, S. Combined multi-wavelength photoacoustic and plane-wave ultrasound imaging for probing dynamic phase-change contrast agents. *IEEE Transactions on Biomedical Engineering*, 1-1, doi:10.1109/TBME.2018.2849077 (2018).

90 Reznik, N., Williams, R. & Burns, P. N. Investigation of vaporized submicron perfluorocarbon droplets as an ultrasound contrast agent. *Ultrasound in medicine & biology* **37**, 1271-1279 (2011).

91 Kabalnov, A. S. & Shchukin, E. D. Ostwald ripening theory: applications to fluorocarbon emulsion stability. *Advances in colloid and interface science* **38**, 69-97 (1992).

92 Yoo, K. *et al.* Impact of Encapsulation on in vitro and in vivo Performance of Volatile Nanoscale Phase-Shift Perfluorocarbon Droplets. *Ultrasound in Medicine and Biology* (2018).

93 Krishnadas, A., Rubinstein, I. & Önyüksel, H. Sterically stabilized phospholipid mixed micelles: in vitro evaluation as a novel carrier for water-insoluble drugs. *Pharmaceutical research* **20**, 297-302 (2003).

94 Barton, J. K., Hoying, J. B. & Sullivan, C. J. Use of microbubbles as an optical coherence tomography contrast agent. *Academic radiology* **9**, S52-S55 (2002).

95 Alexander, A. L., McCreery, T. T., Barrette, T. R., Gmitro, A. F. & Unger, E. C. Microbubbles as novel pressure-sensitive MR contrast agents. *Magnetic resonance in medicine* **35**, 801-806 (1996).

96 Díaz-López, R., Tsapis, N. & Fattal, E. Liquid perfluorocarbons as contrast agents for ultrasonography and 19F-MRI. *Pharmaceutical research* **27**, 1 (2010).

97 Rojas, J. D. & Dayton, P. A. In Vivo Molecular Imaging Using Low-Boiling-Point Phase-Change Contrast Agents: A Proof of Concept Study. *Ultrasound in Medicine and Biology* **45**, 177-191, doi:10.1016/j.ultrasmedbio.2018.08.004 (2019).

98 Hannah, A. S., Luke, G. P. & Emelianov, S. Y. Blinking Phase-Change Nanocapsules Enable Background-Free Ultrasound Imaging. *Theranostics* **6**, 1866-1876, doi:10.7150/thno.14961 (2016).

99 Lajoinie, G. *et al.* Ultrafast vapourization dynamics of laser-activated polymeric microcapsules. *Nature Communications* **5**, 3671, doi:10.1038/ncomms4671 (2014).

100 Yoon, H., Hallam, K. A., Yoon, C. & Emelianov, S. Y. Super-resolution imaging with ultrafast ultrasound imaging of optically triggered perfluorohexane nanodroplets. *IEEE Transactions on Ultrasonics, Ferroelectrics, and Frequency Control*, 1-1, doi:10.1109/tuffc.2018.2829740 (2018).

101 Yoon, H. *et al.* Contrast-enhanced ultrasound imaging in vivo with laser-activated nanodroplets. *Medical Physics* **44**, 3444-3449, doi:10.1002/mp.12269 (2017).

102 Zhu, Y. I., Yoon, H., Zhao, A. X. & Emelianov, S. Y. Leveraging the Imaging Transmit Pulse to Manipulate Phase-Change Nanodroplets for Contrast-Enhanced Ultrasound. *IEEE Trans Ultrason Ferroelectr Freq Control* **66**, 692-700, doi:10.1109/TUFFC.2019.2895248 (2019).

103 Yoon, H., Zhu, Y. I., Yarmoska, S. K. & Emelianov, S. Y. Design and Demonstration of a Configurable Imaging Platform for Combined Laser, Ultrasound, and Elasticity Imaging. *IEEE Trans Med Imaging* **38**, 1622-1632, doi:10.1109/TMI.2018.2889736 (2019).

104 Breslin, J. W. *et al.* Lymphatic vessel network structure and physiology. *Comprehensive Physiology* **9**, 207-299 (2019).

105 Rockson, S. G. Lymphedema. *The American journal of medicine* **110**, 288-295 (2001).

106 Dieterich, L. C. & Detmar, M. Tumor lymphangiogenesis and new drug development. *Advanced drug delivery reviews* **99**, 148-160 (2016).

107 Stacker, S. A. *et al.* Lymphangiogenesis and lymphatic vessel remodelling in cancer. *Nature Reviews Cancer* **14**, 159-172 (2014).

108 Lyman, G. H. *et al.* American Society of Clinical Oncology guideline recommendations for sentinel lymph node biopsy in early-stage breast cancer. *Journal of clinical oncology* **23**, 7703-7720 (2005).

109 Thompson, J. *et al.* Sentinel lymph node status as an indicator of the presence of metastatic melanoma in regional lymph nodes. *Melanoma research* **5**, 255-260 (1995).

110 Mamelle, G. *et al.* Lymph node prognostic factors in head and neck squamous cell carcinomas. *The American journal of surgery* **168**, 494-498 (1994).

111 Chang, G. J., Rodriguez-Bigas, M. A., Skibber, J. M. & Moyer, V. A. Lymph node evaluation and survival after curative resection of colon cancer: systematic review. *Journal of the National Cancer Institute* **99**, 433-441 (2007).

112 Liang, R. *et al.* Liposomes-coated gold nanocages with antigens and adjuvants targeted delivery to dendritic cells for enhancing antitumor immune response. *Biomaterials* **149**, 41-50 (2017).

113 Miteva, D. O. *et al.* Transmural flow modulates cell and fluid transport functions of lymphatic endothelium. *Circulation research* **106**, 920 (2010).

114 Thomas, S. N., Vokali, E., Lund, A. W., Hubbell, J. A. & Swartz, M. A. Targeting the tumor-draining lymph node with adjuvanted nanoparticles reshapes the anti-tumor immune response. *Biomaterials* **35**, 814-824 (2014).

115 Weiler, M., Kassis, T. & Dixon, J. B. Sensitivity analysis of near-infrared functional lymphatic imaging. *Journal of biomedical optics* **17**, 066019 (2012).

116 Haley, P. J. The lymphoid system: a review of species differences. *Journal of toxicologic pathology* **30**, 111-123 (2017).

117 Goldberg, B. B. *et al.* Sentinel lymph nodes in a swine model with melanoma: contrast-enhanced lymphatic US. *Radiology* **230**, 727-734 (2004).

118 Matsunaga, T. O. *et al.* Phase-change nanoparticles using highly volatile perfluorocarbons: toward a platform for extravascular ultrasound imaging. *Theranostics* **2**, 1185 (2012).

119 Sheeran, P. S. *et al.* Decafluorobutane as a phase-change contrast agent for low-energy extravascular ultrasonic imaging. *Ultrasound in medicine & biology* **37**, 1518-1530 (2011).

120 Van den Broeck, W., Derore, A. & Simoens, P. Anatomy and nomenclature of murine lymph nodes: Descriptive study and nomenclatory standardization in BALB/cAnNCrl mice. *Journal of immunological methods* **312**, 12-19 (2006).

121 Pulaski, B. A. & Ostrand-Rosenberg, S. Mouse 4T1 breast tumor model. *Current protocols in immunology* **39**, 20.22. 21-20.22. 16 (2000).

122 Commerford, C. D. *et al.* Mechanisms of tumor-induced lymphovascular niche formation in draining lymph nodes. *Cell reports* **25**, 3554-3563. e3554 (2018).

123 Proulx, S. T. *et al.* Use of a PEG-conjugated bright near-infrared dye for functional imaging of rerouting of tumor lymphatic drainage after sentinel lymph node metastasis. *Biomaterials* **34**, 5128-5137 (2013).

124 Ma, Q. *et al.* Unexpected contribution of lymphatic vessels to promotion of distant metastatic tumor spread. *Science advances* **4**, eaat4758 (2018).

125 Jafarnejad, M., Woodruff, M. C., Zawieja, D. C., Carroll, M. C. & Moore Jr, J. Modeling lymph flow and fluid exchange with blood vessels in lymph nodes. *Lymphatic research and biology* **13**, 234-247 (2015).

126 Skobe, M. *et al.* Induction of tumor lymphangiogenesis by VEGF-C promotes breast cancer metastasis. *Nature medicine* **7**, 192-198 (2001).

127 Tao, K., Fang, M., Alroy, J. & Sahagian, G. G. Imagable 4T1 model for the study of late stage breast cancer. *BMC cancer* **8**, 228 (2008).

128 Bouffet, E. *et al.* Immune checkpoint inhibition for hypermutant glioblastoma multiforme resulting from germline biallelic mismatch repair deficiency. *Journal of clinical oncology* **34**, 2206-2211 (2016).

129 Carlo, M. I., Voss, M. H. & Motzer, R. J. Checkpoint inhibitors and other novel immunotherapies for advanced renal cell carcinoma. *Nature Reviews Urology* **13**, 420 (2016).

130 Dijkstra, K. K., Voabil, P., Schumacher, T. N. & Voest, E. E. Genomics-and transcriptomics-based patient selection for cancer treatment with immune checkpoint inhibitors: a review. *JAMA oncology* **2**, 1490-1495 (2016).

131 Gaillard, S. L., Secord, A. A. & Monk, B. The role of immune checkpoint inhibition in the treatment of ovarian cancer. *Gynecologic oncology research and practice* **3**, 11 (2016).

132 Hamanishi, J., Mandai, M. & Konishi, I. Immune checkpoint inhibition in ovarian cancer. *International immunology* **28**, 339-348 (2016).

133 Hude, I., Sasse, S., Engert, A. & Bröckelmann, P. J. The emerging role of immune checkpoint inhibition in malignant lymphoma. *Haematologica* **102**, 30-42 (2017).

134 Kudo, M. Immune checkpoint inhibition in hepatocellular carcinoma: basics and ongoing clinical trials. *Oncology* **92**, 50-62 (2017).

135 Mahoney, K. M., Freeman, G. J. & McDermott, D. F. The next immune-checkpoint inhibitors: PD-1/PD-L1 blockade in melanoma. *Clinical therapeutics* **37**, 764-782 (2015).

136 Rizvi, N. A. *et al.* Activity and safety of nivolumab, an anti-PD-1 immune checkpoint inhibitor, for patients with advanced, refractory squamous non-small-cell lung cancer (CheckMate 063): a phase 2, single-arm trial. *The Lancet Oncology* **16**, 257-265 (2015).

137 Graff, J. N. *et al.* Early evidence of anti-PD-1 activity in enzalutamide-resistant prostate cancer. *Oncotarget* **7**, 52810 (2016).

138 Ledford, H., Else, H. & Warren, M. Cancer immunologists scoop medicine Nobel prize. *Nature* **562**, 20-22 (2018).

139 Pardoll, D. M. The blockade of immune checkpoints in cancer immunotherapy. *Nature Reviews Cancer* **12**, 252-264 (2012).

140 Shao, K. *et al.* Nanoparticle-based immunotherapy for cancer. *ACS nano* **9**, 16-30 (2015).

141 Almeida, J. P. M., Figueroa, E. R. & Drezek, R. A. Gold nanoparticle mediated cancer immunotherapy. *Nanomedicine: Nanotechnology, Biology and Medicine* **10**, 503-514 (2014).

142 Oberli, M. A. *et al.* Lipid nanoparticle assisted mRNA delivery for potent cancer immunotherapy. *Nano letters* **17**, 1326-1335 (2017).

143 Cho, N.-H. *et al.* A multifunctional core–shell nanoparticle for dendritic cell-based cancer immunotherapy. *Nature nanotechnology* **6**, 675 (2011).

144 Hernot, S. & Klibanov, A. L. Microbubbles in ultrasound-triggered drug and gene delivery. *Advanced drug delivery reviews* **60**, 1153-1166 (2008).

145 Unger, E. C., Hersh, E., Vannan, M., Matsunaga, T. O. & McCreery, T. Local drug and gene delivery through microbubbles. *Progress in cardiovascular diseases* **44**, 45-54 (2001).

146 Santiesteban, D. Y., Hallam, K. A., Yarmoska, S. K. & Emelianov, S. Y. Color-coded perfluorocarbon nanodroplets for multiplexed ultrasound and photoacoustic imaging. *Nano Research* **12**, 741-747 (2019).

147 Alexopoulou, L., Holt, A. C., Medzhitov, R. & Flavell, R. A. Recognition of double-stranded RNA and activation of NF-κB by Toll-like receptor 3. *Nature* **413**, 732-738 (2001).

148 Berger, A. Th1 and Th2 responses: what are they? *Bmj* **321**, 424 (2000).

149 Knutson, K. L. & Disis, M. Tumor antigen-specific T helper cells in cancer immunity and immunotherapy. *Cancer Immunology, Immunotherapy* **54**, 721-728 (2005).

150 Xu, H.-M. Th1 cytokine-based immunotherapy for cancer. *Hepatobiliary & Pancreatic Diseases International* **13**, 482-494 (2014).

151 Cheever, M. A. & Chen, W. Therapy with cultured T cells: principles revisited. *Immunological reviews* **157**, 177-194 (1997).

152 Hood, Z. D. *et al.* Photothermal transformation of Au–Ag nanocages under pulsed laser irradiation. *Nanoscale* **11**, 3013-3020 (2019).

153 Sowers, T. *et al.* Laser threshold and cell damage mechanism for intravascular photoacoustic imaging. *Lasers in surgery and medicine* **51**, 466-474 (2019).

154 Karmali, P. P. & Chaudhuri, A. Cationic liposomes as non-viral carriers of gene medicines: resolved issues, open questions, and future promises. *Medicinal research reviews* **27**, 696-722 (2007).

155 Huang, S.-L. Liposomes in ultrasonic drug and gene delivery. *Advanced drug delivery reviews* **60**, 1167-1176 (2008).

156 Lasic, D. D. *Liposomes in gene delivery*. (CRC press, 1997).

157 Cheng, X. & Lee, R. J. The role of helper lipids in lipid nanoparticles (LNPs) designed for oligonucleotide delivery. *Advanced drug delivery reviews* **99**, 129-137 (2016).

158 Hunter, R. J. *Zeta potential in colloid science: principles and applications*. Vol. 2 (Academic press, 2013).

159 Yu, J., Chen, X., Villanueva, F. S. & Kim, K. Vaporization and recondensation dynamics of indocyanine green-loaded perfluoropentane droplets irradiated by a short pulse laser. *Applied Physics Letters* **109**, 243701 (2016).

160 Hasan, M., Ruksznis, C., Wang, Y. & Leifer, C. A. Antimicrobial peptides inhibit polyinosinic-polycytidylic acid-induced immune responses. *The Journal of Immunology* **187**, 5653-5659 (2011).

161 Ding, A. H., Nathan, C. F. & Stuehr, D. Release of reactive nitrogen intermediates and reactive oxygen intermediates from mouse peritoneal macrophages. Comparison of activating cytokines and evidence for independent production. *The Journal of Immunology* **141**, 2407-2412 (1988).

162 Sun, J., Zhang, X., Broderick, M. & Fein, H. Measurement of nitric oxide production in biological systems by using Griess reaction assay. *Sensors* **3**, 276-284 (2003).

163 Lundberg, J. O., Weitzberg, E. & Gladwin, M. T. The nitrate–nitrite–nitric oxide pathway in physiology and therapeutics. *Nature reviews Drug discovery* **7**, 156-167 (2008).

164 Moshage, H., Kok, B., Huizenga, J. R. & Jansen, P. Nitrite and nitrate determinations in plasma: a critical evaluation. *Clinical chemistry* **41**, 892-896 (1995).

165 Schroder, K., Sweet, M. J. & Hume, D. A. Signal integration between IFN γ and TLR signalling pathways in macrophages. *Immunobiology* **211**, 511-524 (2006).

166 Tripathi, P., Tripathi, P., Kashyap, L. & Singh, V. The role of nitric oxide in inflammatory reactions. *FEMS Immunology & Medical Microbiology* **51**, 443-452 (2007).

167 MacMicking, J., Xie, Q.-w. & Nathan, C. Nitric oxide and macrophage function. *Annual review of immunology* **15**, 323-350 (1997).

168 Kim, Y. J. & Park, W. Anti-inflammatory effect of Quercetin on RAW 264.7 mouse macrophages induced with Polyinosinic-Polycytidylic acid. *Molecules* **21**, 450 (2016).

169 Du, Z., Munye, M. M., Tagalakis, A. D., Manunta, M. D. & Hart, S. L. The role of the helper lipid on the DNA transfection efficiency of lipopolyplex formulations. *Scientific reports* **4**, 7107 (2014).

170 Hattori, Y., Suzuki, S., Kawakami, S., Yamashita, F. & Hashida, M. The role of dioleoylphosphatidylethanolamine (DOPE) in targeted gene delivery with mannosylated cationic liposomes via intravenous route. *Journal of controlled release* **108**, 484-495 (2005).

171 Marsh, J. N. *et al.* Improvements in the ultrasonic contrast of targeted perfluorocarbon nanoparticles using an acoustic transmission line model. *IEEE transactions on ultrasonics, ferroelectrics, and frequency control* **49**, 29-38 (2002).

172 Ellegala, D. B. *et al.* Imaging tumor angiogenesis with contrast ultrasound and microbubbles targeted to α v β 3. *Circulation* **108**, 336-341 (2003).

173 Hamilton, A. J. *et al.* Intravascular ultrasound molecular imaging of atheroma components in vivo. *Journal of the American College of Cardiology* **43**, 453-460 (2004).

174 Klibanov, A. L. *et al.* Detection of individual microbubbles of ultrasound contrast agents: imaging of free-floating and targeted bubbles. *Investigative radiology* **39**, 187-195 (2004).

175 Noguchi, S. *et al.* Mutations in the dystrophin-associated protein γ -sarcoglycan in chromosome 13 muscular dystrophy. *Science* **270**, 819-822 (1995).

176 Fahey, P. *et al.* Lateral diffusion in planar lipid bilayers. *Science* **195**, 305-306 (1977).

177 Lassailly, F., Griessinger, E. & Bonnet, D. "Microenvironmental contaminations" induced by fluorescent lipophilic dyes used for noninvasive in vitro and in vivo cell tracking. *Blood, The Journal of the American Society of Hematology* **115**, 5347-5354 (2010).

178 Carmeliet, P. & Jain, R. K. Angiogenesis in cancer and other diseases. *nature* **407**, 249 (2000).

179 Patan, S., Munn, L. L. & Jain, R. K. Intussusceptive microvascular growth in a human colon adenocarcinoma xenograft: a novel mechanism of tumor angiogenesis. *Microvascular research* **51**, 260-272 (1996).

180 Asahara, T., Kalka, C. & Isner, J. Stem cell therapy and gene transfer for regeneration. *Gene therapy* **7**, 451 (2000).

181 Rafii, S. Circulating endothelial precursors: mystery, reality, and promise. *The Journal of clinical investigation* **105**, 17-19 (2000).

182 Baish, J. W. & Jain, R. K. Fractals and cancer. *Cancer research* **60**, 3683-3688 (2000).

183 Helmlinger, G., Yuan, F., Dellian, M. & Jain, R. K. Interstitial pH and pO2 gradients in solid tumors in vivo: high-resolution measurements reveal a lack of correlation. *Nature medicine* **3**, 177 (1997).

184 Dvorak, H., Nagy, J., Feng, D., Brown, L. & Dvorak, A. in *Vascular Growth Factors and Angiogenesis* 97-132 (Springer, 1999).

185 Jain, R. K. Transport of molecules in the tumor interstitium: a review. *Cancer research* **47**, 3039-3051 (1987).

186 Jain, R. K. & Baxter, L. T. Mechanisms of heterogeneous distribution of monoclonal antibodies and other macromolecules in tumors: significance of elevated interstitial pressure. *Cancer research* **48**, 7022-7032 (1988).

187 Iyer, A. K., Khaled, G., Fang, J. & Maeda, H. Exploiting the enhanced permeability and retention effect for tumor targeting. *Drug discovery today* **11**, 812-818 (2006).

188 Meng, H. *et al.* Use of size and a copolymer design feature to improve the biodistribution and the enhanced permeability and retention effect of doxorubicin-loaded mesoporous silica nanoparticles in a murine xenograft tumor model. *ACS nano* **5**, 4131-4144 (2011).

189 Jain, R. K. *et al.* Endothelial cell death, angiogenesis, and microvascular function after castration in an androgen-dependent tumor: role of vascular endothelial growth factor. *Proceedings of the National Academy of Sciences* **95**, 10820-10825 (1998).

190 Diop-Frimpong, B., Chauhan, V. P., Krane, S., Boucher, Y. & Jain, R. K. Losartan inhibits collagen I synthesis and improves the distribution and efficacy of nanotherapeutics in tumors. *Proceedings of the National Academy of Sciences* **108**, 2909-2914 (2011).

191 Chauhan, V. P. *et al.* Angiotensin inhibition enhances drug delivery and potentiates chemotherapy by decompressing tumour blood vessels. *Nature communications* **4**, 2516 (2013).

192 Stylianopoulos, T. & Jain, R. K. Combining two strategies to improve perfusion and drug delivery in solid tumors. *Proceedings of the National Academy of Sciences*, 201318415 (2013).

193 Williams, R. *et al.* Characterization of submicron phase-change perfluorocarbon droplets for extravascular ultrasound imaging of cancer. *Ultrasound in medicine & biology* **39**, 475-489 (2013).

194 Tang, W. *et al.* Organic semiconducting photoacoustic nanodroplets for laser-activatable ultrasound imaging and combinational cancer therapy. *ACS nano* **12**, 2610-2622 (2018).

195 Muller, W. J. *et al.* Synergistic interaction of the Neu proto-oncogene product and transforming growth factor alpha in the mammary epithelium of transgenic mice. *Molecular and cellular biology* **16**, 5726-5736 (1996).

196 Guy, C., Cardiff, R. & Muller, W. Induction of mammary tumors by expression of polyomavirus middle T oncogene: a transgenic mouse model for metastatic disease. *Molecular and cellular biology* **12**, 954-961 (1992).

197 Howlader, N. *et al.* US incidence of breast cancer subtypes defined by joint hormone receptor and HER2 status. *Journal of the National Cancer Institute* **106**, dju055 (2014).

198 Yang, L. *et al.* Single chain epidermal growth factor receptor antibody conjugated nanoparticles for in vivo tumor targeting and imaging. *Small* **5**, 235-243 (2009).

199 Satpathy, M. *et al.* Active targeting using her-2-affibody-conjugated nanoparticles enabled sensitive and specific imaging of orthotopic her-2 positive ovarian tumors. *Small* **10**, 544-555 (2014).

200 Yang, L. *et al.* uPAR-targeted optical imaging contrasts as theranostic agents for tumor margin detection. *Theranostics* **4**, 106 (2014).

201 Liu, J. *et al.* Low-intensity focused ultrasound (LIFU)-induced acoustic droplet vaporization in phase-transition perfluoropentane nanodroplets modified by folate for ultrasound molecular imaging. *International journal of nanomedicine* **12**, 911 (2017).

202 Litvinov, S. V., Velders, M. P., Bakker, H., Fleuren, G. J. & Warnaar, S. O. Ep-CAM: a human epithelial antigen is a homophilic cell-cell adhesion molecule. *The Journal of cell biology* **125**, 437-446 (1994).

203 Armstrong, A. & Eck, S. L. EpCAM: a new therapeutic target for an old cancer antigen. *Cancer biology & therapy* **2**, 320-325 (2003).

204 Liu, X. *et al.* Epithelial-type systemic breast carcinoma cells with a restricted mesenchymal transition are a major source of metastasis. *Science advances* **5**, eaav4275 (2019).

205 Jenkins, S. V. *et al.* Triple-negative breast cancer targeting and killing by EpCAM-directed, plasmonically active nanodrug systems. *NPJ precision oncology* **1**, 1-9 (2017).

206 Charrois, G. J. & Allen, T. M. Rate of biodistribution of STEALTH® liposomes to tumor and skin: influence of liposome diameter and implications for toxicity

and therapeutic activity. *Biochimica et Biophysica Acta (BBA)-Biomembranes* **1609**, 102-108 (2003).

207 Hallam, K. A. & Emelianov, S. Y. Toward optimization of blood brain barrier opening induced by laser-activated perfluorocarbon nanodroplets. *Biomedical optics express* **10**, 3139-3151 (2019).

208 Hallam, K. A., Donnelly, E. M., Karpiouk, A. B., Hartman, R. K. & Emelianov, S. Y. Laser-activated perfluorocarbon nanodroplets: a new tool for blood brain barrier opening. *Biomedical optics express* **9**, 4527-4538 (2018).

209 Das, S. & Marsden, P. A. Angiogenesis in glioblastoma. *New England Journal of Medicine* **369**, 1561-1563 (2013).

210 Bernstein, J. J. & Woodard, C. A. Glioblastoma cells do not intravasate into blood vessels. *Neurosurgery* **36**, 124-132 (1995).

211 Förster, T. Zwischenmolekulare energiewanderung und fluoreszenz. *Annalen der physik* **437**, 55-75 (1948).

212 Förster, T. *Delocalized excitation and excitation transfer*. (Florida State University, 1965).

213 Hussain, S. A. An introduction to fluorescence resonance energy transfer (FRET). *arXiv preprint arXiv:0908.1815* (2009).

214 Babu, P. S. *et al.* Bis (3, 5-diiodo-2, 4, 6-trihydroxyphenyl) squaraine photodynamic therapy disrupts redox homeostasis and induce mitochondria-mediated apoptosis in human breast cancer cells. *Scientific Reports* **7** (2017).

215 Ramaiah, D. *et al.* Halogenated squaraine dyes as potential photochemotherapeutic agents. Synthesis and study of photophysical properties and quantum efficiencies of singlet oxygen generation. *Photochemistry and photobiology* **65**, 783-790 (1997).

216 Laudien, J. *et al.* Perfluorodecalin-soluble fluorescent dyes for the monitoring of circulating nanocapsules with intravital fluorescence microscopy. *Journal of microencapsulation* **31**, 738-745 (2014).

217 Sletten, E. M. & Swager, T. M. Fluorofluorophores: fluorescent fluorous chemical tools spanning the visible spectrum. *Journal of the American Chemical Society* **136**, 13574-13577 (2014).

218 Zimmermann, T., Marrison, J., Hogg, K. & O'Toole, P. in *Confocal microscopy* 129-148 (Springer, 2014).

219 Gu, Y., Di, W., Kelsell, D. & Zicha, D. Quantitative fluorescence resonance energy transfer (FRET) measurement with acceptor photobleaching and spectral unmixing. *Journal of microscopy* **215**, 162-173 (2004).

220 Li, D. S. *et al.* Polypyrrole-coated perfluorocarbon nanoemulsions as a sono-photoacoustic contrast agent. *Nano letters* **17**, 6184-6194 (2017).

221 Arnal, B. *et al.* Sono-photoacoustic imaging of gold nanoemulsions: Part II. Real time imaging. *Photoacoustics* **3**, 11-19 (2015).

222 Wilhelm, S. *et al.* Analysis of nanoparticle delivery to tumours. *Nature reviews materials* **1**, 1-12 (2016).

223 Kumar, S., Aaron, J. & Sokolov, K. Directional conjugation of antibodies to nanoparticles for synthesis of multiplexed optical contrast agents with both delivery and targeting moieties. *Nature protocols* **3**, 314 (2008).

224 Sheeran, P. S. *et al.* Contrast-enhanced ultrasound imaging and in vivo circulatory kinetics with low-boiling-point nanoscale phase-change perfluorocarbon agents. *Ultrasound in medicine & biology* **41**, 814-831 (2015).